Convectively Generated Internal Gravity Waves in Venus's Middle Atmosphere: Momentum Transport and Radio Scintillations

Thesis by

Stephen S. Leroy

In Partial Fulfillment of the Requirements
for the Degree of
Doctor of Philosophy

California Institute of Technology
Pasadena, California

1994

(Defended May 23, 1994)

Acknowledgments

My thesis advisor and coauthor Andy Ingersoll has been invaluable to my education here at Caltech. Besides the focused guidance and motivation he has provided me along the way, he has also kindly invited me to the Ingersoll Ranch Estates for Thanksgiving dinners and Independence Day picnics at which his family made me feel decidedly welcome. If I truly am a scientist now, Andy is the responsible party.

Several people have provided me with valuable assistance and discussion in the course of my dissertation studies. Peter Goldreich told me how to do the problem on the back of an envelope. Yuk Yung, my academic advisor, always wondered how my work might someday be relevant to atmospheric chemistry on Venus (and someday it still might be). More recently, Bruno Sicardy has provided observational evidence consistent with my work, which is a great relief to me.

My other proposition, involving near infrared observations of the outer planets using the Hale telescope at Mt. Palomar, has been a challenging, fun, and rewarding experience for me. Phil Nicholson of Cornell University provided me with much of the guidance and Keith Matthews taught me how to do experiments with really big telescopes. Someday I hope to publish some of this work.

This thesis looks like several which came before mine because I used a set of TeX macros provided to me by Michelle Santee. The macros were put together by a few preceding generations of planetary science grad students, including Randy Kirk, Don Rudy, Kathy Shah, Julie Moses, and Rich Achterberg. Using these macros I learned alot about TeX, and I highly recommend them to future thesis writers.

Within the planetary science department I have been spoiled as a grad student. My officemates past and present, mainly Rich Dissly, Laszlo Keszthelyi, Mimi Gerstell, and Tomas Svitek, have put up with my pride and occasional ill temperament so well that I can say I have made more friends here than at any other time in my life. There are certainly many other fellow students who have made department life a real joy, and you know who you are. Thanks again to Yuk Yung for entertaining us starving grad students with the best Chinese food in the area and some of the most thought provoking philosophy I have ever heard.

While at Caltech I was able to continue engaging my love of playing piano by participating in Caltech chamber music activities. Much thanks goes to Delores Bing and the many wonderful musicians here with whom I have had the pleasure of playing some challenging and beautiful music. Hopefully, I can continue do so wherever I might end up.

With much sadness, a terrifically close group of friends is parting ways for the time being. Carl and Roxanne Brune, Rob Thompson and Charles Noussair have given me a life outside of my office. If we can stay distributed around the world, we will all always have great places to visit! We should have done more camping trips.

I dedicate this thesis, if it is allowed, to my parents Stanley and Caroline Leroy and my "Oma" Edith Leroy. I think I worried them a little too much about my stay on the west coast with earthquakes and whatnot. Your loving support has kept me going throughout my entire life, especially during those moments when I was most dispirited. This thesis is a testament to what you have created, and hopefully that's a compliment.

During my final months as a student, Eileen Milnes has been a dear, loving, and constant companion. The community at the Church of St. Philip the Apostle has been wonderful spiritual and friendly support for me. Lastly, I humbly thank my Creator who played no small part in providing me with the endurance necessary toward completing a Ph.D. at the California Institute of Technology.

This work has been supported by a graduate fellowship from the National Science Foundation and grant NAGW-1956 of the NASA Planetary Atmospheres program.

Abstract

This work is divided into two papers. Firstly, we theoretically calculate how gravity waves are emitted from the neutrally buoyant dry convection in Venus's middle atmosphere and investigate whether such waves play a significant role in supporting the superrotation of Venus's atmosphere. Secondly, we attempt to explain the radio scintillations seen in the occultations of many spacecraft, particularly Pioneer Venus, as caused by convectively generated gravity waves. Below are the abstracts of the two papers presented in this thesis.

Paper I:

We calculate the emission of internal gravity waves from neutrally buoyant dry convection embedded within a stable atmosphere with static stability and zonal winds varying in height. We apply this theory to Venus's middle atmosphere to investigate whether these waves can help support the superrotation of Venus's atmosphere. Furthermore, we model the radio scintillation data obtained for Venus as caused by such internal gravity waves. The emission mechanism is similar to that suggested for driving the gravity modes of the Sun. We assume a background atmosphere on which we have superimposed linear wave propagation. Waves are damped by reabsorption by the convection, wavebreaking in the stable atmosphere, critical layer absorption, and by wave radiation to space. Wavebreaking is imposed wherever the waves become convectively unstable. Inertial effects are neglected and plane parallel geometry is assumed. Propagation of the waves is handled using a second order WKBJ approximation. A complete three dimensional ensemble of waves is retained.

We show that both westward and eastward propagating waves exert strong accelerations on the mean flow. The westward propagating carry enough momentum to support the westward superrotation between the convection and the cloud-tops;

however, the bulk of the wave momentum flux is critically absorbed and deposited within a kilometer of the convection because most of the waves propagate slowly in the horizontal. The eastward propagating waves are found to exert large decelerations above the zonal wind maximum. The decelerations are larger than 20 m s^{-1} day^{-1}, similar to wave drag in the Earth's mesosphere.

In the course of evaluating our model, we have found that dry convection must have "penetrative" mixed layers above and below it. This arises from wavebreaking of gravity waves immediately after their generation. The effect of the penetrative layer is to filter wave emission and to create a discontinuity in the background temperature lapse rate dT/dz. The latter may be observable in atmospheres.

Paper II:

We simulate radio scintillations as they would appear in Pioneer Venus radio occultation data assuming that the index of refraction fluctuations in Venus's atmosphere responsible for the scintillations are directly caused by gravity wave fluctuations. We assume that the gravity waves are created by a global convection layer between 50 and 55 km altitude in Venus's atmosphere and propagate vertically. Associated with the gravity waves are density fluctuations which create the index of refraction variations. We compare the simulated scintillations with data and argue that this theory for the radio scintillations is preferable to the theory that the scintillations are caused by clear air turbulence in Venus's atmosphere.

We show that these gravity waves can explain the shape and amplitude of the radio scintillation variance spectra in frequency. The shape of the simulated radio scintillation variance spectra in frequency is nearly a direct result of a saturated spectrum of breaking gravity waves. This saturated spectrum is the spectrum of breaking gravity waves in the vertical wavenumber. On the other hand, the overall

amplitude is subject to parameters such as the intensity of the convection, the angle between the zonal winds and the beam path, and the zonal wind profile at polar latitudes. Limits can be placed, though, on the intensity of the convection which generates the waves and on the angle between the radio beam path and the winds in Venus's atmosphere. We find that the convection in Venus's middle atmosphere, even in polar regions, must transport 1 W/m^2 to create gravity waves strong enough to break. This result is dependent on the amplitude of the zonal winds at polar latitudes.

Table of Contents

Acknowledgments iii

Abstract vi

Table of Contents ix

List of Figures xi

List of Tables xii

I. Convective Generation of Gravity Waves in Venus's Atmosphere: Gravity Wave Spectrum and Momentum Transport 1

1. Introduction 5

2. Analytic solutions 20

2.1 The wave generation equation 20

2.2 The formal solution 25

2.3 Homogeneous solutions 28

2.3.1 The homogeneous solution $h(z)$ 31

2.3.2 The homogeneous solution $g(z)$ 39

2.4 The Wronskian $\mathrm{Wr}(g, h)$ 42

2.5 The forcing 43

2.6 Variance properties of the turbulence 47

2.7 Momentum flux 51

2.8 Wavebreaking 58

2.9 Trapped wave amplitudes 60

2.9.1 The thick barrier approximation 61

2.9.2 The thin barrier approximation 67

2.10 Reflection coefficients, finesse, and the thin lid 70

3. Numerical computations 75

3.1 Model I 75

3.2 Model II 88

3.3 Model III 93

3.3.1 The penetrative layer 93

3.3.2 Replacement algorithm for trapped waves 95

3.3.3 Temperature variance spectra and critical layer breaking 97

3.3.4 Momentum and energy deposition 108

4. Summary and Discussion 116

4.1 Summary of results 116

4.2 Discussion 121

4.3 Generalizations and predictions 125

II. Radio Scintillations in Venus's Atmosphere: Application of a Theory of Gravity Wave Generation 129

1. Introduction 132

2. Implementing Gravity Waves 140

3. Scintillation Simulations 146

3.1 Scintillation data 146

3.2 Simulation parameters 148

3.3 Simulations 149

3.4 Varying the background atmosphere 159

4. Summary and Discussion 163

4.1 Summary 163

4.2 Discussion 167

4.3 Gravity waves or turbulence? 169

4.4 Prediction 173

References 175

Appendix A: Tabulating the function $h(z)$ 185

Appendix B: The derivative of $h(z)$ 195

Appendix C: Weak Scintillation Theory 199

List of Figures

PAPER I:

1. Wave cases 37
2. Model wind and stability profiles 76
3. Model I wavemode 78
4. Model I temperature variance spectra 79
5. Model I momentum and energy fluxes 84
6. The forcing efficiencies 87
7. Retrograde wave cases 89
8. Model II momentum and energy fluxes 91
9. Resonances in the wave response 96
10. Temperature variance at emission 98
11. Temperature variance spectrum at 58 km 99
12. Temperature variance spectrum at constant phase speed 102
13. Coarse temperature variance contour plot 105
14. Continuum temperature variance contour plot 106
15. Temperature variance vs. altitude 107
16. Momentum deposition at $W_c=3$ m/s 110
17. Momentum deposition at $W_c=5$ m/s 111
18. Momentum deposition with high altitude superrotation 114

PAPER II:

1. S-band scintillation data 147
2. S-band scintillation power spectrum 147
3. Simulated scintillations, zero entry angle 150
4. Simulated spectra 153
5. Simulated spectra 153
6. Simulation with resolved fringes 155

7. Simulated scintillations 158
8. Simulated scintillations 158
9. Modified background stability 160
10. Modified stability simulations 160
11. Modified zonal winds 161
12. Modified wind simulations 161

APPENDIX A:

1. Turning point solution 189

APPENDIX C:

1. Occultation geometry 201

List of Tables

PAPER I:

1. Resonance properties 69

PAPER I

Convective Generation of Gravity Waves in Venus's Atmosphere: Gravity Wave Spectrum and Momentum Transport

Convective Generation of Gravity Waves in Venus's Atmosphere: Gravity Wave Spectrum and Momentum Transport

Stephen S. Leroy

and

Andrew P. Ingersoll

Division of Geological and Planetary Sciences
California Institute of Technology
Pasadena, California 91125

To be submitted to: *J. Atmos. Sci.*

Abstract

We calculate the emission of internal gravity waves from neutrally buoyant dry convection embedded within a stable atmosphere with static stability and zonal winds varying in height. We apply this theory to Venus's middle atmosphere to investigate whether these waves can help support the superrotation of Venus's atmosphere. Furthermore, we model the radio scintillation data obtained for Venus as caused by such internal gravity waves. The emission mechanism is similar to that suggested for driving the gravity modes of the Sun. We assume a background atmosphere on which we have superimposed linear wave propagation. Waves are damped by reabsorption by the convection, wavebreaking in the stable atmosphere, critical layer absorption, and by wave radiation to space. Wavebreaking is imposed wherever the waves become convectively unstable. Inertial effects are neglected and plane parallel geometry is assumed. Propagation of the waves is handled using a second order WKBJ approximation. A complete three dimensional ensemble of waves is retained.

We show that both westward and eastward propagating waves exert strong accelerations on the mean flow. The westward propagating carry enough momentum to support the westward superrotation between the convection and the cloud-tops; however, the bulk of the wave momentum flux is critically absorbed and deposited within a kilometer of the convection because most of the waves propagate slowly in the horizontal. The eastward propagating waves are found to exert large decelerations above the zonal wind maximum. The decelerations are larger than 20 m s^{-1} day^{-1}, similar to wave drag in the Earth's mesosphere.

In the course of evaluating our model, we have found that dry convection must have "penetrative" mixed layers above and below it. This arises from wavebreaking of gravity waves immediately after their generation. The effect of the penetrative layer is to filter wave emission and to create a discontinuity in the background temperature

lapse rate dT/dz. The latter may be observable in atmospheres.

1. Introduction

In this paper we present a theory of internal gravity wave generation by and propagation from an infinite horizontal convecting layer embedded in an otherwise stable atmosphere with shear. Our intent is to investigate how waves generated by this mechanism may support the rapid rotation of Venus's atmosphere. In the investigation, we theoretically calculate a spectrum of waves emitted from dry convection. In an accompanying paper we test our theory against observations by using our gravity wave spectra in simulating radio scintillation data as if it were obtained by the Pioneer Venus mission and subsequently compare our simulations to the Pioneer Venus data. In the course of determining the gravity wave spectrum, we present some insights into the nature of a fully three dimensional ensemble of waves.

In this introduction we first give a brief description of the state of Venus's atmosphere. This includes pointing out specific criteria that any theoretical explanation for the superrotation must satisfy. Secondly, we present an overview of some models of the dynamical state of its atmosphere in the form of a brief literature review. Thirdly, we present our hypothesis for the support of the Venus superrotation by gravity waves generated by neutrally buoyant convection. Fourthly, since gravity waves have been studied considerably in the Earth's atmosphere, we apply some observational constraints found in gravity wave spectra in the Earth's atmosphere to our theory for gravity wave generation. Finally, we describe our analytic and numerical calculations.

Features in the clouds in Venus's atmosphere rotate with a roughly four day period. Despite early arguments that this feature is only a manifestation of a planetary wave and does not reflect the atmospheric wind speeds (Young 1975), several atmospheric probes have since found that the atmosphere does indeed rotate with a roughly four day period (Marov *et al.* 1973; Marov 1978; Murray, Belton *et al.* 1974;

Seiff *et al.* 1980). Because this rotation rate is approximately sixty times the rotation rate of the solid planet, Venus's atmosphere is said to superrotate. This contrasts starkly with the Earth's atmosphere, which rotates only marginally faster than the solid planet. There must be some mechanism at work in Venus's atmosphere which distinguishes it substantially from the Earth's and those of most other planets. It has been suggested recently, however, that Titan's atmosphere may also be superrotating because of a large obliquity in its atmosphere apparent during the 28-Sgr occultation Hubbard *et al.* 1993).

Venus's winds are entirely westward, the same direction as the planet's rotation. The winds increase monotonically with height from the surface to the cloud-tops ($\sim$ 70 km). The winds are slight within the first ten kilometers of the surface, where convective activity is thought to reduce the shear (Schubert *et al.* 1980). Between 10 and 50 km the winds increase with height with especially strong shears occurring in regions of high static stability. Between 50 and 55 km lies a thick cloud layer which has been observed to convect vigorously. Not only have convective downdrafts been observed *in situ* by the VEGA balloons (Sagdeev *et al.* 1986), but many descent probes indicate that this layer has a nearly neutral static stability and little wind shear within it. Above this layer, the atmosphere becomes strongly stable and the wind shear pronounced. Pioneer Venus orbiter infrared data showed a reversal in the equator-to-pole temperature difference, which is indicative of a reversal in wind shear above 70 km altitude. On the other hand, millimeter interferometric experiments have shown that the atmosphere continues to superrotate near 100 km altitude (Shah 1992), an inconsistency which we do not wish to discuss, but we shall consider in our work.

In determining the zonal winds globally, time sequences of UV and infrared images from Mariner 10, Pioneer Venus, and Galileo have been used. In each of these data sets, it was assumed that the velocities measured were reflective of the winds somewhere in the 60 to 70 km range. At the time of Mariner 10, the cloud-top winds were observed to have constant angular momentum per unit mass from the equator up to about 55° latitude. Poleward of 55°, rotation on spheres was thought to occur meaning that the angular velocity of the fluid flow around the planet's spin axis is only a function of altitude. Early in the Pioneer Venus encounter (1978–1980), the winds were observed to exhibit more nearly global rotation on spheres (Rossow *et al.* 1980). The Galileo project observed winds which had nearly constant velocity up to 60° latitude (Belton *et al.* 1991). Thus, the observations show that the zonal winds vary in time. The behavior common in all of the observations is that the angular momentum per unit mass of the cloud-top winds is always maximized near the equator.

Many theories and papers have been published over the past two dozen years concerning Venus's atmospheric superrotation. Thus far, four of the theories have become the most commonly discussed: the "moving flame" hypothesis, atmospheric tides, equatorward transport of angular momentum by eddies within a Hadley circulation, and vertical transport of momentum by eddies within a Hadley circulation. We distinguish between mass tides, which involve a solar torque on the atmosphere, and radiative tides, which involve an internal redistribution of angular momentum. Radiative tides are generally considered as large scale, dominantly horizontal eddies. For a discussion of the first three theories, see the review article by Schubert. Gravity waves have been invoked within the framework of the third and fourth hypotheses, thus our discussion will only deal with these. Our model of the superrotation fits within the fourth hypothesis.

Any theory of the superrotation must explain how Venus's atmosphere can maintain a maximum in the angular momentum per unit mass at an altitude of about 70 km above the equator. In a zonally symmetric (no eddies to redistribute angular momentum over large scales) Hadley circulation, the only source of angular for the atmosphere is from the surface which exerts a drag on the atmosphere. In the presence of a finite amount of friction, such an atmosphere cannot have a local maximum or minimum in the angular momentum per unit mass, because such a point would imply the presence of an alternate source of angular momentum (Hide 1969 & 1970). Since a maximum in the angular momentum per unit mass does exist at the cloud-tops near the equator, some nonzonally symmetric disturbance, such as an eddy or a wave, must be responsible for creating the maximum in the angular momentum per unit mass at the equatorial cloud-tops.

The Gierasch mechanism (Gierasch 1975) takes advantage of the fact that the Hadley circulation can explain the global net upward transport of angular momentum. In order that the cloud-top angular momentum be maximized, an eddy flux is required to transport angular momentum from high latitudes to low latitudes near the cloud-tops. Gierasch recognized that some eddies can transport angular momentum down an angular velocity gradient in latitude. Such eddies should not transport heat as efficiently as angular momentum, however, lest the mean Hadley circulation be destroyed (Kalnay-Rivas 1975). Barotropic eddies do satisfy these requirements (Rossow and Williams 1979). Indeed, numerical models have shown that a zonal superrotation can be realized with such a mechanism (Del Genio *et al.* 1993). Of the many disturbances seen in UV and near infrared imaging of the atmosphere, none suggest the appropriate horizontal transport of angular momentum, though (Limaye and Suomi 1981).

The Gierasch mechanism does not explicitly require barotropic eddies. Waves observed in the atmosphere may transport eastward momentum to high latitudes and thus westward momentum to equatorial latitudes. Gierasch (1987) and Schinder et al. (1990) suggest that waves are generated in the clouds by the vigorous convection between 50 and 55 km altitude and some of the waves are trapped within ducts above and below the convection layer. These trapped waves are restricted to horizontal propagation and will essentially transport eastward angular momentum toward the poles, thus giving the equatorial middle atmosphere a westward impulse. They suggest that the global horizontal "Y" pattern seen in UV images may be a manifestation of the trapped gravity waves. This theory for superrotation is supported by the large static stability of the middle atmosphere, the likelihood that the convection is more vigorous at the equator than at the poles because of the distribution of solar heating in latitude, and that gravity waves are nearly ubiquitous in the Earth's atmosphere.

Other theories of the superrotation rely on a net upward transport of zonal angular momentum near the equator and advection of angular momentum by a Hadley circulation away toward the poles. If one ignores the effects of eddies, a circulation for the atmosphere can be found by only imposing a diurnally averaged heating profile. This type of circulation is called a mean meridional circulation (see Andrews, Holton, Leovy 1987). Differences between such a flow and the actual flow can be characterized by a pattern of angular momentum sources and sinks created by divergences in the Eliassen-Palm flux (Andrews and McIntyre 1976). Hou and Goody (1985) have performed a diagnostic analysis in which they have calculated how waves and eddies redistribute angular momentum horizontally and vertically in Venus's atmosphere given the heating rates of Young and Pollack (1977). Indeed, their results show patterns of wave flux divergences required to sustain different models of the mean flow. The results tantalizingly imply that both horizontal and vertical transport of angular momentum within the atmosphere must take place. This analysis required that the atmosphere be statically stable throughout the regions of interest, and thus the role of wave transport to or from the neutrally buoyant layer between 50 and 55 km within the clouds may be misrepresented. Nevertheless, the pattern of Eliassen-Palm flux divergences must be explained. Hou and Goody suggest that atmospheric tides may be responsible for the diagnostic pattern of flux divergence and would be responsible for supporting strong vertical shears in the zonal wind. Hou and Farrell (1987) have postulated that small scale gravity waves play an active role in sustaining the strong shear below the cloud-tops and have calculated the necessary momentum flux spectrum in zonal phase speed. That such a spectrum exists has not been demonstrated observationally nor theoretically. In the end, this diagnostic study is helpful in understanding the superrotation, but by its nature it cannot determine what waves and eddies are responsible for driving the superrotation.

Atmospheric tides, which are internal gravity waves characterized by a zonal phase speed equal to that of the Sun's apparent motion over the planet's surface, have long been thought to help sustain the superrotation. The possibility that atmospheric tides may transport a substantial amount of zonal momentum vertically near the equator was first suggested by Fels and Lindzen (1974). Subsequent work is described in the review article by Schubert. Recently, Leovy (1991) and Baker and Leovy (1991) have investigated the role of atmospheric tides in the context of a mean meridional circulation. They performed numerical integrations in time from several initial states with mean and semidiurnal heating rates provided by Crisp (1983). With some horizontal diffusion, the resultant zonal winds were shown to resemble those on Venus, and the tidal divergence was partly balanced by the meridional transport, suggesting a significant role for atmospheric tides in supporting equatorial superrotation. It is not clear in their model, however, to what extent the horizontal diffusion is supporting the superrotation. If the horizontal diffusion is significant, then it is the Gierasch mechanism that is at work. Furthermore, the instability of the model for low static stabilities, however, clouds the picture of how atmospheric tides would interact with the mean meridional circulation to support global superrotation. As with Hou and Goody, unstable layers in the atmosphere cannot be handled when working in the context of a mean meridional circulation. Nevertheless, Pechman and Ingersoll (1984) have successfully shown that atmospheric tides are prominent in the Pioneer Venus Orbiter Infrared data, and thus must play some role in Venus's atmospheric dynamics. They also showed that the atmospheric accelerations which result from the forcing of tides are of the right magnitude to support the zonal winds (Pechman 1983).

We hypothesize that internal gravity waves at cloud levels in Venus's atmosphere can support the superrotation in a manner similar to tidal theories. These waves must act to transport net westward momentum upward from their source region and/or net eastward downward from their source. Vertically propagating waves eventually interact with the atmosphere by depositing their momentum and energy only when they are somehow dissipated. Possible damping mechanisms include radiative and viscous decay, but the damping mechanism of prime importance in this theory is critical layer absorption.

Critical layers refer to altitudes at which individual waves have zero intrinsic frequency (in the local rest frame of the fluid). Waves which encounter their critical layers are commonly thought to deposit most of their momentum and energy at that level (Booker and Bretherton 1967). The intrinsic frequency of a wave can be written as $\tilde{\omega} = k_x(c_x - \bar{u}(z))$ where k_x is the horizontal wavenumber in the direction of the background wind $\bar{u}(z)$ and c_x is the horizontal phase speed of an individual wave in the direction of the wind. We will consider eastward as positive in discussing wind speeds; thus, since winds are westward in Venus's lower and middle atmosphere, $\bar{u}(z)$ becomes more negative with increasing altitude. The horizontal phase speed and the horizontal wavenumber are constant in altitude z for internal gravity waves. As waves propagate vertically, they see the background wind $\bar{u}$ vary in height, and thus their intrinsic frequencies also vary in height. When the wave arrives at an altitude where $c_x = \bar{u}$, its intrinsic frequency is zero and it encounters its critical layer. We assume that the wave cannot propagate through its critical layer.

Critical layer absorption provides the correct orientation for the deposition of momentum by vertically propagating gravity waves. Intuitively, a source of waves located at an altitude z_s will generate gravity waves with horizontal phase speeds c_x slightly higher and slightly lower than the wind speed $\bar{u}(z_s)$ at altitude z_s. These waves should propagate upward and downward from the source region. Waves which propagate upward from the convection with horizontal phase speeds of $\bar{u}(z_s) - \Delta c_x$ (where Δc_x is small and positive) should be critically absorbed by the mean flow because $\bar{u}(z)$ becomes more negative with increasing altitude. Since such a wave moves westward with respect to the flow at the source altitude, it carries westward momentum vertically. Therefore, upon absorption, it will deposit westward momentum in a mean flow which is more westward than at the source altitude. To conserve momentum, an eastward impulse should occur at the source altitude by such a wave. A similar effect should occur below the source altitude, but an eastward impulse should be given by waves which propagate with phase speeds of $\bar{u}(z_s) + \Delta c_x$. Thus, in the rest frame of the source, waves which propagate westward upward from the source should give a westward impulse to the westward mean flow above the source, and waves which propagate eastward downward from the source should give an eastward impulse to the eastward mean flow below the source.

This hypothesis does not immediately answer what the effect of eastward (westward) waves propagating above (below) the source should have on the overlying (underlying) atmosphere. Firstly, how much the waves would accelerate the atmosphere remains unknown. These questions must be answered in our theoretical analysis. Secondly, we must know how much momentum is critically absorbed at each altitude above and below the convection. This requires us to theoretically estimate how much momentum is being carried at different phase speeds Δc_x, both positive and negative. Finally, the pivotal aspect of this theory is identifying an appropriate source and being able to calculate a spectrum of gravity waves it might emit.

We hypothesize that the source for the waves is a nearly global scale dry convective layer which lies between 50 and 55 km altitude in Venus's atmosphere. Because this source is advected by the mean flow, it should emit a spectrum of waves with phase speeds c_x centered about the local zonal wind speed $\bar{u}$, in keeping with our hypothesis. Secondly, its broad scale guarantees that it is not an isolated source and should thus affect the atmospheric dynamics on a large scale. Thirdly, this source is likely to emit a spectrum of waves broad in horizontal phase speed. This is necessary so that the emitted waves can act to enhance the shear in the atmosphere.

Observational evidence for the existence of substantial gravity wave activity in the Venus middle atmosphere is good. Internal gravity waves in the stable layers adjoining the convection are suggested by large horizontal wind fluctuations seen by the VEGA balloons and by the small scale density inhomogeneities sensed in radio scintillation analyses. In the VEGA project, two balloons were floated near an altitude of 54 km in Venus's atmosphere and traversed a horizontal distance of over 11,000 km within about 10° of the equator (Sagdeev, Linkin, Blamont, and Preston 1986). Each balloon typically experienced vertical winds of about 1 m/s but periodically saw downdrafts as large as 3.5 m/s (Sagdeev, Linkin, Kerzhanovich *et al.* 1986). Of the wind and temperature variances encountered, about 15% of the activity has been identified as gravity wave activity (Ingersoll, Crisp *et al.* 1987). Woo and Armstrong (1981) have performed statistical analyses on short time scale fluctuations seen in radio occultation data taken during the first season of the Pioneer

Venus mission. Since the phase fluctuations and the intensity of the radio signal are caused by density variations in the planet's atmosphere, it is assumed that the short time scale fluctuations in both are caused by density variations on short spatial scales in the planet's atmosphere.

Furthermore, there is indirect evidence that a critical layer absorption mechanism might be at work in the Earth's atmosphere. Gravity wave momentum fluxes have been measured in the Earth's atmosphere using HF and MU radars. It was found that the mean winds filtered the waves and that the momentum fluxes in the mesosphere were opposite in sign to the winds below the mesosphere (Reid and Vincent 1987; Tsuda *et al.* 1990). This can be explained by critical layer absorption acting as a filtering process. It is assumed that eastward and westward propagating waves are generated by a source in the troposphere. In the presence of an eastward (westward) wind, the eastward (westward) propagating gravity waves are critically absorbed in the troposphere. At the tropopause, the predominant modes are westward (eastward) propagating modes. It is not known to what extent critically absorbed waves drive winds in the troposphere, though.

There is also a precedent for suspecting convection as a source of gravity waves. A convective source of internal gravity waves has been invoked to drive the quasibiennial oscillation (QBO) in the Earth's atmosphere. A type of internal gravity wave, Kelvin waves, has been observed at the Earth's equator (Wallace and Kousky 1968). Chang (1976) has hypothesized that these waves are created by a convective source, albeit a moist convective source. The Kelvin waves propagate vertically and deposit their momentum in such a way that westerly wind regimes descend in altitude (Holton and Lindzen 1972, Plumb 1977). Given that this theory of the QBO and our theory for the Venus superrotation use a convective source of gravity waves as a momentum source for the overlying atmosphere, we inquire whether there are any similarities between the Earth's equatorial dynamics and Venus's equatorial dynamics.

Optimally, we would like to use an observationally determined spectrum of waves generated by convection to tackle our problem; however, an appropriate spectrum does not exist. A temporal frequency spectrum of $\omega^{-5/3}$ has been observed in the Earth's atmosphere (Vinnichenko and Dutton 1969, Beatty *et al.* 1992), but this is more likely reflective of a $k^{-5/3}$ horizontal wavenumber spectrum of gravity waves in the presence of strong Doppler shifting by horizontal winds. Information on wave phase speed is weak. Typically, only a single dominant phase speed can be extracted, but we are interested in a complete spectrum in phase speed. It is apparent that to find out how waves can accelerate the mean flow in Venus's atmosphere we must do so theoretically.

Even though no gravity wave spectrum has been observed completely enough to be used for solving our problem, nonetheless a theoretical spectrum of gravity waves can be constrained by what we know about their vertical spectrum in the Earth's atmosphere. A "saturated" spectrum for internal gravity waves describes the spectrum of horizontal winds and temperature fluctuations in the vertical coordinate for short vertical scales. This holds that the kinetic energy density spectrum of wind fluctuations is proportional to k_z^{-3} where k_z is the vertical wavenumber. The same law holds for the temperature variance spectrum in k_z. This spectrum is probably the signature of breaking gravity waves (Dewan and Good 1986; Smith, Fritts, VanZandt 1987). Such a spectrum is expected in the neighborhood of critical layers because gravity waves grow large enough that they break as they approach their critical layers (Hines and Reddy 1967). In the process of breaking, they deposit all of their momentum into the mean flow. Since critical layers are central to our theory, wavebreaking and a k_z^{-3} spectrum are required in our theory.

A theoretical study has been applied to the Earth's atmosphere to examine how small scale gravity waves can accelerate the mean flow; however, this theory can only successfully describe how gravity waves can decelerate or act as a drag on the atmosphere. Lindzen (1981) gives an expression for the rate of momentum deposition by gravity waves assuming that they break at the altitude of interest. This technique takes advantage of the fact that gravity waves tend to break via nonlinear processes as they propagate vertically. As in critical layer absorption, when waves break they deposit the momentum they transport into the mean flow. Implicit in this theory is a foreknowledge of the gravity wave spectrum in order to determine where breaking takes place. Lindzen points out that the dominant phase speed of internal gravity waves is given by the motion of their source. This assumption is a good one when determining wave drag in part of the atmosphere but a bad one when calculating acceleration by waves of part of the atmosphere. The reason is that waves having exactly the same speed as their source exert a drag on the atmosphere, not an acceleration. For example, this technique is capable of demonstrating that wave drag may be responsible for zonal wind decelerations in the Earth's mesosphere (Holton 1982). Thus, we cannot use the Lindzen formulation since we wish to compute whether convectively generated gravity waves can enhance rather than dampen a strong shear in Venus's middle atmosphere.

In our work we present numerical computations of the spectrum of gravity waves emitted by convection between 50 and 55 km in Venus's atmosphere and compare these results with more useful analytic approximations. First we use an analytic theory for the generation of gravity waves by convection developed for helioseismological purposes. Then we track a three dimensional ensemble of waves as they propagate vertically from the convection using a second order WKBJ approximation. Then by implementing wavebreaking and/or critical layer absorption, we calculate the accelerations these waves exert on the atmosphere as a function of altitude. In the process, we develop analytic approximations which are necessary for wavebreaking calculations and useful for explaining the numerical results.

The method we use to calculate spectra of gravity waves generated by neutrally buoyant convection is taken from helioseismology (Goldreich and Kumar 1989, GK hereafter). GK solved the problem of convective generation of gravity waves assuming the convection is restricted to below a fixed altitude and that the stable layer is isothermal and has no zonal winds. They have shown that typical periods of waves are given by the turnover times of the largest eddies in the convection and that typical horizontal wavelengths are approximately the horizontal correlation length within the convection. The typical turnover time for eddies in Venus's convection is on the order of one hour (Ingersoll, Crisp *et al.* 1987) and the typical horizontal correlation length is on the order of 5 km if the eddy aspect ratio is on the order of unity. In applying the theory to Venus's atmosphere, we make several generalizations. Ultimately, we use realistic profiles of zonal wind and static stability. Inclusion of a realistic zonal wind profile permits the presence of a critical layer absorption mechanism for driving the mean flow. Also, inclusion of a realistic static stability profile allows us to perform a detailed calculation of wave emission in Venus's middle atmosphere. In addition we assume that the convection is restricted to a 5 km deep layer, which is approximately one scaleheight in Venus's atmosphere. Otherwise, we keep this problem sufficiently general so that it may be applied to the emission of gravity waves from neutrally buoyant dry convection in other planetary atmospheres.

The propagation of the waves into the stable atmosphere is done using the second order WKBJ approximation. This is necessary for two reasons: (1) so that we may obtain a three dimensional spectrum of temperature fluctuations associated with the waves required for modeling radio scintillations, and (2) so that we may determine where waves break and deposit their momentum. We consider the atmosphere as plane-parallel with no Coriolis effects. We consider the atmosphere horizontally infinite because the waves emitted from the convection are much smaller than the radius of curvature of the atmosphere.

In order to understand how the background atmosphere affects gravity wave propagation, we look at three models of the atmosphere. The first one assigns the stable layer a fixed static stability and zero zonal winds. The second model assumes realistic profiles of static stability and zonal winds with each being continuous in altitude. The third model also assumes realistic profiles, but the static stability is made discontinuous at the interface between the convection and the stable layer. Using the first and second models we show that the discontinuity in static stability is necessary.

We use the third model to examine where and how the waves accelerate the atmosphere. We do this by taking the divergence of the gravity wave momentum flux. Even though wavebreaking is completely responsible for momentum deposition when it is implemented, we also perform a calculation in which momentum is deposited only by critical layer absorption. We describe how the zonal wind profile affects the distribution of accelerations. We also use the third model to calculate model radio scintillation power spectra. In the accompanying paper, we shall use the third model to prescribe the spectrum of temperature fluctuations necessary for simulating radio scintillations in the Pioneer Venus radio science data.

This paper is divided into four parts. The first is this introduction. In the second we present the analytic theory for the generation and propagation of internal gravity waves. In the third we present numerical results for each of the three models and profiles of accelerations provided by the waves. We include order of magnitude estimates and analytic approximations of some numerical results in the third section to shed light on the numerical results. Finally, in the fourth we present conclusions and a discussion of practical implications.

2. Analytic solutions

In this section we present the analytic work necessary for the numerical computations. In particular, we present the wave generation equation and how we intend to solve it, characterize the types of waves which can be emitted from the convection, mathematically determine how efficiently each wavemode can be forced by the convection, spectrally quantify the magnitude of the forcing terms, find the momentum flux associated with each individual wavemode, present our wavebreaking mechanism, give approximate expressions for the spectrum of emitted waves, and present a simplified view for understanding the amplitudes of trapped waves.

2.1 The wave generation equation

In deriving the wave generation equation, we follow the method of GK but with a few exceptions. GK use a simple model atmosphere in which there is no horizontal wind nor Coriolis force and a semiinfinite neutrally buoyant atmosphere underlies a semiinfinite isothermal atmosphere, which is strongly stably stratified. We use the anelastic equations (Ogura and Phillips 1962) in order to omit compressional effects and to include nonhydrostatic effects. Compressional effects would otherwise introduce acoustic waves while nonhydrostatic effects are important in atmospheres with strong shears in the zonal winds. Omitting compressional effects is valid because we are only concerned with waves which propagate with phase speeds significantly less than the sound speed in Venus's middle atmosphere. Unlike GK, we retain terms in the anelastic equations which account for zonal winds and static stability which vary in altitude. This added generalization requires us to use approximate methods to solve our problem. Lastly, we must include the effect of damping by the convection because we have introduced the possibility that some waves might not otherwise have a sink of energy.

The anelastic equations are

$$\frac{du}{dt} = -\frac{\partial \phi}{\partial x} \tag{2.1a}$$

$$\frac{dv}{dt} = -\frac{\partial \phi}{\partial y} \tag{2.1b}$$

$$\frac{dw}{dt} - \frac{g}{c_p}S = -\frac{\partial \phi}{\partial z} \tag{2.1c}$$

$$\frac{\partial u}{\partial x} + \frac{\partial v}{\partial y} + \rho^{-1}\frac{\partial}{\partial z}(\rho w) = 0 \tag{2.1d}$$

$$\frac{dS}{dt} = 0 \tag{2.1e}$$

In these equations, ϕ is the Gibbs free energy ("π" in Ogura and Phillips), S is the specific entropy, g is the gravitational acceleration, ρ is the mass density, c_p is the specific heat at constant pressure, u and v are winds in the horizontal plane, and w is the vertical wind, and x, y, and z are the corresponding coordinates. The x coordinate is chosen to represent the direction of the background wind, which we choose to be purely zonal. The density ρ is an independently determined function of z and is considered a background property of the atmosphere. The time derivatives are fully advective, meaning that $d/dt \equiv \partial/\partial t + \vec{u} \cdot \nabla$ where $\vec{u}$ is the wind field given by (u, v, w).

Whereas GK invoked a semiinfinite convection layer beneath an isothermal atmosphere with quantized spatial wavemodes, much as in a "boxed" domain, we assume a vertically finite convection layer between roughly 50 and 55 km altitude with an overlying atmosphere of variable background wind and static stability. The stable layer is considered semiinfinite in extent, and both layers are infinite in horizontal extent. Within the convective layer, there is no static stability and no shear in the zonal winds, typical of dry convection. Although we use three different models for the zonal wind and static stability in the overlying stable layer, we ultimately use profiles which describe the Venus middle atmosphere. This Venus atmosphere will have winds which grow steadily more westward with height above the convection up to about 66 km. Above 66 km the winds grow more eastward, consistent with Pioneer Venus OIR data (Taylor *et al.* 1981). At about 80 km altitude, the zonal wind speed is the same as that of the convective layer. Above 80 km, the zonal wind is eastward with respect to the convection.

As in GK, we find the wave generation equation for ϕ by linearizing about a mean state. Of the dependent variables u, v, w, ϕ, and S, only u and S have mean state components. The mean state component of u is the background zonal wind. We accomplish the linearization using $u = \bar{u}(z) + u'$, $v = v'$, $w = w'$, $\phi = \phi'$, and $S = \bar{S}(z) + S'$. The barred quantities are the mean state quantities and are constant in time. The primed quantities are first order fluctuations about the mean state. The mean state component of S is a consequence of static stability and is realized in the parameter $N^2(z)$, which is defined as

$$N^2(z) \equiv \frac{g}{c_p}\frac{d\bar{S}}{dz}. \tag{2.2}$$

The quantity $N^2(z)$ is the square of the Brunt-Väisälä frequency.

When working with atmospheric waves, it is customary to view all of the "primed" fluctuation terms as small enough so that the nonlinear terms in the equations of motion become insignificant. We do the same, but with a twist. For the waves in the stable layer, we neglect the nonlinear terms associated with the advective derivatives. Thus, the primed terms represent the fluctuations of the gravity waves. The nonlinear terms are large in the convection, though, and these are created by convective motions. We do not wish to solve for the convective motions. Instead, we assume that the convective motions can be adequately described by the mixing length hypothesis (Schwarzchild 1958) and they can be described spectrally using the Kolmogorov spectrum of turbulence. We thus can assume these terms as givens for our problem. We wish to solve for the primed terms and hence find how the convective activity can generate internal gravity waves. [In reality, we should expect the linear and the nonlinear terms to interact in a manner which would partially organize the convection, and indeed this is seen in numerical models (Fovell *et al.* 1992). Since this organizing effect is extremely difficult to evaluate analytically, we do not concern ourselves with it.]

The fluctuations in the stable layer can attain amplitudes large enough such that the nonlinearities may become important. Indeed, the real consequence of this is wavebreaking and possibly scattering. If we were to thoroughly account for breaking and scattering, we would be required to retain the nonlinear terms associated with the waves in the stable layer. Since we wish to consider a three dimensional ensemble of waves and since empirical theories concerning gravity wave breaking already exist (Dewan and Good 1986; Smith, Fritts and VanZandt 1987), we use these empirical theories rather than a complex general theory to describe the behavior of the waves in the stable layer (see Weinstock 1976).

It is necessary that the convection be able to absorb and dissipate wave energy. We call this process *convective reabsorption.* We account for convective reabsorption by imposing a damping time constant which only affects wave amplitudes in the convecting layer. We envision this damping process as diffusion by convective eddies which have horizontal sizes similar to the wavemode in question. We discuss how the damping time constant τ_c is computed in the subsection which analyzes the spectrum of the forcing terms. Mathematically, we essentially replace each partial derivative in time $\partial/\partial t$ with $\partial/\partial t + 1/\tau_c$ only when in the convection. Qualitatively, this means that the convection will destroy the wave energy density within the convection on a timescale of τ_c. In the end, the damping by convective reabsorption serves as the sink of energy for waves which encounter a reflecting layer at an upper boundary and to partially inhibit the convective generation of waves at low frequencies.

The wave fluctuation terms are Fourier transformed using an $\exp(i(\omega t - k_x x -$

$k_y y)$) dependence because of separability in the x, y, and t coordinates. We assume that there is no zonal wind shear ($\partial\bar{u}/\partial z = 0$) and no static stability ($N^2 = 0$) in the convecting layer because of vigorous mixing of momentum and entropy by the convection. We then find a vertical structure equation for the ω, k_x, k_y Fourier component of the Gibbs free energy fluctuation ϕ':

$$\frac{\partial}{\partial z}\left(\frac{\bar{\rho}}{N^2 - \tilde{\omega}^2}\frac{\partial \phi'}{\partial z}\right) + \frac{\bar{\rho}k^2}{\tilde{\omega}^2}\phi' = \frac{1}{\tilde{\omega}^2}\left(F^{(1)} + F^{(2)}\right). \tag{2.3}$$

We have used the following definitions:

$$\omega_D \equiv \omega - k_x(\bar{u}(z) - \bar{u}(\text{convection})) \tag{2.4a}$$

$$\tilde{\omega}(z) \equiv \begin{cases} \omega_D - i/\tau_c & \text{within the convection, and} \\ \omega_D & \text{outside the convection} \end{cases} \tag{2.4b}$$

$$k^2 \equiv k_x^2 + k_y^2. \tag{2.4c}$$

The quantity ω_D is the Doppler frequency and the quantity τ_c is a time constant associated with convective reabsorption. Its magnitude is dependent on the horizontal scale of the waves in a manner laid out later in this section. The nonhomogeneous wave generation terms are

$$F^{(1)} = \nabla \cdot \nabla \cdot (\bar{\rho}\,\mathbf{u}_c\mathbf{u}_c) \tag{2.5a}$$

$$F^{(2)} = -\frac{\partial}{\partial z}\left(\frac{\bar{\rho} g S_c}{c_p}\right). \tag{2.5b}$$

In the terms $F^{(1)}$ and $F^{(2)}$, $\mathbf{u}_c$ is the convective wind velocity field and S_c is the entropy fluctuation associated with the convection. Both of these terms arise from nonlinear terms in the anelastic equations. Even though the term involving the convective entropy fluctuation seems to be linear, it nonetheless arises from a combination of atmospheric heating by radiation and the advection of that heat, a nonlinear effect. The forcing terms are the same as those found and discussed in GK.

We neglect viscous and radiative damping of the wavelike fluctuations. Lindzen and Forbes have shown that damping by eddy viscosity when gravity waves break is sufficient to maintain waves at their saturated amplitude (1983), so we can disregard viscous damping so long as wavebreaking is implemented. Crisp (1983) showed that the radiative damping times for disturbances with vertical scales of 7 km is on the order of a few Earth days, which would be significantly less efficient than any damping resulting from wavebreaking.

Our entire problem rests on solving equation 2.3. It can be regarded as a one dimensional nonhomogeneous differential equation because by transforming only in the time and horizontal spatial coordinates, we have left the vertical coordinate z as the only independent coordinate. We interpret the equation in the form

$$\mathcal{L}\phi' = F. \tag{2.6}$$

The operator on the left side of the equation $\mathcal{L}$ operating on the Gibbs' free energy fluctuation ϕ' is that which forms the homogeneous internal gravity wave equation when $\mathcal{L}\phi' = 0$. The right-hand side is composed of nonhomogeneous forcing terms collected into F which we consider as nonzero only in the regions of convection for reasons given above. Given upper and lower boundary conditions, we can analytically solve for the vertical structure of ϕ' for any choice of ω, k_x, and k_y. We must use an approximate method, however, because the operator $\mathcal{L}$ is dependent on the vertical coordinate z.

2.2 The formal solution

Since the convection is a nonlinear random phenomenon, we treat it statistically as a stationary random process. The consequence is that ϕ' cannot be found explicitly because F cannot be given explicitly. We can solve for ϕ' in a statistical sense, though, given the statistical properties of F. In mathematical notation, $\mathbf{B}_\phi(\omega, k_x, k_y; z)$, the spectral variance of $\phi'(z)$, will be found in terms of $\mathbf{B}_F(\omega, k_x, k_y)$, the spectral variance of the forcing. The reason that the spectral variance of the forcing is missing the dependence on z is that at some point we shall have to integrate in z over the entire forcing region.

The spectral variance notation is useful for describing properties of random processes. In general, the quantity $\mathbf{B}_\chi(a;z)$ is a variance spectrum of χ' in a as a function of z. For example, the quantity $\mathbf{B}_T(\omega;z)\ d\omega$ is the amount of variance of the temperature fluctuations T' at altitude z in the spectral interval between ω and $\omega + d\omega$. The result would have the units of degrees squared. All quantities on the left side of the semicolon within the parentheses are spectral coordinates. The variance also depends on the coordinates on the right side of the semicolon, but not in an integral sense. For a more detailed exposition on the mathematics of random processes, see Ishimaru (1978).

We find the solution to the wave generation equation using a conventional technique for second order nonhomogeneous differential equations with boundary conditions (Morse and Feshbach, 1953):

$$\phi' = h(z) \int_{\text{convection}} dz' \, \frac{g(z')\,\tilde{\omega}^{-2}\ F(z')}{\bar{\rho}\,(N^2 - \tilde{\omega}^2)^{-1}\ \mathrm{Wr}(g,h)}. \tag{2.7}$$

Here, $F(z)$ is the Fourier transform in frequency ω and horizontal wavenumbers k_x, k_y of the sum of the two forcing terms $F^{(1)}$ and $F^{(2)}$ as a function of altitude z within the convection. In the neutrally buoyant convection, $N^2 = 0$ and $\tilde{\omega}^2 = (\omega - i/\tau_c)^2$. The forcing term F is nonzero only in the convecting layer, which is embedded in the neutrally buoyant layer. The functions $g(z)$ and $h(z)$ are homogeneous solutions to the wave equation ($\mathcal{L}g = \mathcal{L}h = 0$) for which $g(z)$ satisfies a boundary condition at the lower boundary and $h(z)$ at the upper boundary. The Wronskian $\mathrm{Wr}(g,h)$ is the Wronskian of $g(z)$ and $h(z)$ and is given by

$$\mathrm{Wr}(g,h) = g(\frac{\partial h}{\partial z}) - h(\frac{\partial g}{\partial z}). \tag{2.8}$$

It effectively determines the coupling between the functions $g(z)$ and $h(z)$. A remarkable property of the Wronskian is that the product of it with the quantity $\rho/(N^2 - \tilde{\omega}^2)$, the product being the denominator of the integrand of equation 2.7, is independent of height. Thus, it is only necessary to calculate it at one convenient altitude. The solution of equation 2.7 holds only above the convecting layer.

Ultimately, three different effects will determine the spectrum of emitted waves. Firstly, the amplitude of the forcing, given simply by $F(z)$ in equation 2.7, directly effects the amplitude of the emitted waves. Secondly, the propagation characteristics of the individual wavemodes effects the overall spectrum. This is reflected in the solution to the homogeneous wave equation $h(z)$. Thirdly, the coupling for each wavemode between the neutrally stable convection and the stably stratified atmosphere determines how efficiently the convection can generate waves. This is reflected by the denominator of equation 2.7, dominated by the Wronskian $\mathrm{Wr}(g, h)$.

For reasons of convenience, we write the solution for the variance spectrum of ϕ' as

$$\mathbf{B}_{\phi}(\omega, k_x, k_y; z) = |h(z)|^2 \, M(\omega, k_x, k_y). \tag{2.9}$$

This solution is valid for all altitudes above the convection. In the term $|h(z)|^2$ we have included the effects which vary the amplitude of individual waves as they propagate vertically. In the term $M(\omega, k_x, k_y)$ we have included the amplitude of the forcing and the effects of coupling the wave between the forcing region and the overlying stable region. Because $M(\omega, k_x, k_y)$ is inherently independent of altitude, it helps us to discuss quantities which are conserved in altitude, such as the vertical transport of horizontal momentum and energy. Also, because it is mostly responsible for describing the amplitude of the emitted waves spectrally, it will prove simple to discuss trapped waves in terms of $M(\omega, k_x, k_y)$.

The spectral forms of the solution to ϕ' is strongly related to the spectral form of the forcing terms $F^{(1)}$ and $^{(2)}$. The forcing terms will contribute most at a frequency given roughly by the turnover time of the largest eddies. Since the convective wind speeds are approximately 3 m/s and the depth of the convection is roughly 5 km, the dominant frequency of the forcing, and most likely the resultant gravity wave spectrum, is $\omega \sim (3 \text{ m/s})/(5 \text{ km}) \sim 6 \times 10^{-4} \text{ s}^{-1}$. Likewise, the dominant horizontal wavenumber should be approximately the inverse of the horizontal correlation length within the convection. Thus, $k \sim (5 \text{ km})^{-1} \sim 2 \times 10^{-4} \text{ m}^{-1}$.

In the following subsections we discuss the different parts of the wave generation equation (equation 2.7). First we discuss the properties of the homogeneous solutions $g(z)$ and $h(z)$. Secondly, we discuss the coupling of individual waves to the convection by evaluating the Wronskian $\mathrm{Wr}(g, h)$. Thirdly, we evaluate the projection of the homogeneous solution $g(z)$ onto the convection by performing the integral over z. Lastly, we present how we evaluate the amplitudes of the forcing terms.

2.3 Homogeneous solutions

We solve the homogeneous wave equation $\mathcal{L}g = \mathcal{L}h = 0$ in order to find the homogeneous solutions $g(z)$ and $h(z)$. The classic approximate solution is found in the WKBJ approximation. This approximation requires that the vertical wavelength be much smaller than the vertical scale over which it varies. This condition does not always hold, and therefore the complete theory incorporates *connection formulas* for those regions in which the WKBJ conditions does not hold.

We start by writing the linearized homogeneous forms for the anelastic equations:

$$\left(\frac{\partial}{\partial t} + \bar{u}\frac{\partial}{\partial x}\right)u' + w'\bar{u}_z = -\frac{\partial \phi'}{\partial x} \tag{2.10a}$$

$$\left(\frac{\partial}{\partial t} + \bar{u}\frac{\partial}{\partial x}\right)v' = -\frac{\partial \phi'}{\partial y} \tag{2.10b}$$

$$\left(\frac{\partial}{\partial t} + \bar{u}\frac{\partial}{\partial x}\right)w' = -\frac{\partial \phi'}{\partial z} + \frac{g}{c_p}S' \tag{2.10c}$$

$$u'_x + v'_y + \frac{(\bar{\rho}w')_z}{\bar{\rho}} = 0 \tag{2.10d}$$

$$\left(\frac{\partial}{\partial t} + \bar{u}\frac{\partial}{\partial x}\right)S' + \frac{c_p}{g}N^2\, w' = 0 \tag{2.10e}$$

The wave terms u', v', w', S', ϕ' are the zonal wind, meridional wind, vertical wind, entropy and Gibbs free energy fluctuations associated with the wave. The Gibbs free energy fluctuation can be determined in terms of other thermodynamic variables by equating the anelastic and elastic vertical force:

$$\left(-\frac{\partial \phi'}{\partial z} + S'g/c_p\right)_{\text{anelastic}} = \left(-\frac{1}{\bar{\rho}}\frac{\partial p'}{\partial z} - \frac{\rho' g}{\bar{\rho}}\right)_{\text{elastic}}. \qquad (2.11a)$$

In the anelastic approximation, the background atmosphere is nearly isentropic, hence

$$\frac{\bar{p}_z}{\bar{p}} \simeq \gamma \frac{\bar{\rho}_z}{\bar{\rho}}. \qquad (2.11b)$$

Using this in conjunction with the thermodynamic equation

$$\frac{S'}{c_p} = \frac{1}{\gamma}\frac{p'}{\bar{p}} - \frac{\rho'}{\bar{\rho}}, \qquad (2.11c)$$

we find that the fluctuation ϕ' is given by

$$\phi' = \frac{p'}{\bar{\rho}}. \qquad (2.12)$$

The WKBJ solution in which the approximation is valid is that of wavelike solutions with a vertical wavenumber $m(z)$ which is given by the well-known internal gravity wave dispersion relation (Bretherton 1966). The gravity wave dispersion relation is

$$m^2(z) = \left(\frac{N^2(z)}{\tilde{\omega}^2(z)} - 1\right) k^2. \qquad (2.13)$$

One will notice that the terms of order the square of the inverse scaleheight are absent in the second order WKBJ theory because the explicit WKBJ condition is that $mH \gg 1$. We show in appendix A, by comparison to a numerical integration of the homogeneous wave equation, that neglecting terms of order $1/H^2$ is valid even when near a turning point. Since the static stability and the zonal wind vary over vertical scales on the order of a scaleheight, we expect the vertical wavenumber m

to vary over vertical scales on the order of a scaleheight. The WKBJ solution for $mH \gg 1$ is

$$\phi'_{\text{homogeneous}} \simeq \tilde{\omega}\sqrt{\frac{m}{\bar{\rho}}}\left(c_1 e^{iq} + c_2 e^{-iq}\right) \tag{2.14}$$

where the phase of the wave q is defined from some arbitrary altitude z^* as

$$q \equiv \int_{z^*}^{z} |m(z')|\, dz' \tag{2.15}$$

and c_1 and c_2 are general coefficients. [A related WKBJ solution was found for w' by Lindzen 1981.] We usually define z^* as the altitude of a particular turning point. Turning points occur where $m^2(z^*) = 0$. The coefficients c_1 and c_2 are specifically associated with the turning point at altitude z^*.

By requiring that ω always be greater than zero, we can guarantee that the solution with the e^{iq} dependence carries energy upward and the horizontal wavevector **k** determines the direction of horizontal propagation. Internally propagating gravity waves have the distinctive property that their vertical group velocity is opposite in sign to the vertical phase speed. This can be shown by calculating the vertical group velocity:

$$\left(\frac{\partial \omega}{\partial m}\right)_{k_x,k_y} = \left(\frac{\omega}{m}\right)\frac{\tilde{\omega}^3 m^2}{\omega N^2 k^2}. \tag{2.16}$$

Since ω/m is the opposite of the vertical phase velocity, it is clear that the solution with the e^{iq} dependence transports energy upward.

The approximate solution wherever $\tilde{\omega}^2 > N^2$ is related to the approximate solution given in equation 2.14. The vertical wavenumber squared, m^2, becomes negative and the solutions are exponential growth and decay in the depth q:

$$\phi'_{\text{homogeneous}} \simeq \tilde{\omega}\sqrt{\frac{|m|}{\bar{\rho}}}\left(c_3 e^{q} + c_4 e^{-q}\right) \tag{2.17}$$

where q retains the definition of equation 2.15 and $m(z')$ is imaginary. Once again, the coefficients c_3 and c_4 are specifically associated with the turning point at altitude

z^*. For every choice of ω, k_x, and k_y, both exponential and wavelike regions of behavior will occur. The WKBJ condition breaks down between regions of sinusoidal character and exponential character where $m^2 \rightarrow 0$. Connection formulas are used to tell us the behavior of the homogeneous solutions in such regions. In essence, the role of the connection formulas is to relate the coefficients c_1, c_2 in equation 2.14 to the coefficients c_3, c_4 in equation 2.17. We derive the connection formulas and how they are used in constructing the homogeneous solutions throughout the stable layer above the convection in appendix A.

2.3.1 The homogeneous solution $h(z)$

The general solution described in appendix A is used to mathematically define the function $h(z)$. Here, however, we wish to only qualitatively describe the nature of this function and roughly how that nature depends on the spectral coordinates ω, k_x, and k_y. The nature of the waves is critical in determining which waves can generate large temperature fluctuations and which can efficiently transport momentum and energy vertically.

The function $h(z)$ gives the vertical structure of an individual wavemode with its characteristic ω, k_x, and k_y above the region of forcing. The major constraint on $h(z)$ is that it satisfies the correct upper boundary condition. The upper boundary condition is fundamentally dependent on the type of wave present above the convection. If N^2 were constant above the convection and there were no shear in the zonal wind, then all waves would radiate to space provided $\omega^2 < N^2$. On the other hand, the more general case of variable N^2 and $\bar{u}(z)$ provides a variety of wave cases. Given typical profiles of $\bar{u}(z)$ and $N^2(z)$, we can get waves which have only an upward propagating component and thus "radiate" their energy to space (*propagating* waves), waves which have equal upward and downward propagating components and are thus trapped beneath a reflection layer in a one dimensional duct (*trapped* waves),

waves which lose all their energy at a critical layer (where $\omega_D = 0$) (another type of *propagating* wave), or no waves at all, depending on the choice of ω, k_x, and k_y.

We define $\bar{u}(z)$ to be positive in the eastward direction. The winds are parameterized in the rest frame of the convection; thus, $\bar{u} = 0$ in the convection itself. Since the Venus cloud-top winds are overwhelmingly westward, wind speeds are negative above the convection. Waves which propagate in the same direction as the winds above the convection are prograde ($\omega/k_x < 0$) while those that propagate in the opposite direction are retrograde ($\omega/k_x > 0$). Waves with zero zonal wavenumber ($k_x = 0$) are zonally stationary, although they can propagate meridionally.

We use profiles for $N^2(z)$ and $\bar{u}(z)$ in the same formulation as Schubert and Walterscheid (1984) with a few adjustments. We have made the entire region between 50 and 55 km neutrally buoyant because of the presence of convection in this layer in our model. For models with continuous profiles of the static stability, we have introduced a sharp corner in the profile of $N^2(z)$ at 55 km in order to simplify our model without losing the generality of a variable N^2 profile. We restrict the profile of $\bar{u}(z)$ above 55 km such that the Richardson number is never less than 1/4. Presumably, unless a shear is weak enough such $|\partial\bar{u}/\partial z| \leq 2N$, a Kelvin-Helmholtz instability would set in and effectively reduce the shear. We "stabilize" the wind profile by imposing a stable shear, setting $|\partial\bar{u}/\partial z| = 2N$, wherever the parameterized profiles of $\bar{u}(z)$ and $N^2(z)$ otherwise might satisfy the Richardson number criterium for Kelvin-Helmholtz instability. Wherever the shear is otherwise stable, we do not adjust the value of $\partial\bar{u}/\partial z$. The only place at which the parameterized profiles are unstable is within 1 km of the top of the convection. The net effect of stabilizing the wind profile is to alter the zonal wind amplitude by less than 1 m/s above the convecting layer. We use these particular profiles of $N^2(z)$ and $\bar{u}(z)$ in the second model of the section on numerical results.

Most prograde waves are propagating waves. Prograde waves whose zonal phase speeds are smaller than the cloud-top wind speed, which is about 60 m/s at 66 km altitude with respect to the convection, will be critically absorbed. Recall that critical absorption takes place when a wave approaches an altitude where its Doppler frequency is zero. Zero Doppler frequencies occur when the zonal phase speed (independent of height) is identically equal to the zonal wind speed (dependent on height). Since the zonal wind speed varies between 0 m/s just above the convection to 60 m/s at the cloud-tops ($\sim$ 67 km altitude), the prograde waves with zonal phase speeds between 0 and 60 m/s will encounter critical layers between the top of the convection and the cloud-tops. Gravity waves cannot transport a significant amount of momentum or energy through critical layers, and thus they deposit their momentum and energy near their encounter with a critical layer. We therefore consider waves which propagate directly into a critical layer as *propagating* waves because the energy they carry from the convection never revisits the convection. Even though waves with prograde zonal phase speeds larger than about 60 m/s do not encounter critical layers below the cloud-tops, it turns out that such waves have very little energy and momentum associated with them and thus we do not concern ourselves with them.

For propagating waves, we set the upper boundary condition by setting $c_1 = \exp(-\pi i/4)$ and $c_2 = 0$. When used in conjunction with equation 2.14, away from turning points, the wavemode structure is

$$h(z) = \tilde{\omega}\sqrt{\frac{m}{\bar{\rho}}}\ \exp(i(q - \pi/4)). \tag{2.18}$$

While setting $c_2 = 0$ is mandatory for propagating waves, the amplitude and phase of c_1 is arbitrary. We have chosen this particular amplitude and complex phase for c_1 so that no numerical coefficients would appear in equation 2.18.

While prograde modes are all propagating, retrograde modes are either propagating or trapped. Retrograde waves are not absorbed between the convection and the maximum in the zonal winds (near $z \approx 66$ km) because $\tilde{\omega}$ increases with height. If $\tilde{\omega}$ grows rapidly enough so that a region of nonpropagation forms ($\tilde{\omega}^2 > N^2$) where the zonal winds peak, we get a trapped wave as long as a region of propagation ($\tilde{\omega}^2 < N^2$) remains between 55 and 66 km. We refer to the region of nonpropagation which forms around 66 km as the *upper lid.* It is not a physical lid, but an abstract one. Since the upper lid formation is a consequence of large $\tilde{\omega}$, accomplished mostly by large Doppler shifting, whether retrograde waves are trapped or not is almost solely dependent on k_x. In particular, retrograde waves are trapped when

$$k_x \gtrsim \frac{(N^2_{\text{maximum}})^{1/2}}{|\bar{u}(\text{cloud-tops}) - \bar{u}(\text{convection})|}. \tag{2.19}$$

The stability N^2 attains its maximum of N^2_{maximum} at $z \approx 60$ km. The inequality in equation 2.19 is found by setting $m^2(z = 66 \text{ km}) \lesssim 0$. We evaluate this expression in section 3 of this paper.

For waves trapped beneath a thick upper lid, we impose the upper boundary condition by setting $c_1 = -1/2\ \exp(\pi i/4)$ and $c_2 = -1/2\ \exp(-\pi i/4)$ for the turning point at the base of the upper lid. This makes $h(z)$ approximately

$$h(z) = \tilde{\omega}\sqrt{\frac{m}{\bar{\rho}}}\ \sin(q - \pi/4) \tag{2.20}$$

where the phase q is defined away from the turning point at the base of the upper lid. In defining c_1 and c_2 at the upper turning point, it was only necessary that c_1 lead c_2 by $\pi/2$ radians in the complex plane so that the wave would decay exponentially with height within the upper lid. The amplitudes and phases of c_1 and c_2 were chosen so that no extra coefficient would appear in equation 2.20.

It is possible that trapped waves be only marginally trapped. This occurs when the upper region of nonpropagation is small enough that the wave can "tunnel" some of its energy through it. When this happens, we expect the wave to be a subtle mix of a propagating wave and a trapped wave. A downward propagating wave does exist but it is not as large as the upward propagating wave. We essentially determine what happens in this case by evaluating how much of the energy carried by the upward propagating wave can tunnel through the lid and by deducting this fraction from the energy carried by the downward propagating wave. Again, a detailed analysis of how this is done is presented in appendix A. As the lid becomes thicker, it asymptotically approaches perfect trapping.

Figure 1 illustrates the basic features of the wavemode structure. In this figure we show how the Doppler frequency ω_D and the Brunt-Väisälä frequency together allow propagating and trapped modes. We have chosen two different modes, one an example of a propagating/critically absorbed mode and the other an example of a trapped mode. Turning points occur where $\omega_D^2 = N^2$ or $m^2 = 0$. For both wavemodes shown, a region of nonpropagation lies between the top of the convection at 55 km and the first turning point above the convection. We refer to nonpropagation regions which lie directly above the convection as barriers. The thickness of this barrier q_b is defined as

$$q_b \equiv \int_{z_{\mathrm{convection}}}^{z_{\mathrm{turning\ point}}} |m(z')|\, dz'. \tag{2.21a}$$

For the critically absorbed wave of figure 1a, the Doppler frequency falls off with height because k_x is negative (recall that $\bar{u}(z)$ directly above the convection is also negative). Because $N^2 = 0$ just above the convection, the square of the Doppler frequency is greater than the square of the Brunt-Väisälä frequency. But since N^2 grows rapidly with height, it becomes greater than the square of the Doppler frequency near 56.5 km. The region between the convection and 56.5 km is the barrier. Above the barrier, the wave is free to propagate vertically away from its source. At about 62 km altitude, the Doppler frequency goes through zero. This is the point of the critical level. It is apparent in the third panel that the vertical wavenumber m approaches infinity near the critical level.

(a)

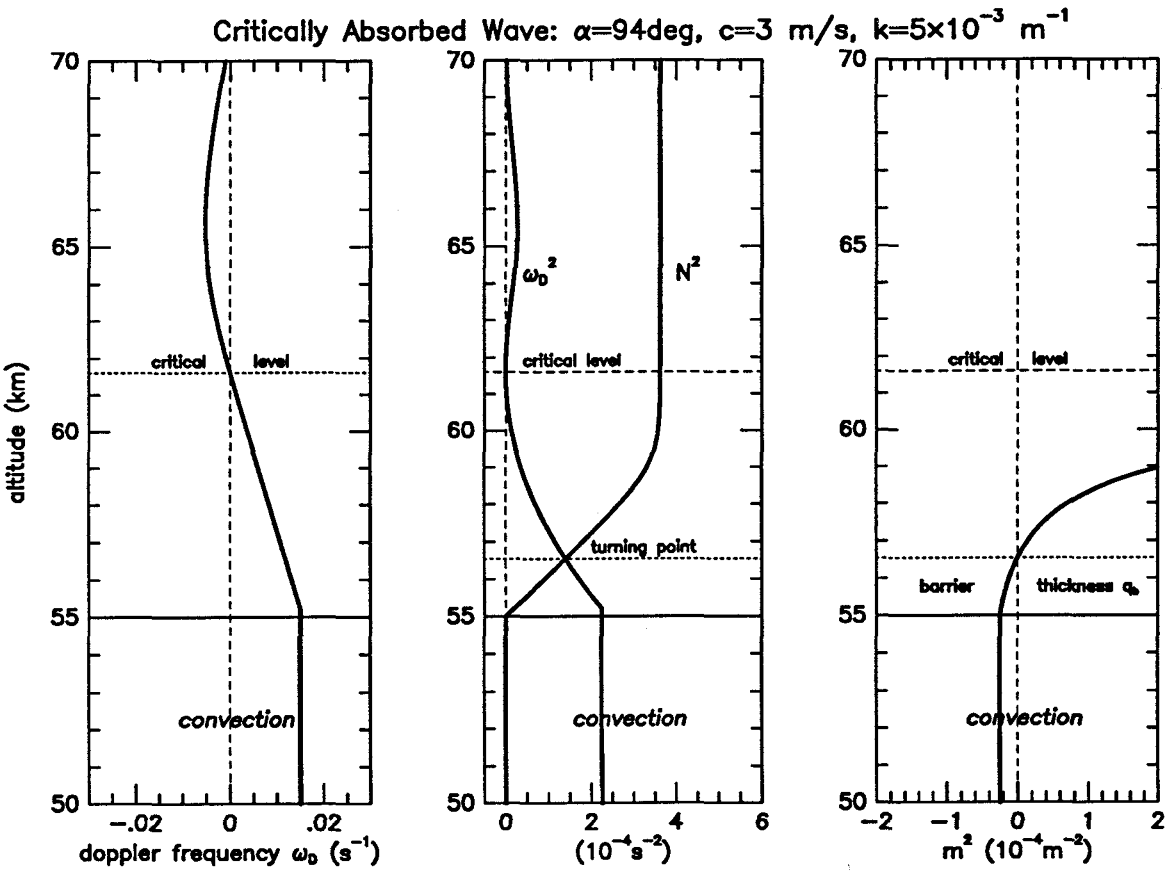
Critically Absorbed Wave: α=94deg, c=3 m/s, k=5×10^{-3} m^{-1}
70
65
60
55
50
altitude (km)
critical
level
convection
−.02
0
.02
doppler frequency ω_D (s^{-1})
$\omega_D{}^2$
N^2
critical level
turning point
convection
0
2
4
6
(10^{-4}s^{-2})
critical
level
barrier
thickness q_b
convection
−2
−1
0
1
2
m^2 (10^{-4}m^{-2})

(b)

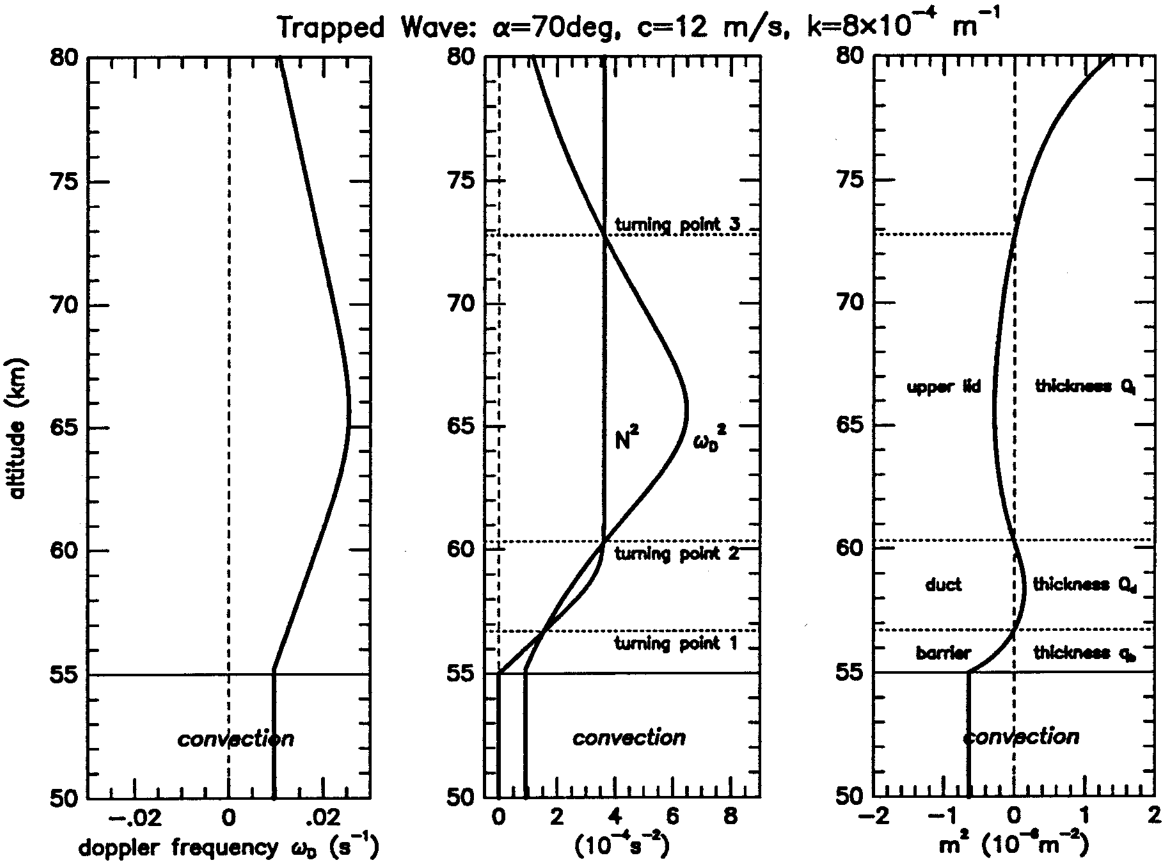

Figure 1. Different Wave Cases. In these panels we show profiles of the Doppler frequency, the square of the Doppler frequency and the square of the Brunt-Väisälä frequency, and the square of the vertical wavenumber for (a) a critically absorbed "propagating" wave and (b) a "trapped" wave. For (a) we use $\omega = 1.5 \times 10^{-2}$ s^{-1}, $k_x = -3.49 \times 10^{-4}$ m^{-1}, and $k_y = 4.99 \times 10^{-3}$ m^{-1}. For (b) we use $\omega = 9.6 \times 10^{-3}$ s^{-1}, $k_x = 2.74 \times 10^{4}$ m^{-1}, and $k_y = 7.52 \times 10^{-4}$ m^{-1}.

For the trapped wave of figure 1b, the Doppler frequency increases with height. Again, because N^2 is small just above the convection, the barrier forms. For this wave, however, the square of the Doppler frequency grows rapidly enough with height so that it becomes greater than N^2 near 60.5 km altitude. This is the second turning point. A region of propagation lies between the first and second turning points which we call the "duct." The total phase within the duct Q_d is defined as

$$Q_d \equiv \int_{\text{turning point 1}}^{\text{turning point 2}} |m(z')|\, dz'. \tag{2.21b}$$

Finally, above 66 km the Doppler frequency decreases with height because the zonal wind becomes more eastward. Near 73 km a third turning point forms, and we get a region of nonpropagation on top of the duct called the "lid." The thickness of this lid is defined as

$$Q_l \equiv \int_{\text{turning point 2}}^{\text{turning point 3}} |m(z')|\, dz'. \tag{2.21c}$$

We consider trapped waves with $Q_l > 3$ as waves trapped by a thick lid and trapped waves with $Q_l < 3$ as waves trapped by a thin lid.

The barrier thickness can be approximated for many of the emitted gravity waves. We consider a continuous profile of $N^2(z)$ to be linear above the convection with a vertical gradient of N_z^2. In this case,

$$q_b \simeq \frac{2}{3}\frac{\omega^2 k}{N_z^2} \tag{2.22a}$$

which holds true for $q_b < 1$. If we approximate N_z^2 as $(0.02\ \text{s}^{-1})^2/(5\ \text{km})$, ω as $(3\ \text{m/s})/(5\ \text{km})$, and k as $(5\ \text{km})^{-1}$, then we can show that $q_b \sim 6 \times 10^{-4}$ and thus $q_b \ll 1$. By this we wish to imply that most often it is appropriate to think of the barrier above the convection as thin when N^2 is continuous. On the other hand, with suitable choices of ω, k_x, and k_y we can find wavemodes with very thick barriers. This is useful, because from quantum mechanics we already have an intuition for the behavior of such barriers against which we can check our mathematics.

When the profile of N^2 is discontinuous at the top of the convection, then only rarely will a barrier exist. In the third model of the following section, we implement a discontinuity in N^2 such that $N^2 = 0$ within the convection and $N^2 = 4 \times 10^{-5}\ \text{s}^{-2}$ immediately above the convection. Even though this value of N^2 is an order of magnitude less than that at $z = 60$ km, nevertheless it is large compared to the square of the dominant forcing frequency in the convection, which is on the order of 10^{-3} s^{-1}. For frequencies smaller than $\sqrt{4 \times 10^{-5}}$ s^{-1}, waves will immediately propagate into the stable layer because $m^2 > 0$ above the convection. In these cases, there is no barrier, and the barrier thickness is $q_b = 0$. When the frequency becomes larger than $\sqrt{4 \times 10^{-5}}$ s^{-1}, a barrier will form. The barrier thickness will be approximately given by

$$q_b \simeq \frac{2}{3} \frac{\omega^2 |m_c|}{N_z^2}. \tag{2.22b}$$

The quantity m_c is the value of m immediately above the convection (notice that $m_c^2 < 0$ for the large frequencies).

If a barrier does form above the convection, the function $h(z)$ within the barrier is

$$\begin{aligned} h(z) \simeq -i\tilde{\omega}\sqrt{\frac{2\pi q|m|}{3\bar{\rho}}} \Big[& (c_2 \exp(\pi i/12) - c_1 \exp(-\pi i/12))\ I_{2/3}(q) \\ & + (c_1 \exp(7\pi i/12) - c_2 \exp(-7\pi i/12))\ I_{-2/3}(q) \Big]. \end{aligned} \tag{2.23}$$

The phase q is measured away from the turning point at the top of the barrier and the coefficients c_1 and c_2 are associated with that turning point. The functions $I_{2/3}$ and $I_{-2/3}$ are modified Bessel functions of order 2/3. This form will eventually be used in evaluating the Wronskian. See appendix A for details on the derivation of this equation.

2.3.2 The homogeneous solution $g(z)$

The homogeneous solution $g(z)$ serves two purposes in this problem: it allows us to project the wavemode onto the forcing mechanism and to calculate the forcing efficiency for each mode through evaluation of the Wronskian of $g(z)$ with $h(z)$. For these reasons, we only need to know the functional form of $g(z)$ below $z = 55$ km. In this region, we have $N^2 = 0$ and $m^2 = -k^2$. The differential equation for $g(z)$ is

$$\frac{\partial^2 g}{\partial z^2} + \frac{1}{\bar{\rho}} \frac{d\bar{\rho}}{dz} \frac{\partial g}{\partial z} - k^2 g = 0. \tag{2.24}$$

If we treat this portion of the atmosphere as compressible and adiabatic, then the solutions for $g(z)$ are fractional Bessel functions in z of order $(2-\gamma)/(2(\gamma-1))$ multiplied by a power law in z. The quantity γ is the adiabatic index given by the ratio of the specific heats c_p/c_v, where c_p is the specific heat at constant pressure and c_v is the specific heat at constant volume. Because of the difficulties involved in calculating a fractional Bessel function, especially for $k < 1/H$, we assume that the convection is Boussinesq and that this assumption retains the physics relevant to this problem. In the Boussinesq case, $d\bar{\rho}/dz = 0$ and

$$g(z) = d_1 \exp(k(z - z_{\rm top})) + d_2 \exp(-k(z - z_{\rm top})). \qquad (2.25)$$

In this equation, $z_{\rm top}$ refers to the top of the convecting layer.

By imposing a downward radiation condition beneath the convection, we can find the general constants d_1 and d_2 in equation 2.25. When $kH \gg 1$, the only physically acceptable solution is that of exponential decay with depth. Hence, we require that d_2 approaches zero as kH approaches infinity. On the other hand, in order to describe the behavior of $g(z)$ for $kH \ll 1$, we must evaluate the behavior of $g(z)$ near the bottom portion of the convection. In this case we impose the radiation condition at the lower boundary, which requires a mix of the growing and decaying exponentials in equation 2.25. For $kH \ll 1$, explicit determination of $g(z)$ at the bottom of the convecting layer is required.

So that we may evaluate d_1 and d_2 at the lower boundary of the convecting layer for $kH \ll 1$, we assume that below the convection the atmosphere is stable with a Brunt-Väisälä frequency N_l. This stability serves to impede convective downdrafts at the lower boundary of the convection. In order to satisfy the lower boundary condition, downward radiation below the convection is required of $g(z)$. This makes the solution $g(z)$ proportional to e^{iq} where the phase q increases downward away from the convecting layer. We find $g(z)$ within the convection by imposing continuity in the vertical wind fluctuation associated with $g(z)$. We show in appendix A that continuity in the vertical wind dictates continuity in the function

$$w' = \frac{-i\tilde{\omega}}{N^2 - \tilde{\omega}^2} \frac{\partial \phi'}{\partial z}. \tag{2.26}$$

Imposing this condition on $g(z)$ and the downward radiation condition gives

$$\frac{1}{g}\left(\frac{\partial g}{\partial z}\right)(z = z_{\mathbf{bottom}} + \epsilon) = -\frac{k^2}{m_l^2}\,(1 - \frac{i}{\omega\tau_c})^{-1} \times (-im_l) \tag{2.27}$$

for the solution $g(z)$ within the convection. We use $z_{\mathbf{bottom}}$ to denote the altitude of the bottom of the convecting layer and ϵ to denote an infinitesimal distance. Recall that the quantity τ_c is the damping time constant in the convective region used to simulate convective reabsorption. For small kH, the damping time is nearly the turnover time associated with the energy bearing eddies in the convection. Solving for the coefficients d_1 and d_2, we find that

$$g(z) = \cosh k(z - z_{\mathbf{bottom}}) - \frac{\omega\tau_c}{1 + i\omega\tau_c} \frac{k}{m_l} \sinh k(z - z_{\mathbf{bottom}}) \tag{2.28}$$

where m_l is given by $\sqrt{N_l^2 - \omega^2}\, k/\omega$ and $z_{\mathbf{bottom}}$ refers to the bottom of the convection. We assume that the depth of the convection is H. This form is valid for those waves with $\omega < N_l$, which we anticipate to nearly always be the case for small kH.

At this point, we argue that the only important term in $g(z)$ at small kH is the hyperbolic cosine. The second term is much smaller than the first for $\omega \ll N_l$. In fact, the two are comparable in amplitude only for unrealistically large phase speeds ω/k. For this reason, we approximate the functional form of $g(z)$ as $\cosh k(z - z_{\mathbf{bottom}})$ in order to fully incorporate its expected behavior for all values of k. This essentially says that the vertical wind associated with wave fluctuations vanishes at the lower boundary, effectively yielding a rigid lower lid. This certainly is valid for convection above a solid surface, and it is arguably legitimate for convection resting on a strongly stable layer. This does not say that emission of gravity waves into the stable lower layer will not occur, only that the emission of waves into the lower layer should not effect the emission of waves into the upper layer, the one with which we are concerned. If we were instead to have studied the emission of waves into the lower layer, we would have set the vertical wind at the upper boundary of the convection to zero. Thus, in our problem we approximate

$$g(z) \approx \frac{\cosh k(z - z_{\mathrm{bottom}})}{\cosh kH}. \tag{2.29}$$

2.4 The Wronskian Wr(g, h)

Earlier we had mentioned that the denominator of the integrand in equation 2.7 is independent of height. For simplicity, we choose to evaluate the Wronskian at $z = z_{\mathrm{top}} - \epsilon$ (z_{top} is the altitude of the top of the convecting layer and ϵ is some infinitesimal distance). The Wronskian Wr(g, h) is given by equation 2.8. It utilizes the boundary conditions in order to describe the response of the waves to forcing. If $g(z)$ and $h(z)$ were in phase with each other, the Wronskian would be exactly zero and the waves would respond infinitely well to any forcing; however, in the presence of damping, this will never be true. Furthermore, evaluation of the Wronskian is prominent in investigating the nature of resonant trapped modes.

In order to evaluate the function $h(z)$ and its derivative at $z = z_{\mathrm{top}} - \epsilon$, we once again note that the vertical wind fluctuation and the Gibbs free energy fluctuation must be continuous for all z. Recall that $\tilde{\omega} = \omega - i/\tau_c$ within the convection. When the profile of N^2 is continuous, the stability is defined to be zero at the top of the neutral layer; hence, the continuity condition in w' would simply reduce to continuity in $\tilde{\omega}^{-1}\partial\phi/\partial z$. When the stability profile is considered discontinuous at the top of the neutral layer, N^2 will take on a nonzero value for $z = z_{\mathrm{top}} + \epsilon$ and the continuity condition in the vertical wind remains continuity of equation 2.26 for $g(z)$. We account for convective reabsorption by including the damping time τ_c. In evaluating equation 2.8 allowing for continuity of the vertical wind (equation 2.26), we find for both continuous and discontinuous profiles of N^2 that

$$\left(\frac{\partial h}{\partial z}\right)_{z=z_{\rm top}-\epsilon} = (1-\frac{i}{\omega\tau_c})\left(\frac{\omega^2}{\omega^2-N_c^2}\right)\left(\frac{\partial h}{\partial z}\right)_{z=z_{\rm top}+\epsilon}. \tag{2.30}$$

We have denoted the stability N^2 at $z=z_{\rm top}+\epsilon$ as N_c^2. By definition, $N_c^2=0$ when the profile of N^2 is assumed to be continuous. We assume the functional form for $g(z)$ given by equation 2.29. We evaluate the Wronskian according to the expression

$$\mathrm{Wr}(g,h) = (1-\frac{i}{\omega\tau_c})\left(\frac{\omega^2}{\omega^2-N_c^2}\right)\, h_z(z=z_{\rm top}+\epsilon) - k\tanh kH\ h(z=z_{\rm top}+\epsilon). \tag{2.31}$$

The subscript z denotes a partial derivative with respect to height. Technically, this is the expression for the Wronskian when evaluated at the top of but still within the convection. In order to be fully consistent in evaluating the denominator in equation 2.7, the factor of $(N^2-\tilde{\omega}^2)^{-1}$ in the denominator must be $-\tilde{\omega}^{-2}$ because $N^2=0$ within the convection.

Throughout this calculation it is necessary to compute the derivatives of $h(z)$ and ϕ' with respect to height. Even though it seems easiest to finite difference the functions, this actually does not work. A finite difference would actually introduce third order WKBJ terms even though we only desire second order accuracy. Although third order terms are small, nonetheless we require certain cancellations to occur at all orders in the vicinity of turning points. The proper way to find the derivatives of $h(z)$ and ϕ' with respect to z is to find its second order WKBJ solution independently. We show how this is done in appendix B. This will be important not only for calculating the Wronskian but also for calculating temperature fluctuations.

2.5 The forcing

The nature of the forcing by convection is discussed in GK. Our formulation is different in two aspects: the vertical extent is limited to a scaleheight H and the convective zone is Boussinesq. The only effect of limiting the vertical extent of the convection is to alter the form of $g(z)$ at low kH. The effect of a Boussinesq convection zone, however, is unclear. GK showed that anisotropy in the convective layer should lead to partial cancellation between the two forcing terms. The degree of cancellation at high kH is uncertain, and an upper limit to the forcing is estimated as the order of magnitude of the larger of the two terms at a given k and ω. Here we estimate the effect of the forcing terms for high and low limits of kH.

Since we desire that the final result of this calculation give a variance spectrum of a random process, we must keep in mind that the properties of the convection are known only in a statistical sense and that performing the integral in z of equation 2.7 is meaningless until we take the square of the result. Implicit in this technique is that we are taking ensemble averages of second order quantities. The proper way to perform the integral then is to square it first and approximate its result. We see the integral essentially as

$$I = \int_{\text{convection}} F(\omega, k_x, k_y; z)\, g(z)\, dz \tag{2.32}$$

in which $F(\omega, k_x, k_y; z)$ is the ω, k_x, k_y Fourier component of the two forcing terms. To find the expected variance of this integral, we square it and take an ensemble average:

$$\overline{I^2} = \int\int_{\text{convection}} g(z_1)g(z_2)\, \overline{F(\omega, k_x, k_y; z_1)\, F^*(\omega', k_x', k_y'; z_2)}\, dz_1\, dz_2. \tag{2.33}$$

The overbar denotes an ensemble average. This integral is nonzero only for $\omega = \omega'$, $k_x = k_x'$, and $k_y = k_y'$ (see Ishimaru 1978).

In order to evaluate the integral for $\overline{I^2}$, we view the convection as a hierarchy of eddies, each of which is nearly isotropic in dimension. Those eddies which contribute power at horizontal wavenumbers of k have horizontal sizes of $1/k$. The assumed isotropy of these eddies dictates that they are correlated over vertical displacements of size $1/k$. Because $\overline{F(z_1)\, F^*(z_2)}$ is nonzero only when $z_1 - z_2 \lesssim 1/k$, it is appropriate to define new coordinates $l_1 = z_1 - z_2$ and $l_2 = (z_1 + z_2)/2$ over which to perform the integral. Since the vertical scale of the eddies is limited by the depth of the convection H, this formulation is valid only for $kH \gg 1$. Nonetheless, by inspection this integral is $\approx k^{-2}\ \sigma_F^2$ where σ_F^2 is the variance of F. Each forcing term contains spatial derivatives. These are handled by assuming that variations of a turbulent tracer at a scale $1/k$ are given by k times the amplitude of that quantity at scale $1/k$. This approach toward solving the integration in z is valid for high kH; however, another approach is needed for solving the integral when kH is small.

When the horizontal scale of the wave exceeds the depth of the convection, forcing of the wave becomes extremely inefficient. For $kH \ll 1$, equation 2.32 must be solved by integration by parts in order to determine the efficiency with which waves are generated. Recall that the forcing terms are in fact differentials of properties of the convection (equations 2.5). In the course of evaluating the integrals over z, we define two intermediate quantities $\overline{I_{(i)}^2}$ as

$$\overline{I_{(i)}^2} \equiv \overline{\left(\int_{-H}^{0} g(z_1)\ F^{(i)}(z_1)\ dz_1\right)\left(\int_{-H}^{0} g(z_2)\ F^{(i)}(z_2)\ dz_2\right)^*} \tag{2.34}$$

in which $i = 1, 2$ depending on the forcing mechanism. When computing this integral, we expect only the largest, energy bearing eddies to significantly contribute when $kH \ll 1$. For each of these eddies, we guess that the Reynolds stress tensor and entropy fluctuations are roughly constant over the depth of the convection. It is then simple to do each integral by parts in order to obtain valid solution for small kH.

For the entropy forcing term, integrating by parts gives us a solution which is valid not only for high kH, but also for low kH. After integrating $I_{(2)}$ by parts we get

$$\overline{I_{(2)}^2} = \left(\frac{\rho_0 g}{c_p}\right)^2 (\Delta g)^2\ \sigma_{S_c}^2 \tag{2.35a}$$

where Δg is the difference in the function $g(z)$ from the bottom of the convection to the top, $\sigma_{S_c}^2$ is the variance of entropy fluctuations, and ρ_0 is the atmospheric density at

55 km. The integration by parts yields no boundary terms because the forcing terms vanish outside the convection. Previously we had argued that $\lim_{kH\to 0}(dg/dz) = 0$ at the bottom of the convection, thus Δg must be at least quadratic in kH. Therefore, for $kH \ll 1$, we expect that $\overline{I_{(2)}^2} \propto (kH)^4$. When $kH \gg 1$, however, we expect $g(z)$ to project entirely onto the forcing, and thus we expect that $\Delta g \simeq 1$. We use the approximate equation 2.29 to arrive at

$$\Delta g = 1 - \operatorname{sech} kH. \tag{2.35b}$$

It is clear that our solution for $\overline{I_{(2)}^2}$ when $kH \gg 1$ is asymptotically approached by equation 2.35*a*. Thus, equations 2.35 are valid for all kH for the entropy forcing term.

For the Reynolds forcing term, integrating by parts also gives a solution which is valid for both high and low kH. It is a subtle problem to integrate $I_{(1)}$ by parts for $kH \ll 1$. We must treat the convection as incompressible to first order (i.e., $\nabla \cdot (\rho \mathbf{u}_c) \simeq 0$). The result is that the integral $I_{(1)}$ takes the form

$$I_{(1)} \simeq \int_{z_{\text{bottom}}}^{z_{\text{top}}} \rho w_c^2 \, \frac{\partial^2 g}{\partial z^2} \, dz. \tag{2.36}$$

In the above notation we have used w_c to describe the vertical component of the convective wind $\mathbf{u}_c$. In the limit $kH \ll 1$, we find an upper limit to $I^{(1)}$ by approximating ρw_c^2 as constant throughout the depth of the convection and integrate $\partial^2 g/\partial z^2$ to find that

$$\overline{I_{(1)}^2} \simeq \rho_0^2 \, (k \tanh kH)^2 \, \sigma_{w_c^2}^2 \qquad \text{for all } kH. \tag{2.37}$$

At small kH, the quantity $\tanh kH$ is proportional to kH. This shows the forcing of gravity waves by Reynolds stresses scales similarly to the forcing by entropy fluctuations when the horizontal scale of the wave is much larger than the depth of the convection ($kH \ll 1$). Since this solution is valid at large and small kH, we use it for the entire range of kH.

We have now presented how the spectrum of Gibbs free energy fluctuations is calculated. We harken back to equation 2.9 in order to present our solution using the factor $M(\omega, k_x, k_y)$. Explicitly, we use equations 2.35 and 2.37 in conjunction with the definition 2.32 and the solution 2.7 to find that

$$M(\omega, k_x, k_y) = |\mathrm{Wr}(g,h)|^{-2} \times \begin{cases} (k \tanh kH)^2 \, \mathbf{B}_{w_c^2}(\omega, k_x, k_y) & \text{for Reynolds-type forcing,} \\ (\Delta g)^2 \, (g^2/c_p^2) \, \mathbf{B}_{S_c}(\omega, k_x, k_y) & \text{for entropy-type forcing.} \end{cases} \tag{2.38}$$

Recall that Δg is given by equation 2.35*b* and $\mathrm{Wr}(g,h)$ is given by equation 2.31. All quantities are evaluated numerically. We have yet to specify what we use for $\mathbf{B}_{w_c^2}(\omega, k_x, k_y)$ and $\mathbf{B}_{S_c}(\omega, k_x, k_y)$. For the sake of convenience, we define

$$\mathcal{C}(\omega, k_x, k_y) \equiv \begin{cases} (k \tanh kH)^2 \, \mathbf{B}_{w_c^2}(\omega, k_x, k_y) & \text{for Reynolds-type forcing} \\ (\Delta g)^2 \, (g^2/c_p^2) \, \mathbf{B}_{S_c}(\omega, k_x, k_y) & \text{for entropy-type forcing.} \end{cases} \tag{2.39}$$

There are two uses of g in this definition. Whenever g is used to denote the wave-mode projection, it is written as a function of z or as Δg, defined by equation 2.35*b*. Whenever g is used to denote the gravitational acceleration, it is unaccompanied by other characters.

2.6 Variance properties of the turbulence

The two forcing terms are related by mixing length theory, and GK shows them to have the same order of magnitude for the largest convective eddies. In mixing length theory, entropy fluctuations are initially created by divergences in the radiation field. Subsequently, the buoyancy forces resulting from the entropy fluctuations act to accelerate hot air parcels upward. The amount of work done by an entropy fluctuation S_c after traveling a vertical distance H is roughly the same as the kinetic energy it releases: $gH\,(S_c/c_p) \approx |\mathbf{u}_c|^2$. Using this relation and approximating the vertical derivative as $\partial/\partial z \simeq 1/H$ shows that the two forcing terms are of the same order of magnitude. We estimate the size of these terms by assuming the vertical wind speeds in the convection were measured by the Vega balloons. The largest convective wind speeds measured by the Vega balloons were on the order of 3–5 m/s. This is in good agreement with the value obtained by estimating the convective energy flux as ρu_c^3 (Ingersoll *et al.*, 1987). If the convective energy flux is balanced by the downward solar flux at 55 km, found to be 30–40 $\mathrm{W/m^2}$ by the solar flux radiometer aboard the Pioneer Venus atmospheric probes (Tomasko et al., 1980), we find a typical convective wind speed of 3–4 m/s given $\rho = 0.9\ \mathrm{kg/m^3}$ (Seiff et al., 1980). Thus we can have some confidence in our estimation of the size of the forcing terms.

We parameterize the variance in the forcing terms at small scales and high frequencies by connecting the mixing length hypothesis with a Kolmogorov energy cascade. The Kolmogorov theory of turbulence essentially asumes that motions on the energy-bearing scales, at which the mixing length hypothesis holds, create turbulence at smaller scales. The energy lost at the energy-bearing scales cascades through smaller and smaller scales until it is eventually dissipated by viscosity. The associated constant of the motion is the energy dissipation rate per unit mass. From the energy cascade we can estimate the amplitude of motions at high horizontal wavenumbers and frequencies.

The spectral forms of $\mathbf{B}_{S_c}(\omega, k_x, k_y)$ and $\mathbf{B}_{w_c^2}(\omega, k_x, k_y)$ can be derived from Kolmogorov principles of turbulence. We assume that entropy mixes like a passive scalar contaminant within the turbulence. That means that motions on small scales advect entropy from a state that has a fixed entropy gradient on the large scales. The advection occurs over a time given by the turnover time of the energy-bearing eddies. Thus the spatial form for the variance spectrum of the entropy fluctuations is the same as that for velocities. A two dimensional spectrum of the variance of the velocity is found by putting together a power of the energy dissipation rate per unit mass ε with a power of the horizontal wavenumber k such that a quantity with the dimensions of velocity variance per unit zonal and meridional wavenumber is found. The correct combination is $\varepsilon^{2/3}k^{-8/3}$. Thus we define the variance spectrum of entropy fluctuations as

$$\mathbf{B}_{S_c}(k_x, k_y) \approx \frac{1}{3\pi}\frac{c_p^2}{(gH)^2}\frac{W_c^4 H_c^2}{(1+(kH_c)^2)^{4/3}}. \tag{2.40}$$

The quantity H_c denotes the horizontal correlation length of the energy bearing eddies. We consider the convective eddies to be roughly isotropic, thus $H_c \simeq H$. We use W_c as the amplitude of the typical vertical wind fluctuation associated with the energy-bearing eddies in the convection.

In finding the frequency variance spectrum of convective entropy fluctuations, we introduce the notion of a timescale of forcing τ_k at wavenumber k. It represents a correlation time constant for eddies of size $1/k$. For large horizontal scales it should reflect the overturn time of the energy-bearing eddies ($\sim H/W_c$). At small scales it should represent the time it takes the energy-bearing eddies to advect features over a distance $1/k$. We assume that τ_k takes the form

$$\frac{1}{\tau_k^2} = \frac{W_c^2}{H_c^2}(1+(kH_c)^2). \tag{2.41}$$

For the energy-bearing eddies, the frequency spectrum can be found by calculating the correct exponents for ε and ω such that the resultant quantity has the dimensions of velocity variance per unit frequency. The correct combination is $\varepsilon\omega^{-2}$. Thus, we use

$$\mathbf{B}_{S_c}(\omega, k_x, k_y) = \frac{1}{3\pi^2}\frac{c_p^2}{(gH)^2}\frac{W_c^4 H_c^2}{(1+(kH_c)^2)^{4/3}}\frac{\tau_k}{1+(\omega\tau_k)^2} \tag{2.42}$$

for the spectrum of S_c. When this spectrum is integrated over all k_x and k_y, it will have an ω^{-2} dependence for $\omega \gg W_c/H_c$. Likewise, when it is integrated over all ω it will have a $k^{-8/3}$ dependence for $kH_c \gg 1$. The leading factor of $1/3\pi^2$ is a normalization constant such that when the entropy variance spectrum is integrated over all ω, k_x, and k_y, we would be left with $\sigma_{S_c}^2 = c_p^2(W_c^2/gH)^2$.

When calculating the spectrum of w_c^2 we cannot treat it as a passive scalar contaminant because the Reynolds stresses play an active role in maintaining the energy cascade. The technique for determining the spectral dependence on k_x, k_y, and ω is similar to that used for calculating the dependence of $\mathbf{B}_{S_c}$ on k_x, k_y, and ω. At high horizontal wavenumbers we find a $k^{-10/3}$ dependence, while at high frequencies we find a ω^{-3} dependence. In putting these two dependences together, we define the variance spectrum of w_c^2 to be

$$\mathbf{B}_{w_c^2}(\omega, k_x, k_y) = \frac{1}{3\pi} \frac{W_c^4 H_c^2}{(1+(kH_c)^2)^{5/3}} \frac{\tau_k}{(1+(\omega\tau_k)^2)^{3/2}}. \tag{2.43}$$

The waves generated by the Reynolds stresses should dominate those generated by entropy fluctuations for $kH_c \gg 1$, and both source terms should have the same effect for $kH_c \ll 1$; however, the waves generated by entropy fluctuations should dominate at high ω. When both the spectrum of forcing and the effect of integrating over depth are included, the response of the waves in $\mathbf{B}_\phi(\omega, k_x, k_y; z)$ at high kH is proportional to $k^{-4/3}$ for waves generated by Reynolds stresses and proportional to $k^{-8/3}$ for waves generated by entropy fluctuations. For low kH, both are proportional to k^4. These proportionalities do not include effects such as the shape of the function $h(z)$ or the amplitude of the Wronskian, but since those are independent of the particular forcing used, these proportionalities serve to indicate which forcing is likely to be more important in generating momentum fluxes and temperature fluctuations. Nonetheless, since Reynolds stress generated waves have an ω^{-3} dependence for large ω and entropy fluctuation generated waves an ω^{-2} dependence, it is not clear which waves will be important in calculations of momentum flux and radio scintillation models. Presumeably, a spectrum with an ω^{-2} dependence may generate more momentum at high phase speeds ω/k than a spectrum with an ω^{-3} dependence. For the above reasons we experiment with both types of forcing.

To this point we have detailed how one goes about calculating the spectrum of

Gibbs free energy fluctuations associated with gravity waves generated by convection in a Venus-like atmosphere. This spectrum is required for the model of radio scintillations as caused by gravity waves. We also need to calculate the momentum flux associated with the gravity waves so that we may determine whether the waves can drive the atmospheric superrotation. The spectral function $M(\omega, k_x, k_y)$ of equations 2.9 and 2.38 will prove very useful in finding the momentum flux spectrum.

2.7 Momentum flux

The equation for conservation of zonal momentum can be found by collecting the second order terms in equation 2.1*a* and using the mass conservation equation 2.1*d*. By symmetry in y we do not expect any meridional accelerations. We use primes to denote the order of each term. The equation for conservation of zonal momentum is

$$\frac{\partial}{\partial t}(\bar{\rho}u'') + \frac{\partial}{\partial z}(\bar{\rho}\overline{u'w'}) = 0 \tag{2.44}$$

where $\partial u''/\partial t$ is a second order acceleration exerted on the mean flow by divergences of the momentum flux $\bar{\rho}\overline{u'w'}$. The overbar denotes an ensemble average. [See Andrews *et al.* (1987), sections 3.5 and 4.6, for justification of this conservation law.]

The momentum flux is broken down by wavemode in the same way as the Gibbs free energy variance, etc. An individual wavemode of frequency ω and horizontal wavenumbers k_x and k_y will contribute a momentum flux at $\bar{\rho}\overline{u'w'}(\omega, k_x, k_y)$. This quantity is defined such that $\bar{\rho}\overline{u'w'}(\omega, k_x, k_y)\, d\omega\; dk_x\; dk_y$ is the amount of momentum flux between the frequencies ω and $\omega + d\omega$, zonal wavenumbers k_x and $k_x + dk_x$, and meridional wavenumbers k_y and $k_y + dk_y$.

So far, the only way we can get a divergence of momentum flux is by absorption at a critical layer. Recall that the critical layer of a gravity wave occurs where the zonal wind speed equals a wavemode's zonal phase speed ω/k_x. For this reason, it is convenient to transform the spectral coordinates of $\bar{\rho}\overline{u'w'}$ from ω, k_x, k_y to

c_x, k_x, k_y. This transformation takes place easily by using our convention for spectral coordinates:

$$\begin{aligned}\overline{\bar{\rho} u'w'}(c_x, k_x, k_y) &= \overline{\bar{\rho} u'w'}(\omega, k_x, k_y)\ (\frac{\partial \omega}{\partial c_x})_{k_x, k_y} \\ &= k_x\ \overline{\bar{\rho} u'w'}(\omega, k_x, k_y)\end{aligned} \quad . \tag{2.45}$$

It appears that a convective source for gravity waves would have a hard time driving the atmosphere at the cloud-tops by critical layer absorption. From GK we know that most of the waves will have total phase speeds c approximately given by W_c, which is 3–5 m/s. Wind speeds at the cloud-tops are about 60 m/s, so it seems that few waves will be able to transport their momentum to high altitudes. Some waves, however, will have large zonal phase speeds $c_x = \omega/k_x$, and there exists a simple geometric method for finding out how much momentum is transported at high zonal phase speeds.

We take advantage of the fact that the horizontal phase speed does not act like a vector in order to give an empirical form for momentum fluxes at high phase speeds. We note that the zonal phase speed c_x is given by ω/k_x whereas the *total* horizontal phase speed of the wave c is ω/k. It is possible to get very large zonal phase speeds c_x for small values of the total phase speed c:

$$c_x = \frac{k}{k_x}\, c = c\ \sec\alpha \tag{2.46}$$

where α is the angle at which the wave is propagating away from purely zonally. Thus, waves which have $\alpha \approx 90°$ have zonal phase speeds which are much larger than the phase speed c. This suggests that even though most gravity waves will have small total phase speeds, there may be enough which propagate meridionally in order to transport a significant amount of momentum to high altitudes in the presence of a strong wind shear.

If we assume that gravity waves are emitted isotropically from the convection, then $\bar{\rho}\overline{u'w'}(\alpha, c)$ must be proportional to $\cos\alpha$. In particular, we set

$$\bar{\rho}\overline{u'w'}(\alpha, c) = \frac{\mathcal{E}(\alpha, c)}{c} \cos\alpha \tag{2.47}$$

in which the quantity $\mathcal{E}(\alpha, c)$ is assumed independent of the angle α. We show later that $\mathcal{E}$ is actually the gravity wave energy flux. Thus, we use $\mathcal{E}(\alpha, c) = \mathcal{E}(c)/2\pi$. We bin the momentum flux spectrum by c_x instead of by α and c by integrating

$$\bar{\rho}\overline{u'w'}(c_x) = \int_{-\pi/2}^{\pi/2} d\alpha \int_0^{c_x} dc \; \bar{\rho}\overline{u'w'}(\alpha, c) \; \delta(c_x - c\sec\alpha) \tag{2.48}$$

in which we use $\delta(\ldots)$ to denote a Dirac delta function. After doing the integral over α, we find that the momentum flux spectrum in the zonal phase speed c_x is

$$\bar{\rho}\overline{u'w'}(c_x) = \frac{1}{\pi c_x^3} \int_0^{c_x} \frac{\mathcal{E}(c)\, c\, dc}{\sqrt{1 - c^2/c_x^2}}. \tag{2.49}$$

With two constraints on $\mathcal{E}(\alpha, c)$, this equation tells us that the momentum flux spectrum in zonal phase speed is proportional to c_x^{-3} for large zonal phase speeds c_x. Firstly, we have already required that the emission be isotropic in the horizontal plane (i.e., $\mathcal{E}(\alpha, c)$ is independent of α). Secondly, the quantity $\mathcal{E}(c)$ is expected to be significant up to some dominant phase speed c_0 and the integral is expected to be significant only over phase speeds c in the vicinity of c_0. Lastly, if $\mathcal{E}(c)$ cuts off more rapidly than c^{-2} at high c, then the integral over c in equation 2.49 yields no dependence on c_x for c_x much larger than the dominant phase speed c_0. Under all of these conditions, the momentum flux at high zonal phase speeds is proportional to $\mathcal{E}c_0/c_x^3$, where $\mathcal{E}$ is the quantity $\mathcal{E}(c)$ integrated over all phase speeds c. In section 3 of this paper, we show that this asymptotic description of the momentum flux at high zonal phase speeds is true numerically as well.

It is possible to solve for the momentum flux if we know the solution to $\mathbf{B}_\phi(\omega, k_x, k_y)$. Explicitly, the momentum flux is found by

$$\bar{\rho}\overline{u'w'} = \frac{\bar{\rho}}{4}(u'w'^* + u'^*w'). \tag{2.50}$$

We caution that on the left side of this equation the winds u' and w' represent the real part of the solution while on the right side of the equation the wind fluctuations are the complex solutions. We wish to relate the quantity on the right to the solution for $\mathbf{B}_\phi$. We do this by substituting for u' and w' using the linearized anelastic equations. We find that

$$\bar{\rho}\overline{u'w'} = \frac{\bar{\rho}}{2}\frac{k_x}{N^2 - \tilde{\omega}^2}\,\mathrm{Im}\{\phi'^{*}\phi'_z\}. \tag{2.51}$$

The operator Im{...} returns the imaginary part of the quantity in the braces. We use the definition of $M(\omega, k_x, k_y)$ given by equation 2.9 along with the formal definitions of $h(z)$ and its derivative h_z given in appendices A and B for propagating waves to show that

$$\bar{\rho}\overline{u'w'}(\omega, k_x, k_y) = \frac{k_x}{2}k^2\, M(\omega, k_x, k_y). \tag{2.52}$$

Using the approximate expression in equation 2.18 is actually sufficient for finding this result. This result only holds for propagating waves. Waves trapped by a thick lid will not transport any momentum vertically. In addition, we do not account for the momentum transported vertically by waves trapped by a thin lid since they do not transport a significant amount of momentum to begin with.

We notice that equation 2.52 has some promising qualities. First of all, this expression is independent of altitude for any mode. This is consistent with wave–mean flow interaction theorems which state that waves which propagate freely without dissipation cannot accelerate the mean flow (Andrews and McIntyre 1976). Secondly, the factor of k_x hints that the convection may be an isotropic emitter of gravity waves. Within $M(\omega, k_x, k_y)$, we have defined the forcing terms to be isotropic, but we do not know whether the Wronskian will introduce any anisotropies. Finally, equation 2.52 allows us to predict how much momentum the trapped waves carry out of the convection before they are reflected by an upper lid. This is done by assuming that $h(z)$ takes on its propagating form when evaluating the Wronskian. This will be useful later in our discussion of the "finesse" of trapped waves.

There are two other conserved second order quantities associated with propagating internal gravity waves: the wave action flux and the energy flux. The wave action flux can be defined as the wave potential energy flux divided by the Doppler frequency ω_D. We denote the wave action flux for each given mode as

$$\mathcal{A}(\omega, k_x, k_y) \equiv \frac{\overline{\bar{\rho}\phi' w'}}{\tilde{\omega}} \tag{2.53}$$

(*e.g.*, Andrews *et al.* 1987). Using the linearized anelastic equations 2.1 for u', w', and ϕ' (or equation 3.7 in Booker and Bretherton 1967), we show that the wave action flux and the zonal momentum flux associated with each mode are related by

$$\mathcal{A}(\omega, k_x, k_y) = k_x^{-1}\ \overline{\bar{\rho} u' w'}(\omega, k_x, k_y). \tag{2.54}$$

We have yet to show that the wave energy flux is conserved and how it relates to the other two conserved quantities. The statement of wave energy density evolution is

$$\frac{\partial}{\partial t}\Big(\frac{\bar{\rho}}{2}(\overline{u'^2} + \overline{v'^2} + \overline{w'^2} + N^2\overline{\xi'^2})\Big) + \frac{\partial}{\partial z}(\overline{\bar{\rho} w'\phi'}) + \overline{\bar{\rho} u' w'}\bar{u}_z = 0. \tag{2.55}$$

The quantity ξ' is the vertical displacement of Lagrangian fluid elements and is related to the vertical wind fluctuation by $\xi' = w'/i\tilde{\omega}$. The quantity $(\bar{\rho}/2)\ N^2\overline{\xi'^2}$ is the potential energy density associated with the wave. This is not a conservation law because it is unclear how the second and third terms on the left-hand side interact. In truth, the formal conservation law for internal gravity wave propagation is the conservation of wave action:

$$\frac{\partial}{\partial t}\Big(\frac{\frac{\bar{\rho}}{2}(\overline{u'^2} + \overline{v'^2} + \overline{w'^2} + N^2\ \overline{\xi'^2})}{\tilde{\omega}}\Big) + \frac{\partial}{\partial z}\Big(\frac{\overline{\bar{\rho} w'\phi'}}{\tilde{\omega}}\Big) = 0. \tag{2.56}$$

If we use the equation

$$\overline{\phi' w'} = (c_x - \bar{u})\ \overline{u' w'}, \tag{2.57}$$

which is the same as equation 3.7 in Booker and Bretherton (1967), we can show that for each mode the statement of energy conservation is

$$\frac{\partial}{\partial t}\Big(\bar{\rho}\bar{u}u'' + \frac{\bar{\rho}}{2}(\overline{u'^2} + \overline{v'^2} + \overline{w'^2} + N^2\,\overline{\xi'^2})\Big) + \frac{\partial}{\partial z}(\bar{\rho}\overline{u'w'}c_x) = 0. \qquad (2.58)$$

Since the energy flux is the product of the momentum flux and the zonal phase speed c_x, we see that the energy flux $\mathcal{E}(\omega, k_x, k_y)$ is given by

$$\mathcal{E}(\omega, k_x, k_y) = \omega\,\mathcal{A}(\omega, k_x, k_y) \qquad (2.59)$$

in which we have measured the energy flux at the point of emission from the convection.

The equation for energy conservation presented above has some interesting characteristics. Firstly, it requires that secular accelerations of the atmosphere be considered as part of the kinetic energy. This term is essential because a nonconservative wave has the potential to deposit heat and kinetic energy. The deposited kinetic energy by definition accelerates the mean flow. Secondly, the equation is frame dependent. Energy conservation will certainly hold true for any frame of reference, but this equation states that the energy flux of interest is dependent on the frame of reference. In fact, this must be the case if we allow the wave to transport kinetic energy. Thirdly, nonconservative waves have the ability to deposit heat and kinetic energy, but we cannot yet distinguish between the two.

In order to deduce the secondary effects of nonconservative waves, we must calculate the rate of heat deposition by such waves. The waves add kinetic energy to the mean flow at a rate of $-\bar{u}\;\partial/\partial z(\bar{\rho}\overline{u'w'})$. The difference between the total energy lost by the wave and the energy added to the mean flow is $(\bar{u} - c_x)\;\partial/\partial z(\bar{\rho}\overline{u'w'})$. Exactly what happens to this energy remains undetermined, but certainly some of it can heat the atmosphere through viscous dissipation and some of it may eventually be reemitted as completely new gravity waves. Notice that this excess energy loss rate is independent of the frame of reference. If a wave were to become nonconservative only at critical levels, where $c_x = \bar{u}$, all of the energy loss would go toward adding kinetic energy to the mean flow. This can be understood in an integral sense: for a critically absorbed wave, $\partial/\partial z(\overline{\bar{\rho}u'w'}) = \overline{\bar{\rho}u'w'}\ \delta(\bar{u}(z) - c_x)\ \bar{u}_z$. In the end, however, we shall see that waves will break before they are critically absorbed; thus, breaking gravity waves have an associated energy deposition which may heat the atmosphere or be radiated away in gravity waves.

It is possible that other stresses may deposit heat in the atmosphere. Such stresses can arise from turbulent eddies or molecular viscosity, for example. We write these stresses as τ''_{xz} and note that they will apply an additional acceleration of $\bar{\rho}^{-1}\ \partial\tau_{xz}/\partial z$ to the mean flow. They will heat the atmosphere by doing work against the shear and do so at the rate of $\tau_{xz}\bar{u}_z$ (Landau and Lifshitz, pp. 50–51). Including heating by nonconservative waves, the total dynamic heating rate of the atmosphere is

$$\bar{\rho}Q'' = (\bar{u} - c_x)\frac{\partial}{\partial z}(\overline{\bar{\rho}u'w'}) + \tau''_{xz}\bar{u}_z. \tag{2.60}$$

If in the long run the atmosphere is in a steady state, then the shear stresses must exactly counteract the momentum transport by the gravity waves. That is, $\tau''_{xz} = \overline{\bar{\rho}u'w'}$. If this is the case, then the rate at which heat is deposited in the atmosphere is given by $-\partial/\partial z(\overline{\bar{\rho}w'\phi'})$. We have used the identity for gravity waves that $\overline{w'\phi'} = (c_x - \bar{u})\ \overline{u'w'}$. This result for heating by gravity waves is the same result found by others (Lindzen 1981); however, it is important to realize that this formulation of the heating rate is dependent on the atmosphere being in a steady state.

The amount of gravity wave energy available to the atmosphere is the quantity $\mathcal{E}(\omega, k_x, k_y)$ integrated over all modes. In a steady state, no kinetic energy change occurs and the total heating of the atmosphere by wave and eddy processes is the same as the gravity wave energy emission rate from the convection. This can be understood by integrating $\partial/\partial z(\bar{\rho}\overline{w'\phi'})$ over depth. At the top of the atmosphere, presumably $\bar{\rho}\overline{w'\phi'} = 0$ and thus the integrated heat deposited in the atmosphere is $\bar{\rho}\overline{w'\phi'}$ evaluated just above the convection. Since $\bar{u}=0$ just above the convection, the total heat deposited in a steady state atmosphere is just the integral of $\mathcal{E}(\omega, k_x, k_y)$ over all modes.

2.8 Wavebreaking

We know from previous work that gravity waves break everywhere in the Earth's atmosphere and there is no reason to assume that the same does not happen on Venus. In fact, gravity waves are known to break before they ever reach their critical layers (Geller *et al.* 1975), so we must take into account the process of wavebreaking.

We assume that waves break just enough so that they are only barely stable against the convective instability condition. Waves can break because of Kelvin-Helmholtz instabilities and convective instabilities, but it was shown that the convective instability dominates for waves in a nonshearing flow (Hodges 1967; Hines 1991). The convective instability criterion is also sufficient in a shear flow provided that the background Richardson number is much larger than 1/4. The convective stability criterion is that the temperature fluctuations associated with the waves cannot exceed the stability of the atmosphere (given in Kelvins per kilometer) at any vertical scalesize. Mathematically this is written as

$$\int_{dm\sim m} m^2 \mathbf{B}_T(m)\, dm \approx \Gamma^2. \tag{2.61}$$

The quantity Γ is approximately the stability of the background atmosphere given by

$$\Gamma \equiv (dT/dz)_{\text{atmosphere}} - (dT/dz)_{\text{adiabat}}. \tag{2.62}$$

We integrate over a unit logarithmic interval $dm \sim m$ because we only desire this condition to hold at individual scalesizes. The result of this condition is that

$$\mathbf{B}_T(m) \lesssim \frac{\Gamma^2}{m^3}. \tag{2.63a}$$

This spectrum is equivalent to the "saturated" spectrum given by Dewan and Good (1986), which is

$$\mathbf{B}_u(m) + \mathbf{B}_v(m) \lesssim \frac{N^2}{m^3}. \tag{2.63b}$$

This is best understood because the temperature fluctuation T' is related to the vertical displacement ξ' through $T' = -\xi'\Gamma$, the vertical displacement is related to the Gibbs free energy fluctuation through $\xi' \sim m\phi'/(N^2 - \omega_D^2)$, and the Gibbs free energy fluctuation is related to the horizontal wind fluctuations through $\omega_D u' \sim k_x\phi'$ and $\omega_D v' \sim k_y\phi'$. Putting this all together, the spectrum of the wave kinetic energy density in vertical wavenumber is approximately $(N^2/\Gamma^2)\ \mathbf{B}_T(m)$. Thus the two above equations are consistent. Dewan and Good had assumed that the waves broke by Kelvin-Helmholtz instability, though. The saturated spectrum has been observed in the Earth's atmosphere at vertical scales between 10 meters and a few kilometers.

In our formulation, we must compute whether or not waves break by integrating over their spectral coordinates and binning by their vertical wavenumbers m. If the computed spectrum of temperature fluctuations exceeds the universal spectrum at m, then every wave with that vertical wavenumber is broken by the same factor until the wave is stable. The vertical wavenumber of each mode is dependent on altitude, though, so it appears that the spectrum $\mathbf{B}_T(m; z)$ would have to be computed at every altitude to find the breaking factor $f_{\text{break}}(z)$ for every mode. This breaking factor would start at unity just above the convection for every wavemode and monotonically decrease with altitude.

As it turns out, we shall only have to integrate the temperature fluctuation spectrum over all the spectral coordinates once for each scenario of wave generation. This is important because such calculations are exceedingly time consuming. Instead, we can find analytic methods for determining how much each wavemode breaks as a function of altitude. We shall show how this is done in the third section of this paper because we must first understand how gravity waves would behave if no breaking takes place.

At this point, we have laid out how our problem is solved numerically. Given background profiles of $\bar{u}(z)$ and $N^2(z)$, we can compute a three dimensional spectrum of gravity waves. We do so by first calculating the factor $M(\omega, k_x, k_y)$ for each mode using equation 2.38. The variance spectra $\mathbf{B}_{S_c}$ and $\mathbf{B}_{w_c^2}$ are computed using equations 2.42 and 2.43. Momentum and energy fluxes are then computed using equations 2.52 and 2.59. Temperature fluctuation spectrum are calculated using

$$\mathbf{B}_T(\omega, k_x, k_y; z) = \left|\frac{\Gamma h_z}{N^2 - \tilde{\omega}^2}\right|^2 M(\omega, k_x, k_y). \qquad (2.64)$$

This arises from equation 2.9 and the identity $T' = \Gamma\phi'_z/(N^2 - \tilde{\omega}^2)$.

2.9 Trapped wave amplitudes

For special situations, relatively simple analytic solutions for gravity wave spectra can be obtained. Such solutions are helpful in understanding some qualitative aspects of gravity wave emission from the convection, but they are not essential to numerically determining momentum and energy flux emission from the convection. They are necessary, however, for estimating the temperature variance of trapped waves, even though trapped waves transport no net momentum of energy vertically. In this subsection we derive some relations which allow us to numerically determine the amplitude of waves trapped beneath an upper lid.

Included in this subsection is discussion of certain approximations and how both propagating and trapped waves react under these approximations. Knowing how propagating waves behave in such situations allows us to better understand how the convection acts as a source for the trapped waves.

In this subsection we assume that $N^2(z)$ can be discontinuous at the top of the convection. When this is the case, N^2 remains zero inside the convection but is

N_c^2 just above the convection. We can deduce the behavior of continuous profiles of N^2 later by taking the limit $N_c^2 \rightarrow 0$. We will be clear about when and where this discontinuity has been implemented in the following discussion.

2.9.1 The thick barrier approximation

When a thick barrier directly overlies the convection ($q_b \gg 1$), the wave emission behaves in the same way as quantum tunneling. The thicker this barrier is, the more the waves are attenuated. For trapped waves, a thicker barrier will create a resonant cavity with higher finesse (*c.f.* subsection "Reflection coefficients, finesse, and the thin lid"), but with the same integrated amplitude in gravity waves. This is best understood because the barrier both separates the cavity from the wave source (emission) and separates the cavity from the wave sink (reabsorption).

Finding approximate analytic expressions for gravity wave amplitudes at this stage demands that we compute the Wronskian $\mathrm{Wr}(g, h)$. The Wronskian depends strongly on the upper boundary condition used in determining the wavemode structure. We compute the Wronskian by evaluating the function $g(z)$ using equation 2.29. We have yet to evaluate the function $h(z)$ near the top of the convection.

In the high q_b expansion, we evaluate the function $h(z)$ and its derivative using equation 2.23. In appendix B we show that in evaluating the derivative of $h(z)$, derivatives in the leading coefficient $\tilde{\omega}/\sqrt{\bar{\rho}}$ in z must be ignored. Evaluating the modified Bessel functions $I_{2/3}$ and $I_{-2/3}$ is a lengthy task, but when their argument is large, we can work with their far simpler asymptotic expansions. Their argument in this case is q_b. Essentially, we are no longer in the immediate vicinity of the turning point (turning point 1 in figure 1), so we can evaluate $h(z)$ using equation 2.17. We are given c_1 and c_2 for both propagating and trapped waves, and the coefficients c_3 and c_4 of equation 2.17 are related to c_1 and c_2 through relations derived in appendix

A. At the top of the convection ($z = z_{\rm top} + \epsilon$) we find that

$$h = \omega\sqrt{\frac{|m_c|}{\rho_0}}\Big[(c_1\exp(\pi i/4) + c_2\exp(-\pi i/4))\,e^{q_b} - \frac{i}{2}(c_1\exp(\pi i/4) - c_2\exp(-\pi i/4))\,e^{-q_b}\Big] \tag{2.65a}$$

and

$$h_z = -\omega|m_c|\sqrt{\frac{|m_c|}{\rho_0}}\Big[(c_1\exp(\pi i/4) + c_2\exp(-\pi i/4))\,e^{q_b} + \frac{i}{2}(c_1\exp(\pi i/4) - c_2\exp(-\pi i/4))\,e^{-q_b}\Big]. \tag{2.65b}$$

The quantity m_c is the value of the vertical wavenumber m immediately above the convecting layer and ρ_0 is the density at the top of the convecting layer. When a barrier occurs at all, such as in this case, m_c is imaginary. The terms which are proportional to e^{q_b} will dominate the above expressions for h and h_z except when $c_1 - ic_2 \approx 0$. Such a cancellation is essential for getting resonantly trapped waves.

For propagating waves, we find that

$$h \simeq \omega\sqrt{\frac{|m_c|}{\rho_0}}\,e^{q_b} \qquad \text{and} \qquad h_z \simeq -\omega|m_c|\sqrt{\frac{|m_c|}{\rho_0}}\,e^{q_b} \tag{2.66}$$

where we have used $c_1 = \exp(-\pi i/4)$ and $c_2 = 0$ for propagating waves. We use equation 2.31 to show that the Wronskian of g and h becomes

$$\mathrm{Wr}(g,h) \simeq -\omega k\sqrt{\frac{k}{\rho_0}}\,e^{q_b}\Big[\sqrt{\frac{|m_c|}{k}}\tanh kH + \sqrt{\frac{k}{|m_c|}}\,(1 - \frac{i}{\omega\tau_c})\Big] \tag{2.67}$$

in the high q_b approximation. With this evaluation of the Wronskian, we can calculate the factor $M(\omega, k_x, k_y)$. For propagating waves in the thick barrier approximation, the general expression for $M(\omega, k_x, k_y)$ is lengthy because of the presence of $\mathrm{Wr}(g,h)$ in the denominator of equation 2.7; however, if we look at $M(\omega, k_x, k_y)$ in the limit of large kH and $N_c^2 \to 0$ (no discontinuity in N^2), we get

$$\lim_{N_c^2\to 0, kH\gg 1}(M(\omega,k_x,k_y)) = \frac{\rho_0}{k^3}\frac{\tau_c^2}{1+4\omega^2\tau_c^2}\,\exp(-2q_b)\ \times C(\omega,k_x,k_y). \tag{2.68}$$

Recall that the quantity $C(\omega, k_x, k_y)$ is defined in equation 2.39.

This result for $M(\omega, k_x, k_y)$ for propagating waves in the limit of large barrier thickness elucidates much about our problem. The barrier which forms above the convection and outside the region of wave generation can behave in a quantum mechanical manner. Even though a barrier is present, internal gravity waves can "tunnel" through it in much the same way as quantum tunneling. We refer to the effect of the barrier as attenuation in spite of the absence of energy dissipation associated with it. Since thick barriers occur only rarely for gravity waves emitted from the convection, this equation is only important to us in the abstract sense that a barrier can exist which inhibits wave emission. We show that there are other types of barrier attenuation in addition to attenuation by a thick barrier.

The nature of trapped waves is fundamentally different than that of propagating waves in the thick barrier limit. The ability of the upward and downward propagating waves in a duct to constructively or destructively interfere sets up resonances. After a gravity wave packet is emitted from the convection and through the lower barrier, it will continuously reflect from the thick upper lid and the lower barrier. Depending upon the phase in the duct, the wave amplitude will add constructively or destructively. When they add constructively, the amplitude response becomes large. This is a resonance. The sharpness and height of the resonance curves is strongly related to the way gravity wave energy is eventually lost. When a thick upper lid is present, the only sink of gravity wave energy is convective reabsorption. The thick lower barrier serves not only to inhibit emission of gravity wave energy from the convection, but also gravity wave absorption by the convection. Thus, barrier attenuation has no net effect on the amplitude of trapped waves.

Mathematically, we get constructive interference when the square of the Wronskian is minimized. This happens in narrow bands, and thus we expect narrow resonant lineshapes in the function $M(\omega, k_x, k_y)$. We find resonances by minimizing the square of the Wronskian. This happens when the large term, $\exp(q_b)$, drops out because of a proper choice of c_1 and c_2. The desired cancellation occurs when $c_1 - ic_2 \approx 0$, which holds true only for specific values of the duct thickness, Q_d. In appendix A, we show that the coefficient of the term proportional to e^{q_b} on the right side of equations 2.65 has the following dependence on the duct phase Q_d:

$$c_1 \exp(\pi i/4) + c_2 \exp(-\pi i/4) = -\cos Q_d \tag{2.69}$$

which is true for trapped waves. This coefficient of e^{q_b} is zero for $Q_d \simeq (n + 1/2)\pi$, and, in the thick barrier approximation, resonances occur under this condition. This makes sense when compared to WKBJ trapping theory. For a resonance to occur, an integral number of half wavelengths is required in the duct plus an additional $\pi/2$ in phase. The extra $\pi/2$ radians of phase is introduced by the connection formulas.

In order to find the cumulative response of each trapped wave we compute its resonant lineshape, linewidth, and amplitude. Most resonant cavities exhibit Lorentzian lineshapes. The amount of temperature or Gibbs free energy variance we can expect from the resonance is proportional to the product of its height and width. Since we wish to know the amount of temperature variance trapped waves can contribute to the temperature fluctuation spectrum, we do an analytic analysis of the structure of gravity wave resonances.

We assume that the spectral variables ω, k_x, k_y remain nearly constant while Q_d varies rapidly when computing the net effect of resonances. We do this in the spirit that $\tilde{\omega}$, k, and hence $m(z)$ remain roughly constant while Q_d varies rapidly in comparison. This is in fact true when the resonant linewidths are small. We can tell *a priori* that the resonant linewidths are dependent on the attenuation factor and decrease with increasing barrier thickness. The thicker the lower barrier becomes, the greater the number of times a gravity wave packet traverses the duct before it loses its energy. This tightens the constraint of constructive interference and thus the linewidth narrows. It is thus valid to treat the spectral variables as nearly constant across a resonance.

We measure the phase δQ away from the nearest resonant Q_n, where $Q_n \equiv (n+1/2)\pi$ for thick barriers. Thus, $\delta Q \equiv Q_d - Q_n$. Assuming narrow resonances, we approximate the coefficients of $\exp(q_b)$ and $\exp(-q_b)$ by taking a small δQ expansion of the coefficients of $h(z)$ in equation 2.65 and find that $c_1 \exp(\pi i/4) + c_2 \exp(-\pi i/4) \simeq \delta Q\,(-1)^n$ and $(i/2)[c_1 \exp(\pi i/4) - c_2 \exp(-\pi i/4)] \simeq (-1)^n/2$. When we use a discontinuous profile of N^2, the square of the Wronskian becomes

$$|\mathrm{Wr}(g,h)|^2 \simeq \frac{\omega^2 k^3}{\rho_0} \tanh kH \left[\left(\frac{1}{a} + 2 + a + \frac{a}{\omega^2 \tau_c^2}\right) (\delta Q')^2\, e^{2q_b} + \frac{1}{4}\left(\frac{1}{a} - 2 + a + \frac{a}{\omega^2 \tau_c^2}\right) e^{-2q_b} \right] \qquad (2.70)$$

where $\delta Q' \equiv \delta Q - \delta Q_{\mathrm{lineshift}}$,

$$a \equiv (k/|m_c|) \coth kH, \qquad (2.71a)$$

and

$$\delta Q_{\mathrm{lineshift}} = \left(\frac{1}{2}\right) \frac{(a^2-1)\,\omega^2\tau_c^2 + a^2}{(a+1)^2\,\omega^2\tau_c^2 + a^2} \exp(-2q_b). \qquad (2.71b)$$

The center of the resonance is located at $Q_d = Q_n + \delta Q_{\mathrm{lineshift}}$. Because of the factor of $\exp(-2q_b)$, the lineshift $\delta Q_{\mathrm{lineshift}}$ is a small quantity. It is already apparent that the resonant lineshape is Lorentzian and the halfwidth δQ_L is

$$\delta Q_L = \frac{a\,\omega\tau_c}{(a+1)^2\,\omega^2\tau_c^2 + a^2} \exp(-2q_b). \qquad (2.71c)$$

The important aspect of this linewidth is that it is directly proportional to the square of the attenuation factor $\exp(-q_b)$ which is a small quantity. Also notice that the linewidth and shift are similar in magnitude.

We evaluate $M(\omega, k_x, k_y)$ in order to demonstrate the effect of resonances. When we use the expression for the square of the Wronskian found above, we find that $M(\omega, k_x, k_y)$ is given by

$$M(\omega, k_x, k_y) \simeq \frac{\rho_0}{\omega^2 k^3} \frac{\omega \tau_c}{\tanh kH} \frac{\delta Q_L}{(\delta Q'^2 + \delta Q_L{}^2)} \mathcal{C}(\omega, k_x, k_y). \tag{2.72}$$

The lineshape of the resonance is clearly Lorentzian with halfwidth δQ_L. The factor $\mathcal{C}(\omega, k_x, k_y)$ is given by equation 2.39.

By integrating over a resonance, we can show that a "continuum" spectrum of trapped waves can be found. We can integrate over the resonance in any of the spectral variables. In the course of integrating, only the Lorentzian factor will vary substantially. This factor will yield a factor of π after integrating. In fact, no factors pertaining to the halfwidth remain after integrating. This suggests that the integrated effect of trapped waves is independent of the structure of the resonances. We use this fact to compute a smooth "continuum" spectrum of trapped waves. Since the resonances are separated by π radians in the duct phase Q_d, the π resulting from the integral over the resonance is cancelled when the integrated amplitude is spread over the interval between resonances. The resultant continuum spectrum is

$$M_{(\text{continuum})}(\omega, k_x, k_y) \simeq \frac{\rho_0}{\omega^2 k^3} \frac{\omega \tau_c}{\tanh kH} \mathcal{C}(\omega, k_x, k_y). \tag{2.73}$$

The concept of a continuum spectrum is powerful. It essentially states that we need not resolve the structure of resonances in order to calculate the temperature variance trapped waves contribute. This is important because resonances can become extremely narrow and highly dense spectrally. Furthermore, in physical reality we cannot know exactly where resonances lie spectrally, so it is good to know what amplitude they give independent of their precise positions. Even though we have only shown that a continuum spectrum of trapped waves exists for thick barriers, this continuum spectrum holds true for all types of lower barriers. We emphasize that the continuum spectrum of equation 2.73 holds only when the upper lid above the duct is thick.

2.9.2 The thin barrier approximation

Attenuation by a thick barrier is commonly known about in the context of "tunneling" in quantum mechanics; however, we find that thin barriers also have the ability to attenuate. In order to investigate how thin barriers ($q_b \ll 1$) effect trapped waves, we shall once again evaluate $M(\omega, k_x, k_y)$ for propagating and trapped waves. Before continuing with a description of thin barriers, we note that when $N^2(z)$ is continuous most waves encounter thin barriers; however, when $N^2(z)$ is discontinuous, most waves encounter no barrier at all ($q_b = 0$) but nonetheless do experience some attenuation.

When evaluating the Wronskian for thin barriers, we use expressions for solutions near turning points given in appendix A. In particular, we must look at the small phase expansion of these turning point solutions when on the nonpropagation side of the turning point ($m^2 < 0$). We note that $h(z)$ within the barrier is given by equation 2.23. When solving for $h(z)$ at $z = z_{\text{top}} + \epsilon$, we use small argument expansions for $I_{2/3}(q)$ and $I_{-2/3}(q)$. In appendix A, when finding the turning point solutions, we considered the $m^2(z)$ profile to be linear in the neighborhood of the turning point. We do the same here when approximating $h(z)$ for small q_b. At $z = z_{\text{top}} + \epsilon$, we consider $m^2 = -m_c^2$. The leading order solution at the top of the convecting layer is

$$\begin{aligned} h(z) \simeq \tilde{\omega}\sqrt{\frac{2\pi|m_c|}{3\bar{\rho}}}\, q_b^{-1/6} \bigg[&(c_2 \exp(\pi i/12) - c_1 \exp(-\pi i/12)) \frac{3q^{4/3}}{2^{5/3}\Gamma(\frac{2}{3})} \\ &+ (c_1 \exp(7\pi i/12) - c_2 \exp(-7\pi i/12)) \frac{2^{2/3}}{\Gamma(\frac{1}{3})} \bigg] \end{aligned} \tag{2.74}$$

where q_b is the barrier thickness as defined in equation 2.21a, q is the phase measured from the lowermost turning point, and the Γ's are gamma functions. It is apparent that the amplitude of $h(z)$ at the convection is almost solely determined by the second term in the brackets whereas its derivative is determined by the first term in the brackets.

We use the form of $h(z)$ in equation 2.74 to evaluate the Wronskian as defined in equation 2.31. Below the turning point, we note from equation 2.15 that $dq/dz = -|m|$. We find that

$$\begin{aligned} \mathrm{Wr}(g,h) \simeq & -i\omega|m_c|\sqrt{\frac{2\pi|m_c|}{3\rho_0}}\,(\tanh kH)^{1/2} \times \\ & \Big[(c_1\exp(7\pi i/12) - c_2\exp(-7\pi i/12))\,\frac{2^{2/3}a^{-1/2}}{\Gamma(\frac{1}{3})}\,q_b^{-1/6} \\ & + \left(1 - \frac{i}{\omega\tau_c}\right)(c_2\exp(\pi i/12) - c_1\exp(-\pi i/12))\frac{2^{1/3}a^{1/2}}{\Gamma(\frac{2}{3})}\,q_b^{1/6}\Big] \end{aligned} \tag{2.75}$$

where we have again used $a \equiv (k/|m_c|)\,\coth kH$.

The factor of a is omnipresent for thin barrier cases. We wish to know whether it is a large or a small number and whether that makes the factor $aq_b^{1/3}$ a large or a small number. This is important because we wish to know which term dominates in equation 2.75. The first term in the brackets is proportional to $(aq_b^{1/3})^{-1/2}$ and the second term is proportional to $(aq_b^{1/3})^{1/2}$. Firstly, for a wave to encounter a lower barrier at all, it is necessary that $\omega > N_c$. Otherwise, a region of propagation would directly overlie the convecting layer. Secondly, the largest waves are forced at frequencies smaller than N_c. The peak in the forcing spectrum occurs for waves with $\omega \lesssim W_c/H$. In the section on numerical results we find a value for N_c when the stability profile is continuous. This value for N_c turns out to be large enough such that most waves have $\omega < N_c$. Therefore, those modes which do encounter a lower barrier contribute the bulk of their amplitude when $\omega \gtrsim N_c$. In this neighborhood, it is possible to have $aq_b^{1/3}$ either very large or small. This is significant, because then either of the two terms in the Wronskian can dominate the other. We emphasize that so far we have only approximated $q_b \ll 1$.

For propagating waves, the analytic solution is rather lengthy; however, a few results are apparent. The thin barrier attenuates the wave depending in which regime of $aq_b^{1/3}$ the mode falls. If $aq_b^{1/3}$ is much less than unity, which is always the

approximation	Q_n	δQ_L	$\delta Q_{\text{lineshift}}/\delta Q_L$
$q_b \gg 1$	$(n+\frac{1}{2})\pi$	$\frac{a\,\omega\tau_c\,\exp(-2q_b)}{(a+1)^2\,\omega^2\tau_c^2+a^2}$	$+\frac{1}{2}\frac{(a^2-1)\,\omega^2\tau_c^2+a^2}{a\,\omega\tau_c}$
$q_b \ll 1,\ aq_b^{1/3} \ll 1$	$(n+\frac{1}{3})\pi$	$\frac{3^{1/2}}{2^{4/3}}\,\frac{\Gamma(1/3)}{\Gamma(2/3)}\,\frac{aq_b^{1/3}}{\omega\tau_c}$	$+\omega\tau_c$
$q_b \ll 1,\ aq_b^{1/3} \gg 1$	$(n+\frac{2}{3})\pi$	$\frac{2^{-2/3}\,\omega\tau_c}{1+\omega^2\tau_c^2}\,\frac{\Gamma(2/3)}{\Gamma(1/3)}\,(aq_b^{1/3})^{-1}$	$-\omega\tau_c$
$q_b = 0$	$(n+\frac{1}{4})\pi$	$a\,(\omega\tau_c)^{-1}$	$+\omega\tau_c$

Table 1. Resonance properties. We show the different resonant conditions, linewidths, and lineshifts depending on the limit of the barrier thickness q_b. The quantity a is defined by equation 2.71a in the text.

case for thin barriers and continuous N^2 profiles (because then $a \equiv 1$), then the barrier attenuation factor is proportional to $aq_b^{1/3}$. Conversely, if $aq_b^{1/3}$ is much greater than unity, then the barrier attenuation factor is proportional to $(aq_b^{1/3})^{-1}$. Therefore, thin barriers can attenuate gravity wave emission.

We must treat trapped waves differently depending on the size of $aq_b^{1/3}$. As before for thick barriers, resonances occur where the Wronskian is minimized. When the parameter $aq_b^{1/3}$ is small, resonances must occur where its coefficient, $c_1\exp(7\pi i/12) - c_2\exp(-7\pi i/12)$, is small. Using relations in appendix A for c_1 and c_2 at the lower turning point for a trapped mode, we find that the coefficient is zero when the duct phase $Q_d \simeq (n+1/3)\pi$. When the parameter $aq_b^{1/3}$ is large, resonances occur near the locus of $c_2\exp(\pi i/12) - c_1\exp(-\pi i/12) \approx 0$, which occurs when the duct phase $Q_d \simeq (n+2/3)\pi$.

As noted above, the continuum spectrum of trapped waves holds true for each of these cases. The resonance conditions and linewidths are different, though. In table 1, we show the results for resonance conditions, linewidths, and line shifts for all types of trapped waves.

We remark here that even though the cases of thick and thin barriers show interesting behavior, when the profile of N^2 is discontinuous, neither of these cases contribute significantly to the amplitude and momentum flux of the emitted gravity waves. In general, $\omega < N_c$ and no barrier at all is present. We refer to this case mathematically as $q_b = 0$. Even though no barrier is present, an attenuation factor does exist. For most waves, a is a small quantity, and it is the attenuation factor for barrierless waves. This is understood by setting the function $h(z) = \tilde{\omega}\sqrt{m/\bar{\rho}}\,\sin(q - \pi/4)$ and evaluating the Wronskian using equation 2.31. The phase q is measured away from the top of the convecting layer.

2.10 Reflection coefficients, finesse, and the thin lid

Using some transformation rules in appendix A for calculating the coefficients c_1 and c_2, we can calculate the response of wavemodes trapped by a thin upper lid, but we have not found the continuum spectrum for these modes as we have for waves trapped beneath a thick upper lid (equation 2.73). Recall that the *upper lid* refers to the abstract barrier that forms at the top of a duct while a *barrier* refers to the region of nonpropagation which may form immediately above the convecting layer. Here we present an alternate way to look at trapped modes which enables us to calculate the continuum spectrum of waves trapped beneath thick and thin upper lids. We shall show that such a calculation requires no knowledge of lower barrier attenuation for waves trapped by a thick upper lid, but that knowledge of barrier attenuation is required to calculate the amplitude of waves trapped by thin upper lids.

The presence of a thin lid rather than a thick lid for trapped waves suggests that there is a sink of energy in addition to reabsorption by the convection, namely radiation of energy to space. Consequently, for these waves there are two mechanisms which limit the size of the wave in the duct. A detailed analysis of such waves is terrifically laborious and not necessarily instructive. Instead, we can view the two sinks of energy as competing with each other to limit the size of the wave. This gives rise to the view of the gravity wave duct as a resonant cavity with a finesse. The finesse of a duct is roughly the number of times a wave packet reflects from the boundaries of the duct before it is dissipated.

We conceptualize the duct for trapped waves as a resonant cavity with upper and lower lids which leak only a little energy. The fraction of gravity wave energy which is retained by a wave packet after traversing the duct upwards and downwards once is r, the total reflection coefficient. The energy lost by the wave packet is done so upon transmission through the lower barrier or through the upper lid. We call r_c the fraction of energy retained after reflection from the lower barrier through which some of the energy is lost to convective reabsorption, and we call r_l the fraction retained after reflection from the upper lid where the energy is lost by tunneling and radiation to space. When the upper lid is thick, $r_l = 1$. The total reflection coefficient r is the product of r_c and r_l.

Simple cavity resonance theory and knowledge of the behavior of propagating modes tells us what the continuum spectra must be (Born and Wolf 1980). We invent a function $M_{(\mathrm{propagating})}(\omega, k_x, k_y)$ which is the function $M(\omega, k_x, k_y)$ for a mode with the same ω, k_x, k_y as the trapped mode in question but with radiation to space imposed as an upper boundary condition. This quantity essentially tells us the amount of gravity wave energy the convection is providing to the middle atmosphere at a given frequency and wavelength. In addition, we view trapped waves as a manifestation of wave packets repeatedly reflected from the upper and lower reflection points with the wave amplitude constructively or destructively adding depending on the amount of phase in the duct. For any resonant cavity, the amount of energy density which accumulates in the duct is

$$M_{(\text{continuum})} = \frac{2M_{(\text{propagating})}}{1-r}, \tag{2.76}$$

where $M_{(\text{continuum})}$ is the continuum version of M. When the upper lid is thick, $M_{(\text{continuum})}$ is given by equation 2.73. For example, this relation can be found for the energy density within a laser cavity of adjustable length in which $M_{(\text{propagating})}$ represents the power provided to the cavity divided by the speed of light and $M_{(\text{continuum})}$ represents the energy density within the cavity. The factor $1/(1-r)$ is the cavity's finesse divided by π. The factor of 2 which appears in the numerator is a result of the upward and downward propagating waves being incoherently phased on average.

This last equation contains some new information for us. Primarily, it tells us what the reflection coefficient of the lower barrier is. We already have an expression for the continuum spectrum of waves trapped by a thick upper lid (equation 2.73) and an expression for the spectrum of propagating waves (equation 2.68 for $q_b \gg 1$—found numerically otherwise). We can thus solve for r_c (because $r_l = 1$). If r_c is a reflection coefficient from the lower barrier, then $1 - r_c$ is a transmission coefficient through the lower barrier. We now see the convection as "trying" to emit a certain amount of energy into the stable layer but that some attenuation mechanism which forms at the interface between the stable layer and the neutral layer prevents much of this emission. The fraction which gets through this barrier is just the transmission coefficient $1 - r_c$, which is generally a small number for thick or thin barriers.

If we are to find the continuum spectrum of waves trapped beneath a thin upper lid, we must next calculate the quantity r_l, the coefficient of a reflection from the upper lid. We find r_l by using the transformation rules across regions of nonpropagation laid out in appendix A. We let an incoming wave encounter a nonpropagation barrier of thickness Q_l and calculate how much of its energy propagates through the barrier. We allow only outward propagation on the transmission side of the barrier. We find in appendix A that if the solution for the transmitted wave is $\tilde{\omega}\sqrt{m/\bar{\rho}}\ \exp(i(q-\pi/4))$ on the emission side, then the solution on the incident side is

$$\tilde{\omega}\sqrt{\frac{m}{\bar{\rho}}} \times (-ie^{Q_l})\Big[(-1+\frac{1}{4}e^{-2Q_l})e^{i(q-\pi/4)} + (1+\frac{1}{4}e^{-2Q_l})e^{-i(q-\pi/4)}\Big]. \tag{2.77}$$

The second term represents the incident wave and the first term represents the reflected wave. By taking the ratio of the square of the coefficients of these two terms, we find that the reflection coefficient associated with the barrier is

$$r_l = \left|\frac{1-\frac{1}{4}e^{-2Q_l}}{1+\frac{1}{4}e^{-2Q_l}}\right|^2 \simeq 1-e^{-2Q_l}. \tag{2.78}$$

We use the expression $r_l = 1-\exp(-2Q_l)$ in our calculations. We note that the transmission coefficient is $\exp(-2Q_l)$, thus implying that gravity wave energy is conserved because the sum of the transmission and reflection coefficients is unity.

In summary, we can calculate the continuum spectrum for modes trapped by a thin lid. We first find r_c by

$$r_c = 1 - \frac{2M_{\text{(propagating)}}}{M_{\text{(continuum, thick lid)}}} \tag{2.79}$$

in which $M_{\text{propagating}}$ is calculated numerically assuming solely upward propagation and $M_{\text{continuum, thick lid}}$ is calculated using equation 2.73. We then define $r \equiv r_c r_l$. Finally,

$$M_{\text{(continuum, thin lid)}} = \frac{2M_{\text{(propagating)}}}{1-r_c r_l}. \tag{2.80}$$

This has the desired property that the function $M_{\text{continuum, thin lid}}$ for waves trapped by a thin lid approaches that for waves trapped by a thick lid as the lid thickness approaches infinity. Furthermore, as the lid phase approaches zero, the function $M_{\text{continuum, thin lid}}$ approaches that for purely propagating waves.

A problem does arise in this description. A discontinuity in $M(\omega, k_x, k_y)$ arises as the upper lid thickness approaches zero. The energy carried vertically by a wave trapped under a lid of zero thickness is just one half that of a wave which encounters no lid at all. This discontinuity is a consequence of using equations 2.77 and 2.78 for all thin lids despite their invalidity for $Q_l \ll 1$. This problem remains unaddressed. Nonetheless, we content ourselves with the knowledge that this is only a very small correction to an order of magnitude analysis. Few of the emitted gravity waves encounter upper lids with thicknesses less than 3. Also, waves trapped by thin upper lids hardly contribute any momentum in the spectrum of momentum flux of gravity waves emitted from convection.

3. Numerical computations

In describing the manifestation of gravity waves generated by convection in the overlying atmosphere, it is useful for us to refer to three different models. The first and simplest model consists of a stable layer with constant N^2 and no wind shear overlying a convective layer with thickness H. This is similar to the model of GK but with a finite depth to the convection and varying temperature in the stable layer. We use $N^2 = 4 \times 10^{-4}$ s^{-2} in the stable layer. The second model has variable zonal wind and a variable static stability in the stable layer. Both profiles are continuous and are intended to mimic the background profiles of zonal wind and static stability of the Venus middle atmosphere. This model is the most general for characterizing the properties of gravity waves generated by dry, neutrally buoyant convection. The third model is similar to the second, except the static stability profile above the convection has been neutralized up to where $N^2 = 4 \times 10^{-5}$ s^{-2}. At that point, the profile is discontinuous. This simulates a discontinuity in the temperature gradient of the background atmosphere. These three models are summarized by figure 2.

3.1 Model I

In this model the stability is fixed at $N^2 = 4.0 \times 10^{-4}$ and the wind is zero above the convecting layer. As in all three models, the background temperature profile is taken from the parameterization of Schubert and Walterscheid (1984). Even though the Brunt-Väisälä frequency is determined directly from the temperature profile, it is not invalid in this case to define the two profiles independently. When the static stability and the temperature structure are considered independent, it is the static stability that is more relevant to the propagation characteristics of the waves. The temperature structure only serves to modify the absolute amplitude of the temperature variance spectra. It would not modify the momentum or energy flux spectra of the waves. Therefore, we can appropriately use the background profile of tempera-

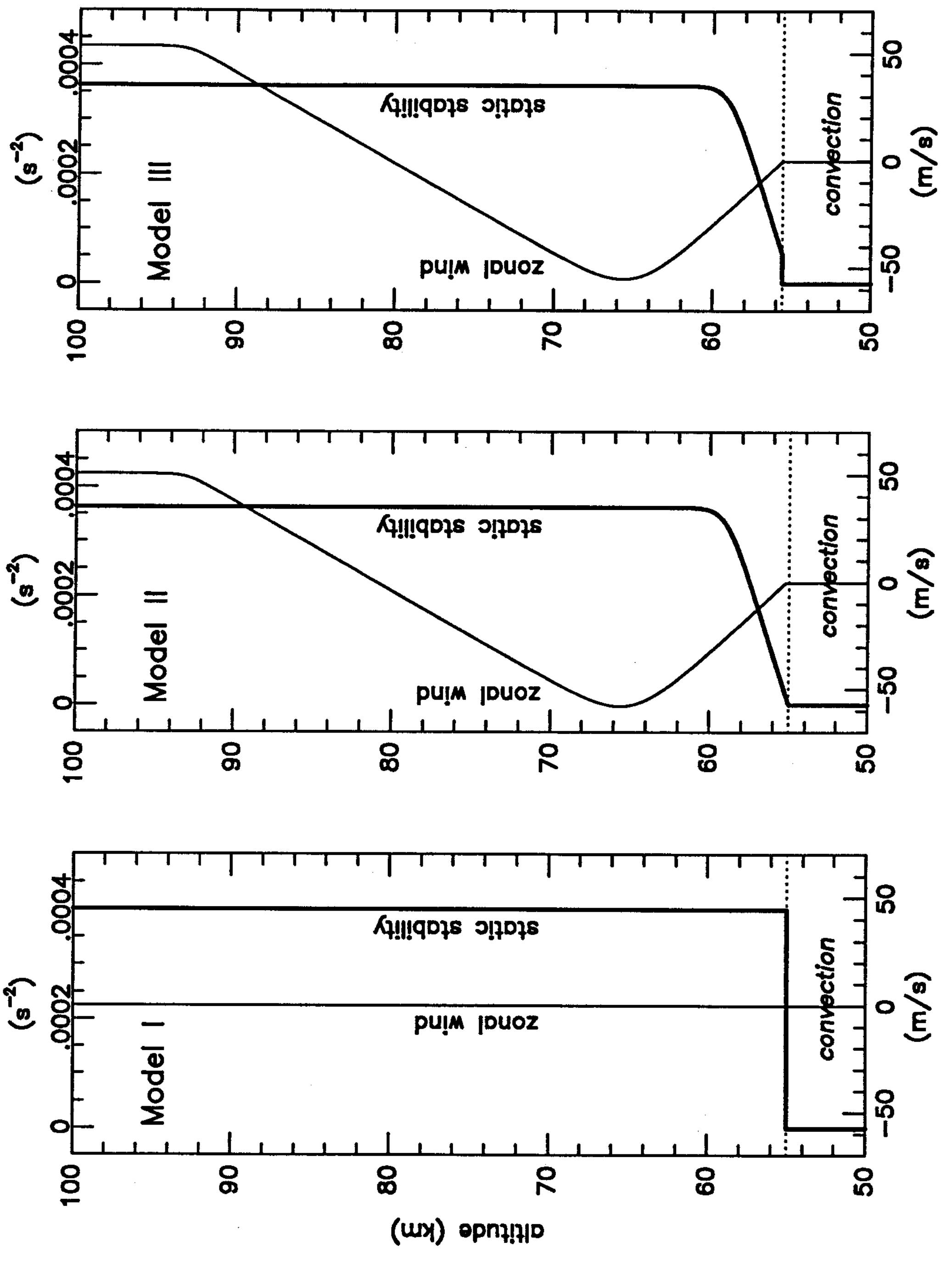

Figure 2. Model wind and stability profiles. For models I, II, and III we show the static stability, or Brunt-Väisälä frequency N^2, and the zonal wind $\bar{u}$ as functions of altitude. The extent of the convecting layer is indicated.

ture and fix the static stability at a constant. The pressure and density profiles are determined using the hydrostatic law in conjunction with the temperature profile.

The only type of wave possible in the first model is propagating. An upper lid cannot form because of the absence of shear and variability in N^2. So long as waves have $\omega < 0.02$ s^{-1} (periods greater than 6 minutes), waves propagate freely out of the convection without encountering a barrier and radiate their energy to space. In figure 3 we present a sample propagating mode. Both the real and imaginary parts of ϕ' are presented. When the $\exp(i\omega t)$ is taken into account, those waves which have an imaginary part lagging the real part by $\pi/2$ radians with increasing height will have a downward phase velocity and hence an upward group velocity.

For the first model we present spectra of temperature fluctuations, momentum fluxes, and energy fluxes for entropy- and Reynolds-type forcing. We use a convective wind speed of $W_c = 3$ m/s and a horizontal correlation length of $H_c = 5$ km for each type of forcing. Temperature variance spectra in vertical wavenumber are computed from $\mathbf{B}_T(\omega, k_x, k_y)$ by integrating over two of the spectral parameters and choosing the other so that m is fixed. Because m is a function of altitude in general, we choose an individual altitude at which to evaluate the temperature variance spectra in m. In this first model, though, the vertical wavenumber is constant in altitude because $\bar{u}$ and N^2 are independent of altitude above the convecting layer; thus, a temperature variance spectrum in m evaluated at one altitude is representative of all altitudes in this model. The momentum and energy fluxes are evaluated as described in the previous section from the function $M(\omega, k_x, k_y)$.

The most important phenomenon to appear in figure 4 is the growth of the temperature variance with increasing vertical wavenumber m for the "unbroken" waves. This is a manifestation of a strong singularity in the spectrum of gravity waves at low frequency. The singularity arises from the factors of ω in the denominator of

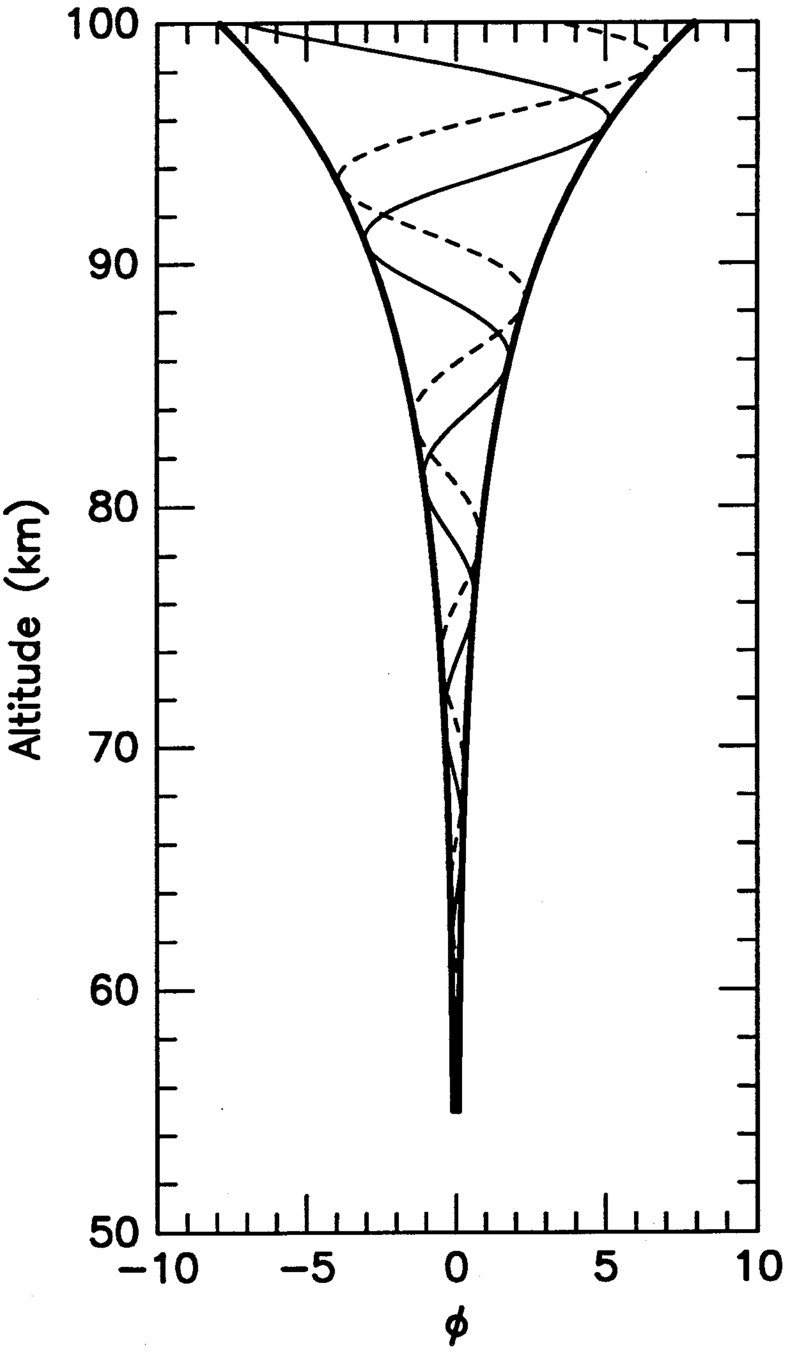

Figure 3. Model I wavemode. This is a wavemode typical of model I waves. The light solid line is the real part and the light dashed line is the imaginary part. The bold line shows the envelope of the wave. We have used $c = 3$ m/s and $k = 2 \times 10^{-4}$ m^{-1}.

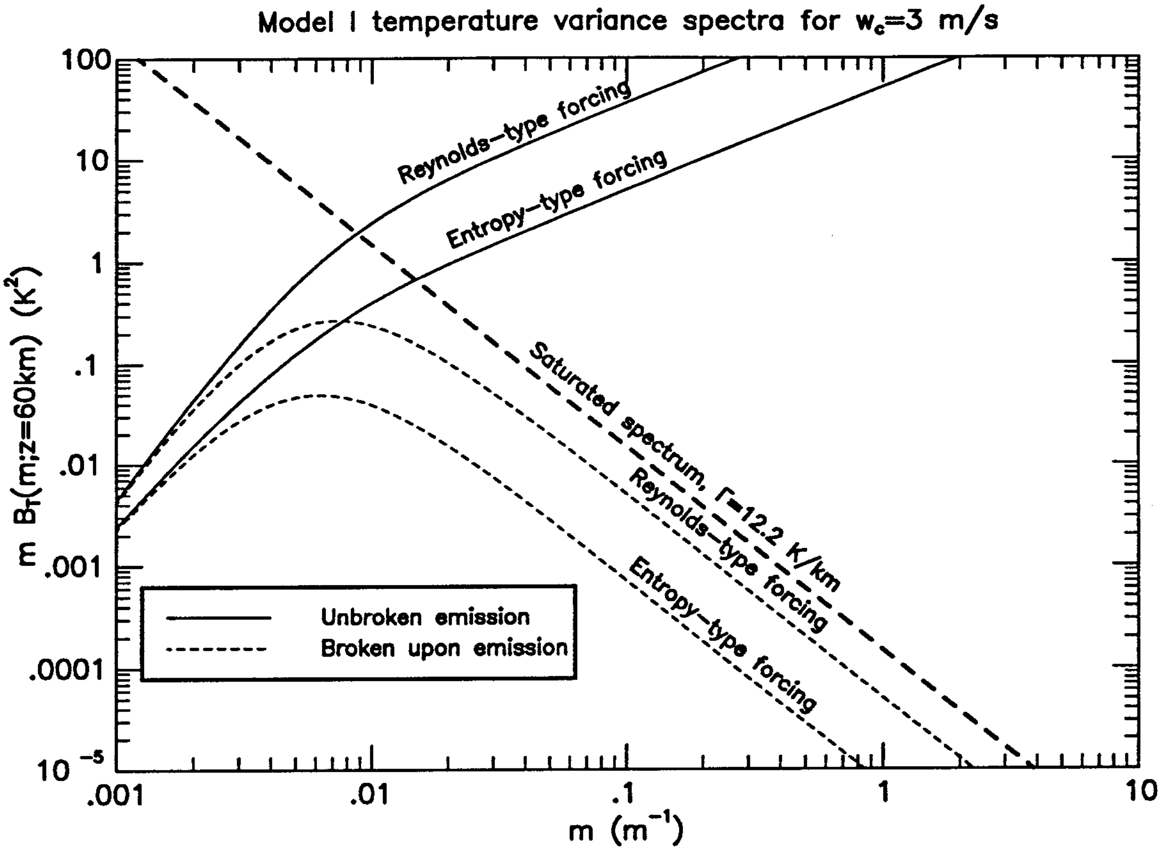

Figure 4. Model I temperature variance spectra. We have plotted the temperature variance spectra in the log of the vertical wavenumber at 60 km altitude. Both types of forcing are represented for both unbroken waves and broken waves. We have taken $W_c = 3$ m/s and $H_c = 2 \times 10^{-4}$ m^{-1} for the forcing. Also present as the bold dashed line is the saturated spectrum as it is defined at 60 km.

the right side of equation 2.3. This is reflected at high vertical wavenumbers m in these spectra because m and ω are inversely proportional (see equation 2.13). Since a divergent spectrum is physically unrealistic, we assume that the waves break as soon as they are emitted from the convection.

In order to calculate which modes break and by how much, we develop an approximate theory for the temperature variance spectrum in the vertical wavenumber. First, we approximate the Gibbs free energy variance spectrum in ω. We start with equation 2.9 and use the expression for $M(\omega, k_x, k_y)$ provided by equation 2.38. The

Wronskian given by equation 2.31 is dominated by the second term on the right at low frequencies, and thus $\mathrm{Wr} \sim h(z_{\mathrm{top}})/H$. The forcing terms are given by equations 2.42 and 2.43. We integrate over k_x, k_y assuming that they and their integrating intervals dk_x, dk_y are all roughly given by $1/H$. The hyperbolic tangent of equation 2.38 is approximated as of order unity. The frequency ω is considered negligible in comparison to the Brunt-Väisälä frequency N because we are interested in the low frequency limit. Retaining the frequency dependence, we find that the Gibbs free energy variance spectrum is

$$\mathbf{B}_{\phi}(\omega) \sim \frac{\rho_0}{\bar{\rho}}\, W_c^4\, (\frac{H}{W_c}) \tag{3.1}$$

where the trailing factor of H/W_c is approximately the correlation time constant of the eddies in the convection. Thus, the Gibbs free energy variance spectrum is roughly independent of ω.

In converting the variance spectrum of ϕ' into a temperature variance spectrum, which is defined by equation 2.64, we note that the only substantial difference between the variance of ϕ' and the variance of T' is the derivative of $h(z)$ in the leading term of equation 2.64. At low frequencies, we assume that the derivative contributes an extra factor of the vertical wavenumber m. We convert from a spectrum in frequency to a spectrum in vertical wavenumber by multiplying by $\partial\omega/\partial m$ at constant k_x, k_y:

$$\mathbf{B}_T(k_x, k_y, m; z) = \left(\frac{\partial \omega}{\partial m}\right)_{k_x, k_y} \mathbf{B}_T(\omega, k_x, k_y) \tag{3.2a}$$

where

$$\left(\frac{\partial \omega}{\partial m}\right)_{k_x, k_y} \simeq \frac{Nk}{m^2} \tag{3.2b}$$

in which we approximate k as $1/H$. The result is that

$$m\mathbf{B}_T(m; z) \approx \frac{\rho_0}{\bar{\rho}(z)}\, \frac{N\bar{T}^2}{g^2}\, m\, W_c^3 \tag{3.3}$$

in which $m\mathbf{B}_T(m;z)$ is the temperature variance spectrum in the log of the vertical wavenumber, which we have found for the sake of comparison with figure 4. The temperature variance spectrum at high vertical wavenumbers is proportional to m. The temperature variance spectrum is not integrable as m approaches infinity. Since large vertical wavenumbers correspond to small phase speeds and small frequency, we call in the low frequency, or low phase speed, singularity. It is unphysical, and we expect the waves to break.

Since the temperature variance spectrum is divergent everywhere above the convection, we must assume that the wavebreaking takes place immediately above the convection. Furthermore, we assume that after the waves break, they never exceed the "saturated" spectrum $\mathbf{B}_T(m) \approx \Gamma^2/m^3$. The waves then each have an associated breaking factor f_{breaking} which tells how much of the energy of each mode is retained after breaking. Since waves do tend to grow with height because of the inverse square root of density growth law, the waves are expected to break throughout the stable atmosphere. Therefore, the breaking factor is a function of height. Nonetheless, we start by finding the breaking factor immediately above the convection.

By our assumptions, the breaking factor at the top of the convection is given by the quotient of the saturated spectrum and the divergent spectrum of equation 3.3. The quotient is $f_{\text{breaking}} \simeq (N/mW_c)^3$ at high vertical wavenumbers. At the top of the convection, $N = N_c$, and using the small phase speed approximation of the dispersion relation (equation 2.13) $m \simeq N/c$, the breaking factor becomes $f_{\text{breaking}} = (c/W_c)^3$.

The temperature variance spectrum of equation 3.3 does not exceed the saturated spectrum at small wavenumbers, though. In fact, the point of intersection of the saturated spectrum and the temperature variance spectrum occurs at a critical wavenumber m_{critical} which is given by

$$m_{\text{critical}} \equiv \left(\frac{\bar{\rho}(z)}{\rho_0}\right)^{1/3} \frac{N}{W_c}. \tag{3.4a}$$

We then formulate wavebreaking in model I by constructing a function proportional to m^{-3} for $m > m_{\text{critical}}$ but does not attenuate for $m < m_{\text{critical}}$. We define this function to be

$$f_{\text{breaking}}(z) \simeq \frac{m^3_{\text{critical}}}{(m^2 + m^2_{\text{critical}})^{3/2}} \tag{3.4b}$$

This breaking factor describes breaking upon emission from the convection when $z = z_{\text{top}}$ and hence $\bar{\rho} = \rho_0$.

A special feature of this breaking factor is its independence from characteristics of the overlying atmosphere. Immediately above the convection the density dependence in the breaking factor falls out. Recall that we arrived at the breaking factor by not permitting waves to exceed the saturated spectrum. It was by no means guaranteed that small nondimensional factors would be introduced. (The only possible nondimensional factor in this model is W_c/NH.) Nevertheless, no nondimensional factors entered. Had such factors become involved, we would have to anticipate a coupling mechanism between the convection and the stable atmosphere in the course of wavebreaking. Instead, the breaking process is solely dependent on the intensity of the convection.

At this point we characterize the process of *breaking upon emission.* We have seen that in the absence of wavebreaking, the convection would emit an unstable amount of gravity waves. For physical relevance, the waves are required to remain stable everywhere above the convection. This means that at some point between the convection and the stable atmosphere, the waves must lose a significant amount of their energy. The energy is lost by wavebreaking at the interface between the convection and the stable atmosphere. The process of breaking immediately upon emission from the convection is breaking upon emission. Because a large amount of wave energy is expected to be lost immediately after emission from the convection, a significant layer of energy dissipation develops immediately above the convection.

We call this layer the *breaking layer* because this is where waves which break upon emission deposit their energy. Since the amount of energy dissipation within this layer is independent of the properties of the overlying atmosphere, the dynamics of the breaking layer is characteristic of the convection alone.

This is not the only breaking process necessary, because the waves can grow and become unstable well above this interface. In the breaking factor above, we have incorporated both breaking upon emission and breaking throughout the stable atmosphere. The factor associated with breaking immediately upon emission is found by setting $\bar{\rho} = \rho_0$ and breaking throughout the rest of the overlying atmosphere is found by letting $\bar{\rho}$ vary with altitude.

In figure 4 we have included the temperature variance spectra resulting from breaking upon emission and the saturated spectrum. In comparison with the saturated spectrum, the broken spectra are smaller by factors of 0.33 for the case of Reynolds-type forcing and 0.049 for the case of entropy-type forcing. This happens because we only use an approximate theory to derive the breaking factor of equation 3.4b. If equation 3.4b were a precise equation, certain numerical coefficients would have entered which would have made the broken spectra fall directly upon the saturated spectrum at high vertical wavenumbers. We do not worry about this problem, mostly because the theory of a saturated spectrum itself is an approximate theory with numerical coefficients involved. For an order of magnitude study, our approach should be sufficient.

We note that the Reynolds-type forcing spectrum falls off more rapidly than the entropy-type forcing spectrum at low m. This is a reflection of the high frequency tail of the forcing functions $\mathbf{B}_{w_c^2}$ and $\mathbf{B}_{S_c}$: Reynolds-type forcing falls off more rapidly at high frequency than the entropy-type forcing by a factor of ω^1. Recall that high frequencies ω imply low vertical wavenumbers m.

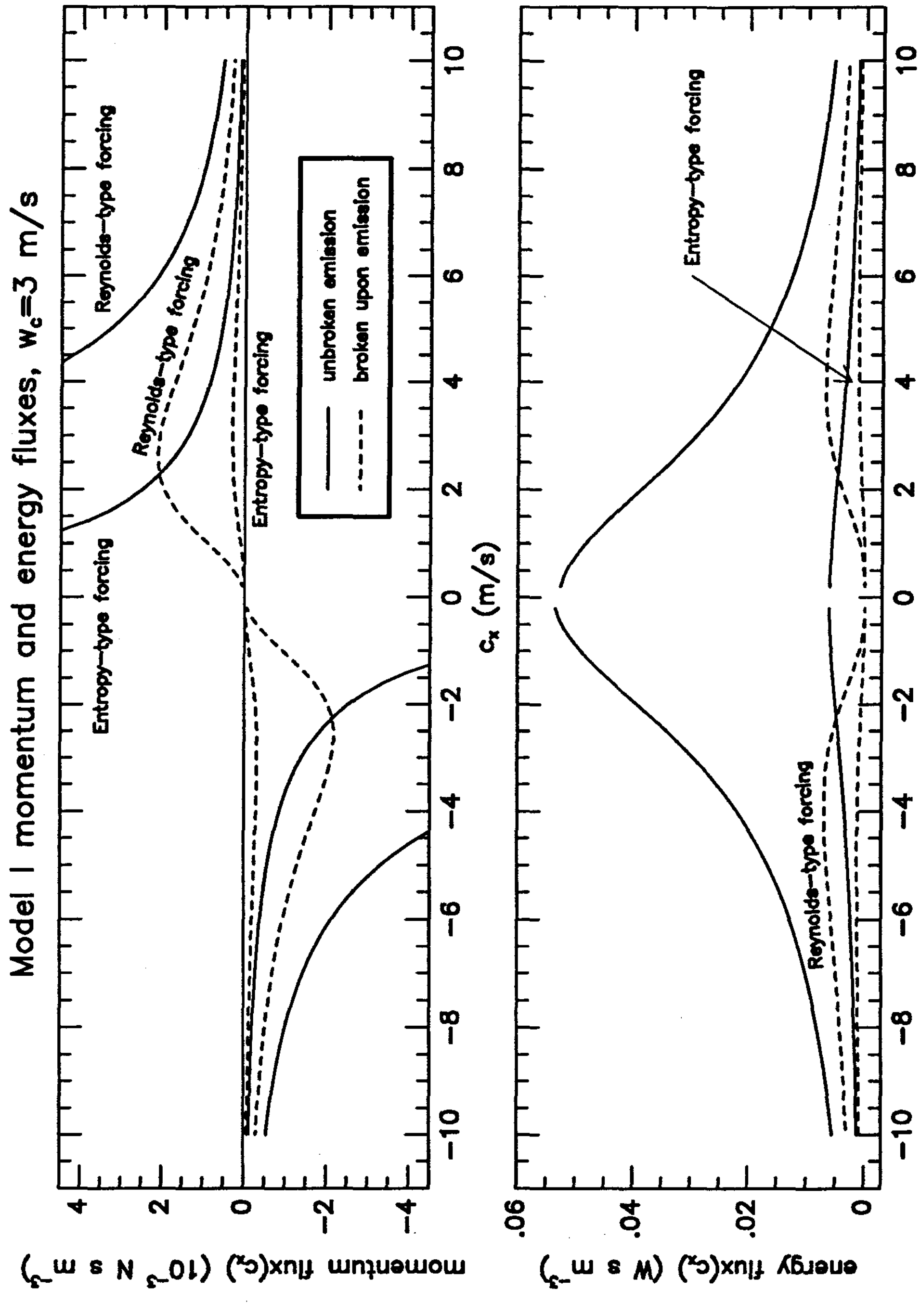

Figure 5. Model I momentum and energy fluxes. In the top figure we show the momentum flux spectrum in zonal phase speed, $\bar{\rho}\overline{u'w'}(c_x)$, for Reynolds-type and entropy-type forcing and for waves unbroken and broken upon emission. In the lower figure we do the same but for the energy flux spectra in zonal phase speed $\mathcal{E}(c_x)$.

For the first model we show "available" momentum and energy fluxes for $W_c = 3$ m/s in figure 5. The vertical transport of zonal momentum carried by gravity waves generated by the convection is considered the available momentum flux: since gravity waves do not affect the mean state atmosphere until they are either broken, damped, or critically absorbed, their momentum flux is available to the entire overlying stable atmosphere should they choose to attenuate in any way. The available fluxes are those carried by waves at the point of emission from the convecting layer after they have been broken upon emission.

We consider Reynolds-type and entropy-type forcing for both unbroken emission and broken upon emission in figure 5. The difference between the momentum flux and energy flux spectra is a factor of c_x (see equations 2.54 and 2.59). In the unbroken spectra, the amount of energy in internal gravity waves generated by the convection is finite despite the amount of prograde/retrograde momentum generated being infinite. The infinity in the momentum flux spectra is another manifestation of the low frequency/high vertical wavenumber singularity. Wavebreaking upon emission rids the momentum flux spectra of the low phase speed singularity. After breaking upon emission, the waves deposit a finite amount of energy. This is the energy which is dissipated in the breaking layer.

The dashed curves in figure 5 are the spectra of momentum and energy flux after breaking upon emission. In the "Analytic solutions" section of this paper we had shown by a geometric argument that the momentum flux spectrum would fall off as c_x^{-3} at large c_x provided that the wave response falls off rapidly enough with frequency and that the wave emission is isotropic. By the symmetries set up in this model, we already know that the wave emission is isotropic. Because the c_x^{-3} does hold at high zonal phase speed, though, we know that the wave response to convective forcing at high frequencies is weak.

So that we may find an expression for the overall amplitude of the momentum flux spectrum $\bar{\rho}\overline{u'w'}(c_x)$, we first approximate the total momentum flux $\bar{\rho}\overline{u'w'}$. We find an approximate expression for the Gibbs free energy fluctuation using equation 2.7. The dominant modes have $k \sim 1/H$ and $\omega \sim W_c/H$. We also approximate $F \sim \rho_0 W_c^2/H^2$. The quantity $N^2 - \tilde{\omega}^2$ is evaluated within the convection where $N^2 = 0$. Lastly, the Wronskian is approximated using equation 2.31 and is approximately h/H. Putting this together tells us that the typical Gibbs free energy fluctuation is $\phi' \sim W_c^2$ at the top of the convection. Using $u' \approx \phi'/c_x$ and $w' \approx (\tilde{\omega}m/N^2)\,\phi'$, we find the integrated momentum flux to be approximately

$$\bar{\rho}\overline{u'w'} \approx \frac{\rho_0 W_c^3}{NH}. \tag{3.5}$$

Given this scaling for the momentum flux and that it falls off as c_x^{-3} above the dominant phase speed W_c, then the momentum flux spectrum in zonal phase speed is

$$\bar{\rho}\overline{u'w'}(c_x) = b\,\frac{\bar{\rho}W_c^2}{NH}\left(\frac{W_c}{c_x}\right)^3 \quad \text{for } c_x \gg W_c. \tag{3.6}$$

The parameter b is a numerical constant which can be found by fitting this spectrum to the one found in figure 5. We find that $b = 0.14$ for Reynolds-type forcing. We have used $H = 5$ km, $N = 0.02$ s^{-1}, and $\rho_0 = 0.9$ kg m^{-3}.

We note that GK found that the gravity wave energy flux is approximately given by the product of the convective energy flux and the Mach number of the convective motions, *i.e.*, $\rho_0 W_c^4/c_s$ in which c_s is the speed of sound. They had assumed that the stable atmosphere was isothermal, for which the speed of sound is approximately NH. Since the dominant phase speed of convectively generated waves is about W_c, our expression for the momentum flux emitted in equation 3.6 from the convection is consistent with the estimates of GK.

A prominent feature of model I is that waves generated by entropy-type forcing are about one fifth as large as those generated by Reynolds-type forcing. It turns out

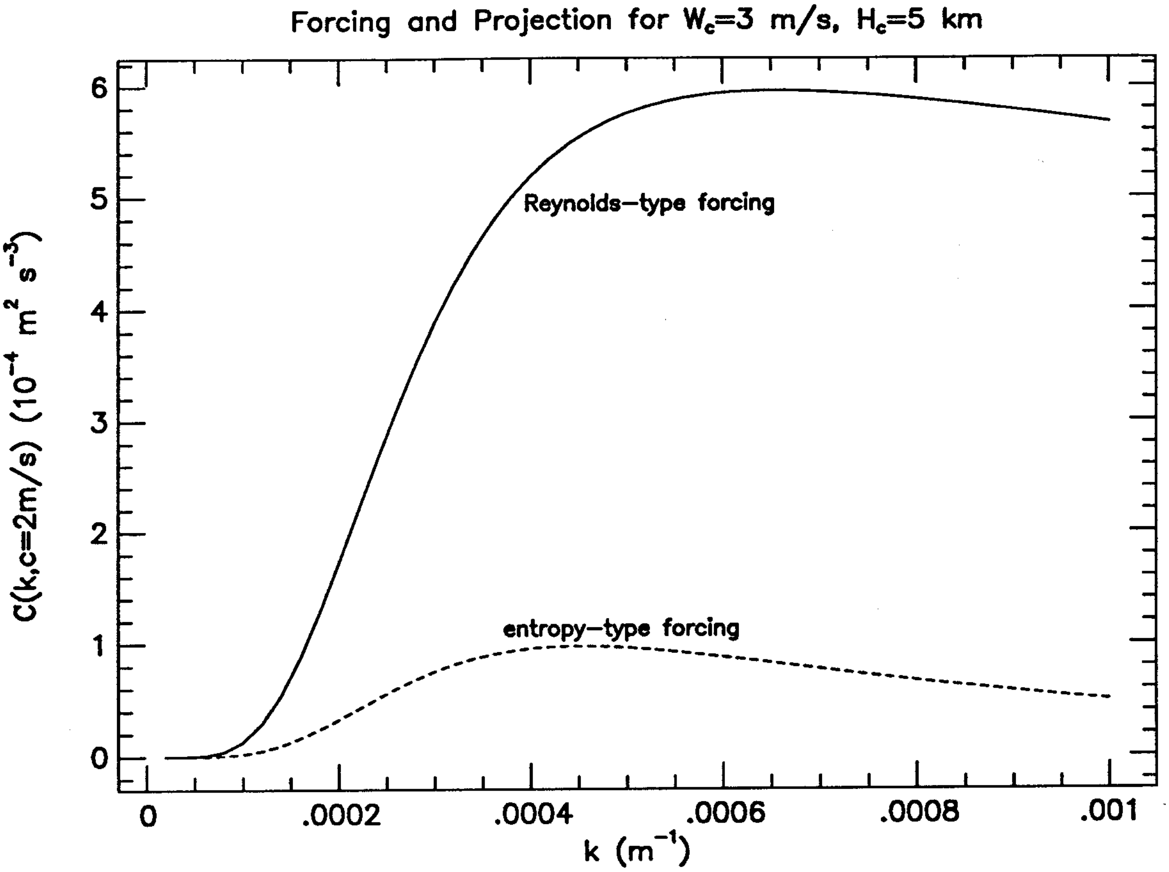

Figure 6. The forcing efficiencies. We plot $\mathcal{C}(k, c)$ for both Reynolds-type and entropy-type forcing. The phase speed c is set to 2 m/s. For the forcing, W_c is set to 3 m/s and H_c is set to 5 km.

that even though the integrated spectra of $(gH/c_p)^2\ \mathbf{B}_{S_c}$ and $\mathbf{B}_{w_c^2}$ are the same, the gravity wave response to forcing is maximized where $\mathcal{C}(\omega, k_x, k_y)$ for Reynolds-type forcing is five times greater than $\mathcal{C}(\omega, k_x, k_y)$ for entropy-type forcing ($\mathcal{C}(\omega, k_x, k_y)$ is given by equation 2.39). In figure 6 we show slices of the temperature variance spectrum at a fixed angle of horizontal propagation α. The model I spectrum is independent of α because zonal winds are absent. Numerically, the greatest gravity wave response occurs near $k \simeq 2 \times 10^{-4}$ m^{-1} and $c \simeq 2$ m/s. In figure 6 we plot $\mathcal{C}(k, c = 2\ \mathrm{m/s})$ for both types of forcing. Clearly, $\mathcal{C}$ is about five times greater for Reynolds-type forcing near $k \simeq 0.2$ km^{-1} than for entropy-type forcing. This is the reason Reynolds-type forcing tends to overwhelm entropy-type forcing in these calculations. Beyond $k \sim 2 \times 10^{-4}$ m^{-1} entropy-type forcing appears much weaker than the Reynolds-type forcing because of the factor of k^2 in the Reynolds-type forcing term of equation 2.39.

The three main points of this model are that we expect waves to break upon emission from the convection because of a low frequency singularity in the wave response to forcing, the momentum flux spectrum is approximately given by equation 3.6 for large zonal phase speeds, and that Reynolds-type forcing generated larger gravity waves than entropy-type forcing. The next step is to examine what happens when variable winds and stability are included.

3.2 Model II

In the second model, realistic profiles of the zonal wind and Brunt-Väisälä frequency are used. The Brunt-Väisälä frequency is continuous in altitude and thus $N_c^2 = 0$.

In this model we demonstrate the nature of the singular response of the waves in a general situation. Whereas in the first model it was possible for a temperature variance spectrum in vertical wavenumber at one altitude to represent such a spectrum at any altitude, evaluating the temperature variance spectrum at just one altitude will not suffice in the second model. Recall that the vertical wavenumber is a function of altitude because both N^2 and $\tilde{\omega}$ are now functions of altitude. For this reason, the second model is complicated because the binning of temperature fluctuations by vertical wavenumber is strongly dependent on altitude. Nonetheless, the momentum and energy flux spectra remain easily calculable.

The introduction of the wind shear provides us with a variety of wave cases. We have explained in the section on analytic solutions that all prograde (westward) waves are propagating. Retrograde (eastward) waves are either propagating or trapped. For

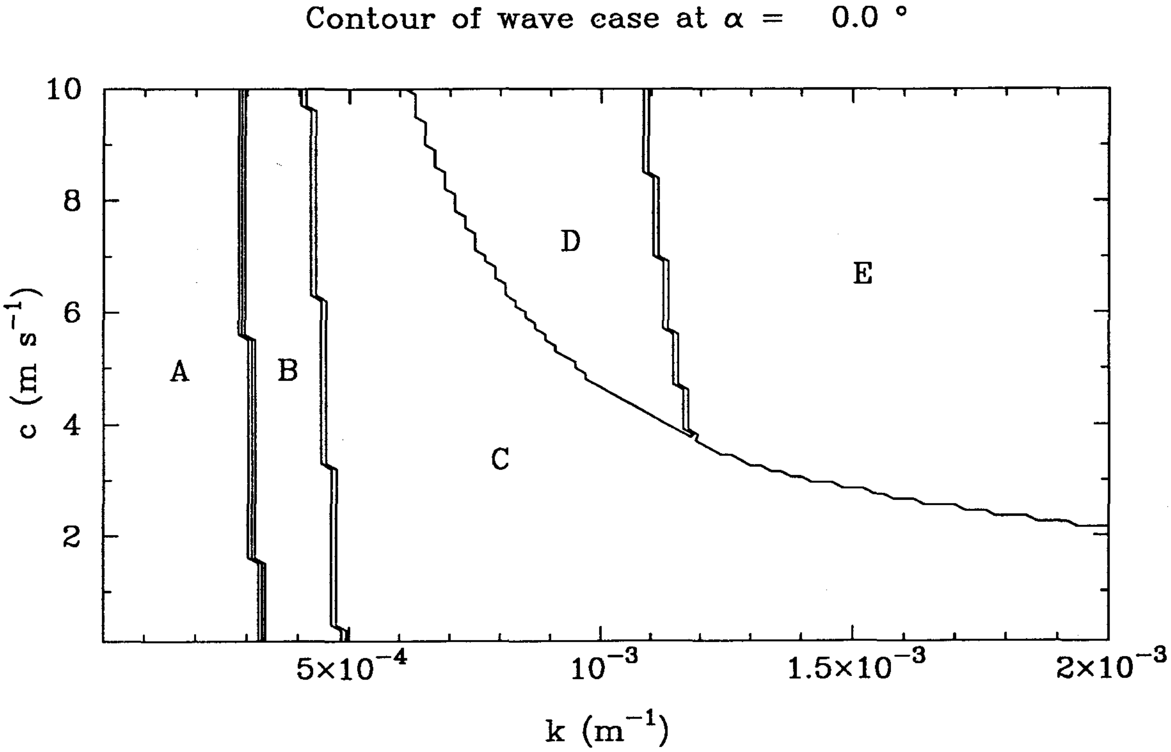

Figure 7. Retrograde wave cases. We plot wave cases as a function of c and k when $\alpha = 0$ (which means $c_x = c$ and $k_x = k$). Region A contains propagating waves, region B contains waves trapped by a thin lid, region C contains waves trapped by a thick lid, regions D and E contain no waves.

some selections of ω and k_x, emission is impossible for retrograde waves. We show in figure 7 where the different wave cases fall in c_x, k_x space. We have taken c_x positive so that we only see the retrograde waves. Whether a wave is trapped or propagating is independent of k_y; however, whether a trapped wave is trapped by a thin or a thick lid is dependent on k_y. In general, the thickness of the upper lid is directly proportional to k, the amplitude of the horizontal wavevector. Thus, larger values of k_y make the upper lid thicker.

We briefly describe why wave cases fall where they do in figure 7. The waves in region A are propagating because the Doppler shifting is so slight (k_x is small) that the Doppler frequency ω_D never exceeds the Brunt-Väisälä frequency above the lowermost turning point. When k_x is increased, however, a lid is formed because

Doppler shifting of ω_D is now large enough that a lid forms near 67 km altitude. At first, the lid is thin; thus waves in region B are trapped by a thin lid. As k_x grows, the lid becomes thicker. When the lid thickness Q_l exceeds 3, we categorize the lid as thick; thus, the waves in region C are trapped beneath a thick lid. Eventually, when c_x and k_x become large enough, no region of propagation exists below 67 km because the Doppler frequency ω_D is so large that it exceeds the Brunt-Väisälä frequency everywhere below 67 km altitude. This is the case for regions D and E.

With figure 7 we check the trapping condition of equation 2.19. In this model, the stability N^2 is 3.63×10^{-4} s^{-2} at its maximum. The maximum wind speed with respect to the convection is 58.0 m s^{-1}. This means that the zonal wavenumber k_x must be greater than 3.3×10^{-4} m^{-1} for trapping to occur. This wavenumber corresponds to a horizontal wavelength of 19 km. In figure 7 we see that the transition between propagating and trapped waves occurs near $k_x \approx 3.6 \times 10^{-4}$ m^{-1}. This agrees well with equation 2.19.

Even though the range of k_x is limited for trapped waves, the zonal phase speed c_x is nearly unlimited. We mentioned in finding equation 2.19 that Doppler shifting of ω_D is more important than the frequency ω in determining whether trapping occurs. This is seen in examining $\omega_D = k_x(c_x - \bar{u}(z))$. Since the phase speeds c_x of the dominant wavemodes have $c_x \ll \bar{u}$ where the zonal wind speed is large, the term $-k_x\bar{u}$ will overwhelm k_xc_x in evaluating ω_D. Thus, the zonal wavenumber k_x is the constrained quantity in determining whether a retrograde wavemode is trapped or propagating.

In figure 8 we plot the "available" momentum and energy flux spectra for model 2. Trapped waves contribute no net available momentum or energy flux because their upward and downward components have the same amplitude. In essence, the convection is both the source and the sink of momentum and energy for trapped

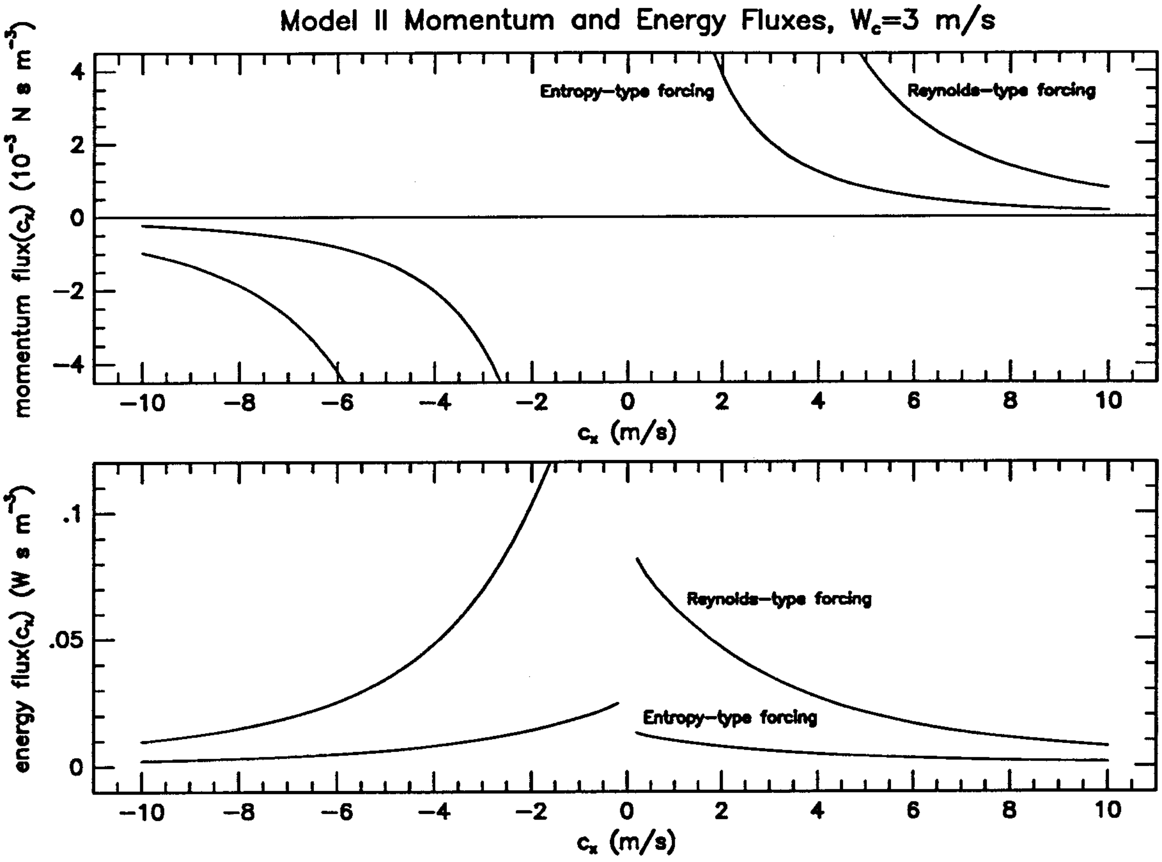

Figure 8. Model II momentum and energy fluxes. We plot the available momentum fluxes in the top figure and the energy fluxes in the bottom figure for the second model. We use both Reynolds-type and entropy-type forcing with W_c set to 3 m/s and H_c set to 5 km.

waves. Since trapped waves propagate eastward and contribute no momentum or energy flux, there is less retrograde ($c_x > 0$) than prograde momentum and energy flux. In addition, we do not include wavebreaking upon emission because the derivation of equation 3.4b, in which $m_{\text{critical}} = N/W_c$, does not hold for continuous profiles of the Brunt-Väisälä frequency.

Even though the energy flux spectrum of this model behaves differently at low phase speeds than the one for model 1, the low frequency singularity still exists. The different behavior at low phase speeds is a consequence of introducing barriers in this model. Recall that a lower barrier forms because the Doppler frequency ω_D is greater than the Brunt-Väisälä frequency N in a small region above the convection, and thus a region of nonpropagation forms (see figure 1). Nevertheless, since the energy and momentum spectra differ only by a factor of c_x, it is clear that the momentum flux spectrum is nonintegrable because the energy flux does not approach zero as c_x approaches zero. The nonintegrability of the momentum flux spectrum is the result of the same low frequency singularity of the first model.

The low frequency singularity is complicated in this model by the nature of the vertical wavenumber profiles. Because the stability profile is continuous, every wavemode has a lower barrier, most of which are thin. As the frequency tends to zero, the barrier grows thinner and vertical wavenumbers just above the barrier in the region of propagation grow infinitely large. Whereas for discontinuous stability profiles it is possible to associate each individual wavemode with a vertical wavenumber above the convection (*e.g.*, for the first model), for continuous static stability profiles it is not possible because vertical wavenumbers above the convection vary rapidly over short vertical scales. For any breaking mechanism within the context of a linear theory, we must know a vertical wavenumber for a wavemode at a particular altitude in order to determine by how much it should break. Since we cannot determine a single vertical wavenumber for wavemodes above the convection, determining how waves break upon emission is impossible in this model.

Because the singularity does exist, some wave energy is expected to dissipate in the immediate vicinity of the convecting layer. The turbulence which results mixes the entropy of the background state and filters the emission of waves. The mixing of entropy neutralizes the background stability in a thin layer above the convection. We associate this layer with convective penetration. At the top of the layer the static stability should have a nonzero value. Effectively the discontinuity in the stability creates a buffer against vertical motions associated with the convective and breaking activity.

We estimate the thickness of the layer by estimating the height to which a parcel with vertical velocity W_c can rise before stability impedes its motion. We assume that the stability profile would otherwise be linear with a slope of N_z^2 and that a penetrative parcel would stop once its potential energy becomes as large as its initial kinetic energy. The potential energy per unit mass is approximately $N_z^2\zeta^3$ where ζ is the height of penetration into the stable atmosphere. We approximate the initial kinetic energy per unit mass as W_c^2. Equating $N_z^2\zeta^3$ and W_c^2 gives an expression for the depth of the penetrative layer:

$$\zeta \approx \left(\frac{W_c^2}{N_z^2}\right)^{1/3}. \tag{3.7}$$

We approximate N_z^2 as N^2/H with H representing a scaleheight. With $N^2 \simeq 4\times10^{-4}$, $H \simeq 5$ km, and $W_c \simeq 3$ m/s, we find that the penetrative layer rises to the point at which $N = 4 \times 10^{-5}$ s^{-2}. This is the value assigned to N_c^2, the square of the Brunt-Väisälä frequency above the neutrally stratified ($N^2 = 0$) layer. Since the frequency associated with the dominant gravity waves is $\omega \sim W_c/H_c \simeq 6\times10^{-4}$ s^{-1}, the dominant waves will have $\omega \ll N_c$.

3.3 Model III

In this model, we anticipate the effects of convective penetration described above. We use $N_c^2 \simeq 4\times10^{-5}$ s^{-2} and raise the neutral layer to the point in the general profile where $N^2 = N_c^2$. In this scenario, the temperature profile remains continuous, but its derivative with height becomes discontinuous. Whereas previously we placed the top of the neutral layer at 55 km altitude, it is now at roughly 55.6 km.

3.3.1 The penetrative layer

The penetrative layer has two roles. Its first role is to mix background entropy sufficiently that the stability profile is discontinuous at its upper boundary. The energy required for the mixing is derived from the convection itself and can be viewed either as penetrative convection or as breaking gravity waves. The second role of the penetrative layer is to filter the emission of the gravity waves. In effect, the penetrative layer contributes a breaking function f_{breaking} which we have found in the first model. As we expect for any breaking mechanism, it dissipates the waves just enough so that the temperature variance spectrum just above the penetrative layer is approximately given by the saturated spectrum.

The fraction of gravity wave energy lost to dissipation in the penetrative layer is a property of the convection alone—it does not depend on the characteristics of the overlying stable atmosphere. Even though the factor of Γ in the saturated spectrum indicates that the breaking factor might have some dependence on the stable layer, this factor is actually cancelled by the factor of Γ required to generate temperature variance spectra (equation 2.64). The breaking factor is dependent only on the wave phase speed in relation to the convective intensity parameter W_c (the typical velocity fluctuation within the convecting layer). The breaking-upon-emission factor is defined as

$$f_{\text{breaking-upon-emission}} \equiv \frac{c^3}{(c^2+W_c^2)^{3/2}}. \tag{3.8}$$

This is the same factor as that in equation 3.4b with $\bar{\rho}=\rho_0$ and $m \simeq N_c/c$.

It is plausible that some wave generation and reabsorption occurs in the penetrative layer, but such effects are small. If the penetrative layer is to generate any waves, it must do so in a narrow layer characterized by eddy motions and neutral static stability. As such the penetrative layer is indistinguishable from the convecting layer, and in computing the integral of equation 2.7, we assume the limits include the convecting layer and the penetrative layer. Also, we assume that the damping time constant τ_c extends into the penetrative layer. The presence of the penetrative layer does imply breaking upon emission, and thus the breaking factor is used.

3.3.2 Replacement algorithm for trapped waves

Trapped waves also require breaking upon emission, but this does not affect the reflection coefficient off of the lower boundary of the trapping duct. For trapped waves, we expect the breaking factor to be part of the propagating wave incident on the duct, the amplitude of which is described by $M_{(\mathbf{propagating})}$ in equation 2.76. So that trapped waves do not go unstable at the point of emission, we also multiply the continuum trapping spectrum of equation 2.73 by the above breaking factor. Thus, the reflection coefficient from the lower turning point r_c, defined by equation 2.79, is independent of the breaking factor.

When computing spectra of trapped waves, we calculate both "coarse" spectra and continuum spectra. The coarse spectra consist of determining gravity wave amplitudes using equation 2.38. The spectrum is coarse because many resonances are undersampled on the α, c, k grid. We determine when this happens by using our knowledge of resonant positions, widths, and amplitudes as described in table 1. When a resonance is undersampled, we account for the full resonant amplitude by substituting

$$M_{(\mathrm{replacement})}(\omega, k_x, k_y) = \left(\frac{\pi}{\Delta Q_l}\right) M_{(\mathrm{continuum})}(\omega, k_x, k_y) \qquad (3.9)$$

at the expected resonance position. The quantity ΔQ_l is the change in the duct phase from one grid point in α, c, k space to the next. For continuum spectra of trapped waves, we use $M_{(\mathrm{continuum})}(\omega, k_x, k_y)$.

So that we may illustrate the effect of the continuum spectra of trapped waves, we display in figure 9 both coarse and continuum spectra of retrograde waves at a fixed angle of propagation α. We include the effects of breaking upon emission, as we do for all cases in this model. We show curves of $M(\omega, k_x, k_y)$ for both coarse and continuum spectra of trapped waves. We have fixed the angle of horizontal propagation α at 60° and the horizontal wavenumber k at 10^{-3} m^{-1}. This makes

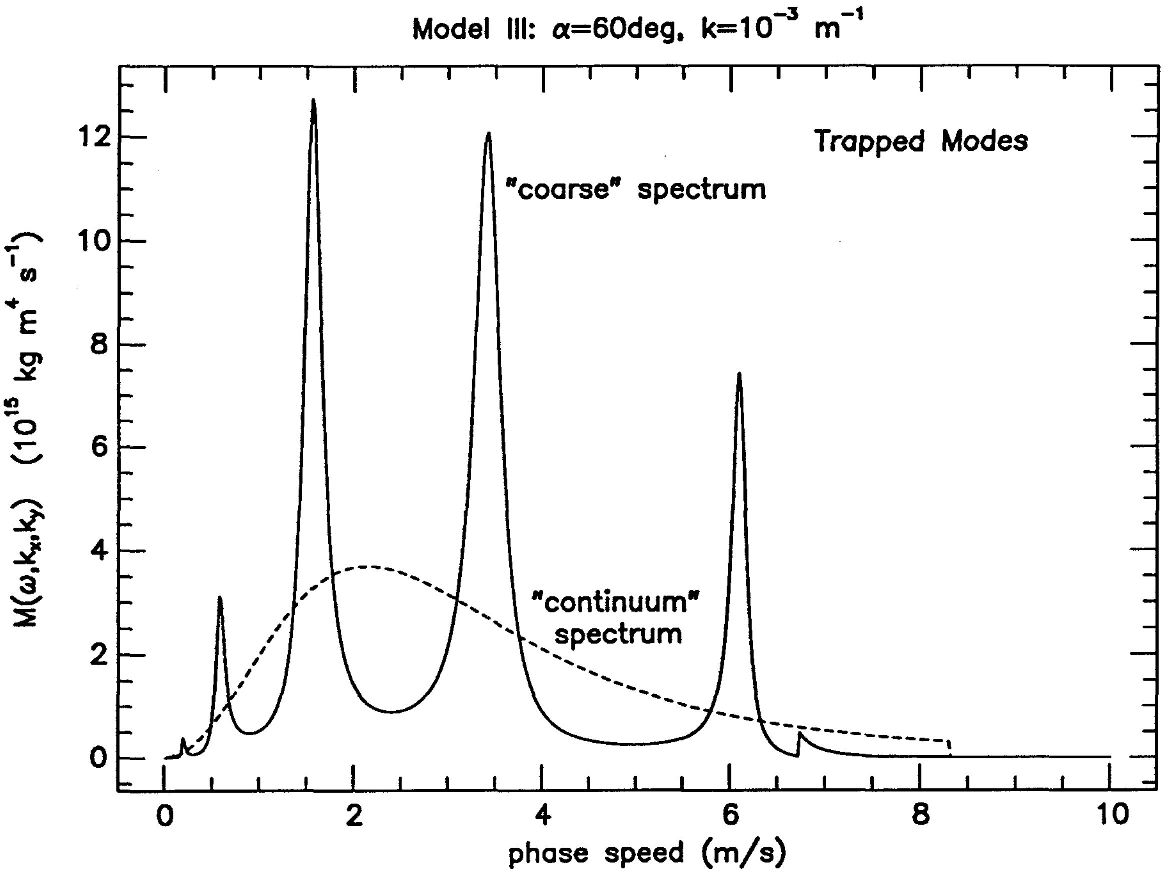

Figure 9. Resonances in the wave response. We show $M(\omega, k_x, k_y)$ of equation 2.9 and $M(\omega, k_x, k_y)$ of equation 2.73. Both k and α are held fixed at 10^{-3} m^{-1} and 60° while c is varied.

$k_x = 5 \times 10^{-4}$ m^{-1}, $k_y = 8.66 \times 10^{-4}$ m^{-1}, and $\omega = kc$. The forcing is Reynolds-type with $W_c = 3$ m/s and $H_c = 4$ km. In the coarse spectrum, the $n = 0$ resonance occurs at $c = 6$ m/s, the $n = 1$ resonance at $c = 3.5$ m/s, etc., where n counts the number of nodes in $h(z)$.

Because of the density of resonances at low phase speeds, the continuum spectrum of trapped waves must be used in order to fully account for all of the temperature variance they contribute. In figure 9, resonances become tightly packed as $c \rightarrow 0$. This is understood by examining the profiles of $m^2(z)$ for this model. The vertical wavenumber becomes very large near the bottom of the duct and an infinite amount of phase accumulates in Q_l (see equations 2.13 and 2.21b. In fact, an infinity of resonances occur as $c \rightarrow 0$. Because the resonances become densely packed, it is impossible to numerically sample the frequency finely enough to account for all of the amplitude of the trapped waves. For this reason, using continuum spectra is mandatory.

Figure 9 demonstrates how continuum spectra work. Continuum spectra integrate over each resonance and spread the calculated amplitude over the spacing between resonances. It is all done implicitly in equation 2.73. The continuum spectrum shows that the amplitude of the trapped waves falls to zero as the zonal phase speed becomes small. Not only does integration over the infinity of modes at small phase speeds become feasible, but these modes have minimal amplitude associated with them.

3.3.3 Temperature variance spectra and critical layer breaking

In figure 10 we show the temperature variance spectrum at the top of the penetrative layer. Spectra are shown for both types of forcing. These spectra are similar to those shown for the first model with one exception: the presence of trapped waves. The trapped waves contribute amplitude at all vertical wavenumbers at 55.6 km altitude. Even though Doppler shifting is chiefly responsible for trapping waves when a strong shear is present, the shear plays no role in determining the vertical wavenumber at 55.6 km. This means that whether or not trapping occurs cannot be determined from the vertical wavenumber at 55.6 km altitude. For this reason, the amplitude of trapped modes is spread out over all vertical wavenumbers when the spectrum is calculated at 55.6 km. In this plot we have used the continuum spectrum of trapped waves. The cutoff at high vertical wavenumber m is the result of breaking upon emission.

The temperature variance spectra above the neutral layer and below the cloudtops exhibit substantially different behavior. A typical temperature variance spec-

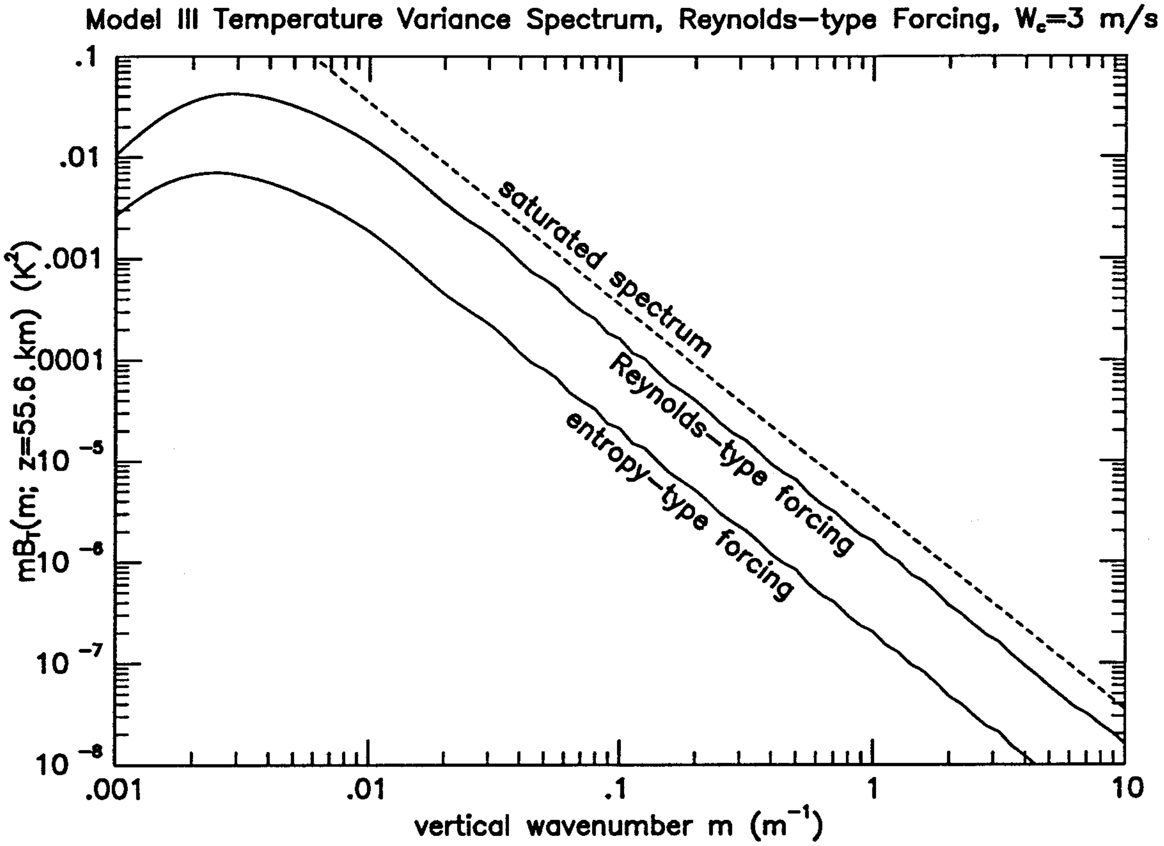

Figure 10. Temperature variance spectrum at emission. We show $\mathbf{B}_T(\log m)$ at the point of emission (z =55.6 km) for both Reynolds-type and entropy-type forcing with $W_c = 3$ m/s. The dashed line indicates the saturated spectrum, which has $\Gamma = 1.87$ K/km at this altitude.

trum of waves broken upon emission but nowhere else is presented in figure 11. The critical layers in this region will cause many modes to have unboundedly large values for the vertical wavenumber, and these modes will contribute a nonintegrable amount of temperature variance. Since modes must break near critical layers, we must find the breaking factor associated with approach to critical layers for these waves.

Since the unbroken temperature variance spectrum varies as a function of altitude, the factor by which waves break depends upon altitude. In order to determine the breaking factor for each wave as a function of altitude, we develop an approximate theory for the unbroken temperature variance spectrum. We start with equation 2.64

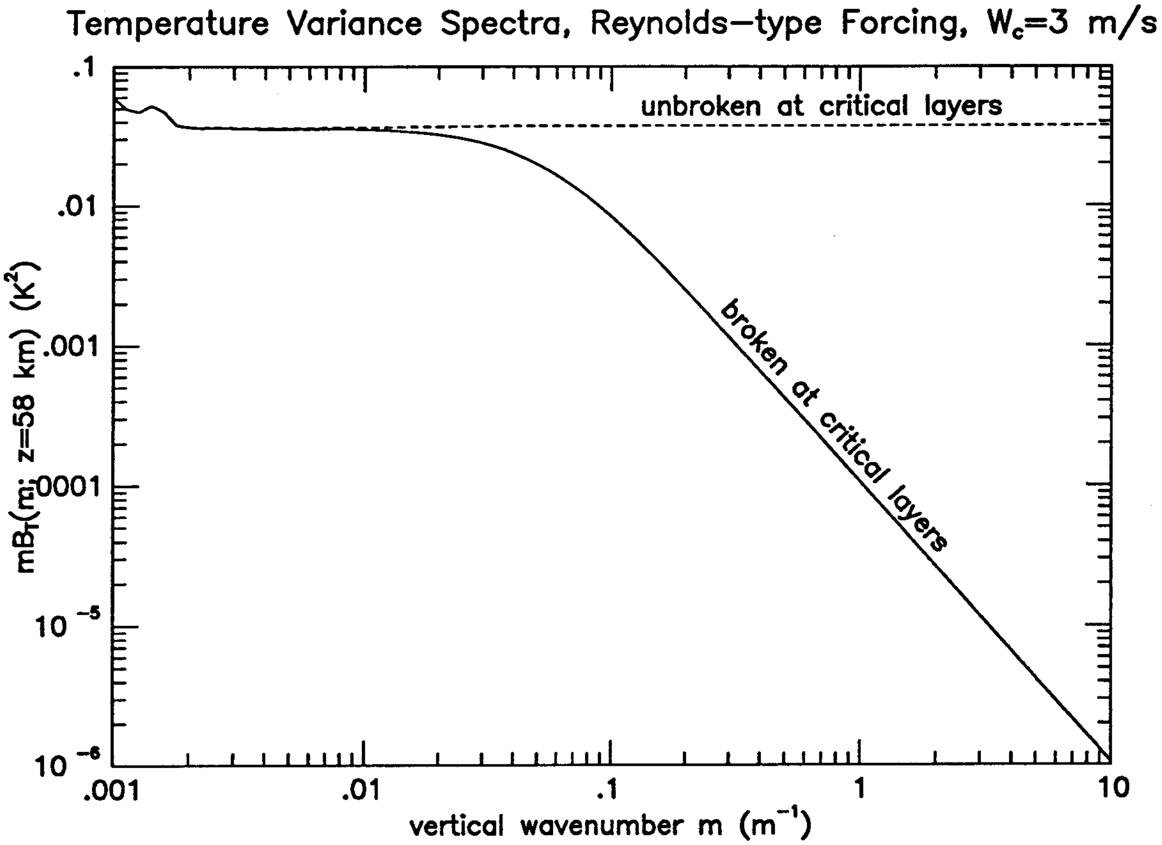

Figure 11. Temperature variance spectrum at 58 km. We show the temperature variance spectrum in the log of the vertical wavenumber. Both spectra are broken upon emission. One of the spectra is unbroken near critical layers and the other is broken near critical layers. We use Reynolds-type forcing with W_c set to 3 m/s.

and transform to the coordinates ω, k, m^2 using the identity

$$\begin{aligned}\mathbf{B}_T(\omega,k,m^2;z) &= \left(\frac{\partial\alpha}{\partial m^2}\right)_{\omega,k}\mathbf{B}_T(\omega,k,\alpha)\\ &= \frac{Nk}{2m^3k_y\bar{u}}\,k\,\mathbf{B}_T(\omega,k_x,k_y).\end{aligned}\tag{3.10}$$

We find that

$$\mathbf{B}_T(\omega,k,m^2;z) = \frac{Nk^2}{2m^3k_y\bar{u}}\left|\frac{\Gamma h_z}{N^2-\tilde{\omega}^2}\right|^2 M(\omega,k_x,k_y).\tag{3.11a}$$

Since the waves are unbounded at high m, we know that $\tilde{\omega}\simeq 0$ and the large waves are those near their critical layers. Thus, $\tilde{\omega}$ can be neglected when compared to N and k^2 can be neglected when compared with m^2. Otherwise, we substitute kN/m

for each appearance of $\tilde{\omega}$. Next we evaluate h_z:

$$h_z \simeq Nk \sqrt{\frac{m}{\bar{\rho}}}. \tag{3.11b}$$

Next we assume that $M(\omega, k_x, k_y)$ is independent of the horizontal angle of propagation α, and thus $M(\omega, k_x, k_y) \simeq M(\omega, k)/(2\pi k)$. The last approximation is that $W_c \ll \bar{u}(z)$ and therefore $k_x \ll k$ for waves near their critical layers. This implies that $k_y \simeq k$. In putting these approximations together, we find that

$$\mathbf{B}_T(\omega, k, m^2; z) \simeq \frac{1}{4\pi} m^{-2} \frac{N^3 \bar{T}^2}{\bar{\rho}\bar{u}g^2} k^2 M(\omega, k) \tag{3.12}$$

in which g is the gravitational acceleration. Integrating this last equation over ω and k and transforming from the temperature variance from m^2 to m gives

$$\mathbf{B}_T(m; z) \simeq m^{-1} \frac{N^3 \bar{T}^2}{\bar{\rho}|\Delta u|} \frac{\mathcal{A}}{\pi g^2} \tag{3.13a}$$

where

$$\mathcal{A} = \int d\omega \, dk \, \frac{k^2}{2} M(\omega, k). \tag{3.13b}$$

The quantity Δu is the difference in $\bar{u}(z)$ between the convecting layer and altitude z. The quantity $\mathcal{A}$ is the integrated wave action flux (see equations 2.54 and 2.52).

Wavebreaking is accomplished by ensuring that the saturated spectrum is not exceeded anywhere in the stable layer. In addition to breaking upon emission, we extend the breaking function f_{breaking} so that it is a function of altitude for each wavemode. In equation 3.13, we find that the spectrum of temperature variance in the log of the vertical wavenumber is flat at large m, as in figure 11. We write this as

$$\mathcal{T}^2(z) = \lim_{m \to \infty} m \mathbf{B}_T(m; z). \tag{3.14}$$

In order to find the new breaking factor, we find the vertical wavenumber at which $\mathcal{T}^2(z) = \Gamma^2/m^2$, in which the latter quantity is the saturated spectrum of temperature variance in the log of the vertical wavenumber. The intersection occurs at

$$m^2_{\text{critical}} \simeq \bar{\rho} \, |\Delta u| \, N \left(\frac{\pi}{\mathcal{A}}\right) \tag{3.15a}$$

and the breaking function is then

$$f_{\text{clb}} = \frac{m^2_{\text{critical}}}{m^2_{\text{critical}} + m(z)^2} \tag{3.15b}$$

for each wave. Since the wavebreaking takes place because gravity waves become unstable as they approach their critical layers, we call the new breaking factor f_{clb}, in which "clb" stands for "critical layer breaking."

This formulation of wavebreaking gives a prediction for the dependence of the "knee" in the saturated spectrum on altitude. Even though $\mathcal{T}^2(z)$ has a strong dependence on the total wave action flux $\mathcal{A}$, only the quantities dependent on height tell us the dependence of m_{critical} on height. The total wave action flux needs to be determined only once by calculating $\mathbf{B}_T(m; z)$ at one altitude. We find that $\mathcal{A}/\pi$ for Reynolds-type forcing at $W_c = 1$ m/s is 58.1 kg s^{-2}, 75.9 kg s^{-2} at $W_c = 3$ m/s, and 279 kg s^{-2} at $W_c = 5$ m/s. For entropy-type forcing at $W_c = 3$ m/s, $\mathcal{A}/\pi$ is 17.3 kg s^{-2}. Given $\mathcal{A}$, we can then figure out absolutely what the critical wavenumber m_{critical} is as a function of height. It depends on the mean state quantities $\bar{\rho}(z)$, $\bar{u}(z)$, and $N^2(z)$.

We constrain f_{clb} to be a monotonically decreasing function of altitude for each mode since we have no mechanism for waves to gain energy as they propagate vertically. Thus, wherever the breaking function might tend to grow with height, we instead hold it constant until it returns to this constant value. The major result of this constraint is that this attenuation factor becomes useless above the peak in the zonal winds. This makes determining the breaking factor everywhere above this point exceedingly difficult. This is unfortunate because we do expect waves to break above 80 km where the zonal wind is eastward with respect to the convection. Above 80 km, many of the eastward vertically propagating waves will encounter critical layers and break. We shall address this point later in connection with momentum deposition.

At this point we present some two dimensional segments out of the full three dimensional spectrum of temperature fluctuations. The coordinates are the horizontal

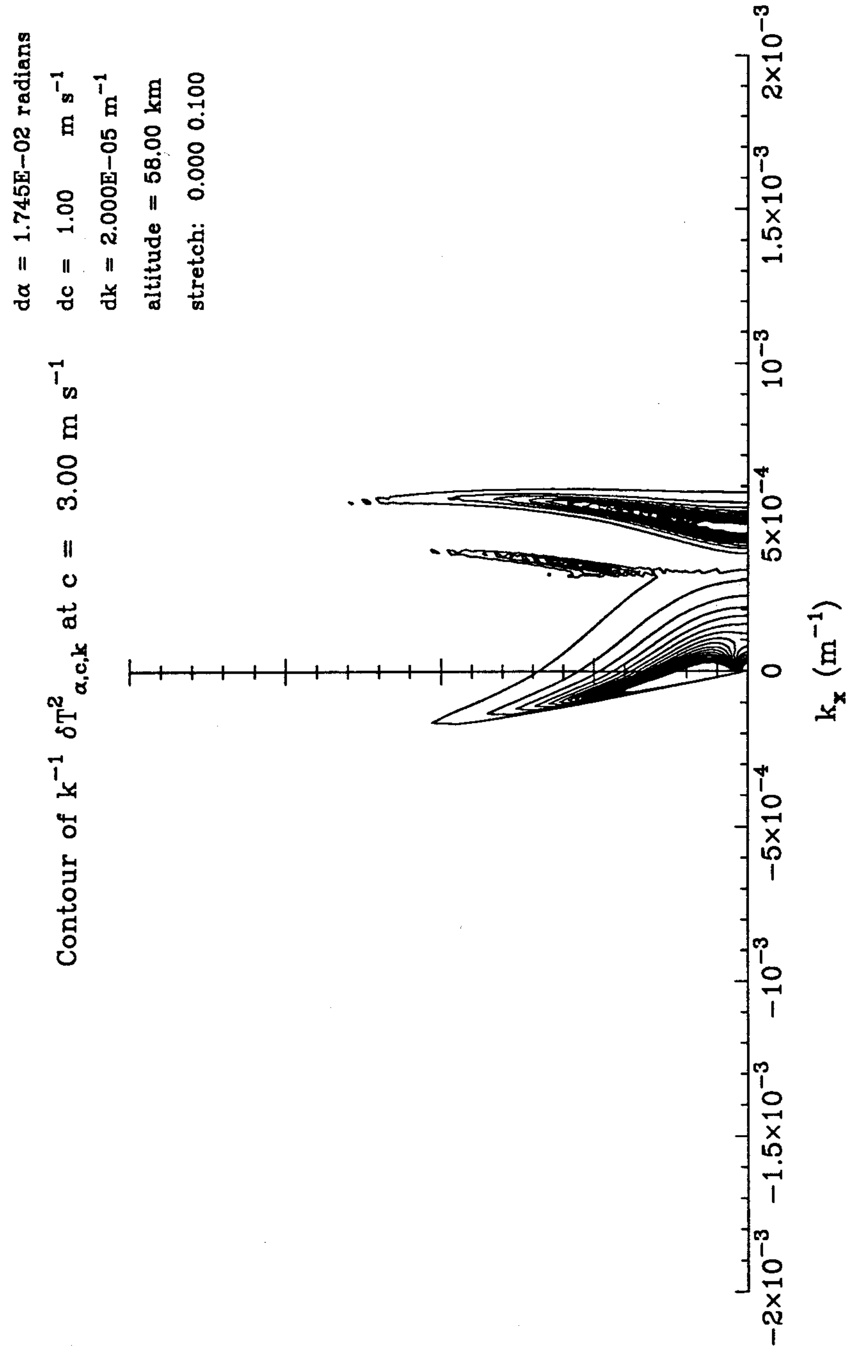

Figure 12. Temperature variance spectrum at constant phase speed. We show the quantity $B_T(\alpha, c, k)/k$, which is the same as $B_T(c, k_x, k_y)$. The horizontal axis is k_x and the vertical axis is k_y. The phase speed c is held constant at 3 m/s and the altitude is set at 58 km. The forcing is Reynolds-type at $W_c = 3$ m/s. Both breaking upon emission and breaking near critical layers is implemented. Contours up to only 10% of the maximum value of the range of this plot are shown.

wavenumber k, the total phase speed c, and the direction of propagation α measured away from the zonal wind direction. The grid point spacing is even in α, c, and k. Such spectra are useful in identifying cloud features seen in Mariner 10 and Pioneer Venus UV images. We chose the above coordinates because all are calculable by analysis of images. Because the phase speed c is the most difficult to measure for lack of a well known rest frame, we show a slice in the three dimensional spectrum with phase speed held constant at 3 m/s which will show the largest wave amplitudes. The forcing is Reynolds-type. The result is figure 12.

The dominant feature in the contour plot in figure 12 is the rapid wave growth near critical levels. Recall that critical levels occur when $\tilde{\omega} = 0$. When written according to an α, c, k coordinate system, critical levels occur when $c = \bar{u}(z) \cos\alpha$. Since c is chosen as a constant, for each altitude a unique direction of propagation α is shared by the modes absorbed at altitude z. In figure 12, we have chosen $z = 58$ km at which $\bar{u} = -16.4$ m/s and thus all prograde waves propagating within 80° of the zonal winds are absorbed below 58 km. This explains the absence of temperature fluctuations in that domain.

The secondary features of figure 12 are the resonances. The dominant resonance in this figure is the $n = 1$ resonance near $k_x \simeq 5 \times 10^{-4}$ m^{-1}. As k_y increases the amplitude decreases because the forcing diminishes at higher ω and k. At higher k_y the resonant peaks become sharper and indeed unresolved. The other resonance apparent is the $n = 2$ resonance. The $n = 1$ and $n = 2$ resonances are dominant in the cut with $c = 3$ m/s. The $n = 0$ resonance is insignificant by comparison because it occurs at higher k_x where the forcing is significantly weaker. Furthermore, we see that all resonances are going to have horizontal wavelengths shorter than 21 km. This is subject to both the background profiles of wind and stratification through equation 2.19. This maximum wavelength would be increased by weaker stability and/or stronger zonal winds (see equation 2.19).

Concerning temperature fluctuations, we use figures 13 and 14 to demonstrate on a two dimensional surface the validity of a continuum spectrum of trapped waves. In figure 13 is a two dimensional slice of the α, c, k spectrum with α held constant at 60°. In a negative shear, no critical levels will develop above the convection for this direction of propagation α. On the other hand, many resonances are apparent. Since we are plotting temperature fluctuations at a given altitude in this figure, it is possible that some wavemodes will have a node in the vertical structure at this fixed altitude. This manifests itself as a zero that can run through the middle of the trapped waves in the contour plot. Indeed, a node in the vertical structure of the trapped waves falls on a curve in figures 13 and 14 that runs from $k \simeq 1.1 \times 10^{-3}$ m^{-1} at $c = 0$ to $k \simeq 6 \times 10^{-4}$ m^{-1} at $c = 10$ m/s. It is this node which cuts through the $n = 2$ resonance near $k \simeq 10^{-3}$ m^{-1} and $c \simeq 2$ m/s. A replacement scheme is responsible for resonant peaks of the $n = 0$ resonance above $c \simeq 8$ m/s; otherwise, the other resonances are sufficiently resolved by the grid spacing. The transition between propagating and trapped waves falls on a nearly vertical curve at $k \simeq 6 \times 10^{-4}$ m^{-1}. Figure 14 shows the same slice of the temperature fluctuation spectrum but with a continuum spectrum of trapped waves. There are no resonant peaks, but the node in the vertical structure and the transition between propagating and trapped waves is still obvious.

Above and to the right of each contour plot are spectra integrated over c and k at $\alpha = 60°$, respectively. The $\mathbf{B}_T(\alpha = 60°, k)$ spectra above each contour plot demonstrate by their agreement the validity of the continuum trapping spectrum. Even though they account for the same integrated amplitude, the $\mathbf{B}_T(\alpha = 60°, c)$ spectra show different natures. The continuum spectrum shows a single peak in temperature fluctuations near $c \simeq 2$ m/s whereas the other shows two peaks at $c \simeq$

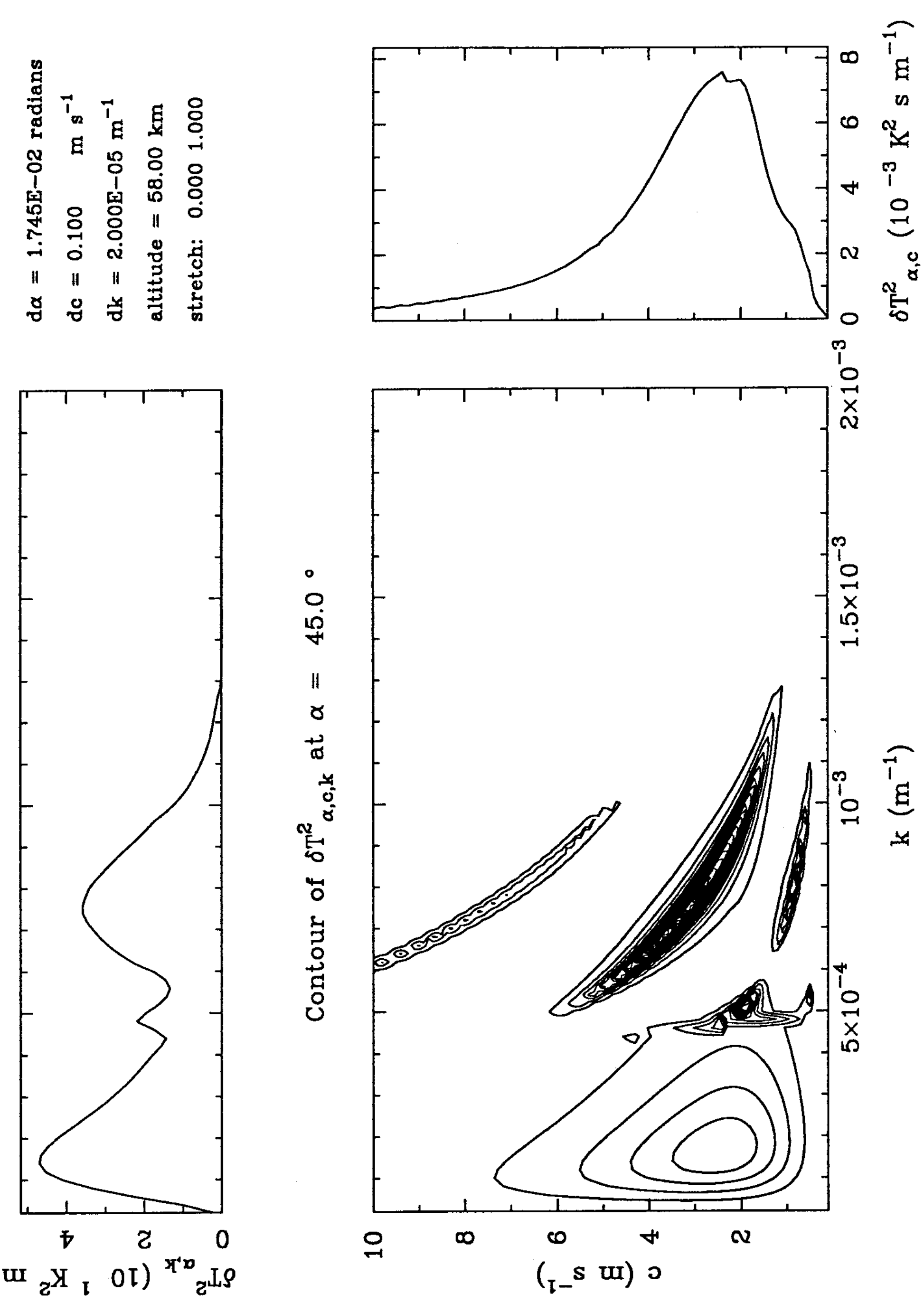

Figure 13. Coarse temperature variance contour plot. We show the coarse temperature variance spectra $B_T(\alpha, c, k)$ at $\alpha = 60°$. At the right of the contour plot is the integral of $B_T(\alpha, c, k)$ over k and above each contour plot is its integral over c. We use Reynolds-type forcing at $W_c = 3$ m/s and both breaking upon emission and breaking near critical layers.

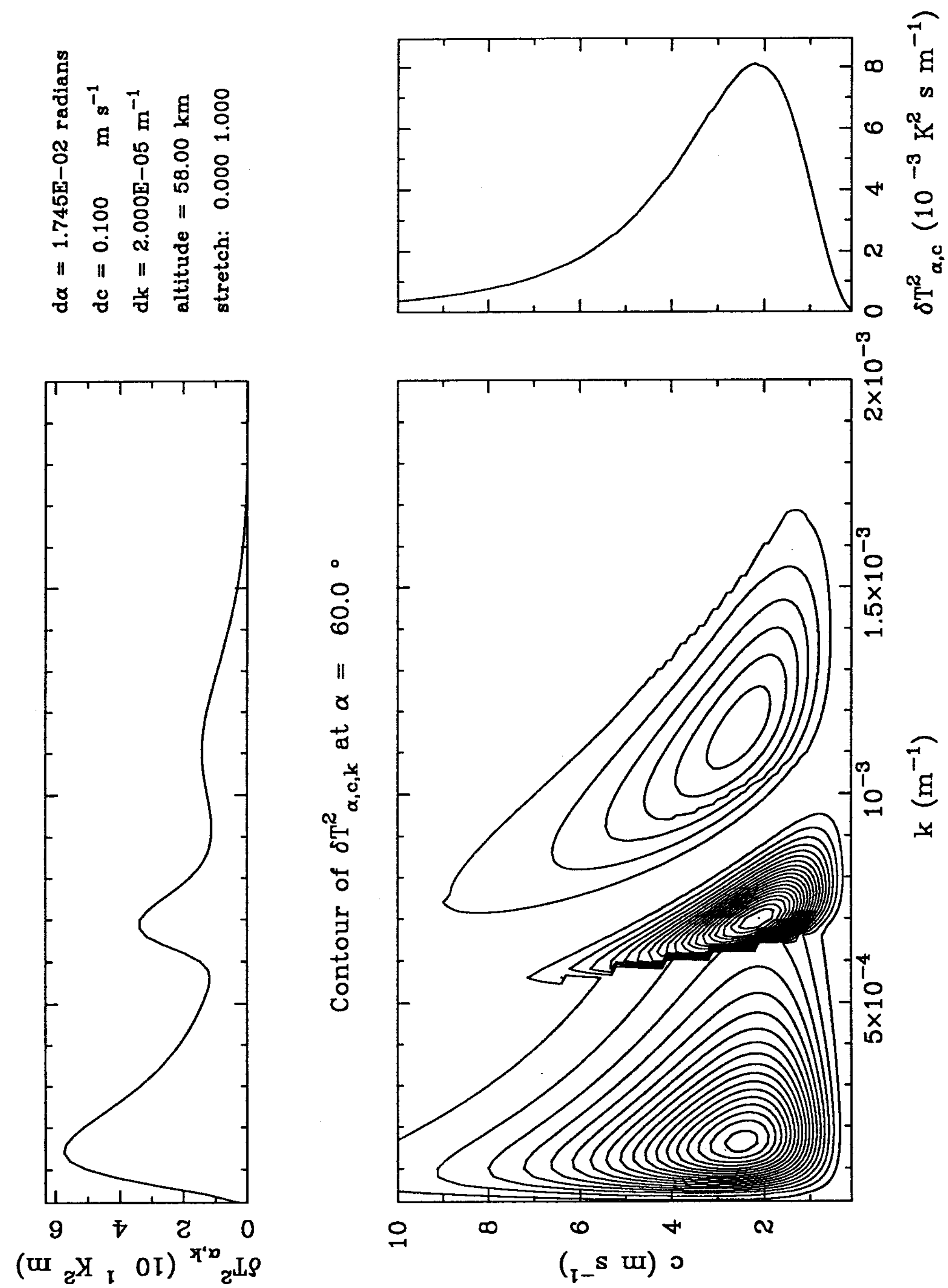

Figure 14. Continuum temperature variance contour plots. This is the same as figure 13 but for a continuum temperature variance spectrum.

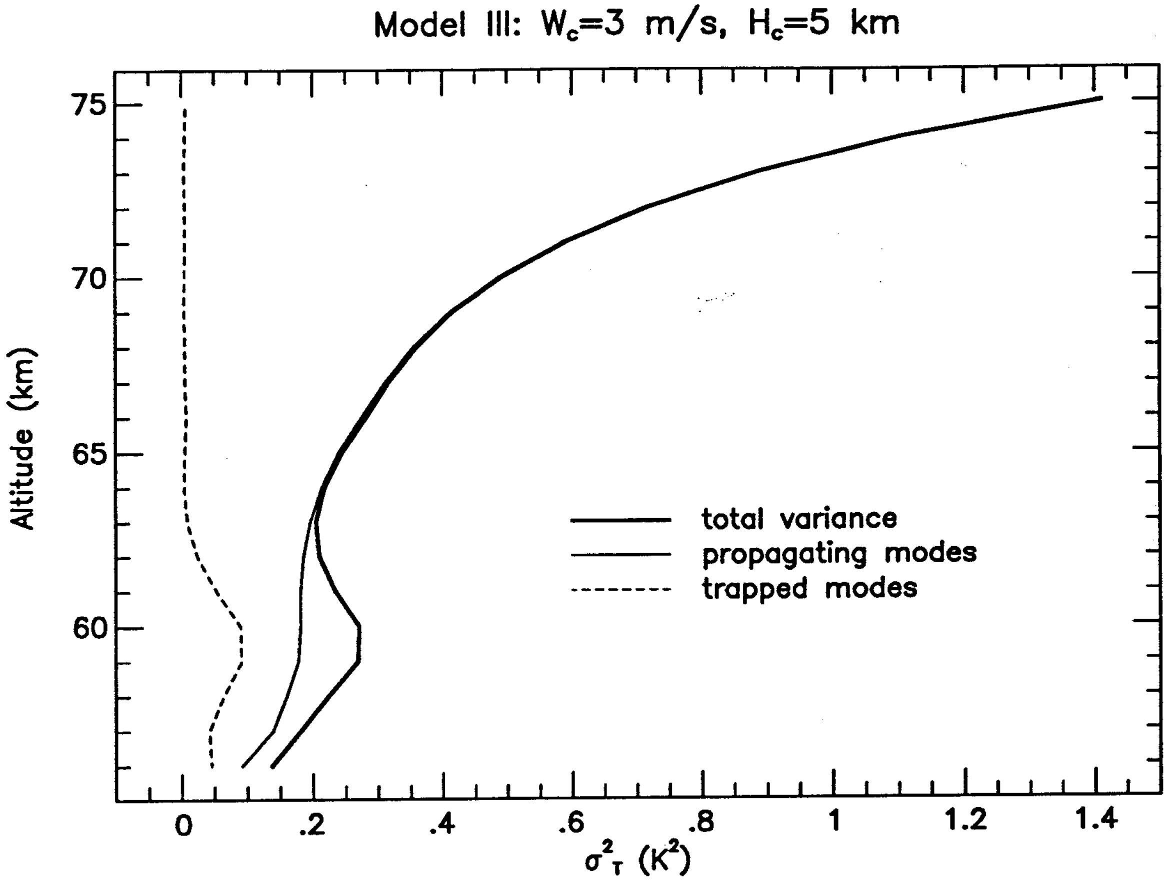

Figure 15. Temperature variance vs. altitude. We show the total temperature variance as a function of altitude z. The contributions from trapped waves and propagating waves are shown. We use Reynolds-type forcing at $W_c = 3$ m/s and $H_c = 5$ km. Both breaking upon emission and critical layer breaking are implemented.

1 m/s and at $c \simeq 3$ m/s. This split peak is a direct consequence of the intersection of the node in the vertical structure with the $n = 2$ resonance. It is this kind of redistribution of wave amplitude for which the continuum spectrum cannot account. Nevertheless, the continuum spectrum does accurately represent how trapped waves will respond to convective forcing.

In figure 15 we show the temperature variance as a function of height. We break it down by propagating and trapped waves. We find the variance by integrating the temperature variance spectrum $\mathbf{B}_T(k_x, k_y, m; z)$ up to $10/H$ in the horizontal wavenumbers k_x, k_y and between 10^{-5} and 10 m^{-1} in the vertical wavenumber.

Clearly the temperature variance profile is dominated by the propagating waves. In particular, those propagating modes with critical layers nearby contribute the greatest variance. Overall, the temperature variance contributed by the propagating modes increases with height, even above the peak in zonal winds, largely because of the inverse density growth law. The temperature variance associated with the trapped modes falls off with altitude because the duct lies below 67 km. The only noticeable effect of the trapped waves in the total variance is that it creates a local maximum at about 58 km altitude. This would correspond with the middle of the duct.

3.3.4 Momentum and energy deposition

Finally, we compute the accelerations of the mean flow, energy dissipation rates, and stresses created by convectively generated gravity waves. For this calculation it is necessary to perform the same calculation as was done for figure 5 in the first model but with a domain in c_x that ranges from -60 m/s to $+60$ m/s.

We take advantage of our approximate theories in conjunction with numerical calculations to devise an empirical form for the available momentum flux in gravity waves. For phase speeds smaller than the convective wind speed W_c, the momentum flux spectrum is determined largely by the wavebreaking upon emission phenomenon. Because the unbroken momentum spectrum of the first model is proportional to c_x^{-1} and because the breaking upon emission factor is proportional to c_x^3 at low phase speeds, the momentum flux emitted is proportional to c_x^2 with constant factors determined by the intensity of the forcing. Also, by a geometric theory, we have shown that for large zonal phase speeds the momentum flux is proportional to c_x^{-3}, again with constant factors determined by the intensity of the forcing. Thus, in an empirical spectrum of the momentum flux, the amplitude is proportional to c_x^2 for small c_x and proportional to c_x^{-3} for large c_x.

We determine constant factors in an empirical momentum flux spectrum by matching the total prograde momentum flux and the point of transition between low and high phase speeds in the empirical spectrum to those in the numerical spectrum. In particular, the empirical momentum flux spectrum is

$$\overline{\rho u'w'}(c_x) \equiv \text{sign}(c_x)\ 2.85804265 \left(\frac{a}{l}\right) \frac{\rho_c W_c^2}{N_c H} \left(\frac{3l^2 W_c^2}{c_x^2} + \left|\frac{2c_x^3}{l^3 W_c^3}\right|\right)^{-1} \tag{3.16}$$

in which we have defined l such that the maximum of this spectrum occurs where $c_x = lW_c$. The numerical constant 2.85804265 is a normalization constant such that the total integrated prograde momentum flux is $a\ (\rho_0 W_c^3/N_c H)$. The normalization constant is found by integrating equation 3.16 over c_x (Handbook of Chemistry and Physics, eq. 614) and is given analytically by $5 \cdot (24)^{1/5} \sin(3\pi/5)/\pi$.

The constants a and l are computed by performing complete numerical integrations. The total prograde integrated momentum flux is 1.10×10^{-3} N m^{-2} for $W_c = 1$ m/s and 2.17×10^{-2} N m^{-2} for $W_c = 3$ m/s. Using $\rho_0 = 0.9$ kg m^{-3} and $N_c^2 = 4 \times 10^{-5}$, we find that a in equation 2.49 is approximately 0.33. Since the maximum momentum flux occurred at $c_x = 0.8$ m/s for $W_c = 1$ m/s and at $c_x = 2.6$ m/s for $W_c = 3$ m/s, we estimate that the constant l of equation 2.49 is 0.83.

The waves accelerate the atmosphere by breaking according to the attenuation factor of equations 3.15. We show acceleration profiles for Reynolds-type forcing at $W_c = 3$ and 5 m/s in figures 16 and 17. Since the approximations we make in deriving the breaking factor f_{clb} (see equation 3.15*b*) are valid only between the convection and the peak in the zonal winds at 67 km, we do not expect the acceleration profile above 67 km to be realistic. This is permissible if we were concerned only with how waves can exert a prograde impulse to the mean winds; however, our wavebreaking theory near critical layers is impractical in computing how convectively generated waves can exert a drag on the mean winds. Thus, the strength of our wavebreaking theory is in predicting the wave-driving of the mean flow. Nonetheless, we can address wave-dragging of the mean flow also.

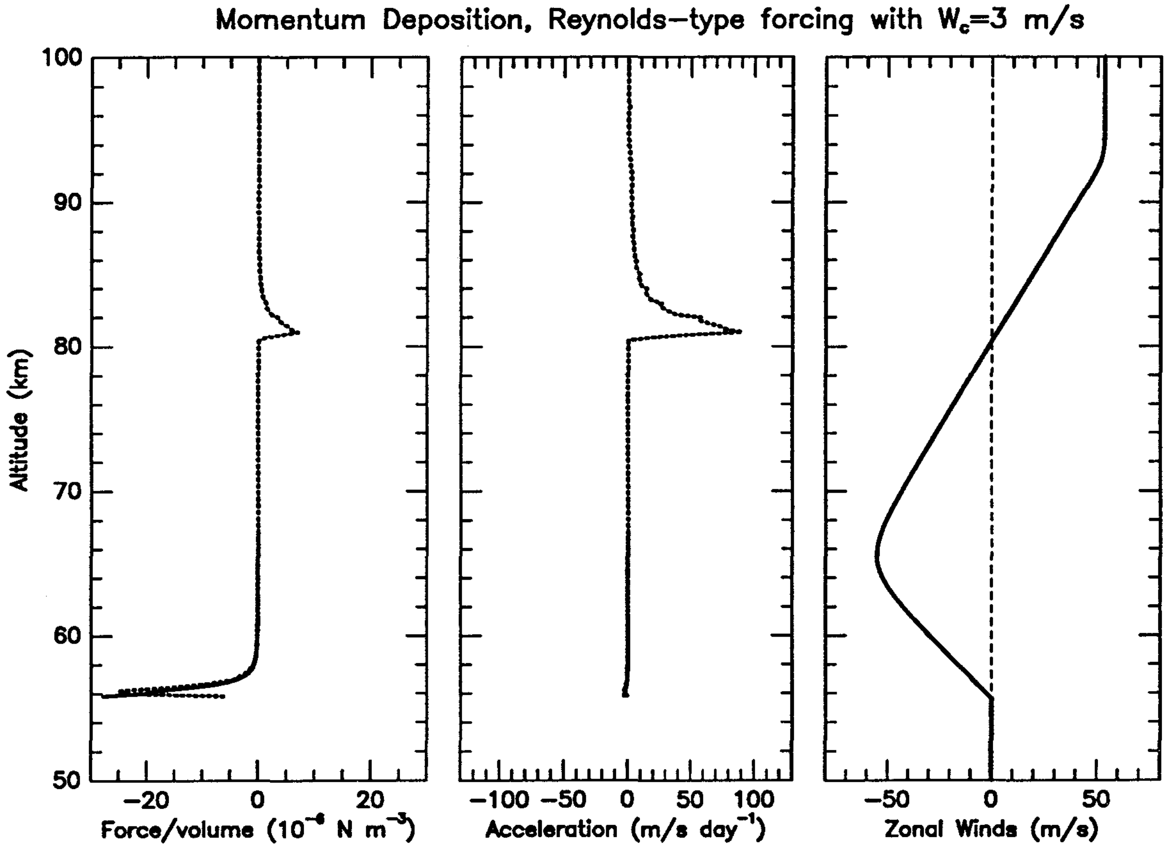

Figure 16. Momentum deposition as a function of altitude for $W_c = 3$ m/s. We show the momentum deposition rate per unit volume, the momentum deposition rate per unit mass, and the zonal wind profile as function of altitude for Reynolds-type forcing at $W_c = 3$ m/s. The solid lines refer to deposition by wavebreaking and the dotted lines refer to deposition by critical layer absorption.

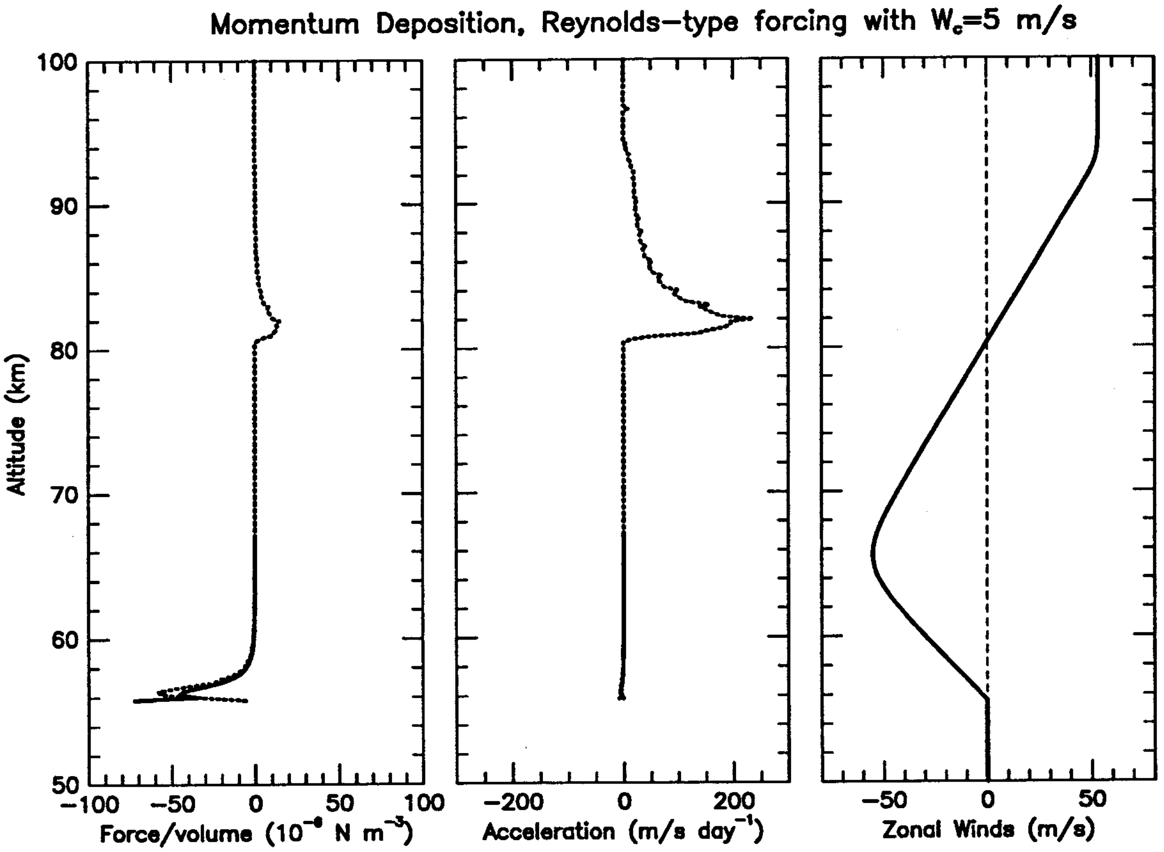

Figure 17. Momentum deposition as a function of altitude for $W_c = 5$ m/s. This is the same as figure 16 but for $W_c = 5$ m/s.

In figures 16 and 17 we see that the waves accelerate the zonal winds between the convection and the zonal wind maximum. For $W_c = 3$ m/s, the total prograde momentum carried and deposited by the waves is 2.17×10^{-2} N m^{-2} and the total retrograde momentum is 1.02×10^{-2} N m^{-2}. For $W_c = 5$ m/s, the total prograde momentum carried and deposited by the waves is 7.44×10^{-2} N m^{-2} and the total retrograde momentum is 3.65×10^{-2} N m^{-2}. The acceleration does fall off with altitude strongly because of the c_x^{-3} tail in the momentum flux spectrum. The distribution of the accelerations is strongly skewed toward the bottom of the stable layer, just outside the convection. For $W_c = 3$ m/s, the largest prograde acceleration is 2.95 m s^{-1} day^{-1} just above the convection. The acceleration falls off to 10^{-2} m s^{-1} day^{-1} at 67 km. For $W_c = 5$ m/s, the prograde acceleration just above the convection is 8 m s^{-1} day^{-1} and the acceleration falls off to 0.1 m s^{-1} day^{-1} at 67 km. In that interval, the momentum deposition rate falls off by a factor of 10^3, but the density falls off by a factor of 4. The falloff of momentum deposition with height is only slightly offset by the falloff of density with height. The accelerations above 67 km, especially those near 80 km, are to be disregarded because our wavebreaking mechanism is invalid above the point at which the wind shear changes direction (recall that $m_{\text{critical}}(z)$ of equation 3.15a can only be determined for monotonically increasing or decreasing winds).

The acceleration profiles obtained by critical layer absorption alone mirrors that of wavebreaking below 67 km. The reason for this is that waves break and deposit their momentum in the immediate vicinity of their critical layers. If each wave deposited all of its momentum exactly at its critical level and not in a small extended area below it, the atmospheric acceleration would be

$$\frac{\partial u''}{\partial t}(z) = -\frac{\bar{u}_z}{\bar{\rho}(z)} \, \bar{\rho}\overline{u'w'}(c_x = \bar{u}(z)) \tag{3.17}$$

(*e.g.*, Hou and Farrell 1987). Because critical layer absorption gives atmospheric acceleration profiles nearly identical to those for wavebreaking in a uniform shear, we assume that critical layer absorption accurately predicts the acceleration profile everywhere. Thus, the accelerations by critical layer absorption above 67 km accurately depict the effects of waves generated by convection on the given background winds. The effect is wave drag.

The wave drag decelerations appear so much larger than accelerations between 55 and 60 km because of the density falloff with height. The integrated retrograde momentum deposition above 67 km is 1.02×10^{-2} N m^{-2} for $W_c = 3$ m/s and is 3.65×10^{-2} N m^{-2} for $W_c = 5$ m/s. Recall that there is less retrograde momentum in gravity waves because some retrograde waves are trapped by a Doppler-created lid. The maximum deceleration is 86 m s^{-1} day^{-1} for $W_c = 3$ m/s and 200 m s^{-1} day^{-1} for $W_c = 5$ m/s.

Given some evidence that the zonal winds do not decay with height above 70 km, we compute what accelerations might occur if we maintain a constant wind above 70 km. The results are presented in figure 18. In this calculation, the westward acceleration profile is the same as that in figure 16, but the high altitude deceleration profile is different. Because the winds do not decay with height, there are no critical layers for the eastward propagating modes. Instead, their momentum is deposited more uniformly and at higher altitudes, because the waves eventually break due to the inverse square-root growth law for vertically propagating waves. At 120 km altitude, where the background density is 1.7×10^{-6} kg m^{-3}, the deceleration reaches about 17 m s^{-1} day^{-1}. The deceleration amplitude grows with height above this point because more eastward propagating modes begin to break. In fact, where densities fall to about 10^{-13} kg m^{-3}, decelerations asymptote to about 5 m/s^2. It is unlikely that the superrotation continues into the Venus thermosphere, but nonetheless, it is worth noting by how much gravity waves might drag the mean flow.

This concludes our computations. We have laid out our calculations of temper-

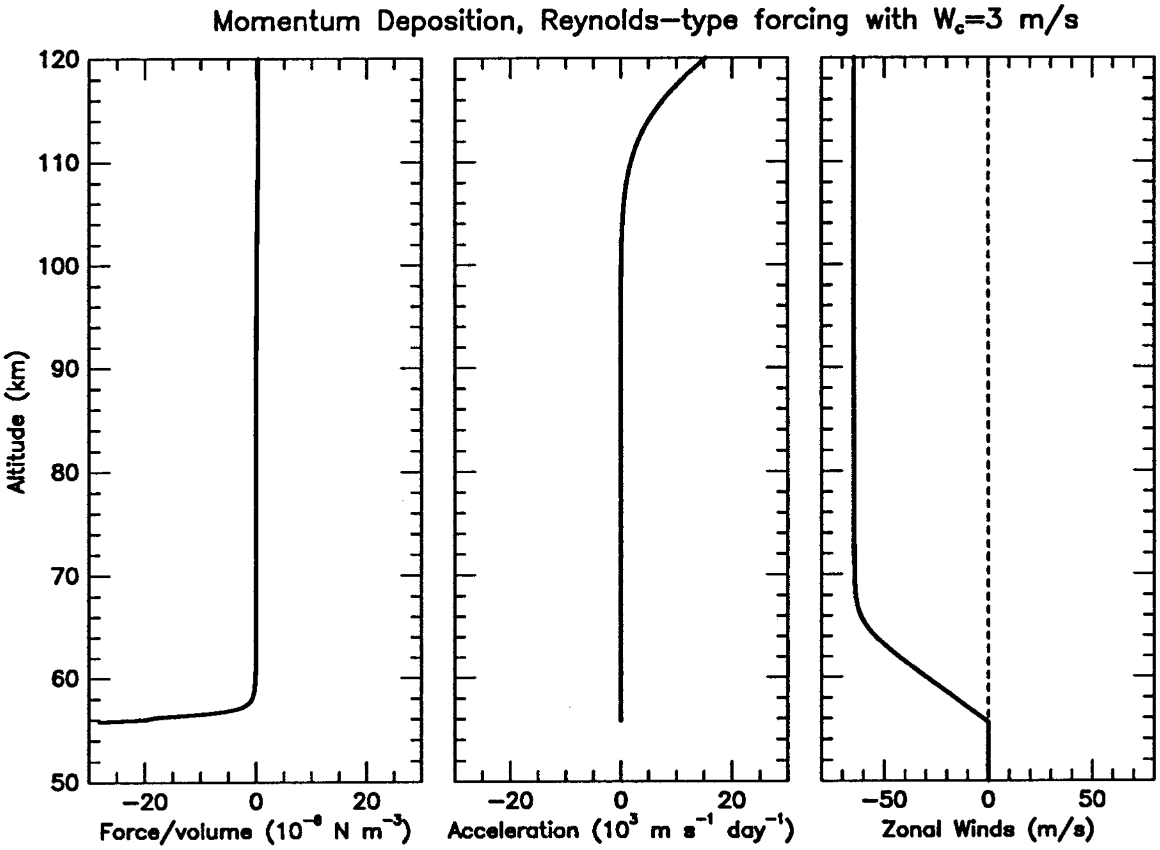

Figure 18. Momentum deposition with high altitude superrotation. This plot is similar to the previous two plots except that the zonal winds do not decay with height above 70 km. The convective wind speed W_c is set to 3 m/s. Only accelerations by wavebreaking are presented.

ature fluctuations and momentum fluxes resulting from convectively generated gravity waves. We have found the necessity of two types of wavebreaking, both of which result from supercritical waves. The first type is breaking upon emission. This gives rise to penetrative convection and discontinuous profiles of static stability. The second type is wavebreaking upon approach to a critical layer. This wavebreaking leads to accelerations of the background atmosphere. Furthermore, we have estimated the accelerations applied to the atmosphere by the breaking waves. Finally, we note that we have determined a three dimensional spectrum of convectively generated gravity waves which will be useful in testing whether they are responsible for the scintillation phenomenon seen in many spacecraft occultation data in Venus's middle atmosphere.

4. Summary and Discussion

We have developed a theory to describe the generation of gravity waves by neutrally buoyant dry convection. This theory is applied to the convection layer in Venus's atmosphere between 50 and 55 km altitude. We have tracked a three dimensional ensemble of these waves as they propagate upward in the adjoining stably stratified atmosphere. The stable layer has realistic background stability and zonal wind profiles. We calculated where the waves would lose their zonal momentum and determined an acceleration profile with respect to height. In this section we first summarize the results of the previous sections and then comment on the implications of our results.

4.1 Summary of results

Three model atmospheres were used in order to understand how the emission and propagation of waves depend on the nature of the stable atmosphere. Goldreich and Kumar found a simple relation for the amount of energy carried by gravity waves from the convection which depends on the Mach number of the convective motions. It was unclear to us *a priori* how the emission might behave when the static stability profile is treated as continuous in altitude. Thus, we started with a model atmosphere as in Goldreich and Kumar, with convection one scaleheight deep, an overlying semiinfinite layer with uniform static stability, and background wind uniform in altitude. The second model contained continuous profiles of static stability and zonal wind intended to resemble typical conditions in Venus at midlatitudes. The third model is the same as the second except that a discontinuity in the static stability is placed at the boundary between the convection and the stable layer.

The first model gives a gravity wave momentum flux consistent with the estimate of Goldreich and Kumar. In finding the energy flux as a function of zonal phase speed, we found that a finite amount of energy is emitted as the zonal phase speed approaches zero. This was problematic because it implied infinitely large temperature fluctuations in the stable layer for waves with small horizontal phase speeds. Because this is not physically realistic, we imposed wavebreaking immediately at the point of emission so that the waves would not be subject to a convective instability. We refer to this process of breaking as *breaking upon emission.* Breaking upon emission requires a discontinuity in the static stability profile at the point of breaking. This discontinuity is a part of the first model by definition of the mean state.

We have shown in our analytic work that the momentum flux spectrum of gravity waves in zonal phase speed is proportional to c_x^{-3} for large zonal phase speeds c_x, and this spectrum is borne out in our numerical results for the first model. The analytic result is purely geometrical and has only two requirements: (1) that the emission of waves be nearly isotropic in the horizontal plane, and (2) that the source emit a momentum flux spectrum in frequency ω with a cutoff steeper than ω^{-3}. This result is expected to be valid at zonal phase speeds larger than the dominant wave phase speed, which is approximately given by W_c, the wind speed associated with the dominant eddies in the convection for this theory of gravity wave generation. The c_x^{-3} tail of the momentum flux spectrum for the first model was demonstrated numerically and shown in figure 5. Isotropy of emission is essentially imposed in the first model; however, a strong cutoff in frequency was not imposed and has been found to be true.

The second model consists of a more realistic Venus middle atmosphere with a convection layer between 50 and 55 km altitude. The static stability profile was considered continuous with $N^2 = 0$ in the convecting layer, increasing monotonically to about 3.6×10^{-4} s^{-2} at 60 km altitude, and then remaining constant above 60 km. The zonal winds were considered constant within the convection with a westward shear between 55 and 67 km altitude, an eastward shear above 67 km where the zonal wind speed at 80 km altitude matched the zonal wind speed of the convecting layer.

In the second model we have verified that the low phase speed singularity of the first model applies to a more realistic atmosphere, and we argue that breaking upon emission cannot be calculated. Despite the continuity of the static stability in altitude, there remains a nonzero energy flux of gravity waves at zero phase speed. Thus a singularity exists in the momentum flux at low horizontal phase speeds. Calculating a realistic breaking mechanism for such waves is beyond our scope because vertical wavenumbers of the singular waves vary rapidly with height at their point of emission. This rapid variation arises because the Brunt-Väisälä frequency approaches zero just above the convection.

The third model is like the second model in that it consists of a realistic model of the Venus middle atmosphere, but it includes a mechanism to break the waves so that there is no low phase singularity as in the previous two models. The waves are anticipated to break immediately upon emission from the convection because wave fluctuations were found to be convectively unstable even directly on top of the convection. We have assumed that vertical mixing resulting from the breaking upon emission would create an adiabatic breaking layer above the convection which is indistinguishable from the convection. This breaking layer would penetrate into the stable layer as far as the stability profile would permit. This created a discontinuity in the stability profile $N^2(z)$ at the top of the breaking layer.

The breaking layer served to break the waves upon emission. The factor by which the waves were broken was determined so that they would be stable to convective and shear instabilities just above the neutral layer. The breaking factor was found to be $\simeq (c/W_c)^3$ where c is the horizontal phase speed and W_c is the wind speed associated with the largest convective eddies. This result is important because of its independence from any properties of the overlying stable layer. We are permitted to think of the convection and the breaking layer as a coupled process independent of the surrounding stable atmosphere for generating internal gravity waves which propagate into the stable atmosphere.

In the context of the third model we have demonstrated the usefulness of a continuum spectrum of trapped waves. Trapped modes were possible in this model because of the presence of strongly shearing zonal winds. We assumed that absorption by the convection served as the major sink of wave energy for trapped waves. When integrating trapped wave temperature variances spectrally, many resonances were found to be narrower than the integration interval. We showed that an analytic theory of trapped wave amplitudes could accurately reproduce the numerical results for trapped wave amplitudes. Not only could we implement the analytic work to "smooth over" the resonances (figure 9), we could use an analytic theory to insert resonance amplitudes where resonances were otherwise unresolved (figures 13 and 14).

In addition, the shearing zonal winds created critical layers at which wavebreaking is required. Waves became unstable as they approached their critical layers, and thus they were required to break. Because we chose to break waves according to their vertical wavenumbers, we found a function which attenuated each individual mode as it propagated vertically. The attenuation function was found to be approximately $(m_{\text{critical}}/m)^2$ for vertical wavenumbers m greater than a critical wavenumber m_{critical}, which itself was found as a function of height. When waves break, they deposit their momentum into the mean flow, thereby accelerating it. We called this wavebreaking process *critical layer breaking.*

The primary cause for momentum deposition is critical layer absorption. We have required that every wave lose all of its momentum and energy at its critical layer. Since the location of critical layers is determined by where the zonal phase speed c_x is equal to the zonal wind speed $\bar{u}(z)$, it was most convenient to determine the available momentum flux as a function of the zonal phase speed.

As mentioned above, we were able to calculate the gravity wave emission to the stable atmosphere from the neutral region as if it acted as an independent gravity wave "engine." In an empirical spectrum we showed that the available momentum flux spectrum in zonal phase speed is roughly $\rho_0 c_x^2/N_c H$ at low zonal phase speeds c_x where ρ_0 and N_c are the density and the Brunt-Väisälä frequency at the top of the convecting layer, and $1/H$ is the horizontal wavenumber of the dominant waves. This form is valid for $c_x \lesssim W_c$, where W_c is the phase speed of the dominant waves and is apprximately 3–5 m/s. For $c_x \gtrsim W_c$, the available momentum flux spectrum falls off proportional to c_x^{-3}. This empirical spectrum was fit to our numerical results.

We calculated profiles of the divergence of the gravity wave momentum flux caused by wavebreaking alone and critical absorption alone. Since our formulation for wavebreaking was valid only as long as the zonal wind monotonically increased or decreased, the profile of momentum flux divergences by wavebreaking above the peak in zonal winds at about 67 km altitude was infeasible. Since the pattern of momentum flux divergences by critical layer absorption was nearly identical to that for wavebreaking below the peak in zonal winds, we assumed that momentum deposition by critical layer absorption accurately determined the effects of the gravity waves on the mean state atmosphere.

The prograde acceleration exerted by the waves was greatest immediately above the convection and decreases with increasing altitude. Because the phase speed of the dominant waves is about 3–5 m/s, most of the wave momentum flux was absorbed in a layer which had zonal winds varying by 3–5 m/s above the convection. Such a layer was less than 1 km thick. For $W_c = 3$ m/s, the prograde acceleration was about 3 m s^{-1} day^{-1} just above the convection and fell off to about 10^{-2} m s^{-1} day^{-1} near 67 km altitude.

The waves were far more effective at dragging the mean winds above the zonal wind maximum. Where the wind speed matched that of the convecting layer, the retrograde propagating modes deposited their momentum near their critical layers. This occurred at about 80 km altitude. The total integrated momentum flux of the retrograde waves was less than that of the prograde waves because many of the retrograde waves were trapped beneath a Doppler-created duct. Nonetheless, because the background density of the atmosphere was much less at 80 km than near the convecting layer, the retrograde waves accelerated the winds in the eastward direction at 80 km much more than the prograde waves accelerated the wind in the westward direction just above the convection. Because the wind was westward above the convection, we refer to the accelerations at 80 km as the wave drag on the atmosphere. This wave drag reached about 86 m s^{-1} day^{-1} for $W_c = 3$ m/s.

4.2 Discussion

In this discussion we describe what our results mean for Venus's atmosphere. The centerpoint of the discussion will be the effect of the momentum deposition by these waves on the dynamics of Venus's atmosphere.

A simple critical layer absorption model for driving the zonal wind shear in the neighborhood of the convecting layer in Venus's middle atmosphere does not qualitatively behave as desired if it were the sole mechanism responsible for the superrotation. Presumeably, in a steady state the gravity wave momentum flux divergence would offset some other atmospheric forcing. This other atmospheric forcing would be an atmospheric drag because it must act opposite to the direction of the zonal wind. If this drag is frictional in nature, then it would act most vigorously near the maximum in the zonal winds and be distributed over roughly a scaleheight. Since we have found the momentum flux divergence to be proportional to $\bar{u}^{-3}$ for large zonal phase speeds, there is little acceleration a few kilometers above the convection, much less near the maximum in the zonal winds. In fact, most of the acceleration takes place near the convection, where we would not expect much drag with respect to the convecting layer.

Even though the prograde accelerations are weak near the zonal wind maximum, it is possible that the eddy drag is also weak near the wind maximum, especially if the eddy viscosity responsible for the drag is caused by the breaking waves. In the analysis section of this paper, we have shown how to compute the energy deposited by the waves which would create local eddies. In order to compute an eddy viscosity which would result from such energy deposition, we would divide by the background atmospheric density and divide by either the square of the local wind shear $\bar{u}_z$ or the local Brunt-Väisälä frequency squared N^2. Which one to use would only be obvious if the Richardson number were of order unity, in which case they would be the same. Nonetheless, because the energy dissipation rate would decrease as a function of height, namely because most of the wave energy is lost near the convection, it is possible that the decrease in the prograde accelerations by the waves is balanced by decreasing eddy drags with height. We suspect, however, that such a situation should only occur when the Richardson number of the mean state is approximately 1/4. In our profiles, the Richardson number is on the order of 10.

The most pronounced effect these waves would have in Venus's atmosphere is in dragging the flow above the zonal wind maximum. Even for moderate forcing amplitudes ($W_c = 3$ m/s), the decelerations reach about 90 m s^{-1} day^{-1} near the altitude at which the zonal wind is the same as at the convecting layer. Coincidentally, this is the same order of magnitude effect gravity waves are thought to have in the Earth's mesosphere (Leovy 1964, Holton 1982).

The profile of the zonal wind would indeed effect the amplitude of the decelerations above the zonal wind maximum. In fact, whether the wind actually does decrease dramatically enough with height to have the same speed as at the convecting layer is uncertain. Even if this were the case, it is uncertain where it might happen in altitude or the horizontal dimension. Nonetheless, even if the winds did not decrease substantially with height so that critical layers for the retrograde waves would not be present, then the waves would eventually break at a high altitude and deposit a net retrograde momentum (Alexander 1992). For this reason we have estimated what deceleration would result if the zonal winds continued to superrotate above the cloud-tops. We found that at 120 km altitude, the eastward propagating waves broke enough to exert a deceleration on the mean flow on the order of 17 m s^{-1} day^{-1}. The deceleration increased with height and asymptoted at approximately 5 m/s^2 where the mean state density fell to 10^{-13} kg m^3. This calculation tells us what kind of decelerations we might expect from convectively generated gravity waves if the superrotation extends above the cloud-tops.

The nature of the prograde accelerations does not change substantially for differing forcing amplitudes or zonal wind profiles. The prograde accelerations just above the convection would change in amplitude but not in shape. The shape of the prograde acceleration profile is governed by the c_x^{-3} component of the momentum flux spectrum because the typical zonal wind variations are much larger than any reasonable value of the typical convective wind fluctuation W_c. The largest waves will break and deposit their momentum within roughly 1 km of the convecting layer. Increases in W_c will increase the total prograde momentum flux roughly proportionally to W_c^3. If the shear $\bar{u}_z$ were stronger just above the convection, waves would break more rapidly. Thus, the accelerations above the convection would be greater but more confined in altitude. On the whole, though, the profile of prograde accelerations would be dominated by a falloff with height up to the zonal wind maximum.

On the other hand, it may be possible for waves to transmit some momentum flux through their critical layers. This may occur because of self-acceleration

(Grimshaw 1974, Fritts and Dunkerton 1984) or scattering. For this reason we estimate the prograde acceleration exerted in the two scaleheight region between the convection and the zonal wind maximum as 0.4 m s^{-1} day^{-1} for moderate forcing amplitudes. This corresponds to a force per unit volume of roughly 4.3×10^{-5} N m^{-3}. This compares well with Hou and Goody (1985), who showed that the average prograde acceleration required is about 5×10^{-5} N m^{-3}.

The drag resulting from the broken waves may balance the momentum deposition by the breaking and absorption of the waves. The waves which break between the convection and the zonal wind maximum would create eddies with associated eddy diffusion effects. This eddy diffusion itself might act as a drag on the atmospheric shear. If the eddy drag were to somehow balance the prograde accelerations exerted by the wave momentum deposition, we would get a series of steady state critical layers. Lamb and Pierrehumbert (1993) showed that a steady state critical layer is possible for a single gravity wave mode. How a three dimensional ensemble of steady state critical layers might work is unknown. Nonetheless, a steady state is attained only for small values of the background Richardson number. For Venus, we can envision an initially weak shear being strengthened by the absorption of waves until the Richardson number of the mean flow falls below unity.

The hypothesis of steady state critical layers driving the mean flow above the convection can be checked first by examining the Richardson number of the mean flow. The best simultaneous measurements of zonal winds and temperature structure come from the Pioneer Venus descent probes (Seiff *et al.* 1980). It is difficult, however, to estimate the Richardson number of the mean flow on large scales because of the presence of fluctuations in the temperature profiles. The profiles as fit by Schubert and Walterscheid show Richardson numbers in the range of 5 to 10. While these are an order of magnitude too high for steady state critical layers to exist, it does not eliminate the possibility that steady state critical layers may exist somewhere in the region between the convection and the cloud-tops.

4.3 Generalizations and predictions

In this subsection we describe how our analytic work can be generalized to apply to different atmospheres and what specific predictions can be made. We discuss the applicability of the empirical momentum flux spectrum, the observability of such a spectrum, the finesse of trapped gravity waves, and a prediction for the "knee" in the saturated spectrum of breaking gravity waves.

The c_x^{-3} tail in the momentum flux spectrum is a simple geometric result of our work. This tail holds under certain restrictions on the gravity wave emission. The restrictions are that the emission is isotropic in the horizontal direction of propagation and that the emission has a cutoff at high frequency stronger than ω^{-3}. Both of these conditions are met in our theory of generation of waves by dry convection. We suggest that the process of generation of waves by moist convection, such as happens in the tropical troposphere of the Earth's atmosphere, may also satisfy the above two conditions, and thus have a high phase speed tail in the momentum flux spectrum proportional to c_x^{-3}. This may apply to the generation of gravity waves by the breakdown of a strong jet, but the condition of isotropic emission might break down because of the presence of a shearing zonal wind. Thus, if nearly isotropic emission of gravity waves is significant in planetary atmospheres, a momentum flux distribution proportional to c_x^{-3} at high phase speeds might be present on global scales.

Optimally, we would like to compare our predicted momentum flux spectrum with observations or a numerical integration; however, a momentum flux spectrum in zonal phase speed is difficult to observe. The only direct way of evaluating the validity of our geometric analysis is through the results of high resolution numerical modeling.

Hauf and Clarke (1989) have modeled dry convection and found nearly isotropic wave emission. They were not able to obtain a spectrum in phase speed, though, because of secular variation in the background state of the atmosphere. Nevertheless, we would need greater anisotropy than this to avoid a strong falloff in momentum flux at high zonal phase speeds.

In the Earth's atmosphere, it is thought that internal gravity waves might help drive the quasibiennial oscillation (QBO), but it is unlikely that a similar oscillation is present in Venus's atmosphere because of the different nature of the gravity waves. The quasibiennial oscillation refers to a process in the Earth's tropical stratosphere in which the zonal winds alternate direction with a period of about 25–27 months. The oscillation takes place by the descent of wind regimes: winds moving in a certain direction descend in altitude to replace the winds moving in the opposite regime. The most widespread theory for this process is a gravity wave absorption mechanism similar to ours for sustaining the superrotation in Venus's atmosphere (Holton and Lindzen 1972). Wallace and Kousky (1968) found that Kelvin waves, a type of gravity wave which is restricted to equatorial latitudes and propagates eastward, contribute a large momentum flux at phase speeds of approximately 30 m/s and greater. Yanai and Maruyama (1966) found equatorially trapped Rossby waves which propagate westward with slightly slower phase speeds. It is most likely that these waves are driving the QBO in the Earth's atmosphere. Convectively generated gravity waves in Venus's atmosphere could not drive a quasi-oscillation such as the QBO because such gravity waves move too slowly. It takes 30–40 m/s phase speeds in the Earth's atmosphere to drive a QBO with an amplitude of 30 m/s, but the gravity waves we have described in Venus's atmosphere move at about 5 m/s and the wind maximum is nearly 60 m/s faster than the source region.

We can offer some new insight into the nature of trapped gravity waves. The duct in which a gravity wave is trapped is analogous to an optical cavity in that they both have a *finesse*. The finesse essentially counts the number of reflections a gravity wave packet undergoes before it escapes from the duct. The finesse is useful because it allows simple calculations of the amplitudes of trapped gravity waves. In particular, the energy density of trapped gravity waves, in a continuum sense, is roughly the product of the finesse of the duct and the energy density a vertically propagating gravity wave would have had. Furthermore, the widths of the resonances of trapped gravity waves is proportional to the product of $(\partial Q_d/\partial\chi)^{-1}$ and the inverse of the finesse, where $\partial Q_d/\partial\chi$ measures the derivate of the integrated phase in the duct in some spectral quantity χ (χ can be ω, k_x, k_y, or any combination of them such as c). Thus, the finesse of trapped gravity waves offers an alternative method to calculating their amplitudes.

Lastly, our theory predicts a “knee” in the saturated spectrum of gravity waves. The saturated spectrum predicts that the gravity wave energy density spectrum in vertical wavenumber is approximately N^2/m^3 above a critical wavenumber m_{critical}. The knee in the spectrum would occur at the critical wavenumber. In our theory we found an expression for the critical wavenumber given as equation 3.15*a*. The assumptions of this prediction is that the source of the waves is isotropic in the horizontal plane and that the zonal winds monotonically increase or decrease in height. The critical wavenumber is found to depend on the mean state density $\bar{\rho}(z)$, the difference in zonal wind $\Delta\bar{u}$ between the source and altitude z, the Brunt-Väisälä frequency N, and the intensity of the wave source given by the wave action flux $\mathcal{A}$.

PAPER II

Radio Scintillations in Venus's Atmosphere: Application of a Theory of Gravity Wave Generation

Radio Scintillations in Venus's Atmosphere: Application of a Theory of Gravity Wave Generation

Stephen S. Leroy

and

Andrew P. Ingersoll

Division of Geological and Planetary Sciences
California Institute of Technology
Pasadena, California 91125

To be submitted to: *J. Atmos. Sci*

Abstract

We simulate radio scintillations as they would appear in Pioneer Venus radio occultation data assuming that the index of refraction fluctuations in Venus's atmosphere responsible for the scintillations are directly caused by gravity wave fluctuations. We assume that the gravity waves are created by a global convection layer between 50 and 55 km altitude in Venus's atmosphere and propagate vertically. Associated with the gravity waves are density fluctuations which create the index of refraction variations. We compare the simulated scintillations with data and argue that this theory for the radio scintillations is preferable to the theory that the scintillations are caused by clear air turbulence in Venus's atmosphere.

We show that these gravity waves can explain the shape and amplitude of the radio scintillation variance spectra in frequency. The shape of the simulated radio scintillation variance spectra in frequency is nearly a direct result of a saturated spectrum of breaking gravity waves. This saturated spectrum is the spectrum of breaking gravity waves in the vertical wavenumber. On the other hand, the overall amplitude is subject to parameters such as the intensity of the convection, the angle between the zonal winds and the beam path, and the zonal wind profile at polar latitudes. Limits can be placed, though, on the intensity of the convection which generates the waves and on the angle between the radio beam path and the winds in Venus's atmosphere. We find that the convection in Venus's middle atmosphere, even in polar regions, must transport 1 W/m^2 to create gravity waves strong enough to break. This result is dependent on the amplitude of the zonal winds at polar latitudes.

1. Introduction

We implement a spectrum of gravity waves generated by convection in Venus's middle atmosphere in simulations of radio scintillations in order to explain the scintillations seen in the radio science data obtained by Pioneer Venus. In this introduction, we first explain what radio scintillations are and what causes them. Secondly, we present our hypothesis that convectively generated gravity waves in Venus's middle atmosphere are responsible for the scintillations. Finally we briefly describe the organization of this paper.

Radio scintillations are a phenomenon which occurs during radio occultation experiments. In our case, a radio occultation occurs when the beam path of the Pioneer Venus radio signal passes through the Venus atmosphere on its course to Earth (Kliore and Patel 1980). During the occultation, the Pioneer Venus spacecraft appears to be moving in the Venus atmosphere from the point of view of an observer on Earth. The data the observer obtains is the amplitude and phase (in the form of frequency shifts) of the radio signal as a function of time during the occultation. Contained in this data is precise information on the index of refraction at radio wavelengths in the atmosphere. Because the density of the atmosphere is the primary source of index of refraction variations, the data can be directly inverted to give profiles of temperature in altitude of the atmosphere, but only at vertical resolutions greater than the width of the radio beam as it appears in the Venus atmosphere (Fjeldbo *et al.* 1971). Variations on scales smaller than the beam width, however, can lead to variations in the signal amplitude and phase as observed at Earth (Tatarskii 1961). It is these variations in amplitude and phase which are radio scintillations.

The beam width is what separates the geometric optics physics of the experiment from the diffraction physics of the experiment. The beam width is defined as the cross-sectional area over which the radio signal constructively adds to create the signal as it appears at Earth. Another term for this area is the first Fresnel zone (Born and Wolf 1980), defined approximately as $\sqrt{\lambda R/\pi}$ where λ is the wavelength of the radio signal in a vacuum and R is roughly the shorter of the distances from the spacecraft (Pioneer Venus) to the target (Venus's atmosphere) or from the target to the observer (Earth). The wavelength we use is 13 cm (S band) and the spacecraft to Venus distance was roughly 4000 km; thus, the beam width at Venus's atmosphere was approximately 200 meters. If variations in the Venus atmosphere are larger than 200 meters, then the experiment is one of geometric ray propagation because fluctuations of the signal phase on small scales are unimportant. Any variations in the index of refraction on scales smaller than 200 meters will cause a diffraction pattern to develop. This diffraction pattern creates the scintillations seen in the Pioneer Venus radio science experiment.

The Fresnel zone/beam width is smaller in the vertical than in the horizontal because of the refractive effects on the beam. Young (1976) pointed out that when a radio beam is refracted by a planetary atmosphere, its beam width is compressed in the vertical direction in the planet's atmosphere. When the overall beam width is smaller than the atmospheric scaleheight, then the compression factor is roughly the differential refraction factor q of the radio beam. The square of the differential refraction factor is the reduction in intensity of the radio beam at the Earth during the occultation compared to its intensity when the atmosphere does not occult the beam. At 60 km altitude in Venus's atmosphere, the signal intensity reduction at 60 km was roughly $q^2 \approx 10$ (Woo and Armstrong 1980, WA hereafter), and thus the vertical beam width was roughly 63 m.

The diffraction (scintillation) effects can be separated from the refraction (ray propagation) effects in the phase and amplitude data by filtering the data in time. Since ray propagation effects are caused by variations of the index of refraction in

Venus's atmosphere on scales greater than the beam width, variations in the phase and amplitude which occur on timescales longer than it takes for the spacecraft to apparently traverse a beam width in the Venus atmosphere are attributed to ray propagation effects. When the log-amplitude is spectrally analyzed, the power for timescales shorter than the beam-crossing timescale is attributed to diffraction effects.

The index of refraction fluctuations responsible for the diffraction are caused primarily by density variations on small spatial scales in Venus's atmosphere (Fjeldbo *et al.* 1971). Where there is a local density increase, the index of refraction increases and the radio beam tends to slow. When the beam slows, a local phase build-up occurs. The diffraction pattern results from net inhomogeneities of the accumulated phase across a plane transverse to the beam path. If the diffraction is large enough so that significant focusing and defocusing of the beam occurs on small scales, then the scintillations are said to be *strong* (*e.g.*, Narayan and Hubbard 1988). If no significant focusing or defocusing occurs, the scintillations are *weak.* Strong scintillations and weak scintillations can be distinguished by the amplitude of the fluctuations in the radio signal amplitude and phase at Earth. The Pioneer Venus radio scintillations are weak because the variance in the log of the amplitude of the signal (χ) is less than unity.

It is impossible to invert scintillation information to obtain three dimensional spatial spectra of the density fluctuations, and thus modelers typically assume a spectrum of density fluctuations in the atmosphere associated with a particular physical mechanism and simulate how the radio scintillations would appear. One cannot directly invert the scintillations for a three dimensional spectrum of density fluctuations in the atmosphere for two reasons. Firstly, any component of the density fluctuation spectrum which has variations along the beam path does not contribute to the scintillations because no net phase accumulates along the beam path for these modes

(Ishimaru 1978). Secondly, the scintillation data is a one dimensional data set, that dimension being time during the occultation; hence, the remaining two dimensions to which scintillations are sensitive are reduced to just one in the data. Since the scintillations cannot be inverted to find spatial density fluctuation spectra in the atmosphere, it is simplest to deduce information on the density pattern responsible for the scintillations by numerically simulating the scintillations given physically reasonable patterns of density fluctuations.

Dynamically, the small scale density inhomogeneities vary in time as well as in space; however, each occultation advances rapidly enough that the processes which generate the inhomogeneities do not have time to substantially alter the density field. For instance, the enhanced scintillations seen at 60 km are apparent primarily in a window of about 10 seconds in the occultation data, but the assumed timescale for motions on small scales in several minutes (the inverse of the Brunt-Väisälä frequency). Thus we use the "frozen-in" hypothesis, namely that the density variations appear to be frozen in the atmosphere and exist only as a function of space where the occultation experiment is concerned. A time series of scintillations is obtained not because the density variations are changing in time, but because the spacecraft appears to be moving through the atmosphere and passes behind the frozen-in density fluctuations.

We use the analogy of sunlight at the bottom of a pool to illustrate how the scintillations work. The sun in this case serves the role of the source, the radio transmitter aboard the spacecraft. The waves on the surface of the pool represent the dynamical motions which refract the sunlight. The observer at Earth would be at the bottom of the pool and see a pattern of rapidly occurring intensity maxima and minima. There are some slight differences between radio scintillations and the sunlight at the bottom of a wavy pool. First of all, the motion of the spacecraft with respect to the atmosphere is so rapid that the dynamical motions in the atmosphere which cause the scintillations appear to be stationary. Secondly, the scintillations at the bottom of the pool are strong scintillations because refraction at the surface of the pool is much more dramatic than in the Venus atmosphere. The scintillations would be weak, and thus more analogous to the Pioneer Venus radio data, if the pool waves were small and frozen on the surface with a sun racing over the top. At any given point on the bottom of the pool, an observer can obtain a time history of intensity maxima and minima. This best represents the scintillation phenomenon in the Pioneer Venus radio data.

Prominent radio scintillations which occur near 45 km altitude and 60 km altitude in Venus's atmosphere have been analyzed by WA. Essentially, they subtracted the background signal, created by refraction, and were left with only the scintillations. Then WA Fourier analyzed the scintillations and calculated log-amplitude (χ) and phase (S) variance spectra in variance spectra in frequency, which is the conjugate to the time elapsed during an occultation. The log-amplitude variance spectra could indicate a power law with an index anywhere between about -2.3 to -3.7. Furthermore, WA estimated that the temperature variance at 60 km required to generate the scintillations is roughly 1 K^2. Finally, they estimated that the density inhomogeneities were elongated by a factor of about 20 in the horizontal direction compared to the vertical.

WA subsequently used a theory for radio scintillations in order to show how small scale turbulent phenomena might be responsible for the data they analyzed. The scintillation theory WA implemented was developed by several authors (Tatarski 1961; Ishimaru 1973; Woo and Ishimaru 1974; Haugstad 1979) and can be used to generate model radio scintillation time series in log-amplitude or phase given a pattern of index of refraction fluctuations in the atmosphere. The index of refraction fluctuations are directly proportional to density fluctuations in the atmosphere through a constant which is determined by the chemical composition of the atmosphere (Essen and Froome 1951, Kliore *et al.* 1980). WA assumed a random pattern of density fluctuations in the Venus atmosphere with a variance spectrum proportional to a power law of -11/3 in the spatial wavenumbers. Such a power law in the density variance spectrum is consistent with a Kolmogorov spectrum of three dimensional dissipative turbulence. In addition they assumed that the fluctuations were anisotropic—highly flattened out in the horizontal direction. This is not the conventional form of fully developed dissipative turbulence, but a modified form because the motions involved are embedded in a stably stratified atmosphere, which strongly resists vertical motion (Houghton 1986). Under these assumptions, they used the weak scintillation theory to simulate scintillation power spectra. In the end they found good agreement between their model and the data with the requirement that the outer vertical scalesize of the density structures was larger than the Fresnel size. This is somewhat inconsistent with turbulence properties in the Earth's stratosphere, in which turbulence is known to be confined to individual pockets on the order of only a few tens of meters thick. Even then, the agreement does not exclude the possibility of power law indices other than -11/3 or altogether different spectra of the density inhomogeneities.

We use the same numerical technique for simulating radio scintillations but we assume that the density inhomogeneities are the fluctuations of internal gravity waves generated by convection in Venus's middle atmosphere. We choose this as the most probable source for the density variations because the convection in Venus's atmosphere is nearly global in scale and is situated in a 5 km thick layer between the stable layers at 45 and 60 km altitude. The source is required to be global in scale because the scintillations in the Pioneer Venus radio science were found to be global in scale. Scintillations were also seen near 60 km by Mariner 5 (Woo *et al.* 1974), Mariner

10 (Woo 1975), and Venera 9 (Timofeeva *et al.* 1978). We choose gravity waves in particular because they can have structure which extends over vertical scales which are easily larger than the beam width. With such criteria, therefore, we presume that gravity waves generated by the middle atmosphere convection in Venus's atmosphere are a probable creator of the scintillations in Pioneer Venus radio science data.

The vertical resolution of the scintillations may obscure the presence of gravity waves in the scintillations data. The scintillations are sensitive to density variations in the Venus atmosphere with vertical scales comparable to the beam width, which is approximately 63 meters. On scales this small in the Earth's atmosphere, the most significant phenomenon is dissipative turbulence (Sato and Woodman 1982, Barat 1982). On the other hand, because turbulence tends to create isentropic patches in small pockets in the atmosphere, it is not clear how turbulence can generate density contrasts which would cause scintillations (Schubert 1983, p. 755). Nevertheless, it would be optimal to search for gravity waves in the resolved refractive data where turbulence effect are presumed to be minimal, but we adamantly pursue the possibility that gravity waves are seen in the scintillation data.

In the first paper we have calculated a temperature variance spectrum associated with the gravity waves generated by the convection in the middle atmosphere. The convecting layer was placed between 50 and 55 km altitude. Just above the convection, the atmosphere is statically stable with the square of the Brunt-Väisälä frequency given by $N_c^2 = 4 \times 10^{-5}$ s^{-2}. The stability increases with altitude to about $N^2 = 3.6 \times 10^{-4}$ s^{-2} at 60 km altitude. The atmosphere is statically stable below the convection as well, but we restrict ourselves to analysis of the overlying stable atmosphere. The winds are westward and increase by about 60 m/s between the convection and 67 km altitude. There is no shear nor static stability within the convection itself.

Prominent in the results of the first paper were two types of wavebreaking:

breaking upon emission from the convection and *critical layer breaking* near critical layers. Immediately upon emission from the convection, low frequency, and hence low phase speed, waves were found to be convectively unstable; thus, we required that they break. Wave amplitude was decreased according to their local vertical wavenumber just above the convection to the point where the saturated spectrum of gravity waves was not exceeded (Dewan and Good 1986, Smith *et al.* 1987). In addition, the presence of a shearing zonal wind created critical layers, near which gravity waves become unstable via both Kelvin-Helmholtz and convective instabilities (Geller *et al.* 1975). Again, waves were attenuated according to their local vertical wavenumber such that the saturated spectrum of gravity waves was never exceeded.

The first section of this paper is the introduction. In the second section we describe how we implement a spectrum of gravity waves generated by dry convection in the weak scintillation theory so that we may simulate scintillations. In the third section of this paper we present our simulations of radio scintillations assuming that gravity waves density fluctuations are responsible for the radio scintillations. In the fourth section we summarize our results and discuss what implications they might have for Venus's atmosphere. Finally, the weak scintillation theory derived by previous authors is suitable for implementing gravity waves; however, certain details of weak scintillation theory which are important in the context of gravity waves are specifically addressed in appendix C.

2. Implementing Gravity Waves

The equation which we use to simulate radio scintillations is derived in appendix C and is repeated here as

$$W_\chi(\nu) = 4\pi^2 k^2 L \int dk_y'\, dm\, \mathbf{B}_{n_1}(k_x'{=}0, k_y', m)\, \sin^2\Big[\frac{R}{2k}({k_y'}^2 + \frac{m^2}{q^2})\Big] \times \Big(\delta(2\pi\nu - k_y'\dot{y}_a - m\dot{z}_a) + \delta(2\pi\nu + k_y'\dot{y}_a + m\dot{z}_a)\Big) \tag{2.1}$$

in which ν is the frequency, $W_\chi(\nu)$ is the simulated log-amplitude variance spectrum of the radio scintillations in frequency, k is the free-space wavenumber of the radio signal, k_x' and k_y' are the horizontal wavenumber in Venus's atmosphere tangent to the radio beam path and the horizontal wavenumber transverse to the beam path, m is the vertical wavenumber, $\mathbf{B}_{n_1}(k_x', k_y', m)$ is the variance spectrum of index of refraction fluctuations in the spatial wavenumbers k_x', k_y', m, and $\dot{y}_a$ and $\dot{z}_a$ are the apparent spacecraft motions in the horizontal and vertical directions. The defocusing factor q^2 is the factor by which the radio signal strength is attenuated by refraction effects in Venus's atmosphere. The δ's are Dirac delta functions. The log-amplitude scintillation spectrum $W_\chi(\nu)$ is defined such that $W_\chi(\nu)\ d\nu$ is the amount of log-amplitude variance between the frequencies ν and $\nu + d\nu$. The index of refraction variance spectrum is defined such that $\mathbf{B}_{n_1}(k_x', k_y', m)\ dk_x' dk_y' dm$ is the amount of index of refraction variance in the spectral volume $dk_x' dk_y' dm$ centered at k_x', k_y', m.

We implement gravity waves in the scintillation simulation equation by introducing polar coordinates in the plane transverse to the beam path in Venus's atmosphere. The motivation behind this is to permit any combination of $\dot{y}_a$ and $\dot{z}_a$ in the simulations. We invent polar coordinates such that $\kappa^2 = {k_y'}^2 + m^2$ and the angle θ measures the angle away from the vertical in which the wave propagates. In particular,

$$\begin{aligned} k_y' &= \kappa \sin\theta \\ m &= \kappa \cos\theta \end{aligned} \tag{2.2}$$

where κ is the amplitude of the wavevector in the y', z' plane. For consistency, we rewrite the apparent spacecraft velocity $\dot{y}_a, \dot{z}_a$ in polar coordinates:

$$\begin{aligned} \dot{y}_a &= v_a \sin\alpha \\ \dot{z}_a &= v_a \cos\alpha \end{aligned} \tag{2.3}$$

where v_a is the apparent velocity of the spacecraft through the atmosphere and α is the angle at which the spacecraft appears to travel in the atmosphere away from purely vertically. Inserting the above expressions into equation 2.1 gives

$$\begin{aligned} W_\chi(\nu) = 4\pi^2 k^2 L &\int \kappa\, d\kappa\, d\theta\, \mathbf{B}_{n_1}(k'_x = 0, k'_y = \kappa\sin\theta, m = \kappa\cos\theta) \\ &\times \sin^2\left[\frac{R\kappa^2}{2k}(\sin^2\theta + \frac{\cos^2\theta}{q^2})\right] \\ &\times \Big(\delta(2\pi\nu - \kappa v_a\cos(\theta-\alpha)) + \delta(2\pi\nu + \kappa v_a\cos(\theta-\alpha))\Big). \end{aligned} \tag{2.4}$$

In this last equation, we take full advantage of the integrating properties of Dirac delta functions and integrate over κ. When we do this integration, we find that we only get contributions for

$$\kappa = \pm\frac{2\pi\nu}{v_a}\sec(\theta-\alpha) \tag{2.5}$$

for each value of θ. Thus, in integrating equation 2.4 we find that the log-amplitude power spectrum becomes

$$\begin{aligned} W_\chi(\nu) = 8\pi^2 k^2 L\,\frac{2\pi\nu}{v_a^2} &\int_{\alpha-\pi/2}^{\alpha+\pi/2} d\theta\, \sec^2(\theta-\alpha) \\ &\times \sin^2\left[\frac{2\pi^2\nu^2 R}{k v_a^2}\sec^2(\theta-\alpha)(\sin^2\theta + \frac{\cos^2\theta}{q^2})\right] \\ &\times \Big\{\mathbf{B}_{n_1}\Big(k'_x = 0, k'_y = \frac{2\pi\nu}{v_a}\sec(\theta-\alpha)\sin\theta, m = \frac{2\pi\nu}{v_a}\sec(\theta-\alpha)\cos\theta\Big) \\ &+ \mathbf{B}_{n_1}\Big(k'_x = 0, k'_y = -\frac{2\pi\nu}{v_a}\sec(\theta-\alpha)\sin\theta, m = -\frac{2\pi\nu}{v_a}\sec(\theta-\alpha)\cos\theta\Big)\Big\}. \end{aligned} \tag{2.6}$$

The power spectrum in this equation is the same as that in equation 2.1 except that the three Fourier components of the index refraction spectrum k'_x, k'_y, m are determined by the frequency ν, the apparent spacecraft velocity v_a, the apparent spacecraft entry angle α, and the angle of integration θ.

As mentioned earlier, the index of refraction fluctuations n_1 are related to the wavelike fluctuations in the atmosphere. It is primarily the density variations which create the index of refraction fluctuations. We can compute the density variations caused by the waves despite not having explicitly noted them in the first paper. We use equations 2.11*c* and 2.12 of the first paper to show that

$$\frac{\rho'}{\bar{\rho}} = \frac{\phi'}{\gamma RT} - \frac{S'}{c_p}. \tag{2.7a}$$

In order to compare the two terms on the right-hand side of this equation, we solve for S' in terms of ϕ' using the following combination of equations 2.10*c* and 2.10*e* of the first paper:

$$S' = \frac{c_p}{g} \frac{N^2}{N^2 - \tilde{\omega}^2} \frac{\partial \phi'}{\partial z}. \tag{2.7b}$$

When the WKBJ approximation is valid, $mH \gg 1$, and the second term dominates the first term on the right in equation 2.7a. Using the above expression for the entropy fluctuation, the density fluctuation ρ' can be written as a function of ϕ':

$$\rho' \simeq -\frac{\bar{\rho}(z)}{g} \frac{N^2}{N^2 - \tilde{\omega}^2} \frac{\partial \phi'}{\partial z}. \tag{2.8}$$

This is how we evaluate the density fluctuation numerically.

Several authors have calculated the coefficient relating density fluctuations and index of refraction fluctuations for Venus's atmosphere (Essen and Froome 1951, Woo 1975). We are content to use the value given by WA, which is

$$n_1 = (1.35 \times 10^{-6} \text{ K/Pa})\, R\, \rho' \tag{2.9}$$

in which R is the gas constant for Venus's atmosphere, $R = 189.0$ J kg^{-1} K^{-1} (Seiff *et al.* 1980).

With the use of equation 2.38 of the first paper, we can write the power spectrum of index of refraction fluctuations as

$$\begin{aligned} \mathbf{B}_{n_1}(k_x, k_y, m) = {} & (2.55 \times 10^{-4}\ \mathrm{m}^3\ \mathrm{kg}^{-1})^2 \left(\frac{\bar{\rho}(z)}{g}\right)^2 \\ & \times \frac{N^4}{(N^2 - \tilde{\omega}^2)^2} \left|\frac{\partial h}{\partial z}\right|^2 M(k_x, k_y, m) \end{aligned} \tag{2.10}$$

where we use the continuum M as determined by equation 2.73 in the first paper for trapped waves and the derivative $\partial h/\partial z$ as described in appendix B.

We have shown how to calculate the modulation factor $M(\omega, k_x, k_y)$, and it is not difficult to transform the coordinates. In particular, since the modulation factor is similar to a power spectral density, we can find $M(k_x, k_y, m)$ by

$$M(k_x, k_y, m) = \left|\frac{\partial \omega}{\partial m}\right|_{k_x, k_y} M(\omega, k_x, k_y). \tag{2.11}$$

It remains for us to determine the relationship between k_x, k_y and k'_x, k'_y. It should be a rotation through an angle Δ which we derive next.

The angle Δ is the angle between the radio beam at closest approach to the planet and the eastward direction at that point. We define a coordinate system x', y', z' in which z' is the north rotation axis, y' is perpendicular to the z' axis and is directed to Venus's east limb as viewed from Earth, and x' is orthogonal to the z' and y' axes and roughly points toward the Earth. Next we define the coordinate system x, y, z such that x is directed along the Venus-Earth line, y is the same axis as y', and the z axis is the orthogonal axis to the x and y axes and directed roughly upward. The two coordinate systems are related by a rotation through an angle B about the y/y' axis. The rotation angle B is the obliquity of Venus to Earth.

We find the angle between the radio beam path and circles of constant latitude on Venus by noting that its cosine is the inner product of the vector $(1, 0, 0)$ in the primed coordinate system and the vector $(1, 0, 0)$ in the unprimed coordinate system with a location constrained to the limb of Venus as viewed from Earth. The set of points on the planet which lie on the limb as viewed from Earth are found by setting $x = 0$. These points are described by

$$\cos B \cos\phi \cos\lambda + \sin B \sin\phi = 0 \tag{2.12}$$

where λ is the longitude measured away from the sub-Earth longitude and ϕ is the latitude. Simultaneously, the vector $(1, 0, 0)$ in the primed system is given by

$$\frac{1}{\cos\phi}\frac{\partial}{\partial\lambda}\begin{pmatrix} x \\ y \\ z \end{pmatrix} = \begin{pmatrix} -\cos B \sin\lambda \\ \cos\lambda \\ \sin B \sin\lambda \end{pmatrix} \tag{2.13}$$

in the unprimed system. The cosine of Δ is found by taking the inner product of this last vector with $(1, 0, 0)$ and eliminating λ using equation 2.12. After some algebra, we find that

$$\sin\Delta = \frac{\sin B}{\cos\phi}. \tag{2.14}$$

This equation tells us that given the latitude of the occultation ϕ and the obliquity of the planet at the time of the occultation B, we can find the angle between the beam path and the eastward direction at the beam's closest approach. The limiting cases make complete sense: for an occultation at the equator, the obliquity is the same as the beam path–eastward angle; for an occultation directly on top of the planet as viewed from Earth ($\phi = 90° - B$), the beam path is oriented directly northward at closest approach ($\Delta = 90°$).

As mentioned previously, the transformation between k_x, k_y and k'_x, k'_y is a rotation through the angle Δ. In particular, the transformation is

$$\begin{aligned} k'_x &= k_x \cos\Delta - k_y \sin\Delta \\ k'_y &= k_x \sin\Delta + k_y \cos\Delta \end{aligned} \tag{2.15a}$$

along with the inverse

$$\begin{aligned} k_x &= k'_x \cos\Delta + k'_y \sin\Delta \\ k_y &= -k'_x \sin\Delta + k'_y \cos\Delta. \end{aligned} \tag{2.15b}$$

We use these transformations in finding $\mathbf{B}_{n_1}(k'_x, k'_y, m)$ of equations 2.1 and 2.6 from equation 2.10.

Even though we have taken care to maintain the correct sign of Δ, upon careful inspection one can see that the power should not depend on the sign of Δ. If one changes the sign of Δ in equations 2.15*b*, noting that k'_x remains zero, both k_x and k_y will change sign. The gravity wave power spectrum is independent of the sign of k_y. Furthermore, symmetry in k_x enters because of the sum of the gravity wave power spectra in the large braces in equation 2.6. Thus, the scintillation power spectrum is independent of the sign of Δ.

Here we conclude the section on how one simulates log-amplitude radio scintillation spectra given a gravity wave spectrum. The simulation equation is 2.6. We implement convectively generated gravity waves through equations 2.10, 2.11, and 2.15*b*, where Δ is given by equation 2.14. The factor $M(\omega, k_x, k_y)$ is calculated using equation 2.38 of the first paper and $\partial h/\partial z$ is calculated as described in appendix B. Values for the parameters v_a, α, q^2, and Δ are different for each occultation.

3. Scintillation Simulations

In this section we present numerical results for log-amplitude scintillation power spectra given the gravity wave spectrum derived in this thesis. The main intention of this section is to simulate log-amplitude radio scintillation power spectra assuming they are a consequence of convectively generated internal gravity waves which have propagated into adjoining stable layers. First we reproduce the data as presented in WA. Then we calculate the different parameters involved in the simulations. Third we present the simulations themselves. Lastly, we look at how changes in the background atmosphere might alter the simulations.

3.1 Scintillation data

For the sake of comparison, we reproduce the power spectrum of log-amplitude fluctuations at 60 km altitude in the S-band originally calculated by WA (oral permission obtained from Armstrong, May 5, 1994). A quadrature fit has been subtracted from the log-amplitude data by WA. First we have manually digitized the data of figure 4 in WA. Over the course of the 6.62 second interval we have obtained 941 individual points. This data is shown in our figure 1. Subsequently we have Fourier transformed it using a fast Fourier transform, squared each coefficient and multiplied them by 2 × 6.62s. The factor of 2 enters because we fold the negative frequencies in with the positive frequencies as already discussed. We trust the power spectrum out to about 150 Hz at which point we run into sampling problems. We essentially use the definition

$$W_\chi(\nu) \equiv 2 \int_{-\infty}^{\infty} d\Delta t \, \overline{\chi(t)\, \chi(t+\Delta t)} \, \cos 2\pi\nu\Delta t \tag{3.1}$$

given in appendix C. The resulting power spectrum is shown in figure 2. The total variance is found by integrating the power spectrum over frequency. We find that ${\sigma_\chi}^2 \simeq 0.044$ in agreement with WA, and thus the scintillations can be considered weak. Upon close comparison with the power spectrum in figure 4 of WA, we see that

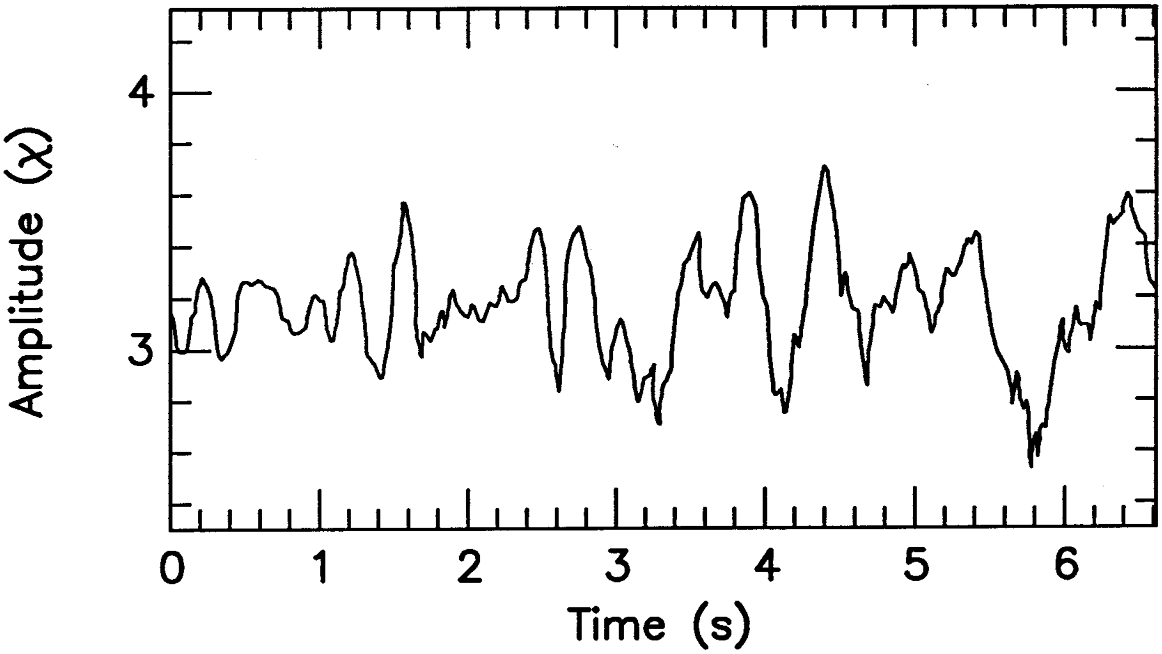

Figure 1. S-band Scintillation Data. This is a reproduction of the S-band radio scintillation data presented by WA. It is taken from the radio occultation data of orbit 18, day of year 356, 1978 from Pioneer Venus. This segment roughly samples 60 km altitude in Venus's atmosphere.

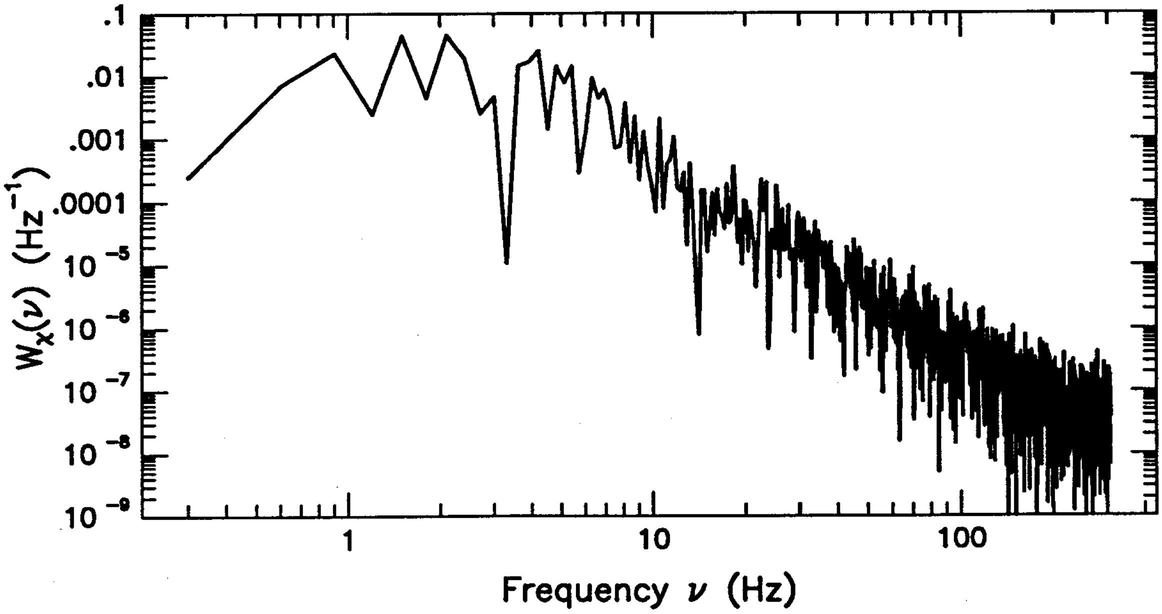

Figure 2. S-band Scintillation Power Spectrum. This is the power spectrum of the data presented in figure 1. The integral over positive frequencies of this curve gives the total variance of the log-amplitude fluctuations of the data.

WA have not folded negative frequencies in with the positive frequencies. Despite the factor of 2 difference between WA and us, our results are consistent with each other except that we use different conventions concerning the range of frequencies.

3.2 Simulation parameters

Many parameters are explicitly determined by the geometry of the occultation in question. For example, WA have presented simulated power spectra given the geometry of the orbit 18 occultation 1978 DOY 356 of Pioneer Venus. The spacecraft trajectory determines $\dot{y}_s$ and $\dot{z}_s$. WA give $v_s = 7.7$ km/s and we have measured the spacecraft trajectory to be about 35° away from the vertical before it entered the atmosphere from figure 1 of Kliore and Patel 1980. Thus, $\dot{y}_s = 4.42$ km/s and $\dot{z}_s = -6.31$ km/s. Analysis of the background occultation gives us q^2 as a function of altitude. For this particular orbit WA have used and we use $q^2 = 10$. Then using equation 2.3 and the transformation in appendix C which gives $\dot{y}_a, \dot{z}_a$ in terms of $\dot{y}_s, \dot{z}_s$, we can determine v_a and α. We find that $\alpha \simeq 82°$ and $v_a \simeq 4.46$ km/s. Other parameters which are determined are the spacecraft to limb distance ($R_1 =$ 3819 km) and the Venus-Earth distance ($R_2 = 69.9 \times 10^6$ km). Because $R_1 \ll R_2$, then $R \simeq 3819$ km (the quantity R is defined in appendix C). Also, we use the S-band occultation data; thus the carrier frequency is $k = 48.2\ \mathrm{m}^{-1}$. We define the Fresnel size to be $a_f \equiv \sqrt{R/2k}$ and thus the Fresnel size is 200 meters. Finally, we approximate the beam pathlength through the atmosphere as $L \simeq \sqrt{8R_{\mathrm{Venus}}H}$ where R_{Venus} is the radius of Venus and H is a scaleheight in the atmosphere (see figure 7 in Woo *et al.* 1974). Using 6050 km as the radius of Venus and 5 km as the scaleheight, we find $L \simeq 540$ km. This is consistent with WA.

The most sensitive parameter in our problem turns out to be the angle Δ. Given that Venus has no annual cycle and that its orbital plane is nearly the same as the Earth's, its obliquity to the Earth $B \simeq 0°$. If this were the case, then the angle Δ

would be 0° for every occultation. In reality, though, $B = -2.23755°$ at the time of the occultation in question (Nicholson, personal communication). The trouble enters because the early entry occultations, including the one in question, took place at very high latitudes. In our case, the latitude $\phi = 86.6°$ north. When these values are used in equation 2.14, we find that $\Delta = -41.2°$. Clearly the angle Δ can vary wildly at high latitudes for even slightly nonzero values of the obliquity B. The problem is compounded by the fact that we do not know that the background winds are exactly zonal at high latitudes. We do know that meridional winds increase as one moves away from the equator to as much as 10 m/s, but we have no measurements of the winds in the polar regions of Venus's atmosphere. For these reasons, we experiment with many different values of the angle Δ between the radio beam path and the background winds.

First of all, the simulated radio scintillation power spectra roughly tell us about the nature of the vertical wavenumber spectrum of temperature fluctuations in the atmosphere. In the integrand of equation 2.1, we compare the terms ${k_y}'\dot{y}_a$ and $m\dot{z}_a$. In order to find out which term is larger, we must assume typical values for ${k_y}'$ and m. For ${k_y}'$, we choose the dominant horizontal scale of the forcing, $1/H_c$. For m, we choose $m > 1/(63 \text{ m})$ because the beam width is approximately 63 meters in the vertical direction (given by the Fresnel size divided by the defocusing factor q). Using equations 2.3, the $m\dot{z}_a$ term is much greater than the ${k_y}'\dot{y}_a$ term when $\tan\alpha \ll 80$. This implies that for most values of the entry angle α, a given frequency ν corresponds to a single vertical wavenumber m.

3.3 Simulations

In order to understand the behavior of the simulated radio scintillation spectra, we first fix the entry angle α at zero so the occultation is purely vertical. The parameters v_s and q^2 remain 7.7 km/s and 10. The Fresnel size a_f is still 200 meters.

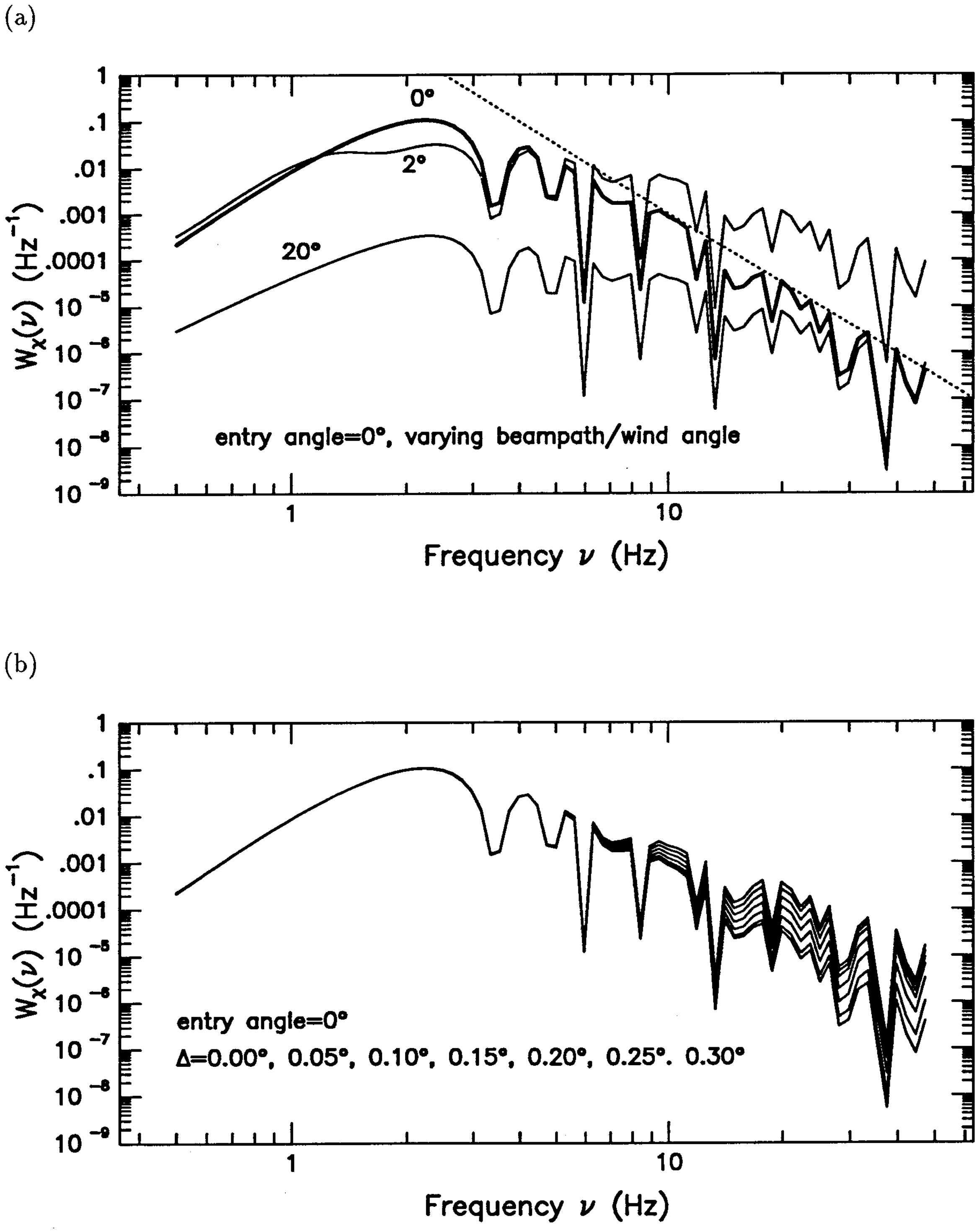

Figure 3. Simulated scintillations. Gravity waves are assumed responsible for the index of refraction fluctuations. The ordinate is the power spectrum of log-amplitude fluctuations. The gravity wave spectrum has $W_c = 1$ m/s and $H_c = 5$ km. The entry angle is set to 0°. For (a), the angle Δ is set to 0° (bold curve), 2°, and 20° in succession. For (b), the angle Δ varies from 0.0° to 0.3° in steps of 0.05°. In figure (a) we include a dotted line with a slope of -5.

In figure 3(a) we set the convective wind speed at $W_c = 1$ m/s, implement the complete breaking of waves as described in section 2 of the first paper, and vary Δ from 0° to 40°. The spectra were determined at 60 km altitude. Recall that $\Delta = 0°$ corresponds to sampling waves which are exactly transverse to the zonal winds. Such waves experience no Doppler shifting because k_x is always zero. As Δ is increased, Doppler shifting does occur and critical layers enter into the scintillation integral. For large values of Δ, much of the wave amplitude is lost through critical layer absorption below 60 km altitude.

The effect of introducing Doppler shifting by increasing Δ away from zero can be seen in figure 3(b). All the parameters except Δ remain the same as in the previous figure. For $\Delta = 0°$, there are two factors which determine the slope of the tail of the spectrum. Since $k_x = 0$ for these waves, waves with large vertical wavenumbers at 60 km altitude will also have large vertical wavenumbers at the point of emission from the convection. Initially, such waves with large vertical wavenumbers will be broken by a m^{-3} law upon emission from the convection (see section 3.1). When $\Delta = 0°$, the waves with $k'_x = 0$ see no effects of horizontal anisotropy because these waves are not Doppler shifted. Thus, the temperature variance spectrum of the slice where $k'_x = 0$ will appear the same as the integrated spectrum over k'_x, k'_y of an atmosphere without winds, but an additional breaking factor of m^{-2} must be included because other waves with large m which have nearby critical layers will also break the waves with large m but not near critical layers. Thus, the tail of the scintillation spectrum for $\Delta = 0°$ reflects a m^{-5} spectrum of gravity waves. In figure 3*b*, the simulated radio scintillation spectrum for $\Delta \approx 0°$ does indeed approach a ν^{-5} power law as it should since m and ν are roughly related by a constant factor.

As the angle Δ increases, Doppler shifting becomes more important. The high frequencies in the scintillation spectrum correspond to high vertical wavenumbers at

60 km altitude. For nonzero Δ, waves with high vertical wavenumbers at 60 km will not have high vertical wavenumbers at their point of emission. This is especially true when $k_x\bar{u} \approx \omega$. The waves are broken while propagating up to 60 km because of the presence of critical layers, but they are not significantly broken upon emission from the convection. The net effect is that the integrated temperature variance spectrum in vertical wavenumber is proportional to m^{-3}. The simulated scintillation spectrum is not exactly proportional to ν^{-2} at high frequencies though because all waves with a fixed m at 60 km altitude are not emitted horizontally isotropically from the convection. Consequently, the slope of log of the simulated scintillation spectrum versus the log of the frequency is somewhere between -2 and -3 (see figure 3(b)). Since $k_x \simeq (1/H) \sin\Delta$ and $\omega \simeq W_c/H$, the spectrum attains a slope of m^{-3} when $\sin\Delta \approx W_c/\bar{u}$ where $\bar{u}$ is the difference in the zonal wind speed between 55 and 60 km altitude.

As Δ is increased even more, the simulated scintillation spectra retain the same dependence on ν but the overall amplitude falls. Most of the energy bearing waves are critically absorbed before they reach 60 km altitude and cannot contribute to the spectrum at 60 km. Only those waves with very large phase speeds can contribute, and thus the overall amplitude will fall as Δ is increased. This effect is obvious in figure 3(a).

Our next step is to use a realistic entry angle for the occultation. As remarked earlier, we have measured the entry angle for the occultation in question to be 35° before entry into the atmosphere. When defocusing is taken into account, the apparent entry angle becomes 81.9°. The frequency ν still corresponds to roughly constant m since $(\tan 81.9^\circ) \ll 250$. In figure 4, we show simulated radio scintillation power spectra for an entry angle of 81.9°. We also show the log-amplitude power spectrum we have computed from digitized data. We retain $v_s = 7.7$ km/s and $q^2 = 10$. First

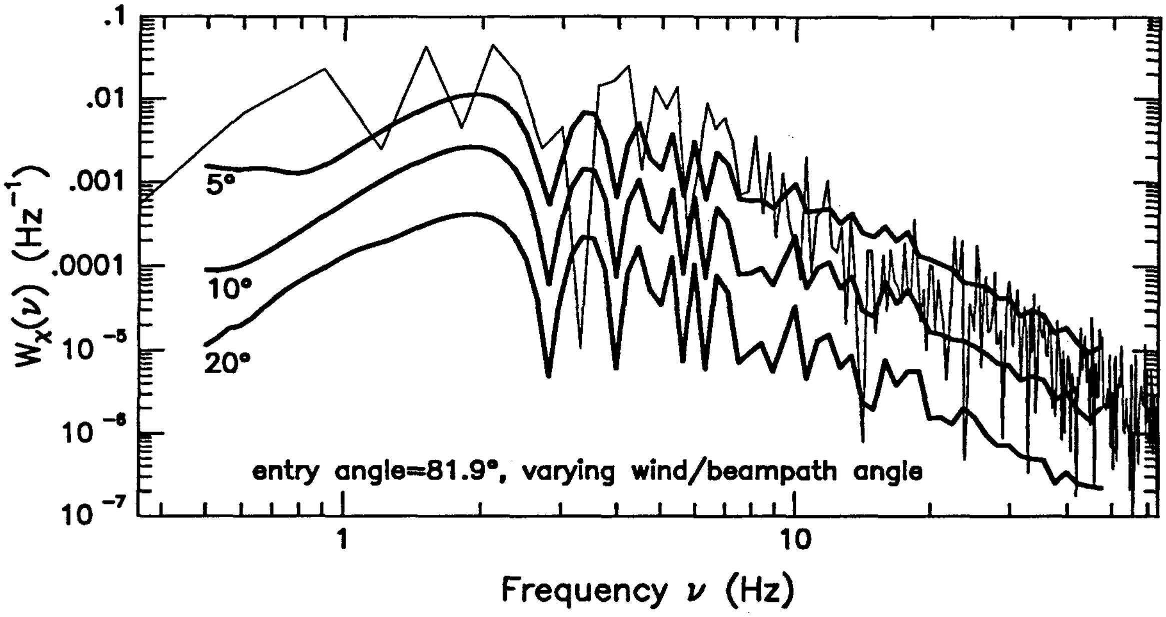

Figure 4. Simulated spectra. The actual entry angle is 35°; the apparent entry angle is 81.9°. The convective wind speed is set to 1 m/s and H_c=5 km. The angle Δ is set to 5°, 10°, and 20°. The deemphasized curve is the data.

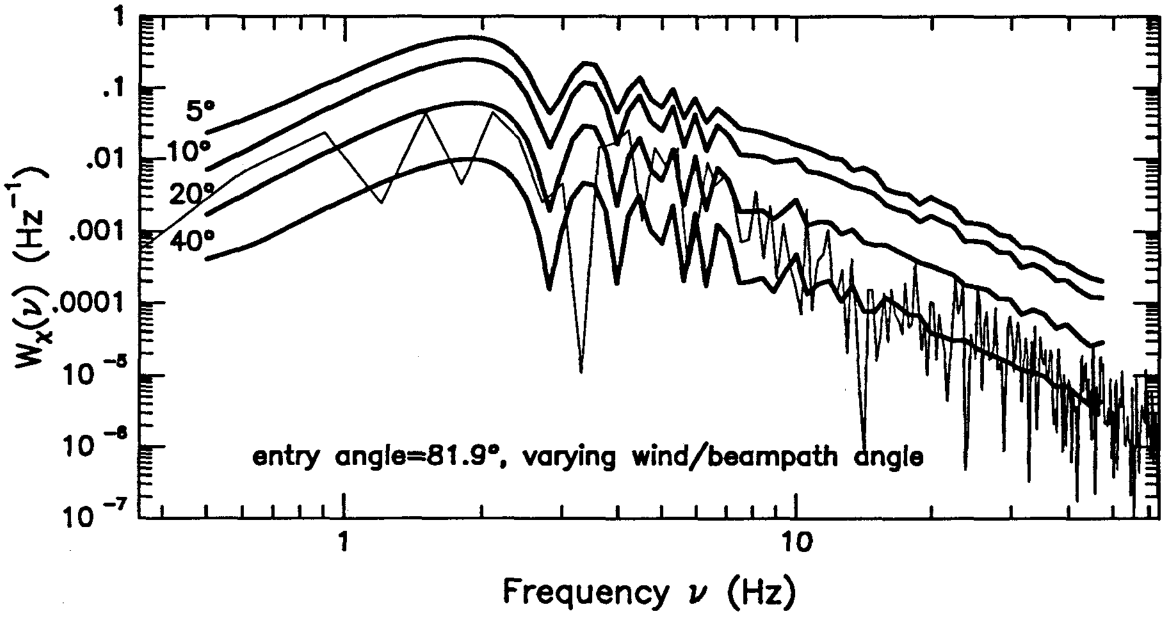

Figure 5. Simulated spectra. The actual entry angle is 35°; the apparent entry angle is 81.9°. The convective wind speed is set to 3 m/s and H_c=5 km. The angle Δ is set to 5°, 10°, 20°, and 40°. The deemphasized curve is the data.

we use $W_c = 1$ m/s and $H_c = 5$ km. We show the results for $\Delta = 5°, 10°$ and $20°$ because these bracket the data nicely. The shape of the simulations matches the data well; however, the overall amplitude for the simulated spectra is highly dependent on loosely constrained parameters such as Δ. Because the overall amplitude of the tail beyond 10 Hz is controlled by the amplitude parameter Γ in the saturated spectrum and the angle Δ, we can only claim a plausible match between the data and our model if the slopes of the spectra are similar. This indeed seems to be the case.

Since the saturated spectrum of waves seems to govern the scintillation simulations, we expect that varying the forcing parameter W_c would not affect the overall amplitude of the scintillations. We vary W_c to check this idea. We retain all the parameters that went into making figure 4 and only change W_c to 3 m/s. Again we vary the angle Δ. The result is figure 5. The simulated power spectra are evidently the same shape as in the previous simulations, but the overall amplitude is larger. The shape can only be preserved if the saturated spectrum is valid throughout the range of vertical wavenumbers represented in the simulations. This is the case as can be seen in figure 11 of the first paper. In that figure, it is apparent that the universal spectrum applies for all wavenumbers greater than $\sim 2\pi/(1 \text{ km})$ for $W_c = 3$ m/s. Since we are sensitive to vertical wavelengths less than 63 meters (the beam width in the vertical) in these simulations, it is obvious that we shall only see the tail of the saturated spectrum. Because the scintillation spectrum is nearly proportional to ν^{-2}, the saturated spectrum of gravity waves somewhat dictates the scintillation spectrum. The overall amplitude of the scintillation simulations is thus independent of the intensity of the convective motions. We suggest that the amplitude in figure 5 is larger than those of figure 4 because the phase speeds of the dominant gravity waves has increased. An increase in the phase speed means that more waves can propagate to higher altitudes. Thus, even though the integrated temperature variance spectrum

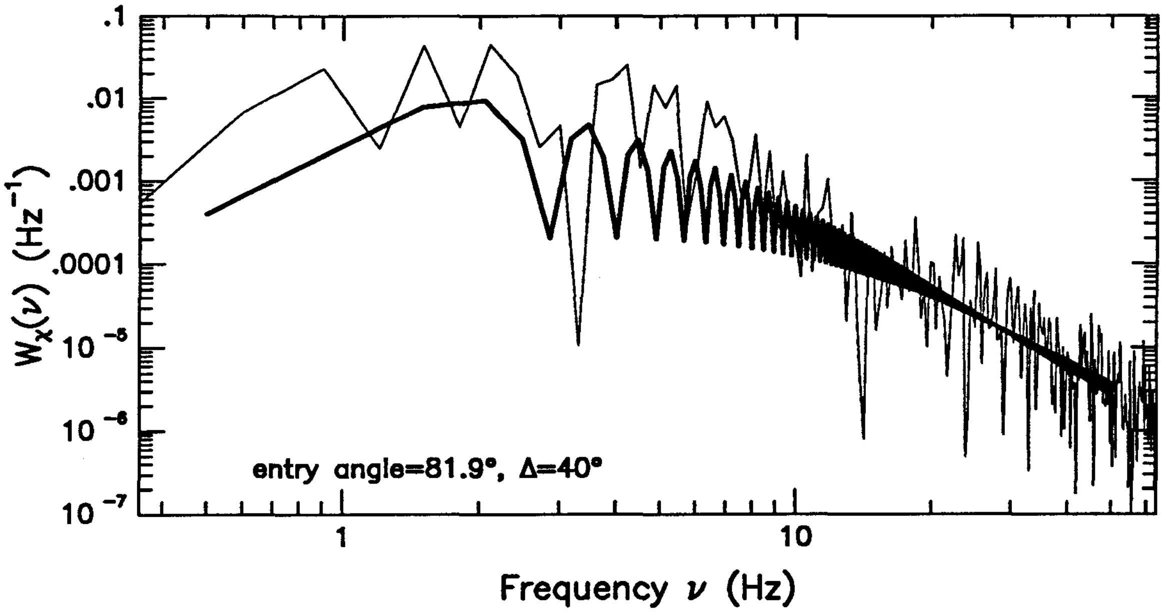

Figure 6. Simulation with resolved fringes. In this simulated log-amplitude variance spectrum in frequency, we sample in ν more finely at high frequencies so that all of the fringes are resolved. We have set the entry angle to 81.9°, W_c to 3 m/s, H_c to 5 km, and the angle between the radio beam path and the winds Δ to 40°. The deemphasized curve is the data.

in vertical wavenumber remains the same, the simulations are sensitive to more waves in the slice $k'_x = 0$ when W_c is increased.

The occasional dips which occur in the simulated scintillation spectra are the familiar fringes associated with Fresnel diffraction patterns. In weak scintillation theory for gravity waves, the fringes occur when the Fresnel filter function $\sin^2[\ldots]$ in equation 2.1 is nearly zero. Because $m^2 \gg k_x^2, k_y^2$ for gravity waves, the fringes are located at

$$\frac{m^2 a_f^2}{q^2} = n\pi \tag{3.2a}$$

where n is a positive integer. We note that $2\pi\nu = m\dot{z}_a$ and that $\dot{z}_2 = q^2 \dot{z}_a$ to show that the sequence of frequencies ν_n at which there are fringes is

$$\nu_n = 2.813 \text{ Hz } \sqrt{n}. \tag{3.2b}$$

We have used an entry angle of 35° and a spacecraft velocity of $v_s = 7.7$ km/s.

In most of the preceding scintillation simulations, the fringes are unresolved at higher frequencies. In figure 6 we show a simulation in which all of the fringes between 0.5 and 50 Hz are resolved. We have used the realistic entry angle, $W_c=3$ m/s, $H_c=5$ km, and only $\Delta=40°$. In general, this simulation shows a higher quality fit to the scintillation data.

We have established that the amplitude of the simulated log-amplitude power spectra is dependent on the phase speeds of the dominant gravity waves W_c, angle between the radio beam path and the zonal wind Δ, and the static stability N^2 of the atmosphere even though the shape of the spectra remains insensitive to changing any of these parameters. The data and the simulations agree well in shape. The parameters W_c and Δ are only loosely constrained, and thus so is the overall amplitude of the simulated spectra. Nevertheless, we can place some limits on the range of permissible values for W_c and Δ.

We take advantage of the fact that the overall amplitude of the simulated spectra is maximized for a certain value of Δ and increases with increasing W_c. The static stability is presumably determined by the reduction of the radio occultation data. Since there is a maximum amplitude in the simulated spectra for a given gravity wave forcing intensity, we can put a lower limit on the dominant wave phase speed if we match the simulations to the data at high frequencies. In our model for the forcing of gravity waves, we make a strong connection between the intensity of the forcing and the phase speeds of the dominant gravity waves. Therefore, we can put a lower limit on the intensity of the local wave forcing.

In order to determine the lower limit on W_c, we would perform a series of runs varying W_c and Δ. For each value of W_c we choose, we vary Δ in order to find the maximum attainable amplitude. We already know that simulated spectra for $W_c=1$ m/s give overall amplitudes which are too large. Thus, the lower limit on W_c must be lower than 1 m/s. In truth, it is extremely difficult to proceed for more than a few values of W_c because for each value of W_c we must compute the integrated wave action flux $\mathcal{A}$ (see equations 3.13 of the first paper) so that we can perform complete wave breaking calculations by using equations 3.15*b* and 3.15*a* of the first paper. Calculating $\mathcal{A}$ requires computing $\mathbf{B}_T(m; z)$ for several different altitudes z. We only perform this task for $W_c = 0.2$ m/s and 0.7 m/s in addition to 3 m/s and 1 m/s which we have already presented.

The scintillation simulations for $W_c = 0.2$ m/s yield significantly different results than for larger values of W_c. The simulations are shown in figure 7. Obviously, these curves are nearly flat in comparison with the previous simulations. The explanation for this is quite simple. The forcing is so much weaker than it was before that the universal spectrum for breaking gravity waves does not set in until very high vertical wavenumbers. For wavenumbers associated with frequencies on the order of a few Hz, the waves are not large enough to break. This is not characteristic of the power spectrum of the log-amplitude scintillation data, so we know that the forcing must be more intense than $W_c = 0.2$ m/s. For this reason, we perform simulations for an intermediate value of W_c.

In figure 8 we show simulations for $W_c = 0.7$ m/s. In these curves the effects of weak forcing are apparent. This would imply that for this value of W_c the waves are not saturated in the relevant portion of the vertical wavenumber spectrum. Obviously, for a valid fit to the data, we need the gravity waves to be saturated according to the universal spectrum for vertical wavenumbers on the order of $(63 \text{ m})^{-1}$. We know that the simulations show saturation for $W_c = 1 \text{ m s}^{-1}$, and thus we require that $W_c \gtrsim 1 \text{ m s}^{-1}$.

For $W_c = 1$ m/s, we found that we could obtain maximum overall amplitudes easily larger than the data exhibit. This means that we can also place a lower limit

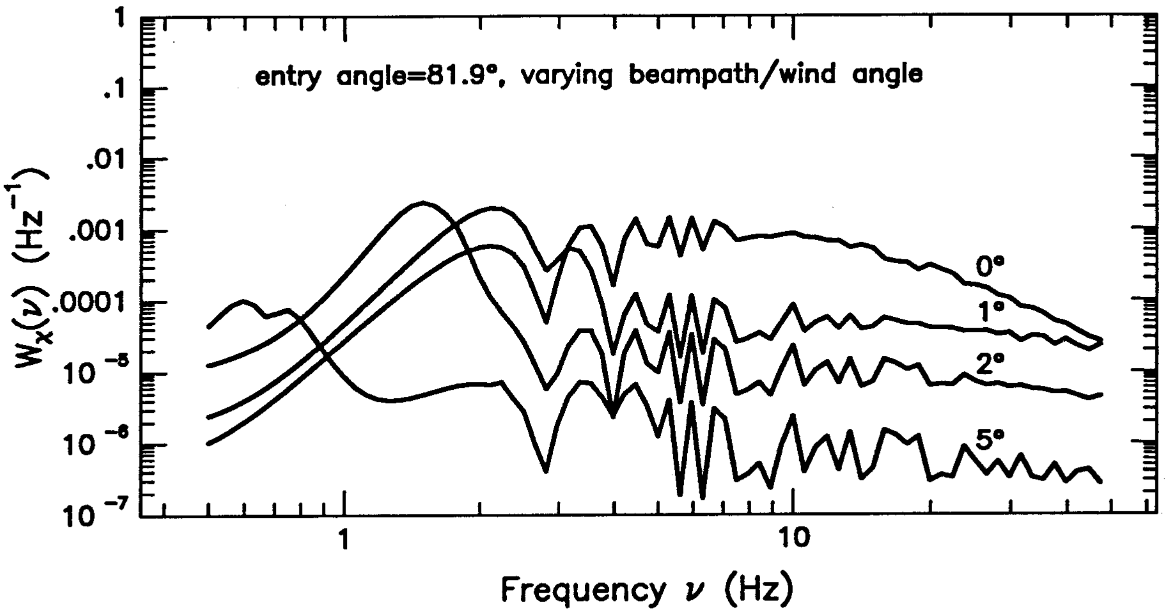

Figure 7. Simulated scintillations. The actual entry angle is 35°; the apparent entry angle is 81.9°. The convective wind speed is set to 0.2 m/s and $H_c = 5$ km. The angle Δ is set to 0°, 1°, 2°, and 5°.

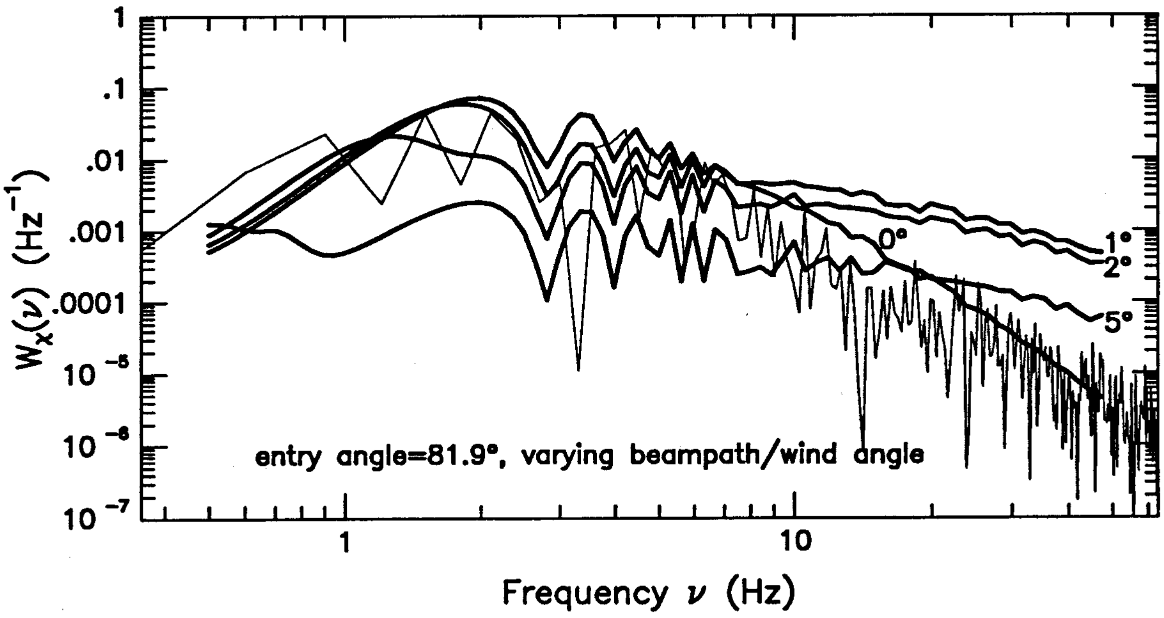

Figure 8. Simulated scintillations. The actual entry angle is 35°; the apparent entry angle is 81.9°. The convective wind speed is set to 0.7 m/s and $H_c = 5$ km. The angle Δ is set to 0°, 1°, 2°, and 5°. The deemphasized curve is the data.

on the angle Δ since the amplitude falls off with increasing Δ. For $W_c = 1$ m/s, we found good fits to the data for Δ between 10° and 20°. This would imply a lower limit for Δ because in order to maintain a good fit as W_c is increased, we would have to increase Δ as well.

3.4 Varying the background atmosphere

Finally, we present how the simulated log-amplitude spectra might vary with the stability profile N^2. For this purpose we introduce a new profile for the Brunt-Väisälä frequency in which we have only decreased the peak value of N^2 by a factor of two. The new profile is shown in figure 9. The slopes in the zonal wind profile have been adjusted so that Kelvin-Helmholtz instabilities are avoided (the Richardson number is always greater than 1/4). The net effect is only a 3 m/s westward shift to the winds above the convection. We have again set $W_c = 3$ m/s and we vary Δ.

The simulated scintillation spectra in figure 10 bear a strong resemblance to the previously computed spectra. Once again the slope above 10 Hz matches the slope of the power spectrum of the data. Also, the overall amplitude falls with increasing Δ, but the overall amplitude does reach a maximum for $\Delta \approx 5°$. The problem remains that a good match at frequencies greater than 10 Hz gives amplitudes which are too small at frequencies less than 10 Hz in the simulated spectra. On the other hand, it is clear that when the static stability is reduced, the amplitude of the simulated spectra is also reduced. This agrees with the concept that the simulated spectra are largely a reflection of the saturated spectrum of breaking gravity waves. When the stability is reduced, so does the amplitude of the saturated spectrum (see equation 2.63a in the first paper; Γ and N^2 are directly proportional to each other).

Because the occultation from which the scintillation data is extracted occurred at 86.6° north latitude, it is extremely likely that the appropriate zonal winds are much smaller than those we have used in the previous simulations. For this reason,

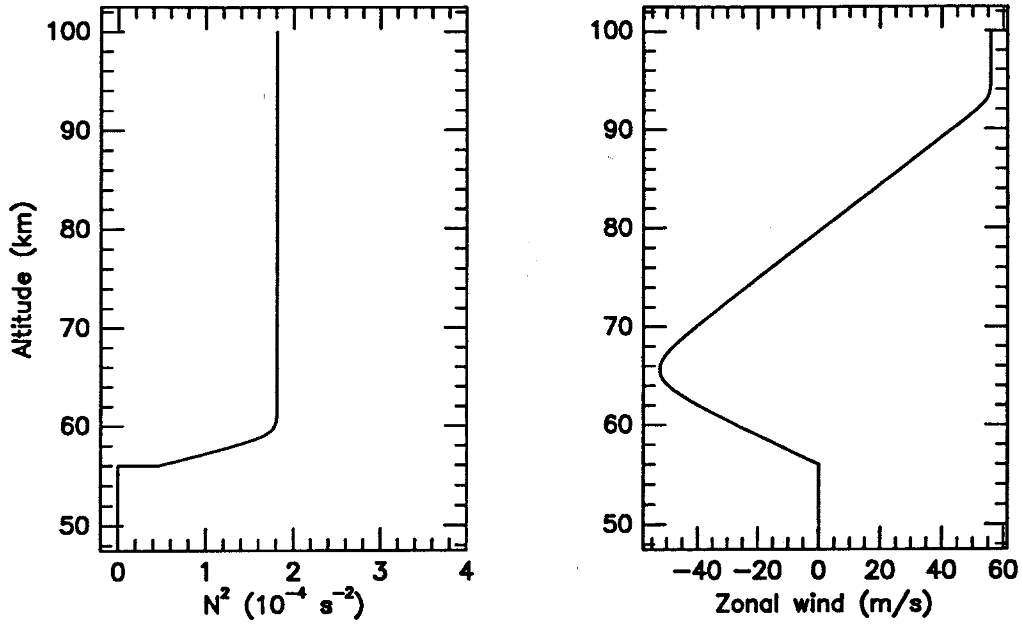

Figure 9. Modified background stability. This is a modified version of the background atmosphere used in model 3. The peak static stability has been decreased by a factor of 2. The zonal wind has been modified so that the Richardson number nowhere exceeds 1/4. Also, the top of the convection was raised because the stable layer is less resilient to vertical motion.

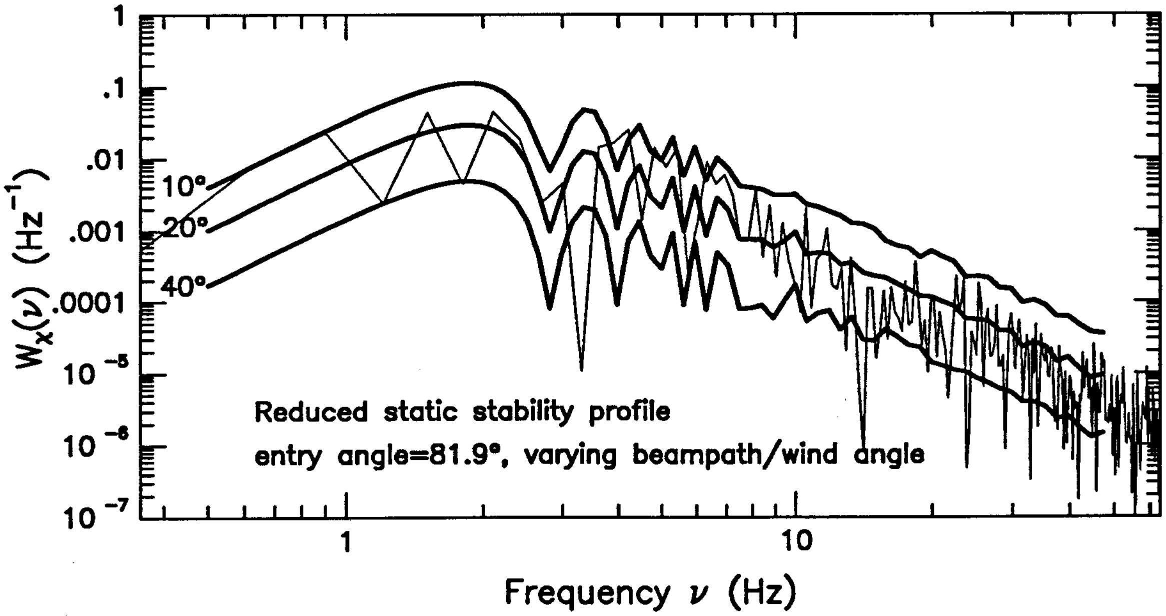

Figure 10. Modified stability simulations. These simulations utilized the reduced static stability profile displayed above. The actual entry angle is 35°; the apparent entry angle is 81.9°. The convective wind speed is set to 3 m/s and $H_c = 5$ km. The angle Δ is set to 10°, 20°, and 40°. The deemphasized curve is the data.

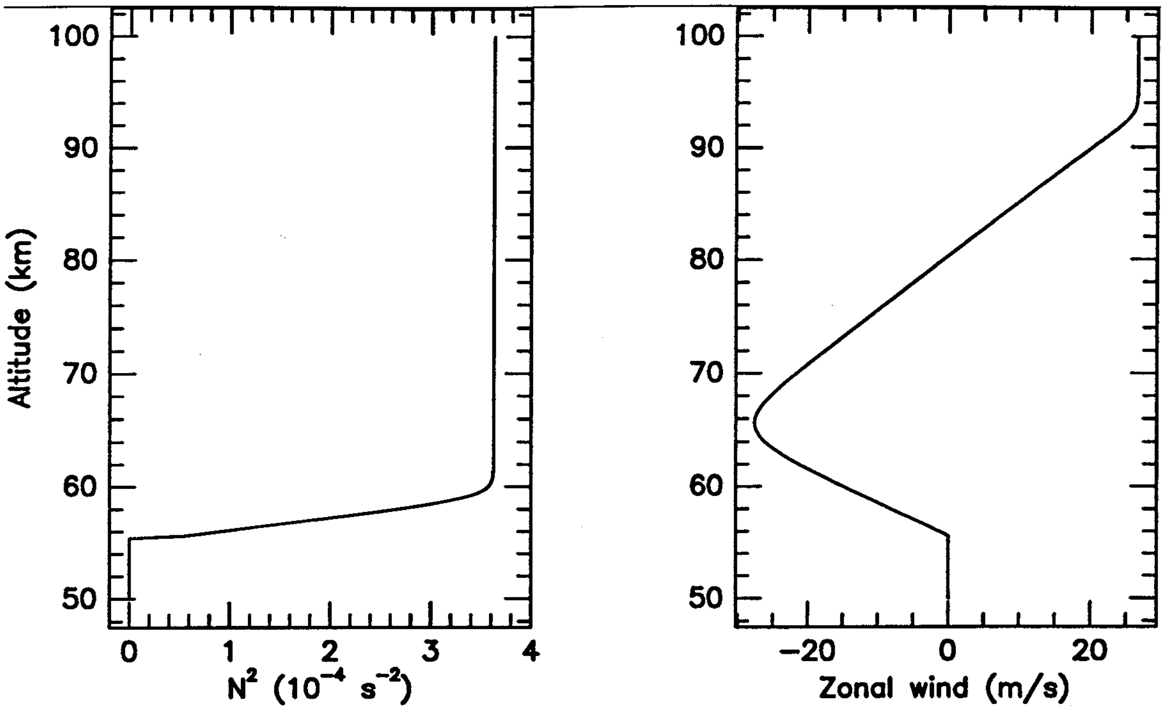

Figure 11. Modified zonal winds. We plot the square of the Brunt-Väisälä frequency and the zonal wind versus altitude we use with which we test the effect of changing the wind profile on the scintillation simulations. Compared to previous profiles of the winds, the shear above the convecting layer in this model has been reduced by a factor of 2. The background stability remains the same as in previous simulations.

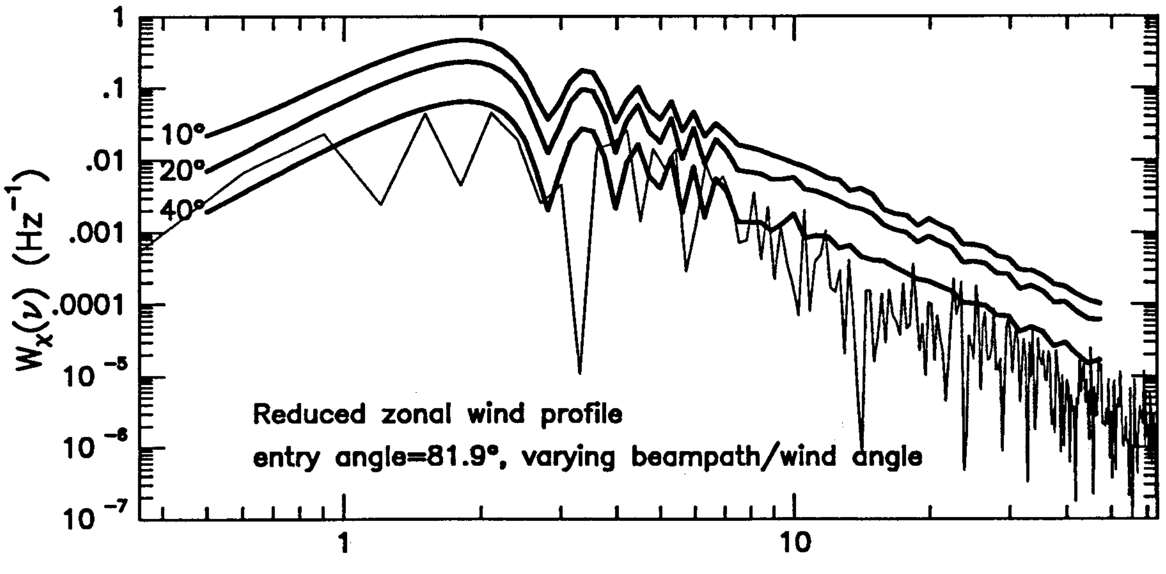

Figure 12. Modified wind simulations. We plot simulated log-amplitude variance simulations in which the entry angle is set to 81.9°, the convective wind W_c is set to 3 m/s, H_c to 5 km, and the angle Δ is set to 10°, 20°, and 40°. We have used the background profiles of stability and zonal wind illustrated in figure 11. The deemphasized curve is the data.

we perform simulations in which we use a zonal wind profile in which the shear is reduced by a factor of 2. Whereas in the previous modeling the zonal wind differed by 55 m/s between the convecting layer and the zonal wind maximum, in an altered profile we use for sensitivity testing, the zonal wind differs by 28 m/s between the convecting layer and the zonal wind maximum. Above the zonal wind maximum, the shear was also reduced by a factor of 2 so that the winds would still pass through zero at about 80 km altitude. The profiles of $N^2(z)$ and $\bar{u}(z)$ we use are plotted in figure 11.

In figure 12 we show simulations of the log-amplitude variance spectra in frequency. We use $W_c = 3$ m/s, $H_c = 5$ km, an apparent entry angle of 81.9°, and we set the wind/beam path angle to 10°, 20°, and 40°. In general, the shape of the simulated spectra remains unchanged compared to previous spectra. This indicates that for $W_c = 3$ m/s the saturated spectrum of gravity waves still manifests itself in the scintillation spectra. Decreasing the zonal wind shear increases the overall amplitude of the simulated spectra. This is consistent with our previous interpretation that the amplitude of simulated spectra when $\Delta \neq 0°$ is determined by the saturated spectrum of gravity waves and the number of waves which propagate to 60 km altitude. When the zonal wind is decreased, fewer modes are critically absorbed below 60 km altitude and thus the simulated scintillation spectra are larger. We discuss the implications of this sensitivity study in the next section.

4. Summary and Discussion

We have simulated radio scintillation power spectra assuming that convectively generated gravity waves in Venus's atmosphere are the prime source of the density fluctuations in Venus's atmosphere which cause the scintillations. We have compared these simulations to a sample radio scintillation power spectrum computed from Pioneer Venus radio data. Then we suggest that our model of the scintillations is more viable than the turbulence model suggested by Woo and Ishimaru 1981 (WI hereafter). Finally, we make a prediction concerning radio scintillations caused by convectively generated gravity waves based on our work.

4.1 Summary

We have shown how index of refraction variations in the atmosphere can lead to the radio scintillations and in particular how a spectrum of gravity waves would appear in the scintillations. This derivation has been done before, but we use some slightly different conventions which are better suited to implementing gravity waves. In particular, we follow Ishimaru (1978) so that we may implement a general spectrum of a random process. We then implement convectively generated gravity waves as that random process. With the spectrum of gravity waves, we can compute simulated radio scintillation power spectra with the intention of comparing them to the power spectra of the data.

We find that the simulations are highly sensitive to the geometry of the occultation to which it is being compared. In order to compute realistic simulations, we use the same geometry as occurred for the occultation in question. In particular, we must know the spacecraft to limb distance, the beam pathlength through the atmosphere, the net defocusing of the radio beam, the spacecraft velocity as viewed from Earth, and the angle Δ between the radio beam path and the zonal winds. The first four of these parameters can be known *a priori*; however, the angle between the winds and the beam path is difficult to figure out. If the background winds were purely zonal, then we have found an expression which gives this angle as a function of the latitude of the occultation and the inclination of the planet to the Earth (both of which are known). We do not know that the orientation of the winds is purely zonal, especially at high latitudes where evidence points toward an increasingly vigorous meridional circulation. Thus, we cannot know the angle between the radio beam path and the background winds with good accuracy and we treat it as a free parameter.

In truth, other free parameters do enter, most of which are used in generating the gravity wave spectrum. These parameters would be the intensity of the convection which generates the waves, the horizontal phase speed W_c of the dominant gravity wave modes, the static stability structure $N^2(z)$, and the zonal wind profile $\bar{u}(z)$. The convective intensity and the dominant horizontal phase speed are of course related through the mixing length hypothesis. Presumeably, the static stability profile can be extracted from the background occultation data, and so we use data consistent with the stability given by WA. Again, the zonal winds remain an unknown, especially at 86.6° latitude, where the occultation in question took place.

Despite the presence of several somewhat free parameters in our problem, we show that the simulations of the radio scintillations are dependent on only a few parameters. Most importantly, we have found the shape of the simulated spectra to be nearly identical for most values of the above listed parameters. The reason for this is that the spectra are nearly recreations of the temperature variance spectra of the gravity waves in the vertical wavenumber, $\mathbf{B}_T(m; z)$, where only waves with vertical wavelengths smaller than the radio beam width (about 63 meters) are counted. These spectra are completely described by the saturated spectrum of gravity waves for sufficiently large m. It turns out that for reasonable values for the forcing intensity, all waves with $m > (63\ \mathrm{m})^{-1}$ obey the power law tail of the saturated spectrum.

Hence the shapes of the spectra are almost all the same.

Exceptional shapes do occur for specific values of certain parameters, though. When the angle Δ is near zero, the slopes of the simulated scintillation power spectra becomes markedly greater. Recall that $\Delta \simeq 0$ means that the simulated scintillations are only sensitive to waves which propagate transversely to the mean flow. Most of the time (when Δ is not close to zero), the only breaking process relevant to the simulated scintillation spectra is that which takes place in the presence of critical layers. This breaking process forces the vertical wavenumber spectrum to be the saturated spectrum for breaking waves. In the presence of the critical layers, wavebreaking takes place for all waves dependent only on the value of their local vertical wavenumber. Thus, waves do not need to have critical layers nearby in order to be broken. The other breaking process relevant to this problem is that of breaking upon emission. This only breaks the waves with large vertical wavenumbers at the point of emission from the convection at about 55 km altitude. When substantial Doppler shifting of the frequency is significant ($\Delta \neq 0$), waves with large vertical wavenumbers at 60 km do not have large vertical wavenumbers at 55 km. Thus, these waves do not experience breaking upon emission. When Δ is near zero, however, no Doppler shifting takes place. This means that waves with large vertical wavenumbers at 60 km also have large vertical wavenumbers at 55 km. These waves do experience breaking upon emission in addition to the breaking that all other waves do because of the presence of critical layers. For this reason, the slope of the simulated scintillation spectra for Δ near zero is much steeper in log-log plots than for Δ not near zero. Since breaking upon emission is effectively proportional to m^{-3}, the slope for Δ near zero is steeper than the others by 3 in log-log plots.

We have repeatedly used the nebulous term "near zero" when talking about the angle Δ, but we can quantify this. The key to the discussion above is whether or not Doppler shifting of the wave frequency is important during vertical propagation. We have shown that Doppler shifting is only important when $\sin\Delta \gtrsim W_c/|\bar{u}|$ where W_c is the horizontal phase speed of the dominant wavemodes and $\bar{u}$ is the difference in zonal wind speed between the convection and the altitude of observation, which is 60 km for the spectra presented.

The shape of the simulated scintillation power spectra is also significantly different for small values of the forcing. In particular, it is possible to make the forcing weak enough so that waves do not break in the vertical wavenumber regime relevant to the scintillation power spectra. When this happens, the scintillation power spectra become flat the same way that temperature variance spectra in vertical wavenumber do. We have shown that this happens for $W_c = 0.2$ m/s. Even for $W_c = 0.7$ m/s, the effects of nonsaturation are apparent in the vertical wavenumber regime relevant to the scintillation data. Since it is clear that the radio scintillation spectra from the data bear no resemblance to the simulations for such small values of W_c, we conclude that the gravity waves must at least be large enough to break for values of $(63\ \mathrm{m})^{-1}$ for the vertical wavenumber. In our model, this means that the typical convective wind velocity must be at least 0.7 m/s.

Aside from the unusual circumstances listed above, the simulated scintillation power spectra have the same shape; however, their amplitude is affected by certain parameters. Since most spectra are a direct consequence of the saturated spectrum, it is natural to assume that changing the stability N^2 would change the overall amplitude of the spectra since it governs the amplitude of the saturated spectrum. This turns out to be the case. Nevertheless, we do not consider the static stability a free parameter since it can be determined by the large scale radio occultation data. We use a value of N^2 which is consistent with that given by WA. The overall amplitude is also affected by the angle Δ. For a given W_c, the overall amplitude is maximized when Δ is around 2°. For larger Δ the amplitude decreases monotonically. Also, the overall amplitude is increased for larger values of W_c. We suspect that these two phenomena are related. As Δ is increased, fewer wavemodes can propagate to high altitudes. This also happens when the dominant phase speed W_c is reduced or the zonal wind shear is increased. When fewer modes reach 60 km, we see a portion of the temperature fluctuation spectrum which has a smaller amplitude, even though the spectrum is still the saturated spectrum when integrated over all Δ.

We have already seen that W_c must be greater than 0.7 m/s so that the shape of the simulated spectra match that of the data. When we consider this in conjunction with largest amplitude obtainable by varying Δ at $W_c = 1$ m/s, we find that we essentially must place a lower limit on the angle Δ. We have eliminated all possibilities of W_c less than 0.7 m/s for reasons described above. We have emphasized the curve on which a model must lie for good agreement between model and data. Two branches of the curve yield good agreement, but one is preferable to the other. One of the branches falls in only a 2° bin of Δ while the other lies in a broad range of Δ. Encountering values for Δ in only a bin of 2° is improbable, and thus we favor the other branch. By choosing the other branch, we essentially place a lower limit on Δ, the angle between the background winds and the radio beam path. When we use 1 m/s for W_c, a good fit is obtained for Δ somewhere between 5° and 10°. For larger values of W_c, we would have to increase Δ to maintain a good fit.

4.2 Discussion

The limit on W_c has important consequences for Venus's atmosphere. Recall that the occultation data from which the scintillations in question were extracted comes from 86.6° north latitude. The minimum value for W_c really represents a lower limit on the strength of the convection which generates the waves. The implication is that there is substantial dry convective activity in Venus's middle atmosphere even at polar latitudes. To date, there has been little effort placed in understanding polar atmospheric dynamics in Venus's atmosphere. That there is enough heat made available in the polar lower atmosphere of Venus so that middle atmospheric convection remains substantial is important. This could imply that the transport of heat in the lower atmosphere could extend to extremely high latitudes. This would not be possible if there were an isolated polar vortex, as is the case for the Earth's southern winter. Thus, we suggest that there is considerable meridional mixing in Venus's lower atmosphere clear up to the north pole.

Such an implication is dependent on our choice of a background wind profile suitable for polar latitudes. For many of our simulations, we had used a background zonal wind profile more appropriate for equatorial conditions, but we did show that wind profiles with decreased shear would increase the amplitude of the simulated scintillations. Because winds are likely to be less vigorous near the pole than near the equator, it is likely that our estimate for the angle between the beam path and the winds is too small for given values of W_c. It is difficult to conclude anything more quantitative since the polar winds are unknown. In the future, we hope to work with individual occultations from equatorial latitudes, where we have a much better knowledge of the zonal wind profiles.

Also, the above conclusion is strongly dependent upon our model for gravity wave generation in Venus's middle atmosphere being the correct one. We offer some support that this is indeed the case. We know that waves with vertical wavelengths of $2\pi \times (63\text{ m})$ and smaller are breaking at 60 km altitude. Because the breaking occurs at high vertical wavenumbers throughout a layer at least 10 km thick, this suggests that the waves are encountering their critical layers. Presumeably, in a strongly shearing atmosphere such as that of Venus, critically absorbed waves must have a local source because gravity waves should not have horizontal phase speeds substantially different than that of their source. Convection in the middle atmosphere is already suggested in the radio occultation data because the scintillations are suppressed at about 55 km altitude (temperature fluctuations are difficult to create in an isentropic portion of the atmosphere). The convection is an obvious source for the waves. There is little latent heat associated with the convection as is implied by the nearly adiabatic gradient in the temperature structure. If critical layers truly do exist throughout a ten kilometer layer above the convection, then the source of the waves must be a continuum source because critical layers for waves must exist throughout. All of this points toward our model for the generation of the gravity waves.

4.3 Gravity waves or turbulence?

The debate remains on whether it is more appropriate to interpret radio scintillations as the result of clear air turbulence or vertically propagating internal gravity waves. Because scintillations are sensitive to density fluctuations on vertical scales of 63 meters and less, it seems most likely that turbulence may be the more appropriate choice. On the other hand, turbulent motions are not likely to create density contrasts in the atmosphere because turbulence mixes so effectively that local isentropic patches develop. It is difficult for a vertically displaced air parcel to create a density fluctuation in an isentropic region of the atmosphere.

Any turbulence would probably be the result of breaking gravity waves, which is a major component of our theory of gravity wave spectra in Venus's middle atmosphere. It has been demonstrated in the Earth's upper troposphere that clear air turbulence is concentrated where the lapse rate at short vertical scales becomes convectively unstable (Barat and Bertin 1984). By the above arguments, we do not expect to see any density contrasts associated with the subsequent turbulent motions; however, the effect of breaking on the waves should be significant in radio scintillations. Effectively, the signature of wavebreaking is included in our determination of the wave spectrum by implementing the saturated spectrum for breaking gravity waves.

Nonetheless, even if it is possible for turbulence to generate density variations and hence radio scintillations, we argue that their required amplitudes are unreasonably large based on energetics requirements. Thus, we briefly outline the work of WA and then show why some of the estimates of WI preclude turbulence as an explanation for the scintillations.

WA calculated radio scintillation simulations, but with a Kolmogorov law for the spectrum of temperature fluctuations in the atmosphere. WA anticipated a nonlinear nonisotropic process to be responsible for the density fluctuations in the atmosphere, so they used a model which mimicked nonisotropic fully developed turbulence where there was significant elongation in the horizontal direction. In essence, they used the following spectrum for atmospheric temperature fluctuations:

$$\mathbf{B}_T(\mathbf{k}) = \frac{\beta^2\, c_T^2}{\left(\beta^2(k_x^2 + k_y^2) + k_z^2 + L_z^{-2}\right)^{-11/6}} \tag{4.1}$$

where $\mathbf{k}$ is a three dimensional spatial wavenumber, c_T is the structure constant of the temperature fluctuations, β is the aspect ratio of the turbulence, and L_z is the outer vertical scale of the turbulence. The structure constant is fundamental to describing the intensity of the spectrum at small spatial scales. WA found good fits for $L_z \gtrsim 1$ km, $c_T \simeq 0.15$ K m$^{-1/3}$, and $\beta \gtrsim 10$.

WI suggest that dissipative atmospheric turbulence is responsible for the density inhomogeneities in the atmosphere. Using parameters determined from their best fits, they then proceeded to describe the intensity of the turbulence. The parameter most commonly used to describe the vigor of turbulence is the energy dissipation rate ε, which is the mechanical power per unit mass dissipated. They find values for ε which are consistent with mild conditions in the Earth's atmosphere; however, we find that this is not true, largely because of an error made in their estimation of ε.

Here we intend to give an intuitive view of the turbulence in the stably stratified medium and how one can relate the parameter c_T to the energy dissipation rate ε. We view this turbulence similarly to fully developed turbulence in that there are large eddies which eventually lose their energy to smaller eddies in an energy cascade. This turbulence is different than fully developed turbulence, though, in that the size and lifetime of the largest eddies are constrained by the atmospheric stability. The Brunt-Väisälä frequency approximates in the inverse of the turnover time of the largest eddies because vertical motions in a stably stratified atmosphere occur on such timescales. Thus, the typical velocity in the turbulence must be approximately NL_z. We assume that the turnover timescale of the largest eddies also approximates their lifetime and thus

$$\varepsilon \approx N^3\, L_z^2. \tag{4.2}$$

Thus, given an energy dissipation rate ε, one can determine the vertical length scale of the turbulence.

The vertical length scale alone is not sufficient for us to connect the parameter c_T to the energy dissipation rate; however, L_z can tell us about the size of the temperature fluctuations. We assume that motions over the course of a turnover time are adiabatic. If a parcel moves vertically and adiabatically over a length L_z, it will exhibit a temperature contrast against the background atmosphere. We assume that the square of this temperature contrast approximates the temperature variance associated with the turbulence:

$$\sigma_T^2 \approx \Gamma^2\, L_z^2 \tag{4.3}$$

where $\Gamma \equiv (dT/dz)_{\mathbf{atmosphere}} - (dT/dz)_{\mathbf{adiabatic}}$ and σ_T^2 is the temperature variance. We can calculate the temperature variance by integrating the temperature variance spectrum, though. This will let us fully relate the above equations to the parameters determined by WA:

$$\sigma_T^2 \approx c_T^2 \, L_z^{2/3}. \tag{4.4}$$

After eliminating L_z and σ_T^2 from the above three equations, we find that

$$\varepsilon \approx \left(\frac{N\, c_T}{\Gamma}\right)^3. \tag{4.5}$$

Thus we have found a relation between the intensity of the turbulence ε and the amplitude of the high frequency portion of the temperature variance spectrum.

This formulation agrees with that of WI (equation 6 with Ri=1/4):

$$c_T^2 = \frac{b}{3N^2}\left(\frac{\partial\theta}{\partial z}\right)^2 \varepsilon^{2/3} \tag{4.6}$$

where $b \simeq 2.8$ is a nondimensional constant (Monin and Yaglom 1975), provided that $\partial\theta/\partial z = \Gamma$. Unlike kinetic temperature T, the potential temperature θ is only a relatively defined quantity which is ordinarily calculated by integrating

$$\frac{1}{\theta}\frac{d\theta}{dz} = \frac{\Gamma(z)}{T(z)}. \tag{4.7}$$

It is apparent that for all of the above equations to be consistent, the potential temperature must be defined relative to the local temperature, *i.e.*, $\theta = T$.

WI used a potential temperature profile which used a reference temperature defined at Venus's surface. They calculated the gradient of the potential temperature $(\partial\theta/\partial z)_{\mathrm{W}}$ by finite differencing an integrated potential temperature profile. Thus,

$$\left(\frac{\partial\theta}{\partial z}\right)_{\mathrm{W}} = \left(\frac{\theta_{\mathrm{W}}}{T}\right)\Gamma \tag{4.8}$$

in which the subscript W's denote the values used by WI. Substituting for Γ in equation 4.5 gives

$$\varepsilon = \left(\frac{\theta_{\mathrm{W}}}{T}\right)^3 \varepsilon_{\mathrm{W}} \tag{4.9}$$

where ϵ_{W} is the value of the energy dissipation rate calculated by Woo *et al.* (1982). They used the following parameters in their calculations: $T = 260$ K, $N^2 = 1.7 \times$

10^{-4} s^{-2}, and $(\partial\theta/\partial z)_W = 16$ K/km. Using 8.80 m/s^2 for gravity, we find that $\Gamma = 5.0$ K/km and $\theta_W = 814$ K. Woo *et al.* (1982) calculated $\varepsilon_W = 20$ cm^2/s^3, and thus the true energy dissipation rate is $\varepsilon = 610$ cm^2/s^3.

The increase in the estimate of the energy dissipation rate may dismiss dissipative turbulence as an alternative explanation of the radio scintillation data. Firstly, the value of the diffusion coefficient estimated by WI is consistent with an independent estimation of the eddy diffusion coefficient by cloud-particle distribution studies; however, the value of the diffusion coefficient estimated by WI is small by a factor of 30 like the energy dissipation rate (see equation 8 in WI). Secondly, the intensity of turbulence as indicated by the energy dissipation rate occurs only rarely in the Earth's atmosphere. Turbulence studies have been done in the Earth's stratosphere where the shear environment is similar to that of Venus at 60 km. In the Earth's atmosphere, Crane (1980) used shears of $\partial u/\partial z = 10^{-2}$ s^{-1} and found that typical energy dissipation rates were on the order of 0.1 to 1.0 cm^2/s^3 at 10 km altitude. The shear at 60 km in Venus's atmosphere is about 2.6×10^{-2} s^{-1} and the intensity of the scintillations is nearly global on Venus. Thirdly, the energy available for dissipation is greater in the Earth's atmosphere than in Venus's. For daytime conditions in the Earth's atmosphere, on the order of 400 W/m^2 can be transported vertically at mid-latitudes. At 60 km in Venus's atmosphere, though, only ≈ 40 W/m^2 is available for vertical transport (Tomasko *et al.* 1980). For the above reasons, it is unlikely that dissipative turbulence is the source of the radio scintillations.

4.4 Prediction

Of course, the source of gravity waves need not be the middle atmospheric convection as has been suggested here. Nonetheless, this theory does make a specific prediction which would be unique to this mechanism of gravity wave generation. Recall that when the angle between the radio beam path and the background winds is near zero, damping at the point of emission manifests itself by strongly attenuating high frequencies in the radio scintillations. Thus, this signature should be apparent in a few of the occultation profiles. Because of the apparent poleward meridional circulation in Venus's clouds, they would most likely be found in the southern hemisphere when Venus's north pole is slightly inclined toward the Earth.

References

Abramowitz, J. and I.A. Stegun. *Handbook of Mathematical Functions.* Dover Publications, 1972.

Alexander, M.J., 1992: A mechanism for the Venus thermospheric superrotation. *Geophys. Res. Lett.*, **19**, 2207–2210.

Andrews, D.G., J.R. Holton and C.B. Leovy. *Middle Atmosphere Dynamics.* Academic Press, 1987.

Andrews, D.G. and M.E. McIntyre, 1976: Planetary waves in horizontal and vertical shear: the generalized Eliassen-Palm relation and the mean zonal acceleration. *J. Atmos. Sci.*, **33**, 2031–2048.

Baker, N.L. and C.B. Leovy, 1987: Zonal winds near Venus' cloud top level: a model study of the interaction between the zonal mean circulation and the semidiurnal tide. *Icarus*, **69**, 202–220.

Barat, J., 1982: Some characteristics of clear-air turbulence in the middle stratosphere. *J. Atmos. Sci.*, **39**, 2553–2564.

Barat, J. and F. Bertin, 1984: Simultaneous measurements of temperature and velocity fluctuations within clear air turbulence layers: analysis of the estimate of dissipation rate by remote sensing techniques. *J. Atmos. Sci.*, **41**, 1613–1619.

Beatty, T.J., C.A. Hostetler and C.S. Gardner, 1992: Lidar observations of gravity waves and their spectra near the mesopause and stratopause at Arecibo. *J. Atmos. Sci.*, **49**, 477–496.

Belton, M.J.S., P.J. Gierasch, M.D. Smith, P. Helfenstein, P.J. Schinder, J.B. Pollack, K.A. Rages, A.P. Ingersoll, K.P. Klaasen, J. Veverka, C.D. Anger, M.H. Carr, C.R. Chapman, M.E. Davies, F.P. Fanale, R. Greeley, R. Greenberg, J.W. Head

III, D. Morrison, G. Neukum and C.B. Pilcher, 1991: Images from Galileo of the Venus cloud deck. *Science*, **253**, 1531–1536.

Belton, M.J.S., G.R. Smith, G.S. Schubert and A.D. Del Genio, 1976: Cloud patterns, waves and convection in the Venus atmosphere. *J. Atmos. Sci.*, **33**, 1394–1417.

Blamont, J.E., R.E. Young, A. Seiff, B. Ragent, R. Sagdeev, V.M. Linkin, V.V. Kerzhanovich, A.P. Ingersoll, D. Crisp, L.S. Elson, R.A. Preston, G.S. Golitsyn and V.N. Ivanov, 1986: Implications of the VEGA balloon results for Venus atmospheric dynamics. *Science*, **231**, 1422-1425.

Booker, J.R. and F.P. Bretherton, 1967: The critical layer for internal gravity waves in a shear flow. *J. Fluid. Mech.*, **27**, 513–539.

Born, M. and E. Wolf. *Principles of Optics.* Pergamon Press, 1980.

Chang, C.P., 1976: Forcing of stratospheric Kelvin waves by tropospheric heat sources. *J. Atmos. Sci.*, **33**, 740–744.

Crisp, D., 1989: Radiative forcing of the Venus mesosphere, II. Thermal fluxes, cooling rates, and radiative equilibrium temperature. *Icarus*, **77**, 391–413.

Deardorff, J.W., G.E. Willis and D.K. Lilly, 1969: Laboratory investigation of non-steady penetrative convection. *J. Fluid. Mech.*, **35**, 7–31.

Del Genio, A.D. and W.B. Rossow, 1990: Planetary-scale waves and the cyclic nature of cloud top dynamics on Venus. *J. Atmos. Sci.*, **47**, 293–318.

Del Genio, A.D., W. Zhou and T.P. Eichler, 1993: Equatorial superrotation in a slowly rotating GCM: implications for Titan and Venus. *Icarus*, **101**, 1–17.

Dewan, E.M. and R.E. Good, 1986: Saturation and the "universal" spectrum for vertical profiles of horizontal scalar winds in the atmosphere. *J. Geophys. Res.*,

91, 2742–2748.

Dunkerton, T.J. and D.C. Fritts, 1984: Transient gravity wave–critical layer interaction. Part I: convective adjustment and the mean zonal acceleration. *J. Atmos. Sci.*, **41**, 992–1007.

Endlich, R.M. and R.C. Singleton, 1969: Spectral analysis of detailed vertical wind speed profiles. *J. Atmos. Sci.*, **26**, 1030–1041.

Essen, L. and K.D. Froome, 1951: The refractive indices and dielectric constants of air and its principal constituents at 24,000 Mc/s. *Proc. Roy. Soc. London, Ser. B*, **64**, 862–875.

Fels, S. and R.S. Lindzen, 1974: The interaction of thermally excited gravity waves with mean flows. *Geophys. Fluid Dyn.*, **6**, 149–192.

Fjeldbo, G., A. Kliore and V.R. Eshleman, 1971: The neutral atmosphere of Venus as studied with the Mariner V radio occultation experiments. *Astron. J.*, **76**, 123–140.

Fovell, R., D. Durran and J.R. Holton, 1992: Numerical simulations of convectively generated stratospheric gravity waves. *J. Atmos. Sci.*, **49**, 1427–1442.

Fritts, D.C., M.A. Geller, B.B. Balsley, M.L. Chanin, I. Hirota, J.R. Holton, S. Kato, R.S. Lindzen, M.R. Schoeberl, R.A. Vincent and R.F. Woodman, 1983: Research status and recommendations from the Alaska workshop on gravity waves and turbulence in the middle atmosphere, Fairbanks, Alaska, 18–22 July 1983. *Bull. Am. Meteor. Soc.*, **65**, 149–159.

Geller, M.A., H. Tanaka and D.C. Fritts, 1975: Production of turbulence in the vicinity of critical levels for internal gravity waves. *J. Atmos. Sci.*, **32**, 2125–2135.

Goldreich, P. and P. Kumar, 1990: Wave generation by turbulent convection. *Astrophys. J.*, **363**, 694–704.

Gossard, E. and W. Munk, 1954: On gravity waves in the atmosphere. *J. Meteor.*, **11**, 259–269.

Grimshaw, R., 1974: Internal gravity waves in a slowly varying dissipative medium. *Geophys. Fluid Dyn.*, **6**, 131–148.

Hauf, T. and T.L. Clark, 1989: Three-dimensional numerical experiments on convectively forced internal gravity waves. *Quart. J. Roy. Meteorol. Soc.*, **115**, 309–333.

Haugstad, B.S., 1979: Turbulence in planetary occultations, IV: power spectra of phase and intensity fluctuations. *Icarus*, **37**, 322-335.

Held, I.M. and A.Y. Hou, 1980: Nonlinear axially symmetric circulations in a nearly inviscid atmosphere. *J. Atmos. Sci.*, **37**, 515–533.

Hide, R., 1969: Dynamics of the atmospheres of the major planets. *J. Atmos. Sci.*, **26**, 841–847.

Hide, R., 1970: Equatorial jets in planetary atmospheres. *Nature*, **225**, 254–255.

Hines, C.O., 1991: The saturation of gravity waves in the middle atmosphere. Part I: Critique of linear-instability theory. *J. Atmos. Sci.*, **48**, 1348–1359.

Hines, C.O. and C.A. Reddy, 1967: On the propagation of atmospheric gravity waves through regions of wind shear. *J. Geophys. Res.*, **72**, 1015–1034.

Hodges, R.R. Jr., 1967: Generation of turbulence in the upper atmosphere by internal gravity waves. *J. Geophys. Res.*, **72**, 3455–3458.

Holton, J.R., 1982: The role of gravity wave induced drag and diffusion in the momentum budget of the mesosphere. *J. Atmos. Sci.*, **39**, 791–799.

Holton, J.R., 1983: The influence of gravity wave breaking on the general circulation of the middle atmosphere. *J. Atmos. Sci.*, **40**, 2497–2507.

Holton, J.R. and R.S. Lindzen, 1972: An updated theory for the quasi-biennial cycle of the tropical stratosphere. *J. Atmos. Sci.*, **29**, 1076–1080.

Hou, A.Y. and B.F. Farrell, 1987: Superrotation induced by critical-level absorption of gravity waves on Venus: an assessment. *J. Atmos. Sci.*, **44**, 1049–1061.

Hou, A.Y. and R.M. Goody, 1985: Diagnostic requirements for the superrotation on Venus. *J. Atmos. Sci.*, **42**, 413–432.

Houghton, J.T., *The Physics of Atmospheres, second edition*, p. 5, Cambridge University Press, 1986.

Hubbard, W.B., B. Sicardy and R. Miles, 1993: The occultation of 28-Sgr by Titan. *Astron. Astrophys.*, **269**, 541–563.

Ingersoll, A.P., D. Crisp, A.W. Grossman and the VEGA balloon science team, 1987: Estimates of convective heat fluxes and gravity wave amplitudes in the Venus middle cloud layer from VEGA balloon measurements. *Adv. Sp. Res.*, **7**, (12)343–(12)349.

Ishimaru, A., 1973: A new approach to the problem of wave fluctuations in localized smoothly varying turbulence. *IEEE Trans. Antennas Propagat.*, AP-**21**, 47–53.

Ishimaru, A. *Wave Propagation and Scattering in Random Media, v.1. Single scattering and Transport Theory.* Academic Press, 1978.

Kalnay-Rivas, E., 1975: Further numerical calculations of the circulation of the atmosphere of Venus. *J. Atmos. Sci.*, **32**, 1017–1024.

Kerzhanovich, V.V., M.Ya. Marov and M.K. Rozhdestvensky, 1972: Data on dynamics of the subcloud Venus atmosphere from Venera spaceprobe measurements. *Icarus*, **17**, 659–674.

Kliore, A.J. and I.R. Patel, 1980: Vertical structure of the atmosphere of Venus from Pioneer Venus orbiter radio occultations. *J. Geophys. Res.*, **85**, 7957–7962.

Landau, L.D. and E.M. Lifshitz. *Fluid Mechanics, 2nd edition.* Pergamon Press, 1987.

Leovy, C.B., 1964: Simple models of thermally driven mesospheric circulation. *J. Atmos. Sci.*, **21**, 327–341.

Leovy, C.B., 1987: Zonal winds near Venus' cloud top level: an analytic model of the equatorial wind speed. *Icarus*, **69**, 193–201.

Limaye, S.S. and V.E. Suomi, 1981: Cloud motions on Venus: global structure and organization. *J. Atmos. Sci.*, **38**, 1220–1235.

Lindzen, R.S., 1981: Turbulence and stress owing to gravity wave and Tidal Breakdown. *J. Geophys. Res.*, **86**, 9707–9714.

Lindzen, R.S. and J. Forbes, 1983: Turbulence originating from convectively stable internal waves. *J. Geophys. Res.*, **88**, 6549–6553.

Marov, M.Ya., 1978: Results of Venus missions. *Ann. Rev. Astron. Astrophys.*, **16**, 141–169.

Marov, M.Ya., V.S. Avduevsky, V.V. Kerzhanovich, M.K. Rozhdestvensky, N.F. Borodin and O.L. Ryabov, 1973: Venera 8: Measurements of temperature, pressure, and wind velocity on the illuminated side of Venus. *J. Atmos. Sci.*, **30**, 1210–1214.

Morse, P.M. and H. Feshbach. *Methods of Theoretical Physics, v.1..* McGraw-Hill, 1953.

Murray, B.C., M.J.S. Belton, G.E. Danielson, M.E. Davies, D. Gault, B. Hapke, B. O'Leary, R.G. Strom, V. Suomi and N. Trask, 1974: Venus: atmospheric motion and structure from Mariner 10 pictures. *Science*, **183**, 1307–1314.

Narayan, R. and W.B. Hubbard, 1988: Theory of anisotropic refractive scintillation: application to stellar occultations by Neptune. *Astrophys. J.*, **325**, 503–518.

Ogura, Y. and N.A. Phillips, 1962: Scale analysis of deep and shallow convection in the atmosphere. *J. Atmos. Sci.*, **19**, 173–179.

Pechmann, J.B. (1983). *Thermal tides in the atmosphere of Venus* Ph.D. Thesis, California Inst. of Tech., Pasadena, CA.

Pechmann, J.B. and A.P. Ingersoll, 1984: Thermal tides in the atmosphere of Venus—comparison of model results with observations. *J. Atmos. Sci.*, **41**, 3290–3313.

Plumb, R.A., 1977: The interaction of two internal waves with the mean flow: implications for the theory of the quasi-biennial oscillation. *J. Atmos. Sci.*, **34**, 1847–1858.

Reid, I.M. and R.A. Vincent, 1987: Measurements of mesospheric gravity wave momentum fluxes and mean flow accelerations at Adelaide, Australia. *J. Atmos. Ter. Phys.*, **49**, 443–460.

Rossow, W.B., A.D. Del Genio, S.S. Limaye and L.D. Travis, 1980: Cloud morphology and motions from Pioneer Venus images. *J. Geophys. Res.*, **85**, 8107–8128.

Rossow, W.B. and G.P. Williams, 1979: Large-scale motion in the Venus stratosphere. *J. Atmos. Sci.*, **36**, 377–389.

Sagdeev, R.Z., V.M. Linkin, V.V. Kerzhanovich, A.N. Lipatov, A.A. Shurupov, J.E. Blamont, D. Crisp, A.P. Ingersoll, L.S. Elson, R.A. Preston, C.E. Hildebrand,

B. Ragent, A. Seiff, R.E. Young, G. Petit, L. Boloh, Yu.N. Alexandrov, N.A. Armand, R.V. Bakitko and A.S. Selivanov, 1986: Overview of VEGA Venus balloon in situ meteorological measurements. *Science*, **231**, 1411–1414.

Sato, T. and R.F. Woodman, 1982: Fine altitude resolution observations of stratospheric turbulent layers by the Arecibo 430 MHz radar. *J. Atmos. Sci.*, **39**, 2546–2552.

Schinder, P.J., P.J. Gierasch, S.S. Leroy and M.D. Smith, 1990: Waves, advection, and cloud patterns on Venus. *J. Atmos. Sci.*, **47**, 2037–2052.

Schubert, G., 1983: General circulation and the dynamical state of the Venus atmosphere. *Venus*, D.M. Hunten, L. Colin, T.M. Donahue and V.I. Moroz, Eds., University of Arizona Press, 681–765.

Schubert, G. and R.L. Walterscheid, 1984: Propagation of small-scale acoustic-gravity waves in the Venus atmosphere. *J. Atmos. Sci.*, **41**, 1202–1213.

Schwarzschild, M. *Structure and evolution of the stars.* Princeton University Press, 1958.

Seiff, A., D.B. Kirk, R.E. Young, R.C. Blanchard, J.T. Findlay, G.M. Kelly and S.C. Sommer, 1980: Measurements of thermal structure and thermal contrasts in the atmosphere of Venus and related dynamical observations: results from the four Pioneer Venus probes. *J. Geophys. Res.*, **85**, 7903–7933.

Shah, K.P. (1992). *Interferometric observations of the J(0,1) CO line on Venus: upper mesospheric winds and CO abundance* Ph.D. Thesis, California Inst. of Tech., Pasadena, CA.

Smith, S.A., D.C. Fritts and T.E. VanZandt, 1987: Evidence for a saturated spectrum of atmospheric gravity-waves. *J. Atmos. Sci.*, **44**, 1404–1410.

Stull, R.B., 1976: Internal gravity waves generated by penetrative convection. *J. Atmos. Sci.*, **33**, 1279–1286.

Tatarskii, V.I. *Wave Propagation in a Turbulent Medium.* McGraw Hill, 1961.

Taylor, F.W., J.T. Schofield and S.P. Bradley, 1981: Pioneer Venus atmospheric observations. *Phil. Trans. Roy. Soc. London*, **303**, 215–223.

Timofeeva, T.S., O.I. Yakovlev and A.I. Efimov, 1978: Radio wave fluctuation and turbulence of the nighttime Venusian atmosphere from radioscopy data of the space probe Venera 9. *Cosmic Res. (USSR)*, **16**, 285–293.

Tomasko, M.G., L.R. Doose, P.H. Smith and A.P. Odell, 1980: Measurements of the flux of sunlight in the atmosphere of Venus. *J. Geophys. Res.*, **85**, 8167–8186.

Tsuda, T., Y. Murayama, M. Yamamoto, S. Kato and S. Fukao, 1990: Seasonal variation of momentum flux in the mesosphere observed with MU radar. *Geophys. Res. Lett.*, **17**, 725–728.

VanZandt, T.E., 1982: A universal spectrum of buoyancy waves in the atmosphere. *Geophys. Res. Lett.*, **9**, 575–578.

Vinnichenko, N.K. and J.A. Dutton, 1969: Empirical studies of atmospheric structure and spectra in the free atmosphere. *Radio Science*, **4**, 1115–1126.

Wallace, J.M. and V.E. Kousky, 1968: Observational evidence of Kelvin waves in the tropical stratosphere. *J. Atmos. Sci.*, **25**, 900–907.

Weinstock, J., 1976: Nonlinear theory of acoustic-gravity waves 1. Saturation and enhanced diffusion. *J. Geophys. Res.*, **81**, 633–652.

Winters, K.B. and E.A. D'Asaro, 1989: Two-dimensional instability of finite amplitude internal gravity wave packets near a critical level. *J. Geophys. Res.*, **94**, 12709–12719.

Woo, R., 1975: Observations of turbulence in the atmosphere of Venus using Mariner 10 radio occultation measurements. *J. Atmos. Sci.*, **32**, 1084–1090.

Woo, R. and J.W. Armstrong, 1980: Radio occultation measurements of turbulence in the Venus atmosphere by Pioneer Venus. *J. Geophys. Res.*, **85**, 8031–8038.

Woo, R. and A. Ishimaru, 1973: Remote sensing of the turbulence characteristics of a planetary atmosphere by radio occultation of a space probe. *Radio Science*, **8**, 103–108.

Woo, R. and A. Ishimaru, 1981: Eddy diffusion coefficient for the atmosphere of Venus from radio scintillation measurements. *Nature*, **289**, 383–384.

Woo, R., A. Ishimaru and W.B. Kendall, 1974: Observations of small scale turbulence in the atmosphere of Venus by Mariner 5. *J. Atmos. Sci.*, **31**, 1698–1706.

Yanai, M. and T. Maruyama, 1966: Stratospheric wave disturbances propagating over the equatorial Pacific. *J. Met. Soc. Japan*, **44**, 291–294.

Young, A.T., 1975: Is the four-day "rotation" of Venus illusory?. *Icarus*, **24**, 1–10.

Young, A.T., 1976: Scintillations during occultations by planets: I. An approximate theory. *Icarus*, **27**, 335–357.

Young, R.E. and J.B. Pollack, 1977: A three-dimensional model of dynamical processes in the Venus atmosphere. *J. Atmos. Sci.*, **34**, 1315–1351.

Young, R.E., R.L. Walterscheid, G. Schubert, A. Seiff, V.M. Linkin and A.N. Lipatov, 1987: Characteristics of gravity waves generated by surface topography on Venus: comparison with the VEGA balloon results. *J. Atmos. Sci.*, **44**, 2628–2639.

APPENDIX A

Tabulating the function $h(z)$

In this appendix we lay out the explicit formulation for the function $h(z)$. We have already shown that in general a variety of types of waves exists when in the presence of strong zonal wind shear and static stability varying in altitude. For each type of wave, we intend to show how the amplitude can be computed as a function of height everywhere above the convection. Because waves encounter regions where they propagate and regions where they cannot propagate, we must determine how to connect these different types of wave behavior. Connecting regions of propagation to regions of nonpropagation requires *connection formulas.* Thus, this appendix uses connection formulas to show how $h(z)$ is computed.

We review the general solution to the homogeneous wave equation $\mathcal{L}h=0$ for regions of propagation and regions of nonpropagation. For regions of propagation, the square of the vertical wavenumber is greater than zero and

$$h(z) \simeq \tilde{\omega}\sqrt{\frac{q|m|}{\bar{\rho}}}\left(c_1e^{iq} + c_2e^{-iq}\right). \tag{A1a}$$

For regions of nonpropagation, the square of the vertical wavenumber is less than zero and

$$h(z) \simeq \tilde{\omega}\sqrt{\frac{q|m|}{\bar{\rho}}}\left(c_3e^{q} + c_4e^{-q}\right). \tag{A1b}$$

We note that the dispersion relation m^2 and the phase q are defined by equations 2.13 and 2.15 of the first paper.

The importance of both of these solutions is apparent in figure 1 of the first paper. We know that a propagating wave must have $c_2=0$ in its solution in the region of propagation above the lowermost turning point. Many propagating waves, though, exhibit a region of nonpropagation between the convection and the turning point. Before propagating waves can reach the region of propagation, they must somehow penetrate through this region of nonpropagation which we call the barrier. This same barrier also forms above the convection for trapped waves. For trapped waves, a region of propagation lies between turning points 1 and 2. Between turning points 2 and 3 another region of nonpropagation forms. We call this the upper lid. We must describe each region of propagation by specifying c_1 and c_2, and we must describe each region of nonpropagation by specifying c_3 and c_4. Sets of coefficients c_1, c_2, c_3, c_4 are associated with each turning point for a given wavemode. Because of uniqueness, there are relationships between the sets of coefficients for a given wavemode. In addition, since the equation which $h(z)$ solves is a second order partial differential equation, only two coefficients are necessary and thus we can find c_1, c_2 in terms of c_3, c_4 and vice versa for each turning point.

We find the relationship between the sets of coefficients by modeling the behavior of the solution between regions of propagation and regions of nonpropagation. We do this in much the same manner as has been done for the Schroedinger equation. The major difference between finding connection formulas for the Schroedinger equation and those for gravity waves is that the zero of the vertical wavenumber occurs in the numerator of the undifferentiated term for the Schroedinger equation versus in the denominator of the differentiated term for gravity waves. This difference leads to slightly different solutions.

In finding the connection formulas, we assume that m^2 is continuous, approximate $m^2 = a^3 z$ and account for the $\tilde{\omega}$ and $\bar{\rho}$ dependence with a factor $\tilde{\omega}/\sqrt{\bar{\rho}}$. The remaining equation is

$$\frac{\partial}{\partial z}\left(\frac{1}{m^2}\frac{\partial}{\partial z}\left(\frac{\sqrt{\bar{\rho}}}{\tilde{\omega}}h\right)\right) + \frac{\sqrt{\bar{\rho}}}{\tilde{\omega}}h = 0. \tag{A2}$$

The solution to this equation is

$$\frac{\sqrt{\bar{\rho}}}{\tilde{\omega}}h' = \left(\tfrac{2}{3}a^3\right)^{1/2} z \begin{cases} A J_{2/3}(\frac{2}{3}(az)^{3/2}) + B J_{-2/3}(\frac{2}{3}(az)^{3/2}) & \text{for } z>0,\ m^2>0 \\ A I_{2/3}(\frac{2}{3}|az|^{3/2}) + B I_{-2/3}(\frac{2}{3}|az|^{3/2}) & \text{for } z<0,\ m^2<0. \end{cases} \tag{A3}$$

The functions $J_{2/3}$ and $J_{-2/3}$ are Bessel functions of the 2/3 order. The functions $I_{2/3}$ and $I_{-2/3}$ are modified Bessel functions of the 2/3 order. The coefficients A, B are general. The phase q is defined from $z=0$ so that $q=(2/3)\,|az|^{3/2}$.

In order to verify our approximation that the background density can be considered as constant near a turning point, we perform a numerical integration of the homogeneous internal gravity wave equation. We keep $\tilde{\omega}$ constant but define the background density as a $\bar{\rho} \equiv 1-(z/H)$. After nondimensionalizing the homogeneous portion of equation 2.3 of the first paper, we are left with only one nondimensional number, namely aH where a is defined above. In figure 1 we show a comparison between a numerical integration of the wave equation and our approximate connection formulas. In computing the numerical solutions, we use the approximate solution for the initial condition at $az=-1$. We show the functions $J_{2/3}$, $J_{-2/3}$, and their derivatives. The approximate derivatives are calculated using the rules proscribed in appendix B. We set $aH=10$, which is typical for turning points just above the convection. Clearly, the derivative of the approximate solution compares well with the numerical integration. The only approximate function which deviates slightly from the corresponding numerical integration is that for $J_{-2/3}$. Despite this slight deviation, it does not cause any significant error in the derivative of the solution. We use this comparison to justify neglecting terms of order $1/H^2$ in the dispersion relation 2.13 of the first paper, which may have otherwise seemed invalid when near turning points.

We wish to find out how equation A3 relates to the usual WKBJ solutions. To do so, we examine the asymptotic expansions of the Bessel functions (asymptotic expansions to these Bessel functions can be found in Abramowitz and Stegun, p. 365 and pp. 377-378). We require a solution proportional to $\sqrt{m}$ in the far field and substitute $m^2=a^3z$. We find that

$$h(z)=\tilde{\omega}\sqrt{\frac{m}{\bar{\rho}}}\left(A\cos(q-\frac{7\pi}{12})+B\cos(q+\frac{\pi}{12})\right) \tag{A4}$$

in the asymptotic expansion. Therefore, for some substantial value of the phase q from

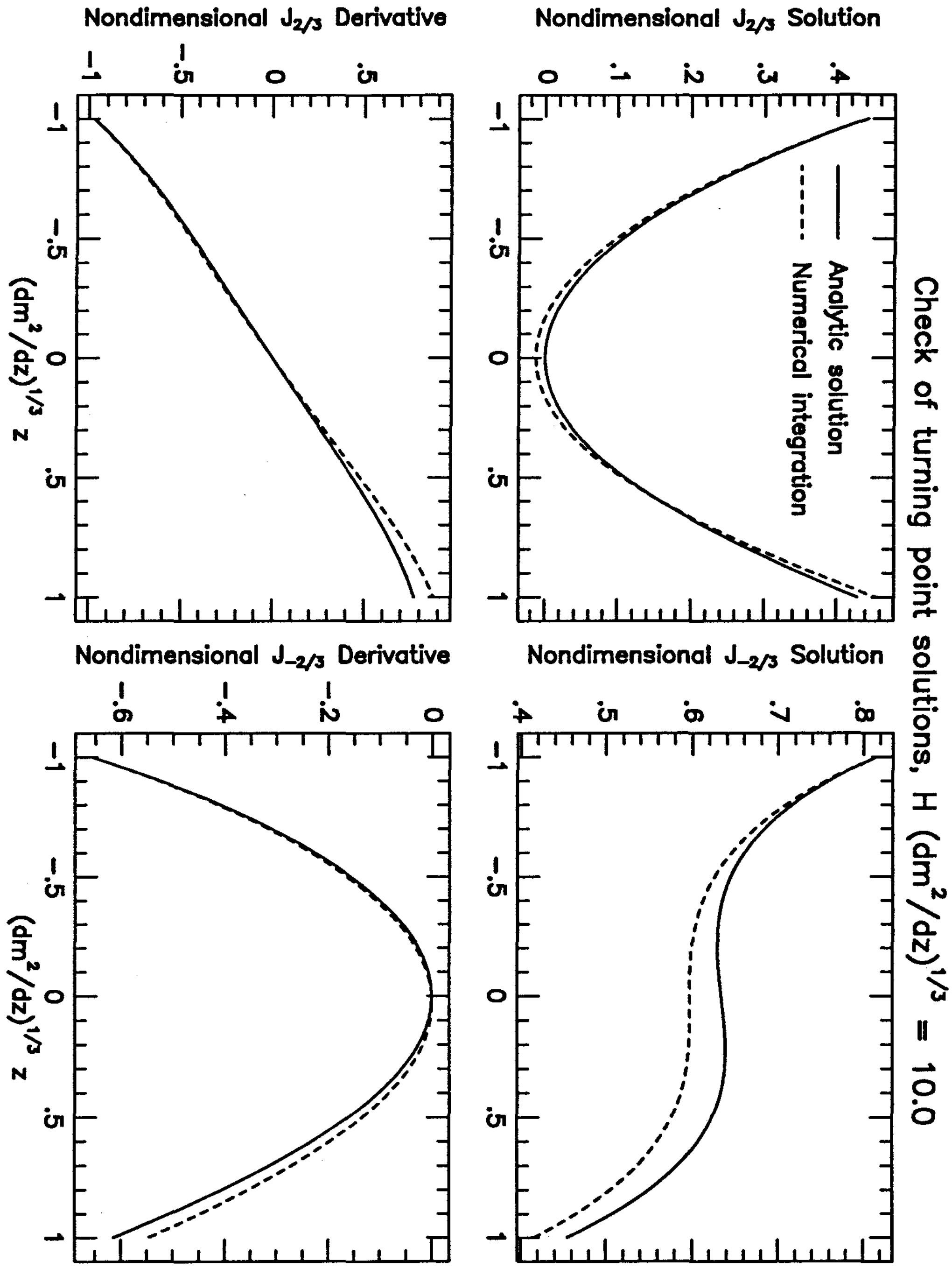

Figure 1. Turning point solution. In this figure we compare a numerical integration of the homogeneous internal gravity wave equation with the solutions used in connection formulas near a turning point. The derivatives are calculated as described in appendix B.

a turning point, the connection formulas accurately reproduce the general WKBJ solutions. With some algebra, one can find the relationship between A, B and c_1, c_2. This relationship is

$$\begin{aligned} c_1 &= \frac{1}{\sqrt{2\pi}}(A\exp(-7\pi i/12) + B\exp(\pi i/12)) \\ c_2 &= \frac{1}{\sqrt{2\pi}}(A\exp(7\pi i/12) + B\exp(-\pi i/12)) \end{aligned} \tag{A5}$$

in which q is positive and defined from the turning point ($m^2 = 0$).

In comparing the solution for $m^2 < 0$ to the solution in the WKBJ approximation, we notice that even though the asymptotic form for both $I_{2/3}(q)$ and $I_{-2/3}(q)$ is a growing exponential, the asymptotic form for $I_{2/3}(q) - I_{-2/3}(q)$ is a decaying exponential. For this reason we find the asymptotic form of the general solution for $m^2 < 0$ to be

$$h(z) = \tilde{\omega}\sqrt{\frac{|m|}{2\pi\bar{\rho}}}\Big((A+B)e^{q} - \frac{\sqrt{3}}{2}(A-B)e^{-q}\Big). \tag{A6}$$

Like the solution for $m^2 > 0$, the asymptotic form of the connection formula for $m^2 < 0$ matches the WKBJ approximate solution in character for sufficiently large q. This enables us to relate A, B and c_3, c_4:

$$\begin{aligned} c_3 &= \frac{1}{\sqrt{2\pi}}(A + B) \\ c_4 &= -\sqrt{\frac{3}{8\pi}}(A - B). \end{aligned} \tag{A7}$$

Eliminating A, B from equations A5 and A7 gives the following relationships between c_1, c_2 and c_3, c_4:

$$\begin{aligned} c_1 &= \exp(-\pi i/4)\,(\frac{1}{2}c_3 + ic_4) \\ c_2 &= \exp(\pi i/4)\,(\frac{1}{2}c_3 - ic_4) \end{aligned} \tag{A8}$$

and the inverse

$$\begin{aligned} c_3 &= c_1\exp(\pi i/4) + c_2\exp(-\pi i/4) \\ c_4 &= -\frac{i}{2}(c_1\exp(\pi i/4) - c_2\exp(-\pi i/4)). \end{aligned} \tag{A9}$$

Thus we have computed how c_1, c_2 are related to c_3, c_4 across a turning point.

We note that a set of coefficients A, B, c_1, c_2, c_3, c_4 is anchored to a particular turning point and the phase is measured from that turning point. A difficulty then arises for trapped waves because more than one turning point then exists. Given a set of coefficients tied with the third turning point in figure 1(b), we need to know what the coefficient sets are for the lower two turning points. This is done by way of transformations.

We derive a transformation across a region of nonpropagation so that we can relate the c_3, c_4 pair associated with the second turning point for trapped waves to the c_3, c_4 pair associated with the third turning point. We define q_2 to be the phase measured into the lid from the second turning point and q_3 to be the phase measured into the lid from the third turning point. We note that $q_2 + q_3 = Q_l$ where Q_l is the thickness of the lid defined by equation 2.21c of the first paper. We find the relationship between the coefficient pairs by matching the the general WKBJ solutions defined from each turning point. The equality is

$$\tilde{\omega}\sqrt{\frac{m}{\bar{\rho}}}\,(c_3^{(2)}e^{q_2} + c_4^{(2)}e^{-q_2}) \simeq \tilde{\omega}\sqrt{\frac{m}{\bar{\rho}}}\,(c_3^{(3)}e^{q_3} + c_4^{(3)}e^{-q_3}). \tag{A10}$$

We solve for c_3, c_4 in terms of c_1, c_2:

$$\begin{aligned} c_3^{(2)} &= c_4^{(3)}\ \exp(-Q_l) \\ c_4^{(2)} &= c_3^{(3)}\ \exp(Q_l). \end{aligned} \tag{A11}$$

The coefficients $c_3^{(3)}, c_4^{(3)}$ are associated with the third turning point and the coefficients $c_3^{(2)}, c_4^{(2)}$ are associated with the second turning point. This formula will prove helpful for finding the function $h(z)$ for trapped waves.

Next we derive a transformation across a region of propagation so that we may relate the coefficient sets of the second turning point to the coefficient sets of the first turning point. We define q_1 measured away from the first turning point. Notice that $q_1 + q_2 = Q_d$ where Q_d is the total phase in the duct defined by equation 2.21b. By a similar procedure we show that

$$\begin{aligned} c_1^{(1)} &= c_2^{(2)} \exp(-iQ_d) \\ c_2^{(1)} &= c_1^{(2)} \exp(iQ_d). \end{aligned} \tag{A12}$$

This, too, will be helpful in finding $h(z)$ for trapped waves. We now have the tools necessary to properly evaluate $h(z)$ everywhere above the convection.

For propagating waves, including those absorbed into critical layers, the upper boundary condition is simple. To satisfy the radiation to space boundary condition, we set $c_1^{(1)} = \exp(-\pi i/4)$ and $c_2^{(1)} = 0$. This makes the general WKBJ solution for propagating waves

$$h(z) \simeq \tilde{\omega}\sqrt{\frac{m}{\rho}}\, e^{i(q-\pi/4)} \tag{A13a}$$

above the turning point. Below the turning point, we do not know whether the asymptotic expansion holds, so we just write

$$h(z) \simeq \tilde{\omega}\sqrt{\frac{2\pi|m|q_1}{3\bar{\rho}}}\, \left(\exp(\pi i/6)\, I_{2/3}(q_1) + \exp(-\pi i/6)\, I_{-2/3}(q_1)\right) \tag{A13b}$$

for propagating waves.

The function $h(z)$ is more complicated for trapped waves. The coefficients associated with the first turning point are dependent on the duct phase Q_d and the lid thickness Q_l. We first assume that the upper lid is thick, i.e., $Q_l \gg 1$. In this case we expect $h(z)$ to exponentially decay with height within the lid so that the upper boundary condition is satisfied. Thus we set $c_3^{(2)} = 0$ and $c_4^{(2)} = -1/2$. This makes the solution within the duct

$$h(z) = \tilde{\omega}\sqrt{\frac{m}{\bar{\rho}}}\, \sin(q_2 - \pi/4).$$

We can then use the transformation of equation A12 to find the coefficients c_1, c_2 associated with the first turning point. It turns out that

$$h(z) \simeq \tilde{\omega}\sqrt{\frac{2\pi|m|q_1}{3\bar{\rho}}}\, \left(-\sin(Q_d + \pi/3)\, I_{2/3}(q_1) + \sin(Q_d - \pi/3)\, I_{-2/3}(q_1)\right) \tag{A14}$$

below the first turning point. We have also used the relation of equation A9.

The function $h(z)$ is most complex for a wave trapped beneath a thin upper lid. In this case, the upper boundary condition becomes the radiation condition above the third turning point. Thus, we set

$$\begin{aligned} c_2^{(3)} &= 0 \\ c_1^{(3)} &= (1/2)\, e^{-Q_l}\, e^{-\pi i/4}. \end{aligned} \tag{A15}$$

We carry out the transformation of equation A11 and use equation A8 to find that the c_1, c_2 pair for the second turning point are

$$\begin{aligned} c_1^{(2)} &= \frac{i}{2} \exp(-\pi i/4)\, (1 - \frac{1}{4} e^{-2Q_l}) \\ c_2^{(2)} &= -\frac{i}{2} \exp(\pi i/4)\, (1 + \frac{1}{4} e^{-2Q_l}). \end{aligned} \tag{A16}$$

We wish to bring out two points about this c_1, c_2 pair. Firstly, it approaches the $c_1^{(2)}, c_2^{(2)}$ pair for waves trapped beneath a thick lid as $Q_l \rightarrow \infty$. Secondly, the upward and downward propagating waves carry slightly different amounts of energy. Appropriately, the upward propagating wave carries a little more energy (recall that the phase is measured downward away from the second turning point into the duct). To find the coefficients associated with the first turning point, one only needs to carry out the transformation of equation A12.

We note in passing that we have implicitly assumed that $Q_l \gg 1$ in deriving $h(z)$ for waves trapped beneath a thin upper lid. In fact, this is inappropriate by definition of a thin upper lid. Nevertheless, we assume that this adequately describes the behavior of the thin upper lid case. A problem does arise, though, as $Q_l \rightarrow 0$. In this case, the downward propagating wave still exists. This gives rise to a spectral discontinuity of the gravity wave response to forcing. We discuss this in the main text.

In general, the most consequential waves will have $q_b = 0$. For these cases, no barrier will be present between the neutral layer and the stable layer. Even though at no point does $m^2=0$, we nevertheless associate a set of coefficients with the point at which N^2 is discontinuous. Furthermore, regardless of the value of q away from this turning point, we always use the asymptotic form of the solution. Thus, we have defined $h(z)$ to be $\tilde{\omega}\sqrt{m/\bar{\rho}}\,\exp[i(q-\pi/4)]$ above the convecting layer for propagating waves with $q_b=0$.

APPENDIX B

The derivative of $h(z)$

In this appendix we investigate the derivative of the homogeneous solution to $\mathcal{L}h = 0$. It was mentioned in the text that simply taking a finite difference of $h(z)$ is incorrect because it would introduce third order terms. We instead wish to find a correct second order WKBJ solution for $\partial h/\partial z$.

We start by taking the derivative of $\mathcal{L}h$ with respect to z after multiplying it by $\tilde{\omega}^2/\bar{\rho}$. After defining $\eta \equiv \bar{\rho}/(N^2 - \tilde{\omega}^2)\ \partial h/\partial z$, we get

$$\frac{\partial}{\partial z}\Big(\frac{\tilde{\omega}^2}{\bar{\rho}}\frac{\partial \eta}{\partial z}\Big) + \frac{(N^2 - \tilde{\omega}^2)k^2}{\bar{\rho}}\,\eta = 0. \tag{B1}$$

The solution for h is given in appendix A by equation A3. The asymptotic expansion of this solution gave exactly the general WKBJ solutions (equations A4 through A6). In the same spirit, we find the connection formulas for η and in solving for $\partial h/\partial z$ we get

$$\frac{\partial h}{\partial z} = \tilde{\omega}\sqrt{\frac{q|m|}{\bar{\rho}}}\begin{cases} CJ_{1/3}(q) + DJ_{-1/3}(q) & \text{for } m^2 > 0, \text{ and} \\ CI_{1/3}(q) + DI_{-1/3}(q) & \text{for } m^2 < 0. \end{cases} \tag{B2}$$

This is the correct second order WKBJ solution for the derivative of $h(z)$ with respect to height.

Near a turning point, an explicit derivative of equation A3 agrees with the derivative in equation B2 above provided that the coefficient $\tilde{\omega}/\sqrt{\bar{\rho}}$ is held constant. Near a turning point we can validly approximate $m^2 = a^3 z$ and thus $q = (2/3)\ |az|^{3/2}$. We account for the altitude dependence through the phase q and find that

$$h(z) = (\frac{3}{2}a^3)^{1/6}\,\frac{\tilde{\omega}}{\sqrt{\bar{\rho}}}\,q^{2/3}\begin{cases} AJ_{2/3}(q) + BJ_{-2/3}(q) & \text{for } m^2 > 0, \\ AI_{2/3}(q) + BI_{-2/3}(q) & \text{for } m^2 < 0. \end{cases} \tag{B3}$$

We can take a derivative in z of this expression by recognizing that $dz = dq/m$. The result is

$$\frac{\partial}{\partial z}(h(z)) = \tilde{\omega}\sqrt{\frac{q|m|^3}{\bar{\rho}}}\begin{cases} AJ_{-1/3}(q) - BJ_{1/3}(q) & \text{for } m^2 > 0, \\ AI_{-1/3}(q) - BI_{1/3}(q) & \text{for } m^2 < 0. \end{cases} \tag{B4}$$

We hold $\tilde{\omega}$ and $\bar{\rho}$ constant near the turning point. This solution is the same as the solution of equation B2 when we equate the coefficients A, B to the coefficients C, D.

With some simple algebra, we find that

$$\begin{aligned} C &= -|m|B \\ D &= |m|A. \end{aligned} \tag{B5}$$

Thus, in order to properly take the derivative of $h(z)$ near a turning point, we must hold the leading coefficient $\tilde{\omega}/\sqrt{\bar{\rho}}$ constant while finite differencing $h(z)$. In the end, this is is the correction to the WKBJ approximation required when near a turning point.

Finally, we note that our rule for taking derivatives of $h(z)$ holds even when far from a turning point. We show this by comparing the derivative of the asymptotic solution for $h(z)$ to the asymptotic expansion of the derivative solution of equation B2. We implement the relationships between c_1, c_2 and A, B given by equations A5. The asymptotic solution of equation A3 is given by equation A4 for $m^2 > 0$. Its derivative is

$$\frac{\partial h}{\partial z} = -\tilde{\omega}\sqrt{\frac{q|m|}{\bar{\rho}}}\,\left(|m|A\sin(q - \frac{7\pi}{12}) + |m|B\sin(q + \frac{\pi}{12})\right)\,\mathrm{sign}(\frac{dq}{dz}). \tag{B6}$$

We have held the leading coefficient $\tilde{\omega}\sqrt{|m|/\bar{\rho}}$ constant. The asymptotic solution of equation B2 is

$$\frac{\partial h}{\partial z} = \tilde{\omega}\sqrt{\frac{|m|}{\bar{\rho}}}\left(C\cos(q - \frac{5\pi}{12}) + D\cos(q - \frac{\pi}{12})\right)\,\mathrm{sign}(\frac{dq}{dz}) \tag{B7}$$

for $m^2 > 0$ where we have held $\tilde{\omega}\sqrt{|m|/\bar{\rho}}$ constant. This is just the same as the previous equation given the relationships of equations B5. Even though it appears we have broken our rule of only holding $\tilde{\omega}/\sqrt{\bar{\rho}}$ constant, there is no problem because holding an extra factor of m constant is valid under the WKBJ approximation, and by definition the WKBJ approximation is valid when the solution can be given by the asymptotic solutions.

In conclusion, the derivative of the function $h(z)$ is found numerically by finite differencing $h(z)$ holding the leading factor of $\tilde{\omega}/\sqrt{\bar{\rho}}$ constant:

$$\frac{\partial h}{\partial z} = \frac{\tilde{\omega}}{\sqrt{\bar{\rho}}} \frac{\partial}{\partial z}\left(\frac{\sqrt{\bar{\rho}}}{\tilde{\omega}} h(z)\right). \tag{B8}$$

APPENDIX C

Weak Scintillation Theory

We use a method for simulating scintillations which has been used frequently in the past for modeling scintillations under the hypothesis that they are caused by turbulence in the atmosphere. We use the same theory but with some minor details added so that a spectrum of gravity waves can be implemented instead. In this appendix, we start with an expression for the log-amplitude of the scintillation as a function of time and proceed with a derivation of weak scintillation of the log-amplitude spectrum in frequency keeping careful track of how gravity wave modes are sampled.

The theory of radio scintillations in its current form was pioneered by Tatarskii (1961) and the notation we use is that of Ishimaru (1973, 1978). The derivation of the frequency spectrum for log-amplitude scintillations is given in Woo and Ishimaru (1973). Subsequently, improvements involving the effects of the flattening of the Fresnel zone were implemented (Young 1976, Haugstad 1979). We start with equations given in Ishimaru (1978) with corrections due to flattening of the Fresnel zone, explain them briefly, and find the equation for log-amplitude variance spectra in frequency required for our simulations. Whenever we refer to Ishimaru, we are referring to his 1978 book.

In figure 1 we show the geometry of the occultation. We use x' to denote the line-of-sight coordinate along the beam path, y', z' to denote the coordinates transverse to the beam path in the Venus's atmosphere, y_s, z_s to denote the spacecraft coordinates as projected onto a plane perpendicular to the beam path, y, z to denote transverse coordinates at the Earth with the observer at $x = y = 0$, R_1 to denote the distance from the spacecraft to Venus's atmosphere, and R_2 to denote the distance from Venus's atmosphere to the Earth. The position of the spacecraft as it appears in Venus's atmosphere to the observer is given by y_a, z_a in

$$y_a(t) = \frac{y_s(t)R_2 + yR_1}{R_1 + R_2} \tag{C1a}$$

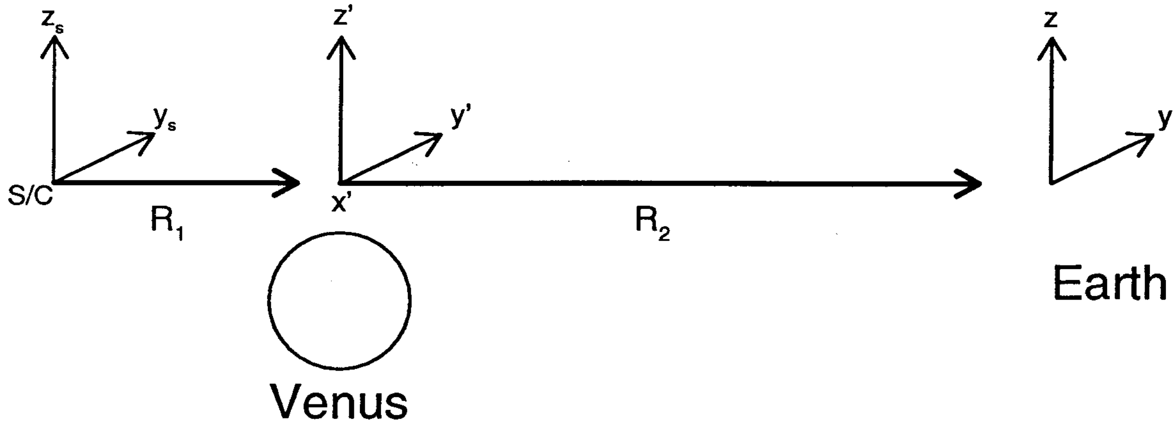

Figure 1. Occultation geometry. The spacecraft position is at "S/C" and the observer position is at "Earth." The coordinates with the subscript "s" describe the spacecraft position, the primed coordinates describe positions in Venus's atmosphere, and the unprimed, unsubscripted coordinates describe the observer's position. The x coordinates represent distance along the beam path.

and

$$z_a(t) = \frac{z_s(t)R_2 + zR_1}{R_1 + R_2} \tag{C1b}$$

(*c.f.* equations 17-27 in Ishimaru).

The expression for the log-amplitude fluctuation as a function of time is given by

$$\chi(t) = k \int dx' \int d\nu(k'_y, m; x')\, e^{i(mz_a + k'_y y_a)} \sin\Big[\frac{R}{2k}(k'^2_y + \frac{m^2}{q^2})\Big] \tag{C2a}$$

where the quantity $d\nu(k'_y, m; x')$ is the Fourier component of the index of refraction fluctuation $n_1(x', y', z')$:

$$n_1(\mathbf{r}') = \int e^{i(mz' + k'_y y')}\, d\nu(k'_y, m; x') \tag{C2b}$$

(*c.f.* equation A-17 in Ishimaru). The index of refraction fluctuation is written this way because we expect it to be a random process. The quantities k'_y and m are the Fourier conjugates to the coordinates y' and z' in Venus's atmosphere. The quantity q^2 is the defocusing factor: the Fresnel zone is flattened by a factor of q^2 in the vertical compared to the horizontal. The distance R is defined by

$$R \equiv \left(\frac{1}{R_1} + \frac{1}{R_2}\right)^{-1} \tag{C2c}$$

and is nearly the same as the spacecraft to planet distance R_1. The quantity k is the free space wavevector of the radio signal.

Equations C.2 describe a Fresnel diffraction pattern of a random process. It is derived under the Rytov approximation, which allows a calculation of the log-amplitude and phase of the radio signal under the approximation that scintillations are weak. It is essentially the same as the Born approximation except that one solves for different quantities. The index of refraction in equation C.2 is written differentially in the space of Venus's atmosphere so that a spatial spectrum of gravity waves can eventually be implemented. The factor sin[...] is referred to as the Fresnel factor. It essentially filters out components of the index of refraction fluctuation spectrum which have spatial scales greater than the radio beam width. Lastly, the integral over x' essentially integrates the accumulated phase delay along the beam path through the atmosphere.

The time dependence is found by accounting for the spacecraft motion. We do this by making the apparent spacecraft position y_a, z_a time dependent:

$$\begin{aligned} y_a(t + \Delta t) &= y_a(t) + \dot{y}_a \Delta t \\ z_a(t + \Delta t) &= z_a(t) + \dot{z}_a \Delta t \end{aligned} \tag{C3}$$

where $\dot{y}_a, \dot{z}_a$ give the apparent velocity of the spacecraft through the atmosphere. Finding the correct expression for the apparent velocity of the spacecraft is a tricky proposition. Simply taking derivatives of equations C.1 is not sufficient because the y_s, z_s coordinate system itself is dependent on time because of the refractive effect. In reality, the apparent velocity can be found from the spacecraft velocity in the y_s, z_s plane by

$$\dot{y}_a = \dot{y}_s\left(\frac{R}{R_1}\right) \qquad \text{and} \qquad \dot{z}_a = \frac{\dot{z}_s}{q^2}\left(\frac{R}{R_1}\right). \tag{C4}$$

The quantities $\dot{y}_s, \dot{z}_s$ give the actual spacecraft motion transverse to the beam axis.

Using the time dependence we find the correlation function of χ in time:

$$\begin{aligned}\overline{\chi(t)\,\chi(t+\Delta t)} = k^2 \int dx'\,dx'' \int &\overline{d\nu(k'_y, m; x')\,d\nu^*(k''_y, m'; x'')} \\ &\times \exp\Big(i((k'_y - k''_y)y_a + (m-m')z_a)\Big)\, e^{-i(k''_y \dot{y}_a + m'\dot{z}_a)\,\Delta t} \\ &\times \sin\Big[\frac{R}{2k}(k'^2_y + \frac{m^2}{q^2})\Big]\ \sin\Big[\frac{R}{2k}(k''^2_y + \frac{m'^2}{q^2})\Big]\end{aligned} \tag{C5}$$

This somewhat daunting equation can be simplified by using an identity for random processes. Namely, the correlation of the Fourier coefficients can be rewritten as

$$\begin{aligned}\overline{d\nu(k'_y, m; x')\,d\nu^*(k''_y, m'; x'')} = &\,\mathbf{B}_{n_1}(k'_y, m)\,\mathrm{Corr}_{n_1}(x' - x'') \\ &\times \delta(k'_y - k''_y)\,\delta(m - m')\end{aligned} \tag{C6}$$

(equation 17-43 in Ishimaru; discussed in appendix A in Ishimaru). Once again, $\mathbf{B}_{n_1}$ is a spectral representation of the index of refraction variation n_1. In addition, we have a correlation function in $x' - x''$ written as $\mathrm{Corr}_{n_1}(x' - x'')$. This correlation function is identically unity when $x' - x'' = 0$. The other terms in this equation are Dirac delta functions. Inserting this identity into equation C5 and integrating over k''_y, m', and $x' - x''$ gives

$$\begin{aligned}\overline{\chi(t)\,\chi(t+\Delta t)} = 2\pi k^2 \int dx' \int &dk'_y\,dm\,\mathbf{B}_{n_1}(k'_x\!=\!0, k'_y, m; x') \\ &\times e^{-i(k'_y \dot{y}_a + m\dot{z}_a)\,\Delta t}\ \sin^2\Big[\frac{R}{2k}(k'^2_y + \frac{m^2}{q^2})\Big]\end{aligned} \tag{C7}$$

in which the power spectrum of index of refraction fluctuations is three dimensional, but only the $k'_x\!=\!0$ component is of interest. The component k'_x is the Fourier conjugate of x'. We take the Fourier transform of this last equation in order to find a log-amplitude power spectra. Ishimaru gives the following formula for the log-amplitude power spectrum:

$$W_\chi(\nu) \equiv 2\int_{-\infty}^{\infty} d\Delta t\,\overline{\chi(t)\,\chi(t+\Delta t)}\,\cos 2\pi\nu\Delta t \tag{C8}$$

where ν is the frequency conjugate to elapsed time during the occultation. This is the same as equation A-12 in Ishimaru. Using this definition in conjunction with equation C7 gives

$$\begin{aligned} W_\chi(\nu) = 4\pi^2 k^2 L \int dk'_y \, dm \, \mathbf{B}_{n_1}(k'_x = 0, k'_y, m) \, \sin^2\Big[\frac{R}{2k}({k'_y}^2 + \frac{m^2}{q^2})\Big] \\ \times \Big(\delta(2\pi\nu - k'_y \dot{y}_a - m\dot{z}_a) + \delta(2\pi\nu + k'_y \dot{y}_a + m\dot{z}_a)\Big) \end{aligned} \tag{C9}$$

where L is the radio beam's pathlength through Venus's atmosphere. The quantity W_χ is the most common term in the literature for the power spectrum of log-amplitude fluctuations. Two Dirac delta functions arise because the index of refraction fluctuations in the atmosphere are real quantities as opposed to imaginary quantities. This makes sense because one cannot tell whether a sinusoidal wave in the data has a positive or a negative frequency. In fact it has both.

Equation C9 is consistent with the work of Haugstad (1979) (*c.f.*, equation 2.5) and Woo, Ishimaru and Yang (1980) (*c.f.*, equation 8). The major difference is that we have two Dirac delta functions in our formulation. When implementing turbulence, only one delta function is necessary, as long as an extra factor of 2 is included, because of symmetry of k_x, k_y in the spectrum of turbulence. For gravity wave spectra, similar symmetries are not expected; thus we must retain both delta functions.